Functionalisation of Metal-Organic Frameworks via Post-Synthetic Modification

Amer Hamzah, Harina

Award date:
2017

Awarding institution:
University of Bath

Functionalisation of Metal-Organic Frameworks *via* Post-Synthetic Modification

Harina Amer Hamzah

A thesis submitted for the degree of Doctor of Philosophy

University of Bath
Department of Chemistry

June 2017

To my late grandfather, Hj. Md. Nasir Hj. Hamid

Table of Contents

i. Acknowledgments

First and foremost, I would like to extend my utmost gratitude to both of my supervisors, Prof. Andrew Burrows and Dr. Mary Mahon, who have never failed to provide me with continuous support and guidance throughout the course of my PhD.

I am also grateful to the current and past members of the Burrows group particularly Jane Knichal, Dr. Laura Cadman, Dr. Sébastien Rochat, Dr. William Gee, Dr. Robert Dawson and Dr. Luke Keenan for useful discussions, friendship and entertaining chats in the office.

I am beyond grateful to my family, especially my mum for her emotional support and motivation during my student years, without which, my time being abroad and away from the family would have been difficult. A special thank you goes to my eldest brother, Md. Hafiidz Amer Hamzah, for setting a good example to his younger siblings, by proving that success can be achieved with hard work and pure dedication.

It is also a pleasure to thank all my friends outside of Chemistry for their encouragement and support. A particular mention goes to Poppy Baines, who has provided a supportive ear and for making my PhD journey less stressful and more joyful.

I would like to dedicate this work to my late grandfather, Hj. Md. Nasir Hj. Hamid, who passed away on Dec 7th 2015. He had always been my greatest inspiration by instilling the importance of education in me since I was very young and therefore played a significant role on my success up to this day. May you rest in peace, grandfather.

Finally, I would like to thank both the University of Bath and Majlis Amanah Rakyat for financial support, making the research carried out in this thesis possible.

ii. Abstract

This thesis is built upon two areas of research concerning metal-organic frameworks (MOFs). The first focuses on the functionalisation of MOFs *via* post-synthetic modification (PSM). The second involves the investigation on the potential of MOFs as hosts for insect pheromones.

Chapter 1 introduces the field of MOF chemistry, and covers their properties along with a brief description of their applications. The concept of PSM is introduced and a review of recent literature given. The aims of the thesis are also detailed at the end of this chapter.

Chapter 2 describes the PSM of $[Zr_6O_4(OH)_4(BDC\text{-}NH_2)_6]$, UiO-66-$NH_2$, *via* Aza-Michael reactions. Different functionalities were successfully introduced into its pores and the degrees of conversion were determined *via* ^{1}H NMR spectroscopy. Gas sorption measurements (CO_2 and N_2) of the PSM products were carried out and compared. In particular, two PSM products were shown to exhibit higher CO_2 over N_2 selectivity than that for the starting MOF, UiO-66-NH_2.

Chapter 3 describes a new PSM route in obtaining azole-functionalised MOFs *via* Mannich reactions. The amino groups in three different MOFs were converted into a range of azole-functionalised MOFs with conversions up to 100%. In particular, one of the PSM reactions afforded a new material, formulated as $[Zn_3(BDC\text{-}NH_2)_{1.32}(BDC\text{-}NHCH_2N_2C_3H_3)_{1.68}(C_6H_{12}N_2)]$, based on single crystal X-ray crystallography, ^{1}H NMR and TGA analyses. Gas sorption studies demonstrate increased selectivity for CO_2 over N_2 for the PSM products. One of the modified MOFs was shown to exhibit a high Hg(II) uptake from aqueous solutions.

Chapter 4 introduces the concept of using MOFs as hosts for ant pheromones. The factors which influenced the pheromone loading in zinc and zirconium based MOFs were investigated. The MOFs containing the linker BDC-NHPr (2-(propylamino)benzene-1,4-dicarboxylate) were found to be effective at hosting two types of ant pheromones, 3-octanone and (*S*)-4-methyl-3-heptanone.

iii. List of Abbreviations

AAS	Atomic absorption spectroscopy
AES	Atomic emission spectroscopy
AL	2-Allyl-1,4-benzenedicarboxylate
ALY	2,5-Bis(allyloxy)-1,4-benzenedicarboxylate
ASU	Asymmetric unit
AZPY	4,4'-Azo(bis)pyridine
BBC	4,4,4-(Benzene-1,3,5-triyl-tris(benzene-4,1-diyl))tribenzoate
BDC	1,4-Benzenedicarboxylate
BET	Brunauer–Emmett–Teller
BHEHPI	5,5',5"-((((benzene-1,3,5-triyltris(benzene-4,1-diyl))tris(ethyne-2,1-diyl))-tris(benzene-4,1-diyl))tris(ethyne-2,1-diyl))triisophthalate)
2,2′-BIPYM	2,2'-Bipyrimidine
BPP	1,3-Di(4-pyridyl)propane
BPY	Bipyridine
BTB	4,4′,4″-Benzene-1,3,5-triyl-tris(benzoate)
BTTri	1,3,5-Tri(1*H*-1,2,3-triazol-4-yl)benzene
CAT	Catechol
DABCO	1,4-Diazabicyclo[2.2.2]octane
DBCO	Dibenzylcyclooctyne
DCBP	4,4'-Dicyanobiphenyl
DEF	*N*,*N*-Diethylformamide
DFT	Density Functional Theory
DHBDC	2,5-Dihydroxy-1,4-benzenedicarboxylate
DMDB	2,5- Dimercapto-1,4-benzenedicarboxylate
DMSO	Dimethyl sulfoxide
DMF	*N*,*N*-Dimethylformamide
GCMC	Grand Canonical Monte Carlo
EDX	Energy-dispersive X-ray spectroscopy
EXAFS	Extended X-ray absorption fine structure
FTIR	Fourier transform infrared
H_2ADB	(*E*)-5,5'-(Diazene-1,2-diyl)diisophthalic acid
H_2BDC	1,4-Benzenedicarboxylic acid

H_2BPDC	Biphenyl-4,4’-dicarboxylic acid
H_3BTB	4,4′,4″-Benzene-1,3,5-triyl-tris(benzoic acid)
H_2BTC	Benzene-1,3,5-tricarboxylic acid
H_3BTE	4,4',4"-(benzene-1,3,5-triyltris(ethyne-2,1-diyl))tribenzoic acid
H_2FU	Fumaric acid
HINA	Isonicotinic acid
H_2-1,4-NDC	1,4-Naphthalenedicarboxylic acid
H_2BDC-NH_2	2-Amino-1,4-benzenedicarboxylic acid
H_2BDC-$(OH)_2$	2,5-Dihydroxy-1,4-benzenedicarboxylic acid
HFIP	Hexafluoroisopropanol
HKUST	Hong Kong University of Science and Technology
H_2OX	Oxalic acid
H_2TPDC	*p*-Terphenyl-4,4"-dicarboxylic acid
ICP-AES	Inductively coupled plasma atomic emission spectroscopy
IM	Imidazolate
INA	Isonicotinate
IRMOF	Isoreticular metal-organic framework
IUPAC	International Union of Pure and Applied Chemistry
LAG	Liquid-assisted grinding
MHP	(*S*)-4-Methyl-3-heptanone
MIL	Materials Institute Lavoisier
MMEN	*N*,*N*-Dimethylethylenediamine
MOF	Metal-organic framework
NBIM	5-Nitrobenzimidazolate
NIM	2-Nitroimidazolate
NMR	Nuclear magnetic resonance
NU	Northwestern University
OCT	3-Octanone
PSM	Post-synthetic modification
PSD	Post-synthetic deprotection
PSE	Post-synthetic exchange
PXRD	Powder X-ray diffraction
PZY	Pyrazine
SBU	Secondary building unit
TFE	2,2,2-Trifluoroethanol

TCNE	Tetracyanoethylene
TCPA	Tris((4-carboxyl)-phenylduryl)amine
TCPM	Tetrakis(4-cyanophenyl)methan**e**
TPDC	Triphenyldicarboxylate
TPTZ	2,4,6-Tri(pyridin-4-yl)-1,3,5-triazine
1,2,4-TRZ	1,2,4-Triazolate
UiO	University of Oslo
UMCM	University of Michigan Crystalline Material
ZIF	Zeolitic imidazolate framework

1. Introduction

1.1. A Brief History of Metal-Organic Frameworks

In the past few decades, the study on coordination polymers has increased dramatically due to their potential applications in different fields such as materials science, biochemistry and pharmacology.[1-3] Coordination polymers are compounds consisting of central atoms, usually metal ions or metal ion aggregates coordinated to bridging ligands which can result in one-, two- or three- dimensional networks, Figure 1.1.

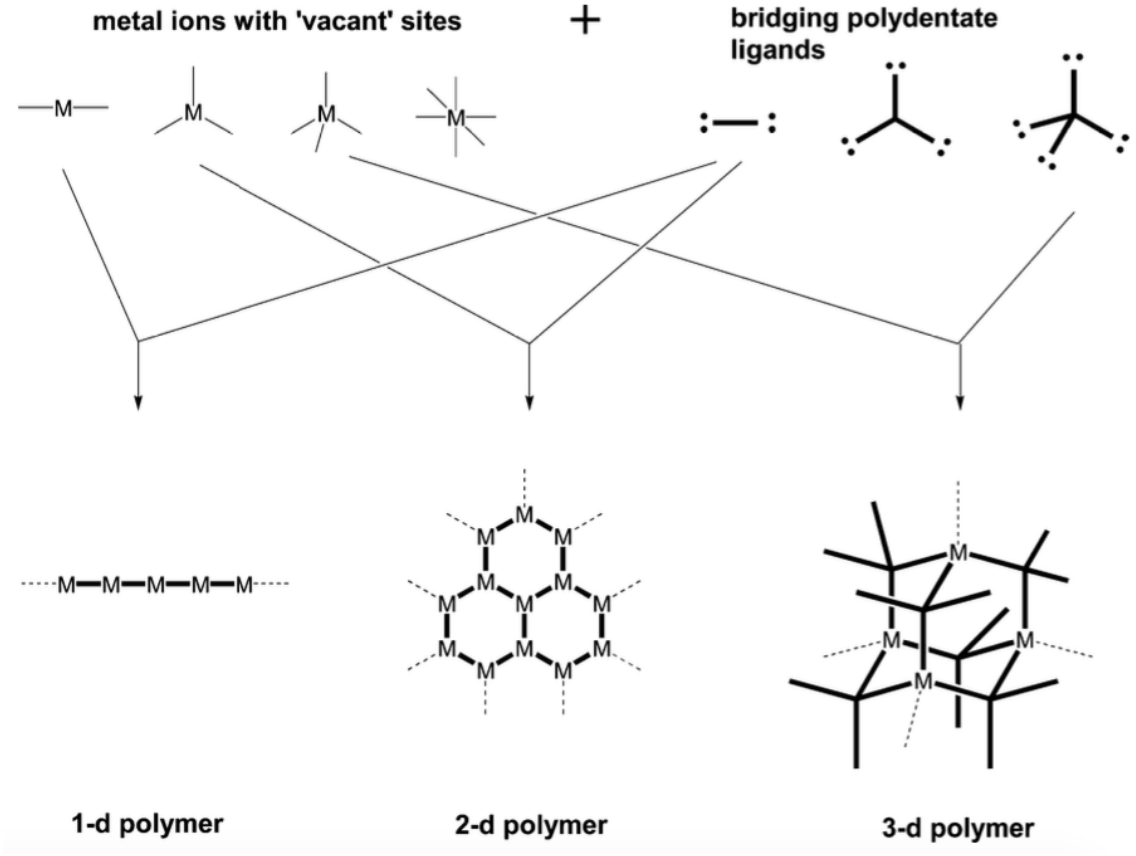

Figure 1.1 Construction of coordination polymers *via* the combination of metal ions/aggregates and bridging ligands with different geometries.[4]

In recent years, much attention has focussed on metal-organic frameworks (MOFs), a class of coordination polymers. This is due to their favourable properties such as high surface areas, high porosities and tunable pore surfaces.[5,6,7] In terms of MOF inception, Yaghi *et al.* are widely known for introducing the term 'metal–organic framework' in a paper published in 1995 but it has been argued that the study of MOFs started prior to this publication.[8] Some confusion has arisen due to different terminologies used which include coordination polymers and coordination networks.[9,10,11] In 2013, IUPAC revised

the definition of coordination polymer, coordination network and MOF as follows:

Coordination Polymer: "A coordination compound with repeating coordination entities extending in 1, 2 or 3 dimensions."

Coordination Network: "A coordination compound extending, through repeating coordination entities, in 1 dimension, but with cross-links between two or more individual chains, loops or spiro-links, or a coordination compound extending through repeating coordination entities in 2 or 3 dimensions."

Metal-Organic Framework: "A Metal-Organic Framework, abbreviated to MOF, is a coordination network with organic ligands containing potential voids."

Based on the above recommendations by IUPAC, it can be deduced that coordination networks are a subset of coordination polymers and MOFs are a further subset of coordination networks.[12]

One of the early reports on coordination networks occurred in 1989, in the work by Hoskins and Robson. They described an infinite framework consisting of copper(II) metal centres linked together by nitrile-containing ligands, tetrakis(4-cyanophenyl)methane, Figure 1.2.[13] The crystalline solid was obtained by the substitution of acetonitrile within $[Cu(CH_3CN)_4]BF_4$ with the nitriles by slow evaporation. The structure is positively charged and counterbalanced by $[BF_4]^-$ anions which could be exchanged by $[PF_6]^-$ by suspending the crystals in a solution of NBu_4PF_6. Based on this finding, Hoskins and Robson anticipated the potential of using a MOF as an ion-exchange medium and a molecular sieve. They also had the foresight to see MOF potential as heterogeneous catalysts, through the introduction of appropriate functional groups on the ligands.

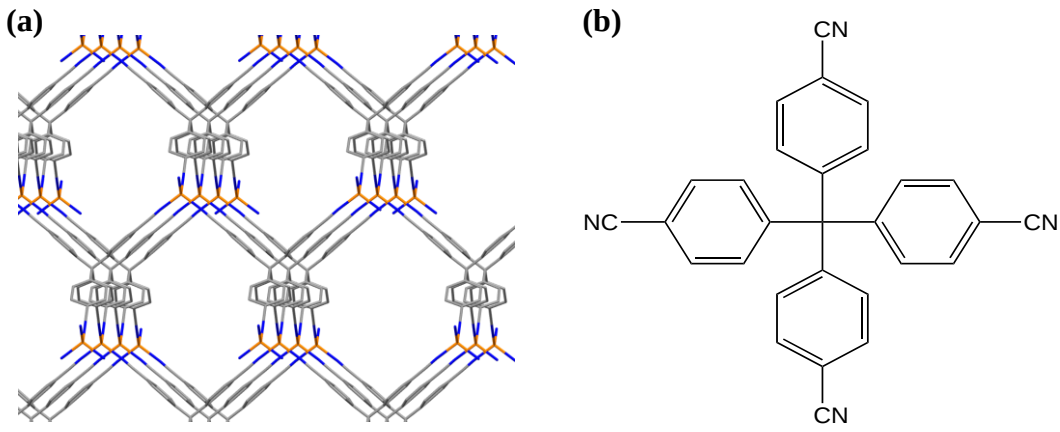

Figure 1.2 (a) Framework of $[Cu(C(C_6H_4CN)_4)]BF_4$. Cu: orange, C: grey, N: blue. Hydrogen atoms and $[BF_4]^-$ anions are ommited for clarity.[13] **(b)** Structure of tetrakis(4-cyanophenyl)methane.

Although the role of MOFs in catalysis was first suggested by Hoskins and Robson, the first actual example was not reported until 1994, when Fujita *et al*. reported a two-dimensional square network $[Cd(4,4'\text{-}BPY)_2(NO_3)_2]$ (BPY = bipyridine), Figure 1.3.[14] They reported that the crystalline material could be used as a catalyst for the cyanosilylation of aldehydes. They also showed that the material was able to selectively clathrate *o*-dibromobenzene and *o*-dichlorobenzene over their *meta* and *para* isomers.

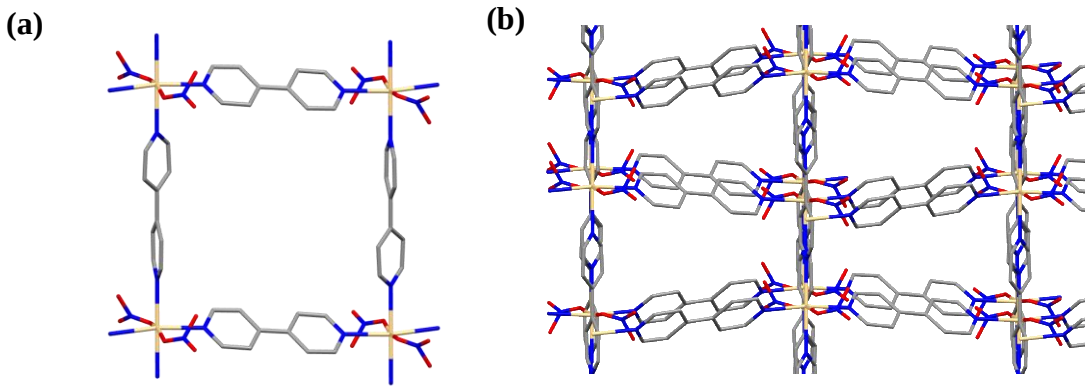

Figure 1.3 (a) A square unit of $[Cd(4,4'\text{-}BPY)_2](NO_3)_2]$. **(b)** View along the *c*-axis showing 2 layers of the square network. Cd: yellow, C: grey, N: blue, O: red. Hydrogen atoms are omitted for clarity.[14]

Secondary Building Units (SBUs) are an important and common concept in MOF chemistry as they form the basis of the design and prediction of MOF topologies. SBUs are aggregates consisting of metal ions and the donor atoms of the bridging ligands.[15] SBUs can be referred to as nodes as they are repeated throughout the network structure. Each SBU is linked together to the neighbouring SBU by the bridging ligands.

An example of an SBU within one of the first reported MOFs, $[Zn_2(BDC)_2(OH_2)_2]$ MOF-2, (BDC = 1,4-benzenedicarboxylate) is shown in Figure 1.4.[16] This common SBU consists of a paddle-wheel unit which is constructed from two metal centres bridged by four carboxylates from BDC ligands, Figure 1.4(a). The SBUs exhibit a square geometry, Figure 1.4(b), and are linked together by the benzene rings to form two-dimensional layered sheets, Figure 1.4(c). The axial positions on the zinc atoms are occupied by water molecules which hydrogen bond with the carbonyl oxygens on the adjacent sheets thus holding the sheets together.

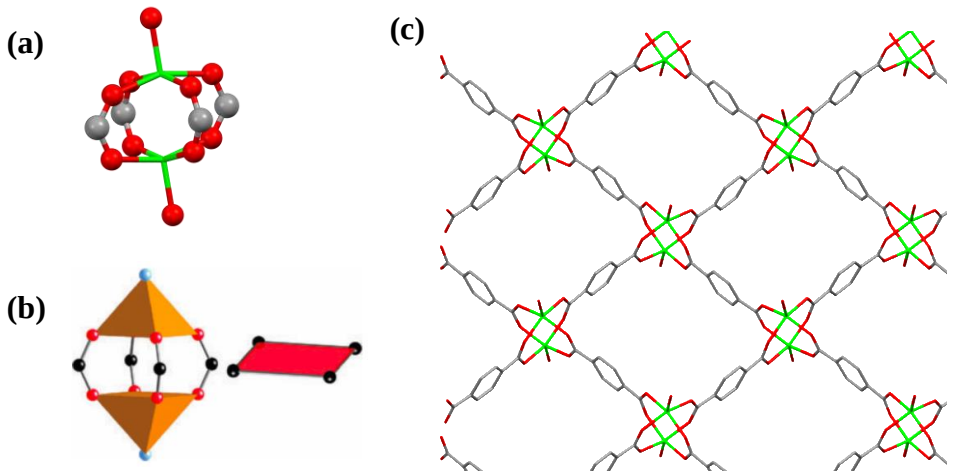

Figure 1.4 (a) SBU of MOF-2 in a paddle-wheel fashion. **(b)** The SBU shown as a square geometry. **(c)** 2-D framework of MOF-2. Zn: light green, C: grey, O: red. Hydrogen atoms are omitted for clarity.[16,17]

As one can expect, the choice of metal centres and organic ligands are important in determining MOF structures. Carboxylates are the most commonly used linkers in MOF construction. There are over 131 different SBUs based on carboxylate linkers and different transition metals, some of which are shown in Figure 1.5.[17] Transition metals are commonly used as they are able to exhibit a variety of coordination geometries thus leading to different types of SBU. Recently, MOFs that contain heavy metal atoms such as bismuth, silver and lead have also been explored.[18,19,20] SBUs typically adopt different geometries compared to that for their metal ions. For instance, the metal centres and SBU in Figure 1.5(a) adopt tetrahedral and octahedral geometry, respectively.

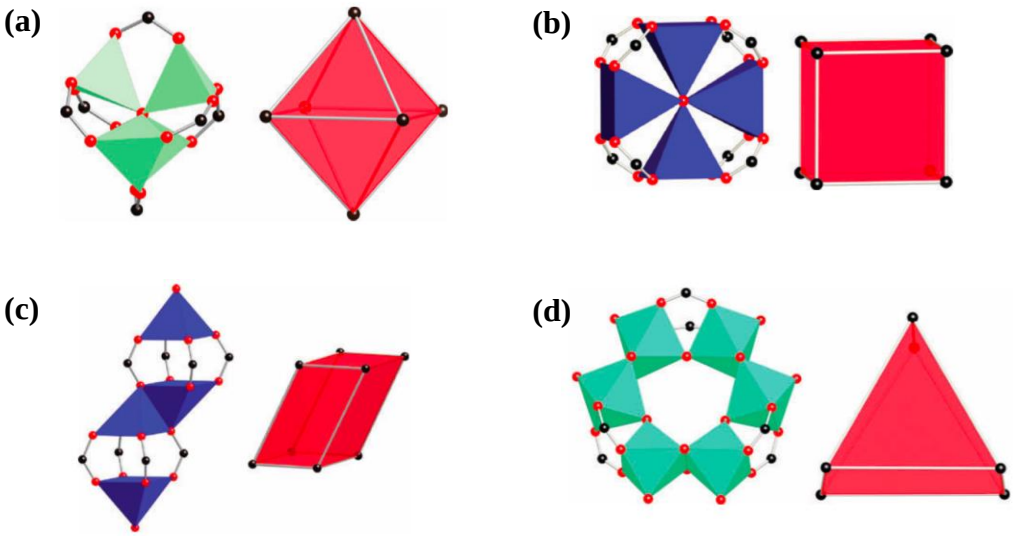

Figure 1.5 Examples of SBUs based on carboxylate linkers. **(a)** Octahedra. **(b)** Cube. **(c)** Rectangular prisms. **(d)** Trigonal prism. Metal centres are located at the polyhedron centres. The SBUs adopt different geometries compared to that for the metal centres. C: black, O: red.[17]

Although it is possible to predict MOF structures by the judicious choice of metal centres and organic linkers, oftentimes the structures are not as one expected them to be. This observation could be explained by the nature of MOF synthesis which is by self-assembly. The typical method of MOF synthesis is by mixing a metal salt with the acidic ligand of interest. Metal ions can adopt different geometries thus making it difficult to control the metal's coordination preference. One way of addressing this issue is by employing a preformed metal aggregate instead of a metal salt in the MOF synthesis. In this way, one could expect that the SBU of the targeted MOF would exhibit the same geometry as the metal aggregate. An example of a three-dimensional MOF which was synthesised via this approach is $[Fe_3O(H_2O)_2(DHBDC)_3](CH_3COO)$ PCN-240, (DHBDC = 2,5-dihydroxy-1,4-benzenedicarboxylate), Figure 1.6(c).[21] PCN-240 was formed by ligand substitution reaction of acetate anions in $Fe_3(\mu_3\text{-}O)(CH_3COO)_6$, which serves as the preformed metal aggregate, with carboxylates from DHBDC ligands. The structural integrity of the $Fe_3(\mu_3\text{-}O)$ core is maintained by strong electrostatic interaction between Fe^{3+} and $\mu_3\text{-}O^{2-}$ while undergoing the ligand exchange reaction. The SBU consists of three iron(III) centres, each coordinated to a μ_3-oxo ligand and four bridging DHBDC ligands, Figure 1.6(a). The axial positions of the iron metals are capped with water molecules. Overall, the SBU exhibits a trigonal prism geometry, Figure 1.6(b).

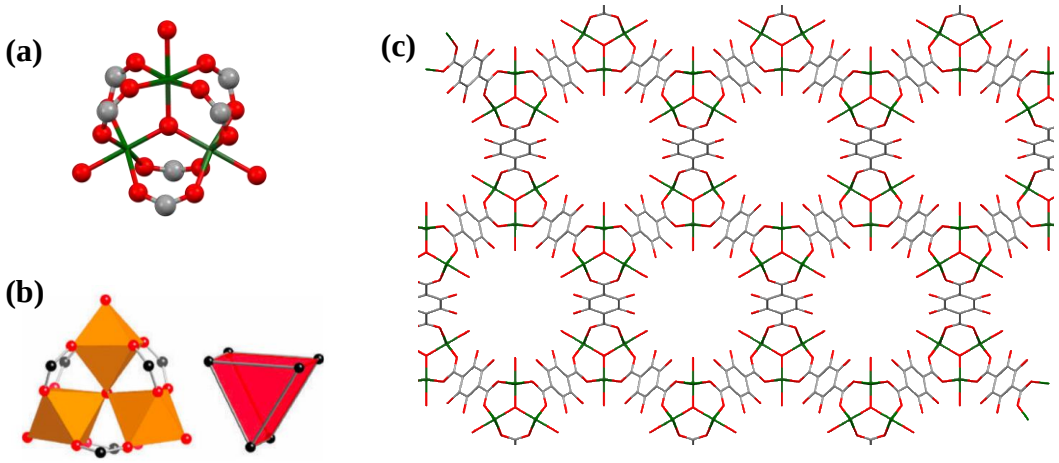

Figure 1.6 (a) SBU of PCN-240. **(b)** The SBU exhibiting a trigonal prism geometry **(c)** View down the channels of PCN-240 with disordered hydroxy groups shown. Fe: dark green, C: grey, O: red.[17]

1.2. MOF Design: Organic Bridging Ligands

1.2.1. Carboxylate-based Linkers

Carboxylate-based linkers are widely used as ligands as the carbonyl oxygen atoms can 'lock' the metal aggregates into place thus leading to rigid network structures. A range of polycarboxylic acids that have been used in MOF syntheses are shown in Figure 1.7.

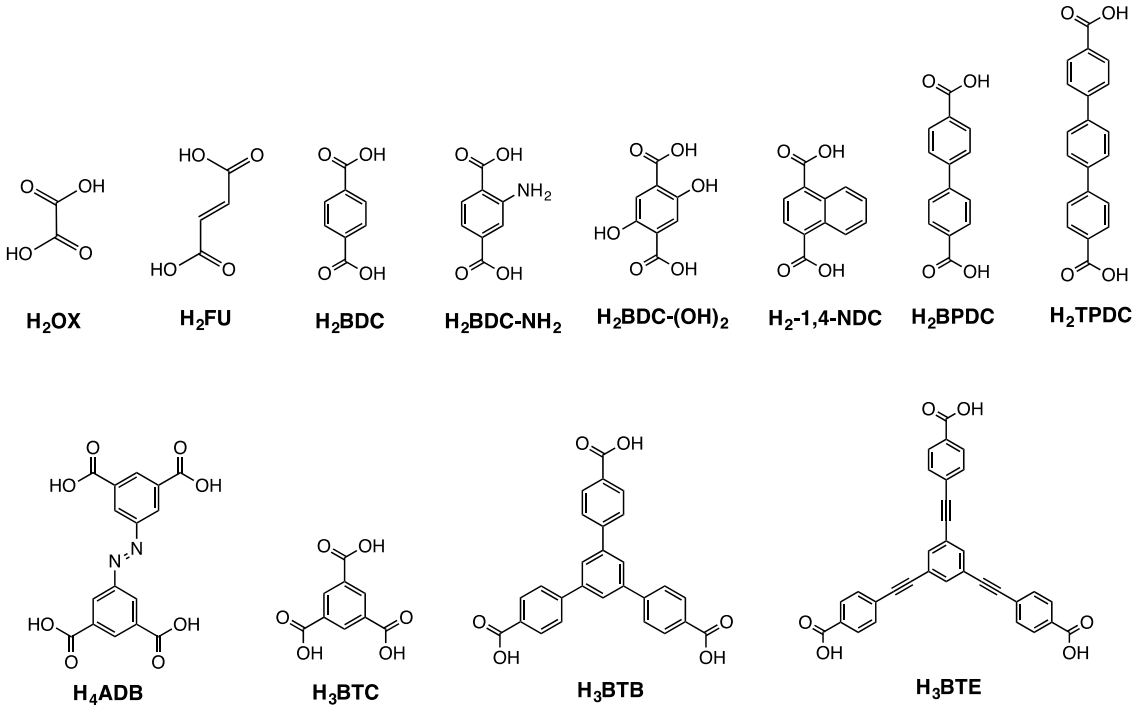

Figure 1.7 Examples of polycarboxylic acids used in MOF syntheses.

One of the most studied MOFs is $[Zn_4O(BDC)_3]$, MOF-5 which was first synthesised by Yaghi *et al*. in 1999.[22] It is widely recognised that the discovery of this MOF ignited the exponential growth of research in MOF chemistry. The SBU of MOF-5 is constructed from four zinc centres linked together by a central O^{2-} and six carboxylates from BDC ligands, Figure 1.8(a), giving rise to an SBU with octahedral geometry overall, Figure 1.8(b). The repetition of this building block leads to a three-dimensional primitive cubic structure, Figure 1.8(c), which upon removal of solvent in the pores leads to a porous solid with a surface area of S_{BET} = 3800 m^2/g. The discovery of high porosity in MOF-5 was a breakthrough in the study of open frameworks, as the coordination networks reported before then were not able to support permanent porosity, with the structures collapsing in the absence of guest molecules in the pores.

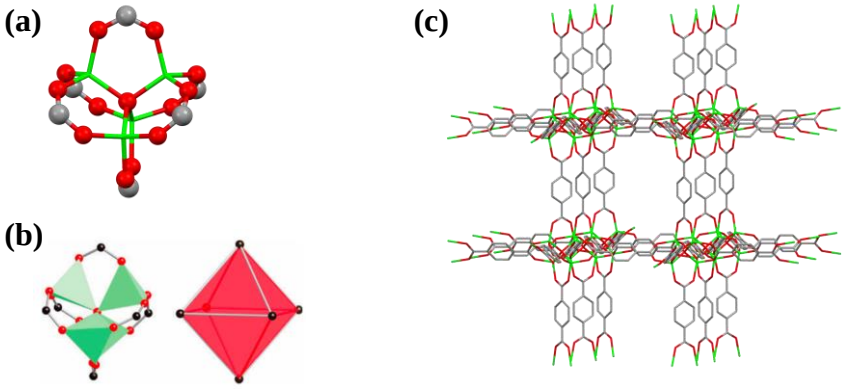

Figure 1.8 (a) SBU of MOF-5. **(b)** The SBU shown as an octahedral geometry. **(c)** 3-D network of MOF-5. Zn: light green, C: grey, O: red.[22,17]

The first report on the synthesis of MOF-5 involved vapour diffusion of triethylamine into a solution of zinc(II) nitrate and H_2BDC in *N*,*N*-dimethylformamide (DMF). Although large crystals (0.2 mm) could be formed by this synthetic method, the yield was very low. In 2002, Yaghi *et al*. addressed this issue by developing a new synthetic method of crystallising MOF-5.[23] This new synthetic route involved heating a solution of $Zn(NO_3)_2 \cdot 4H_2O$ and H_2BDC in *N*,*N*-diethylformamide (DEF) at 105°C to form MOF-5 in 90 % yield. Yaghi *et al*. reported that the DEF molecules could be exchanged with chloroform and a porous network could be obtained by evacuating the chloroform guests under reduced pressure. The open space created by the removal of the guest molecules was calculated to be 79.2 % of the crystal volume which exceeded with that found in zeolites such as faujasite which has free space of 45 - 50 % of the crystal volume. The high free space in MOF-5 resulted in the framework having a low crystal density (0.61 g/cm^3).

Yaghi *et al*. also deduced that the aperture size (diameter of a sphere that would pass through the aperture) of MOF-5 (11.2 Å) could be expanded by using longer bridging ligands. The MOFs that were synthesised using this approach are referred to as IRMOFs (IRMOF = IsoReticular MOF) as they adopt the same topology as MOF-5 (IRMOF-1), Figure 1.9.[23]

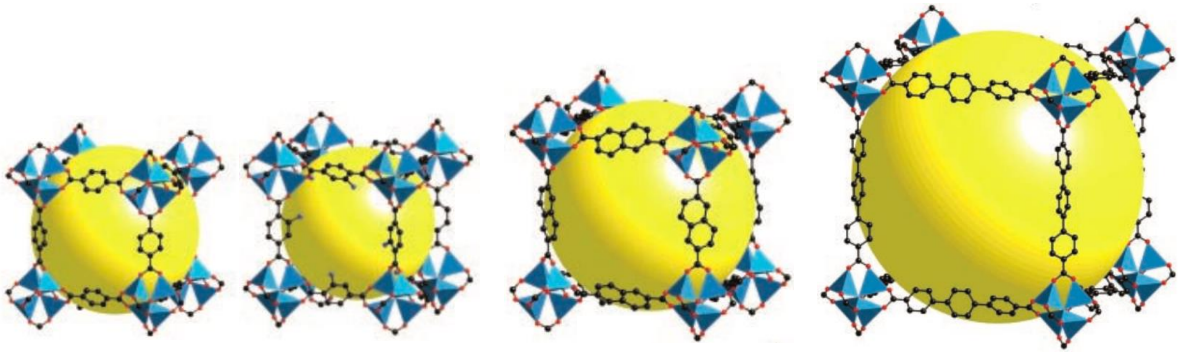

Figure 1.9 Examples of MOFs in the IRMOF series showing functionalisation and augmentation. Zn: blue tetrahedra, C: black, O: red, N: grey. Yellow spheres represent the relative pore sizes.[23]

$[Zn_4O(TPDC)_3]$ IRMOF-16, (TPDC = triphenyldicarboxylate) is isoreticular to MOF-5. The SBUs in IRMOF-16 adopt octahedral geometry, which is the same with that in MOF-5. The SBUs are linked together by TPDC ligands in three-dimensions resulting in a cubic network structure with an aperture size of 19.1 Å. Due to the high void space created by the longer ligand, IRMOF-16 has the highest free volume (91.1 %) and lowest crystal density (0.21 g/cm^3) among the IRMOF series.

One phenomenon that Yaghi and co-workers observed whilst synthesising the IRMOF series was interpenetration. Interpenetration occurs when two or more frameworks mutually intertwine together. This observation is commonly seen in MOFs with large space within the frameworks. For example, IRMOF-15 has the same extended structure as IRMOF-16 but the former has a doubly interpenetrating network, Figure 1.10.[23] The degree of interpenetration (non- or doubly interpenetrated) can be controlled by varying the synthetic conditions.

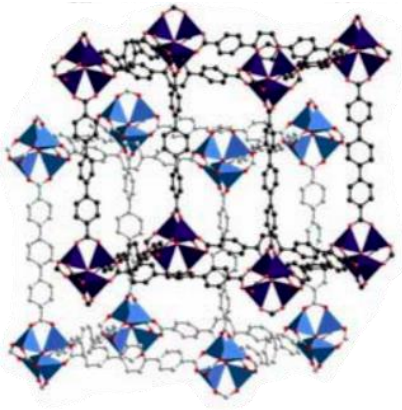

Figure 1.10 3-D framework of IRMOF-15 showing doubly interpenetrating network. Zn: light- and dark blue tetrahedra, C: black and grey, O: red.[23]

The versatility of MOFs has been extended by the ability to incorporate functionalised dicarboxylates into the networks.[23] For example, –Br, $–NH_2$, $–OC_3H_7$, $–OC_5H_{11}$, $–C_2H_4$ and $–C_4H_4$ were successfully incorporated into MOF-5 analogues via the linkers, giving rise to IRMOF-2, IRMOF-3 (Figure 1.9), IRMOF-4, IRMOF-5, and IRMOF-6, respectively. The aperture size of the IRMOFs are smaller than the parent MOF-5, due to the partial blockage of the pore by the functional groups. For example, the aperture size of IRMOF-3 which has amino groups pointing in the pores is 9.6 Å, ~2 Å smaller than that for MOF-5. In terms of thermal stability, it was shown that the IRMOF series could retain their frameworks up to ~450 °C.

Yaghi *et al.* demonstrated that more than one functional groups could be incorporated in a MOF structure. The MOFs, termed "multivariate MOFs" (MTV-MOFs), were synthesised by mixing $Zn(NO_3)_2$ and H_2BDC with up to seven of its derivatives, H_2BDC-R, (R = $–NH_2$, –Br, $–(Cl)_2$, $–NO_2$, $–(CH_3)_2$, $–C_4H_4$, $–(OC_3H_5)_2$, and $–(OC_7H_7)_2$), Figure 1.11.[24]

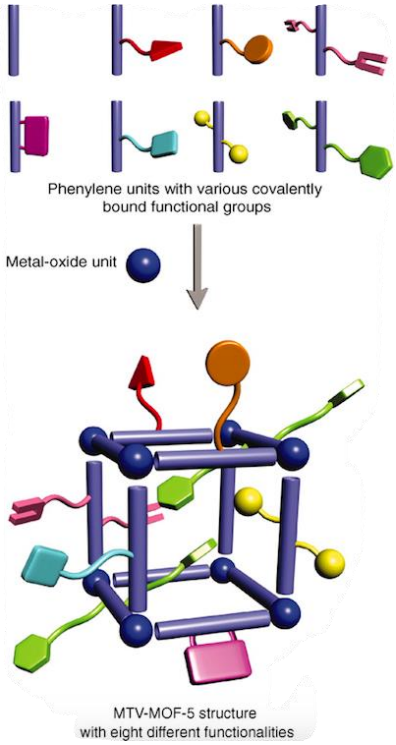

Figure 1.11 An example of MTV-MOF-5 with eight different functionalities incorporated in the framework structure.[24]

The MOFs that have been mentioned thus far contain zinc as the metal centres. One of the drawbacks of zinc-based MOFs is their sensitivity towards moisture. For example, members of the IRMOF series are widely known to have low stability in a humid

environment. Contact with acids and bases is also detrimental to the MOF structures, with the solids undergoing a digestion process which is due to the H^+ ions re-protonating the carboxylates or OH^- coordinating to the zinc(II) cations. Several measures have been taken to address this issue, which include increasing the hydrophobicity of the MOFs.

As the strength of metal-ligand bond is one of the main parameters in determining the stability of a MOF, another method of increasing the material stability is by increasing the charge on the metal centres. This can be achieved by employing tri- or tetravalent cations in the MOF syntheses. A well-known MOF that was synthesised using this strategy is a zirconium-based MOF $[Zr_6O_4(OH)_4(BDC)_6]$ UiO-66, Figure 1.12.[25] The highly charged zirconium cations (Zr^{4+}) have been shown to form strong electrostatic bonds with the oxygen atoms from the BDC ligands. The strong bonds result in the formation of robust SBUs extended in three-dimensions with the MOF possessing strong resistance towards water and acids. The high chemical stability coupled with high decomposition temperature (~540 °C) make UiO-66 favourable for potential industrial applications where harsh conditions are typically required.

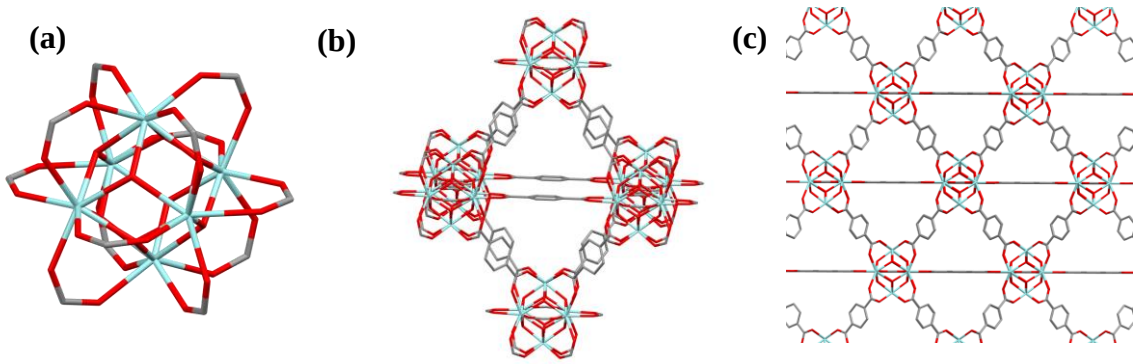

Figure 1.12 (a) SBU of UiO-66. **(b)** Triangular apertures in UiO-66. **(c)** Framework of UiO-66. Zr: cyan, C: grey, O: red. Hydrogen atoms are omitted for clarity.[25]

The MOFs described hitherto involve linear ditopic linkers such as BDC as the organic ligands. Multitopic linkers have also been widely explored as they can give rise to MOFs with different topologies. For example, Furukawa *et al*. used a tritopic linker in the synthesis of $[Cu_3(BBC)_2(H_2O)_3]$ MOF-399, (BBC = 4,4,4-(benzene-1,3,5-triyl-tris(benzene-4,1-diyl))tribenzoate).[26] The SBUs are constructed from $[Cu_2(CO_2)_4]$ paddle-wheel units, Figure 1.13(a), which are linked together by the BBC linkers to form a 3-D network, Figure 1.13(b). The crystal density of MOF-399 with empty pores (0.126 g/cm^3) is the lowest of the MOFs reported to date.

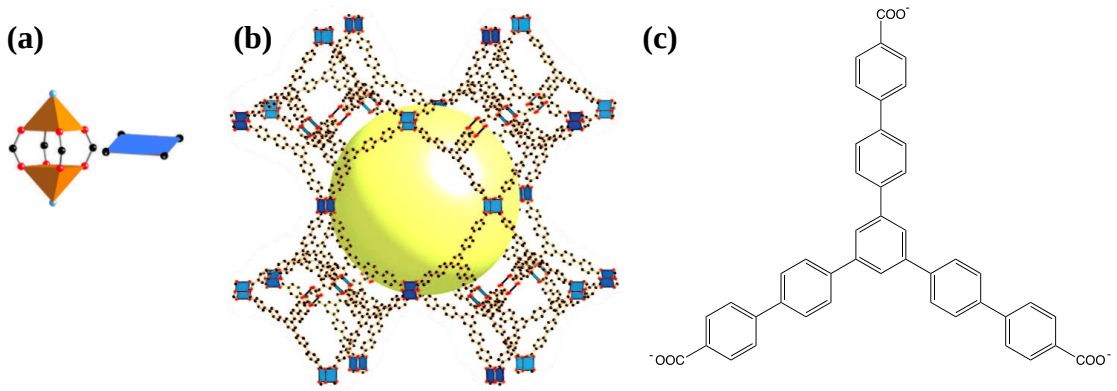

Figure 1.13 (a) SBU of MOF-399 showing a square paddle-wheel unit. **(b)** The repetition of SBUs leading to a 3-D network. **(c)** BBC ligand used in the formation of MOF-399. Yellow sphere represents the pore.[27]

In 2012, Farha *et al*. discovered a remarkably high-pore volume MOF $[Cu_3(BHEHPI)(H_2O)_3]$ NU-110, (BHEHPI = 5,5',5"-((((benzene-1,3,5-triyltris(benzene-4,1-diyl))tris(ethyne-2,1-diyl))-tris(benzene-4,1-diyl))tris(ethyne-2,1-diyl))triisophthalate)), which consists of $[Cu_2(CO_2)_4]$ paddle-wheel units, Figure 1.14(a), coordinated to hexadentate linkers, BHEHPI, Figure 1.14(c).[6] The SBUs are linked together in such a way that three distinct pores are present, Figure 1.14(b). The BET surface area of this MOF is 7140 m^2/g, which is one of the highest determined experimentally. Farha *et al*. reasoned that the high surface area was attributed to the 'open space' created by the acetylene moieties in the BHEHPI ligands. In other words, they postulated that the adsorption sites could be increased by substituting the conventional phenyl struts with acetylenes as linker components.

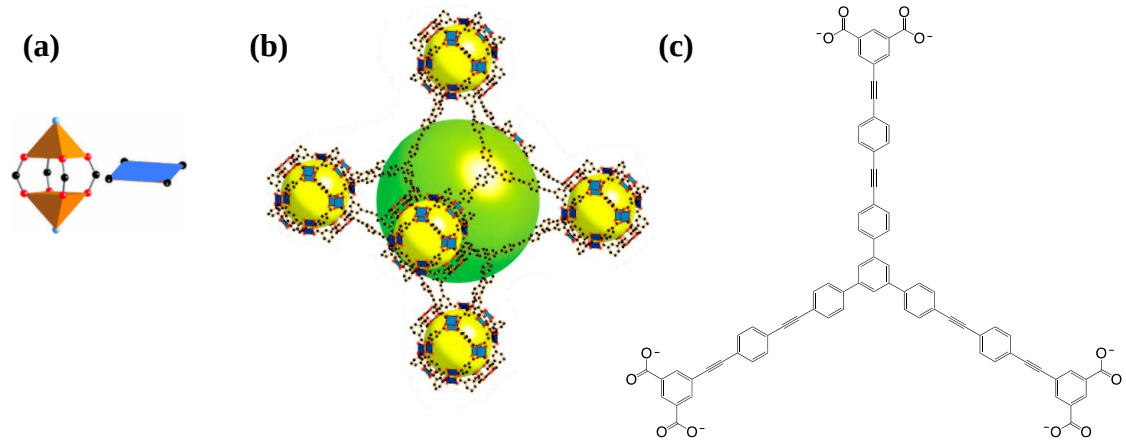

Figure 1.14 (a) SBU of NU-110 showing the square paddle-wheel unit. **(b)** The repetition of SBUs leading to a 3-D network. **(c)** BHEHPI ligand used in the formation of NU-110. Yellow and green sphere represent the pores.[6]

MOFs can also be formed using a combination of two (or more) different organic linkers. For example, Matzger *et al*. reported the structure of a zinc-based MOF containing two different carboxylate linkers, $[(Zn_4O)_3(BTB)_4(BDC)_3]$ UMCM-1, (BTB = benzene-1,3,5-tribenzoate).[28] The SBUs consist of Zn_4O aggregates (as seen in MOF-5) held together by two BDC and four BTB linkers, Figure 1.15(a). The combination of nine SBUs leads to the formation of a 17 Å microporous cage, Figure 1.15(b). Six of the cages are further linked together to form a one-dimensional hexagonal channel with the size of 32 Å, Figure 1.15(c). The BET surface area of UMCM-1 is 4160 m^2/g, one of the highest reported for a MOF. One important aspect to consider whilst synthesising MOFs with two or more linkers is the stoichiometry of the reactants. For example, Matzger *et al*. observed three different phases depending on the ratio of the BDC and BTB ligands used in the synthesis, Figure 1.16.

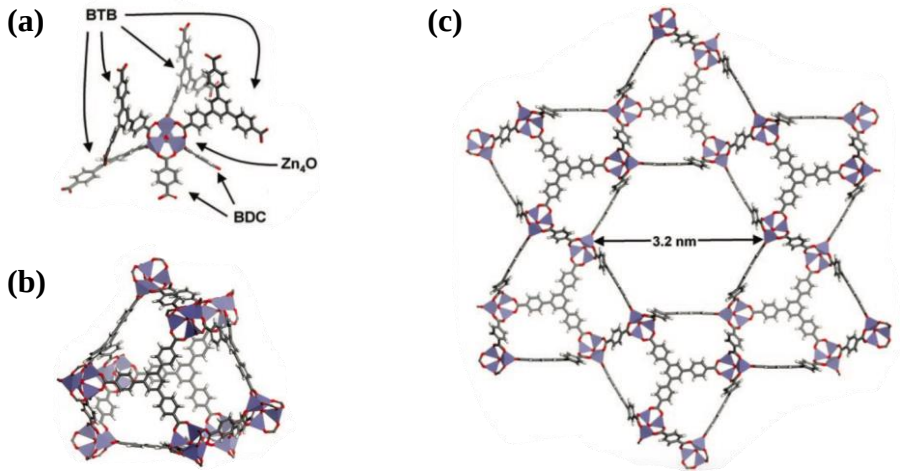

Figure 1.15 (a) BDC and BTB linkers surrounding the SBU of UMCM-1. **(b)** A microporous cage of UMCM-1. **(c)** View down hexagonal channel of UMCM-1.[28]

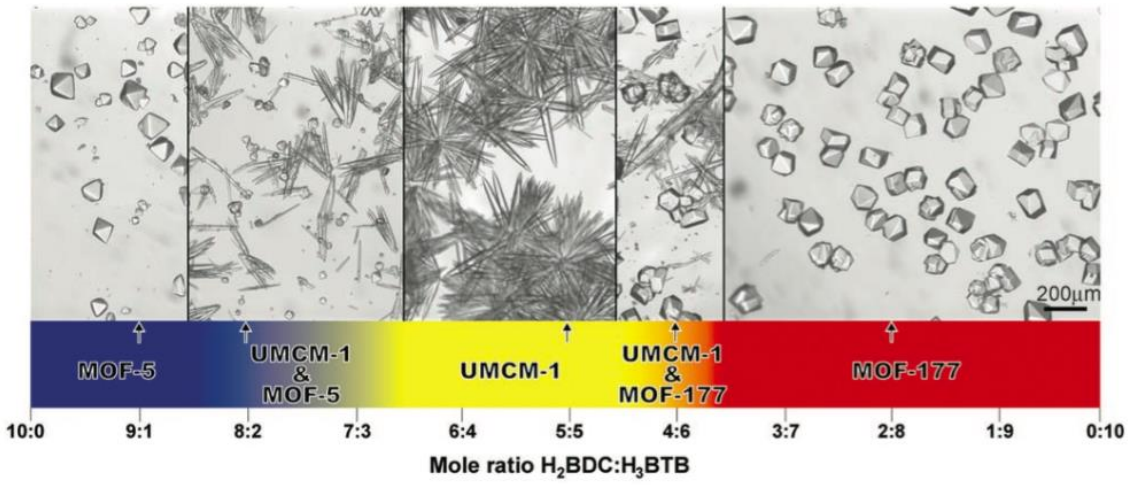

Figure 1.16 Formation of three different MOF phases depending on the stoichiometry of BDC and BTB ligands.[28]

1.2.2. Nitrogen-donor Linkers

Nitrogen-based linkers can also be used to form MOFs. Figure 1.17 shows some examples of nitrogen-donor linkers that have been used in MOF syntheses.

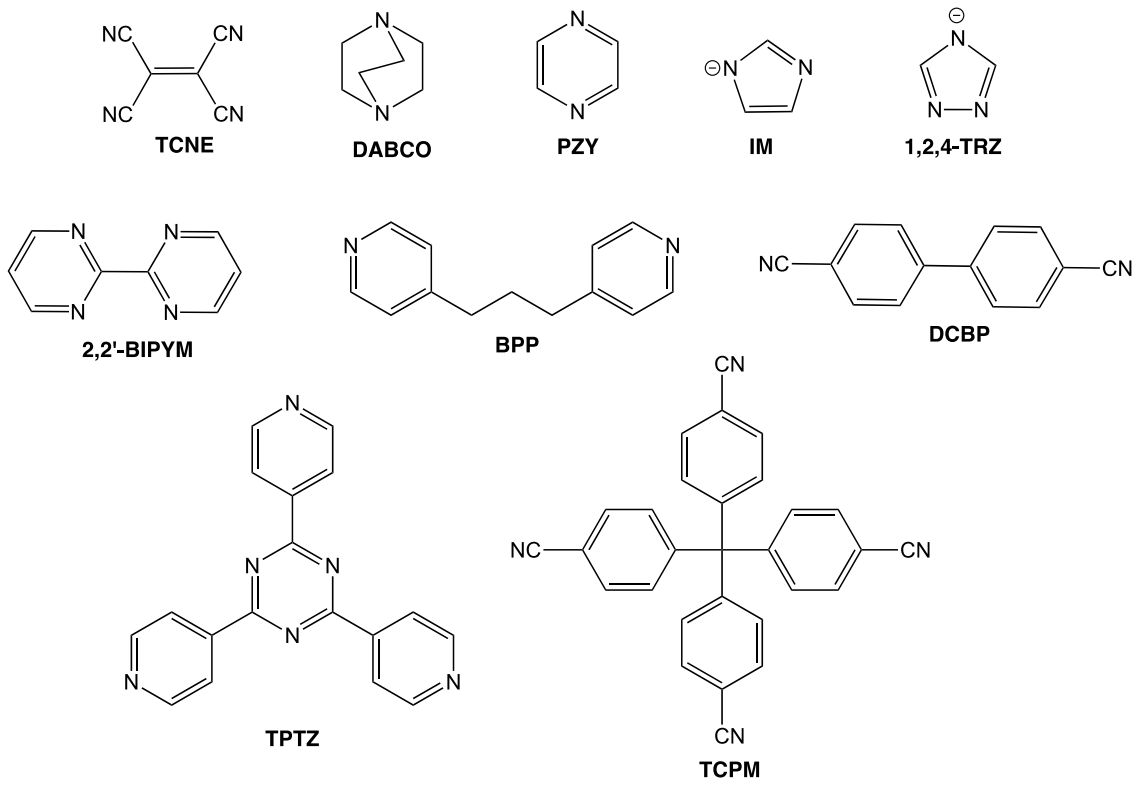

Figure 1.17 A range of nitrogen-donor linkers used in MOF syntheses.

Most of the nitrogen-based linkers are neutral, thus the inclusion of counter ions in the framework structure or pores is necessary to retain a neutral framework. *N*-heterocyclic ligands based on pyridyl, imidazole and tetrazole are generally favoured over alkyl amines due to their better binding ability towards metal centres. An example of a MOF which contains a pyridyl- based ligand is $[Co(AZPY)_2(NCS)_2]$ (AZPY = 4,4'-azo(bis)pyridine).[29] In this MOF, each cobalt centre is coordinated to four pyridine nitrogens and two thiocyanato nitrogens, Figure 1.18(a), which leads to a neutral framework. The MOF possesses rhombus-shaped two-dimensional channels (10 x 10 Å). Due to its large pores, the framework encounters double-interpenetration which gives rise to a three-dimensional gross network. The doubly-interpenetrated network has small channels (3 x 3 Å), Figure 1.18(b), which upon the removal of solvents, shows methane uptake of 0.685 mmol/g. This was one of the earliest reports on the potential of pyridyl-based MOFs to exhibit permanent porosity.

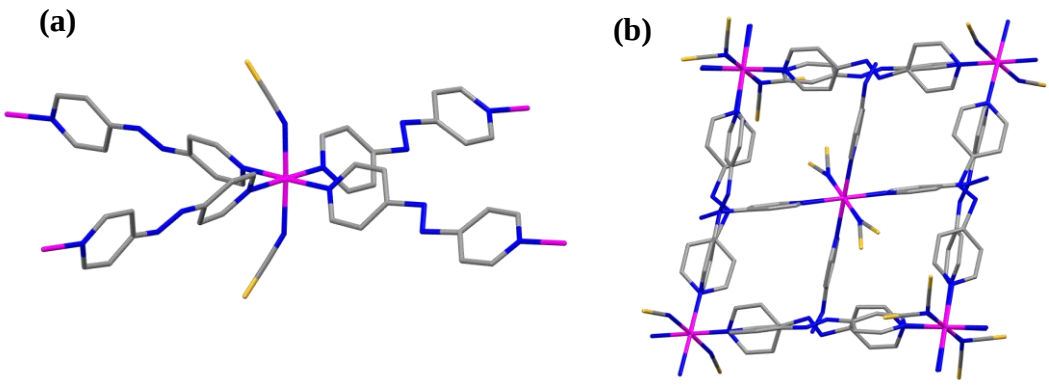

Figure 1.18 (a) Coordination environment of a cobalt centre in $[Co(AZPY)_2(NCS)_2]$. **(b)** View of the small channels formed by the doubly-interpenetrated network. Co: magenta, C: grey, N: nitrogen, S: yellow. Hydrogen atoms are omitted for clarity.[29]

One distinct difference between carboxylates and *N*-heterocyclic ligands is their metal-ligand bond strength. Metal-pyridyl bonds are weaker than metal-carboxylate bonds. The lability of metal-pyridyl bonds can allow for the formation of new SBUs *in-situ* due to the rearrangements of metal ions-ligands during self-assembly process. Additionally, the labile metal-N bonds can give rise to flexible structures. This can be seen in a mixed-ligand MOF $[Zn_2(BDC)_2(DABCO)]$, DMOF-1 (DABCO = 1,4-diazabicyclo[2.2.2]octane) which shows different structural features in different solvent systems.[30] The SBUs consist of $[Zn_2(CO_2)_4]$ paddle-wheel units which are bridged by BDC ligands to form two-dimensional sheets. DABCO ligands act as pillars linking the two-dimensional sheets together to form a three-dimensional framework, Figure 1.19. Kim *et al*. probed the flexibility of this framework and reported that the framework adopts a rhomboidal geometry whilst solvated but square geometry upon the removal of guest molecules. They noted that the structural transformation process is reversible and the framework could shrink back to its original framework (rhomboidal geometry) upon the re-inclusion of the guest molecules.

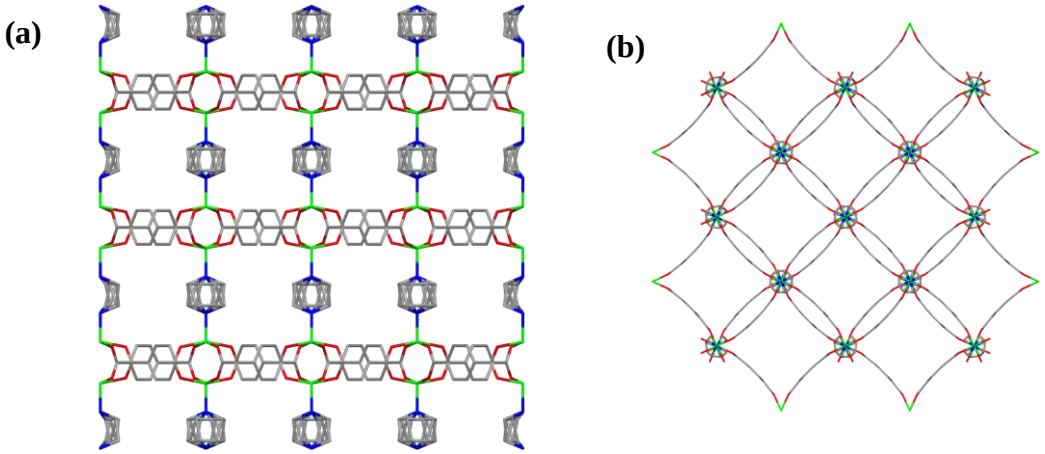

Figure 1.19 (a) View down the *a*-axis of 2-D layered structure of $[Zn_2(BDC)_2(DABCO)]\cdot 4DMF\cdot 0.5H_2O$, DMOF-1, pillared by DABCO ligands. **(b)** View down *c*-axis. Zn: light green, C: grey, N: blue, O: red. Solvent molecules and hydrogen atoms are omitted for clarity.[30]

Another type of *N*-heterocyclic ligand that has gained a lot of attention is anionic nitrogen-donor linkers. One of the advantages of using anionic linkers is that counter-ions are not required to neutralise the framework. This can be beneficial as the presence of counter-ions in the pores could in some cases impede the formation of porous frameworks. Zeolitic imidazolate frameworks (ZIFs) are a class of MOFs which contain anionic imidazolates as the linkers. The term 'ZIFs' was introduced by Yaghi *et al*. by virtue of ZIFs adopting similar structural features as zeolites.[31] In this context, the metal-imidazolate-metal bond angle (~145°) is similar to Si-O-Si bond angle in zeolites. Transition metals such as Zn, Cu and Co are widely utilised in ZIF syntheses. The metal centres in ZIFs generally adopt tetrahedral geometry.

$[Zn(MeIM)_2]$, ZIF-8 (MeIM = 2-methylimidazolate) is one of the prototype ZIFs. It has a sodalite-like structure which is commonly observed in zeolites, Figure 1.20(a).[31,32] The framework has small apertures (3.4 Å) with large pores (11.6 Å) which can be evacuated to form a highly porous network (S_{BET} = 1947 m^2/g). ZIF-8 possesses high chemical stability in comparison to many other MOF structures. For example, it has been shown that the porosity and crystallinity of ZIF-8 can be preserved despite treating the solid in boiling water, organic solvents and alkaline solutions. In addition, ZIF-8 displays high thermal stability (~500 °C) which is potentially attractive for industrial processes.

Although not commonly observed, ZIFs with octahedral metal centres have been successfully synthesised.[31] Yaghi *et al*. reported a mixed-metal ZIF with each metal

centre adopting different geometries. The Zn^{2+} and In^{3+} ions in $[In_2Zn_3(IM)_{12}]$, ZIF-5 (IM = imidazolate) adopt tetrahedral and octahedral coordination environments, respectively. The resulting framework possesses a garnet-like structure, Figure 1.20(b), which has yet to be reported for zeolites. This observation emphasises the diverse ZIF structures that can be synthesised by the variation of metal centres and imidazolate linkers as opposed to zeolites which require templating agents as 'structure-directing' components.

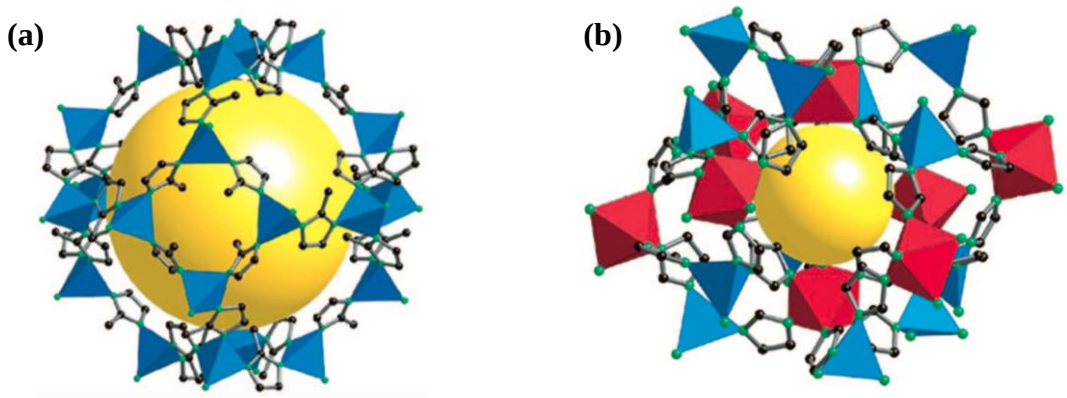

Figure 1.20 (a) Framework of ZIF-8 showing a sodalite-like structure. **(b)** Framework of ZIF-5 showing a garnet-like structure. Yellow spheres represent the pores. Zn: blue, In: red, C: black, N: green. Hydrogen atoms omitted for clarity.[31]

1.3. Syntheses of MOFs

1.3.1. Conventional Synthesis: Electrical Heating

Since the discovery of MOFs, there have been numerous reports on different methods of synthesising MOFs.[33, 34] The most common and widely used method is the conventional synthesis which involves heating the reaction mixture by the means of electrical heating. Conventional synthesis can be further classified into two methods which are solvothermal and nonsolvothermal. According to Rabenau, solvothermal synthesis can be defined as a reaction that is carried out in a closed vessel under autogenous pressure above the solvent's boiling point.[35] Nonsolvothermal synthesis on the other hand, involves a reaction that takes place at or below the solvent's boiling point under ambient pressure.

One of the main parameters of growing MOF crystals is the reaction temperature. In most cases, MOF crystals can be grown from a clear solution given that the nucleation

energy barrier is exceeded. This can be achieved by increasing the concentration of the reactants by increasing the reaction temperature. The choice of solvent is also crucial in MOF syntheses. A good solvent should have the ability to dissolve a wide range of metal salts and acids. Other favourable characteristics include low reactivity and high boiling point. An example of a solvent which obeys these requirements and widely used in MOF syntheses is *N*,*N*-dimethylformamide (DMF). DMF is a polar aprotic solvent which can accept protons from the acids used in the reactions thus it is able to dissolve a range of acids. Furthermore, a wide reaction temperature range can be employed as DMF has a high boiling point (153 °C). Advantages of conventional synthesis include the ease of carrying out the reactions and in most cases, large crystals suitable for structure determination are obtained *via* this method.[36] On the other hand, long reaction times and high reaction temperatures make this method less energy efficient. Figure 1.21(a) shows the synthesis of IRMOF-3 *via* electrical heating.

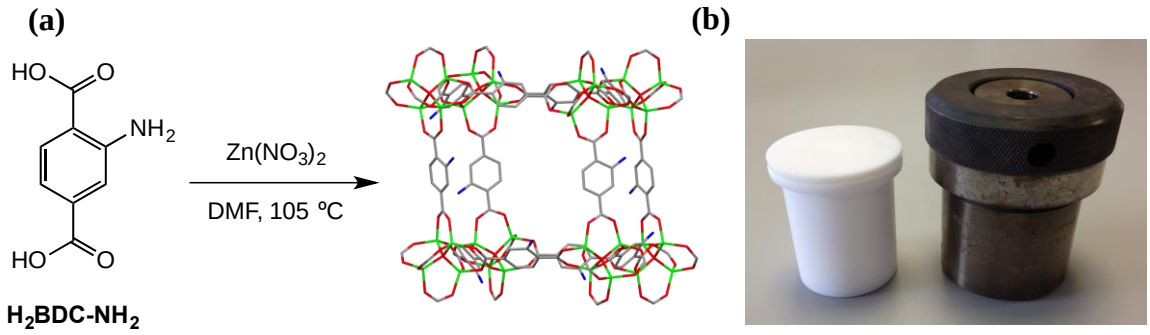

Figure 1.21 (a) Synthesis of $[Zn_4O(BDC\text{-}NH_2)_3]$, IRMOF-3 via electrical heating. **(b)** An autoclave and a Teflon liner used in the synthesis. Zn: light green, C: grey, N: blue, O: red. Hydrogen atoms omitted for clarity.

1.3.2. Solvent Evaporation/Vapour Diffusion

A number of previous work on MOF syntheses focused on solvent evaporation method.[13] Typically, the reagents are fully dissolved in a solvent, which is then allowed to evaporate slowly. As this happens, there is an increase of the solute/reactants concentration above the solubility threshold. This step can induce the precipitation of MOF crystals, Figure 1.22.

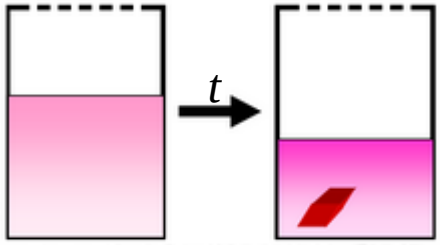

Figure 1.22 Crystal formation *via* solvent evaporation.

Solvent evaporation can be regarded as an energy efficient process as most reactions take place at room temperature and do not require external energy supply. One of the drawbacks of this method is the long reaction times compared to other synthetic methods. In some cases, a mixture of solvents is used in order to aid the solubility of the reactants and shorten the reaction time by speedier evaporation of the low boiling solvents.

Vapour diffusion is an alternative technique used in producing MOF crystals. In a typical vapour diffusion reaction, a solution of metal salt and ligand is placed in an open container, Figure 1.23(a). This container is placed in another larger vessel that contains a volatile base. The larger vessel is sealed and over time the volatile base will diffuse into the reaction mixture thus increasing the acidic ligand:conjugate base ratio by deprotonation. This step can facilitate nucleation of the MOF and subsequently crystallisation. An example of a three-dimensional MOF which was synthesised *via* vapour diffusion is $[Zn(INA)_2]$ (INA = isonicotinate), Figure 1.23(b).[37] Chen *et al.* reported that the diffusion of ammonia into the aqueous solution of $Zn(NO_3)_2$ and HINA (HINA = isonicotinic acid) induced a pH gradient on the surface of the solution which led to optimum conditions for crystal growth.

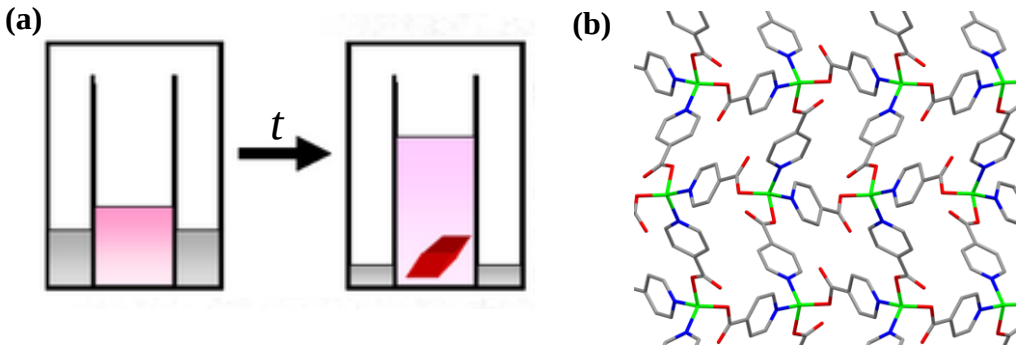

Figure 1.23 (a) Crystal formation *via* vapour diffusion. **(b)** View down the *b*-axis of $[Zn(INA)_2]$. Zn: light green, C: grey, N: blue, O: red. Hydrogen atoms omitted for clarity.[38]

1.3.3. Microwave-Assisted Synthesis

Microwave-assisted synthesis is an alternative method of producing MOFs using microwave radiation. The energy or heat required to drive the chemical reactions originates from the collisions between molecules as they attempt to align themselves in an electromagnetic field. One of the advantages of microwave-assisted synthesis is shorter reaction times due to direct heating of the solvent which arises from direct interaction of molecules and radiation. MOFs successfully synthesised using microwave-assisted synthesis include MOF-5 and $[Cu_3(BTC)_2]$ HKUST-1, (BTC = 1,3,5-benzenetricarboxylate), Figure 1.24(a). Choi *et al*. reported that MOF-5 microcrystals (2 - 4 μm) could be synthesised in 9 minutes at 95 °C *via* microwave-assisted synthesis.[39] Similar observations were noted for the microwave-assisted synthesis of HKUST-1, in which crystals of HKUST-1 were obtained in a short reaction time (30 minutes) at 180 °C.[40] Schlesinger *et al*. reported that the choice of solvent has an effect on the reaction rate and product yield, Figure 1.24(b). Although fast reactions can be anticipated, obtaining single crystals can be challenging due to the high nucleation rates. Thus, microwave-assisted synthesis is normally tailored for the synthesis of nano- or microcrystalline materials.

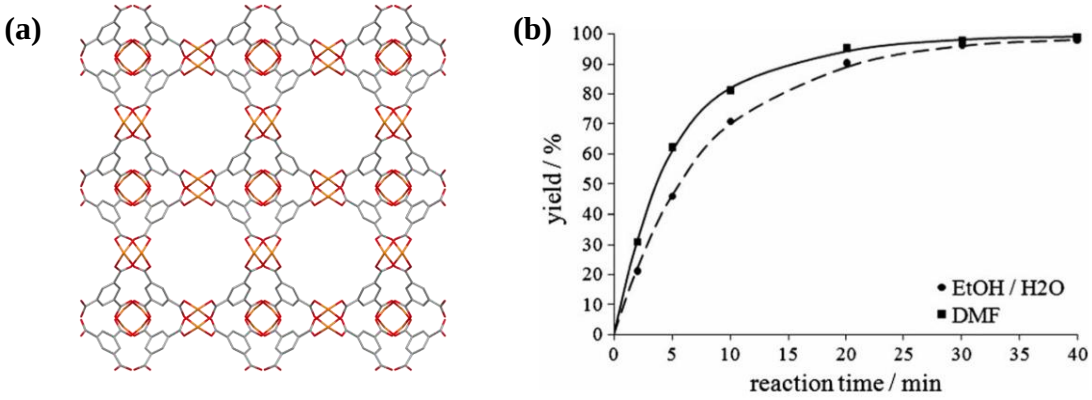

Figure 1.24 (a) Framework of HKUST-1 viewed along [100] direction. **(b)** Yield of HKUST-1 depending on the reaction time and solvents in a microwave-assisted synthesis. Cu: orange, C: grey, O: red. Hydrogen atoms omitted for clarity.[40]

1.3.4. Electrochemical Synthesis

In 2005, researchers at BASF developed a synthetic method for producing MOFs, which was termed electrochemical synthesis.[41] This method eliminates the use of metal salts with the potential of affording products with high purity due to the absence of

anions such as nitrate and chloride used in other synthetic methods. In a typical electrochemical reaction, metal ions are continuously fed into the reaction medium which contains a ligand and a conducting salt *via* anodic dissolution. This method is very desirable in large scale processes, as the reactions can be carried out continuously, leading to higher yields in comparison to normal batch type reactions. A number of zinc(II) and copper(II) based MOFs have been successfully synthesised using this method such as ZIF-8 and HKUST-1.[41, 42]

1.3.5. Mechanochemical Synthesis

All of the synthetic methods described thus far require the presence of solvent in the reactions. Elimination of, in particular, organic solvents in syntheses is advantageous, as it addresses some environmental issues related to the treatment of liquid waste. Mechanochemical synthesis is a solvent-free method to produce MOFs which can be carried out at room temperature. The method is based on the cleavage of intramolecular bonds due to mechanical force followed by chemical transformations. First reported for MOFs in 2006, reaction times are typically short (10 - 60 min) and generally afford micro- or nanocrystalline products.[43] In some cases, metal oxides can be used instead of metal salts thus leading to non-toxic water as the only side-product. Liquid-assisted grinding (LAG) is a modified mechanochemical synthesis which requires the addition of a minute amount of solvent to assist with the mobility of reactants on the molecular level. This typically accelerates the reactions thus products are obtained at a shorter time in comparison to conventional mechanochemical synthesis. A series of isostructural MOFs, [Ln(BTC)(H_2O)] (Ln = Y, Sm, Gd, Tb, Dy, Er, Yb) were successfully synthesised using the LAG method employing a small quantity of DMF.[44]

1.3.6. Sonochemical Synthesis

Sonochemical synthesis was first used in the formation of MOFs in 2008, with the primary aim of investigating energy efficient and green methods of producing crystalline MOFs.[45] This method is based on ultrasound wave to produce small bubbles or cavities which produce ultrasonic energy with temperatures reaching 5000 K and pressures of up to 1000 bar. Chemical reactions can take place in the cavity, on the surface, or in the bulk media. Qiu *et al.* discovered that [$Zn_3(BTC)_2$], Figure 1.25(b),

could be obtained at room temperature in an ultrasonic bath.[45] They reported that the reaction time had an important role in the size and product morphology. Spherical particles (100 – 200 nm) were obtained in short reaction times (5 and 10 min) whilst needle-shaped crystals up to 900 nm length were produced with longer reaction times (30 and 90 min), Figure 1.25(c).

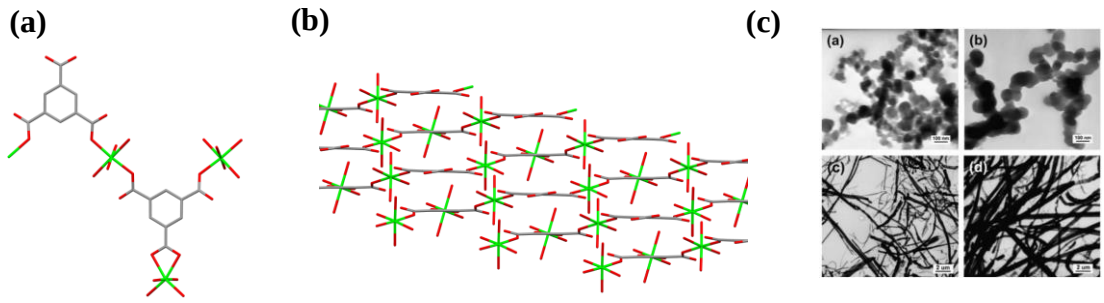

Figure 1.25 (a) Metal coordination in $[Zn_3(BTC)_2]$. **(b)** Layers of $[Zn_3(BTC)_2]$ view down the *b*-axis. **(c)** TEM images of $[Zn_3(BTC)_2]$ synthesised using sonochemical synthesis for various reaction times: (a) 5, (b) 10, (c) 30, and (d) 90 min. Zn: light green, C: grey, O: red. Hydrogen atoms omitted for clarity.[38, 45]

1.4. MOF Applications

1.4.1. MOF Activation

One of the main reasons for the growing interest in MOFs is the possibility to use them in a multitude of applications such as gas storage and separation, catalysis, drug delivery, and in fuel cells.[18, 46-48] These are made possible by the favourable characteristics of MOFs such as high surface area, high porosity, and high thermal stability.[6, 23, 31] The majority of MOFs are synthesised in the presence of solvents and in some cases, unreacted starting materials and/or by-products are trapped within the pores of the resulting MOFs. In order to use the MOFs in different applications, the removal of guest molecules within the pores, termed *activation*, is essential. Careful consideration should be taken whilst activating MOFs, as in some cases, the removal of guest molecules can lead to the collapse of the network structures. To date, there are a variety of activation methods that have been explored. In general, the most suitable method for the activation of a specific type of MOF relies on its chemical and thermal stability and the interactions between the framework and guest molecules.

Solvent-exchange and conventional activation (heat and vacuum treatment) are the most common methods of activating MOFs. These two methods are frequently combined

together, in order to optimise the activation process and obtain the highest surface area for a MOF. For example, Cohen *et al*. reported that IRMOF-3 could be activated by exchanging DMF used in the synthesis with a low boiling solvent, $CHCl_3$ followed by vacuum drying of the crystals at 75 °C.[49]

In some cases, a different method such as activation by supercritical CO_2 is required to empty the pores. This method is an optimisation of the solvent-exchange process whereby the solvent used in the MOF synthesis is exchanged with liquid CO_2 at high pressure (above 73 atm). The MOF containing liquid CO_2 is then heated above 31 °C and transformed into supercritical CO_2 and left to evaporate thus causing the supercritical-to-gas phase change. The merit of this approach is the absence of the surface tension associated with liquid-to-gas phase transitions. It is known that surface tension can lead to the collapse of MOF structures. A number of MOFs with the highest surface areas such as NU-110 (S_{BET} = 7140 m^2/g) were activated using this technique.[50] Furthermore, Nelson *et al.* emphasised the advantage of using supercritical CO_2 as a means of activation by describing the high surface areas of some IRMOF series.[51] For example, they reported that the surface area for IRMOF-3 was increased by 1.6-fold (S_{BET} = 2850 m^2/g) when using supercritical CO_2 as the activation method as opposed to conventional activation.

Another technique that utilises the absence of surface tension to minimise the effect of structure collapse is freeze-drying. This technique involves the sublimation of benzene in order to generate porosity in MOFs. Non-carcinogenic cyclohexane can also be used instead of benzene as described by He *et al*. for the activation of $[Zn_2(TCPA)(IM)]$, FIR-3 (TCPA = tris((4-carboxyl)-phenylduryl)amine).[52] The sample of FIR-3 was first soaked in cyclohexane at 60 °C for 3 days, followed by freezing the suspension at 0 °C for 5 hours. Sublimation of cyclohexane occurred whilst the sample was placed under vacuum in an ice bath for 24 hours.

1.4.2. Gas Adsorption and Storage

For many years, N_2 adsorption at 77 K has been widely used as a standard method to probe the surface area of porous materials.[53] N_2 is used as adsorbate due to its low cost and inertness. The calculation of surface areas is carried out using Brunauer–Emmett–

Teller (BET) or Langmuir analyses derived from the N_2 adsorption isotherms.[54, 55] In general, the former is a more popular approach, and this is partly attributed to numerous computational studies which demonstrate the reliability of this method, by showing high similarities between the computational and experimental values.[56, 57]

Porous materials are typically classified according to their adsorption isotherms. IUPAC has identified six types of isotherms, Figure 1.26, which explain the relationship between the shape of the isotherms and pore sizes (< 2 nm = microporous, 2 - 50 nm = mesoporous and > 50 nm = macroporous).[58]

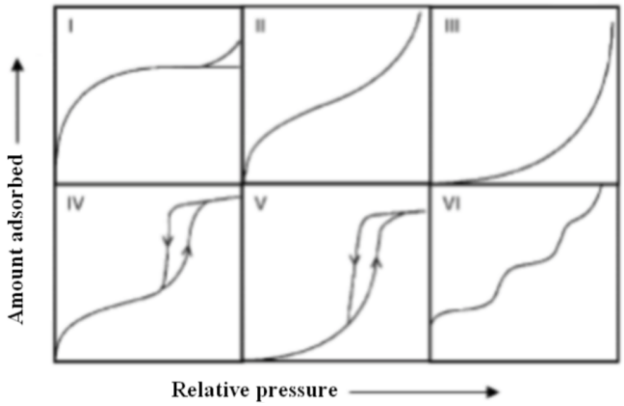

Figure 1.26 Adsoprtion isotherm classifications by IUPAC.[58]

A type I isotherm is characteristic of a microporous material in which the amount of adsorbate increases steeply at low relative pressure before reaching a plateau once the available adsorption sites are occupied. Type II isotherms are commonly seen in non- and macroporous materials where unrestricted monolayer and multilayer adsorption is observed. Another pattern that is commonly seen in non-porous materials is the type III isotherm in which low adsorption at low gas pressure indicates weak interactions between the adsorbent and adsorbate. Furthermore, only multilayer adsorption is observed (monolayer formation is absent) in the type III isotherm. Meso- and macroporous materials commonly exhibit type IV isotherms where complete pore filling occurs and a hysteresis loop is observed during the desorption step due to capillary condensation in the pores. Type V isotherms, on the other hand, are characteristic of mesoporous materials. A type VI isotherm has a stepwise layer upon layer adsorption and is only observed in macroporous materials.

A MOF can exhibit micro-, meso- or macroporosity depending on its structure. The

wide range of pore sizes in MOFs makes them suitable for different applications. In recent years, there has been a growing interest in developing MOFs as adsorbents for CO_2 capture. CO_2 is the primary anthropogenic greenhouse gas and is well-known for being a major contributor to global warming. The concentration of CO_2 in the atmosphere has been increasing exponentially and is expected to reach 550 ppm by 2050 even if CO_2 emission remains stable.[46] The criteria that a MOF needs to have in order to be considered as a material for CO_2 capture varies according to specific applications. For example, high CO_2 loading at low pressure (~0.15 bar) is desirable if a MOF was to be used to capture CO_2 from flue gas. On the other hand, applications such as CO_2 capture from natural gas require a MOF to have a high adsorption capacity at high pressures (60-70 bar). Nonetheless, some of the important criteria for a good CO_2 adsorbent include high CO_2 selectivity over other gases, ease of regeneration and high stability towards water and contaminants.

$[Mg_2(DHTP)]$ CPO-27(Mg,) (DHTP = 2,5-dihydroxyterephthalate) is considered to be one of the most promising MOFs in terms of adsorption capacities at low pressures (30 wt%, 1 bar, 298 K).[59] The MOF resembles honeycomb-like structure with one-dimensional channels (11-12 Å), Figure 1.27(a). The water molecules attached to the metal coordination sites can be removed by thermal treatment to yield the activated framework structure, Figure 1.27(b). The activated framework has a high concentration of open metal sites (OMS), which can act as primary coordination centres for certain guest molecules and it has been reported that the high CO_2 adsorption capacity in CPO-27(Mg) is due to the strong interactions between CO_2 and the OMS.

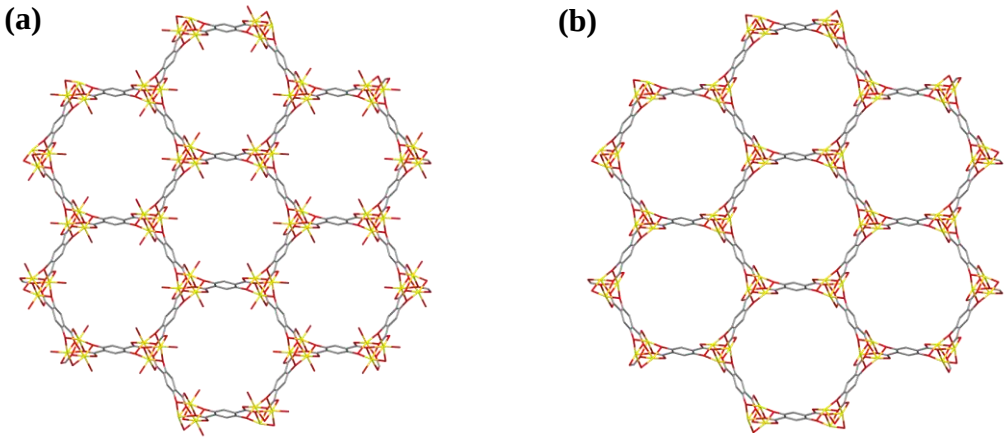

Figure 1.27 (a) View of 1-D channels of CPO-27(Mg) showing the oxygen from water molecules protruding into the pores. **(b)** Activated framework of CPO-27(Mg) showing open metal sites (OMS) upon removal of coordinated water molecules via thermal treatment. Mg: yellow, C: grey, O: red. Hydrogen atoms are omitted for clarity.[59]

Another strategy that can be used to improve the CO_2 capture performance in a MOF is to have basic nitrogen-containing organic groups, alkylamines in particular, protruding into the pores. Electrostatic forces and chemisorptive interactions between the amine groups and CO_2 molecules are generally responsible for the enhanced CO_2 adsorption. For example, Long *at el*. reported that the amine containing MOF $[(Cu_4Cl)_3(BTTri)_8(MMEN)_{12}]$ MMEN-Cu-BTTri, (BTTri = 1,3,5-tri(1*H*-1,2,3-triazol-4-yl)benzene, MMEN = *N*,*N*-dimethylethylenediamine) exhibits a 3.5 fold increase in CO_2 adsorption capacity (10 wt%, 1 bar, 298 K) compared to the non-functionalised parent Cu-BTTri framework.[60] MMEN-Cu-BTTri was synthesised by grafting MMEN onto the OMS of Cu-BTTri, Figure 1.28.

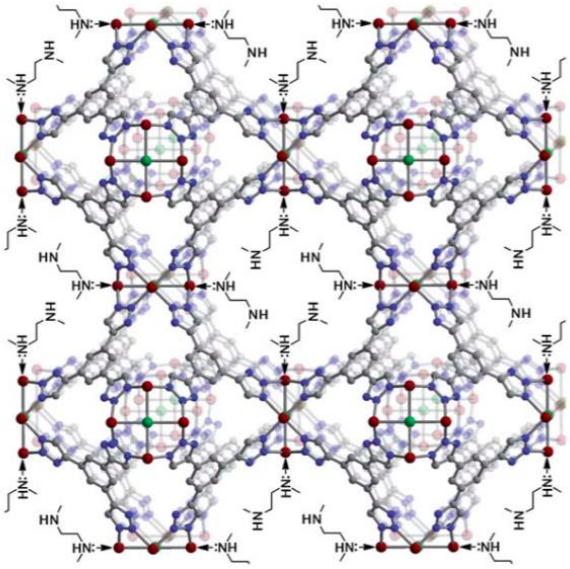

Figure 1.28 Incorporation of MMEN on the open metal sites (OMS) of Cu-BTTri framework. Cu: green, C: grey, N: blue, O: red. Hydrogen atoms are omitted for clarity. [60]

In addition to amine-containing ligands, other polar functional groups such as hydroxy, nitro, cyano, thio, and halide groups have been shown to enhance CO_2 adsorption capacity.[46] For example, the MOF [Zn(NBIM)(NIM)] ZIF-78, (NBIM= 5-nitrobenzimidazolate, NIM = 2-nitroimidazolate) exhibits the largest CO_2 adsorption capacity (60.2 cm^3 cm^{-3}) within the ZIF series due to the presence of polar nitro groups protruding into the pores, Figure 1.29.[32]

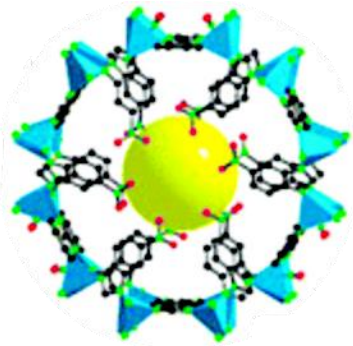

Figure 1.29 Framework of ZIF-78 showing nitro groups in the pores. C: black, N: green, O: red. Zn metals are located at the tetrahedral centres. Hydrogen atoms are omitted for clarity. Yellow sphere represents the pore.[32]

1.4.3. Removal of Environmental Contaminants

In recent years, the removal of heavy metal ions and organic contaminants from wastewater has become an emerging application of MOFs.[61] This is due to the possibility to tailor MOF surfaces towards specific targets. Contamination of wastewater from domestic activities and industrial processes continues to be a pressing issue as it can cause detrimental impacts on the environment and human health. A number of MOFs have been shown to effectively remove hazardous organic molecules. These include $[Fe_3O(BDC)_3(DMF)_3]\cdot FeCl_4$, MOF-235 for the removal of organic dyes (methylene blue and methyl orange) and UiO-67 for the removal of organophosphates.[62, 63]

Unlike many organic contaminants, inorganic heavy metal pollutants are non-degradable, thus necessitates the use of materials that can directly capture these toxic molecules. The breakthrough in arsenic decontamination was reported in 2015, when Wang *et. al.* observed a significant arsenic uptake capacity in UiO-66.[64] The adsorption capacity (303 mg/g) is the highest reported to date and exceeds that for commercial adsorbents such as activated alumina, activated carbon and powdered zeolite. The high arsenic uptake in UiO-66 is attributed to the presence of terminal –OH groups in the SBUs which act as binding sites for arsenate, As(V), Figure 1.30(a). This conclusion was based on the FTIR spectrum of the arsenate-loaded sample in which a new band corresponding to Zr-O-As group was observed. They also proposed that adsorption could take place by exchanging some BDC ligands with arsenate, Figure 1.30(b).

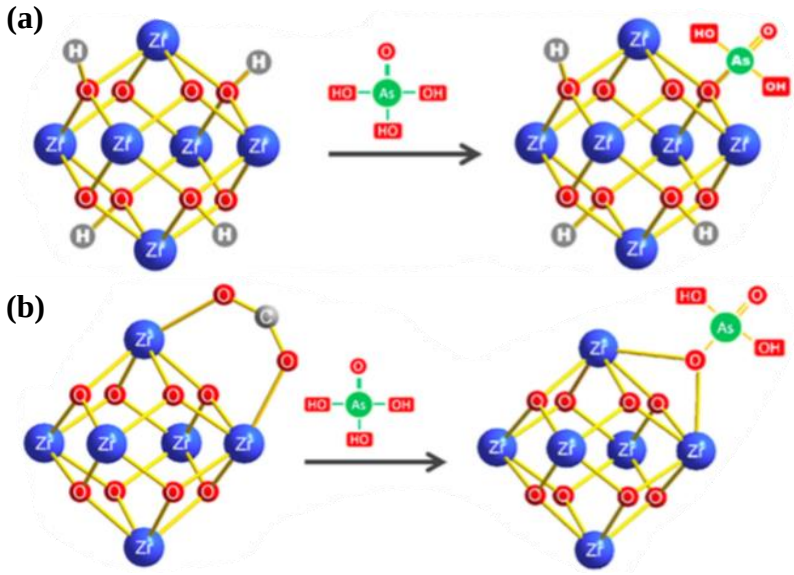

Figure 1.30 Proposed adsorption mechanism of arsenate on UiO-66 *via* (a) coordination at -OH groups and (b) BDC ligand replacement.[64]

In 2013, Yee *et. al.* reported a high mercury loading in a thiol-functionalised MOF $[Zr_6O_4(OH)_4(DMDB)_6]$ UiO-66-$(SH)_2$, (DMDB = 2,5- dimercapto-1,4-benzenedicarboxylate), Figure 1.31(a).[65] The significant mercury uptake from a $Hg(NO_3)_2$ solution (99.9%) was attributed to the high percentage of thiol groups protruding into the pores. UiO-66-$(SH)_2$ was also shown to effectively adsorb mercury from the vapour phase. It was shown that the UiO-66-$(SH)_2$ host framework featured a nearly white photoluminescence which was distinctly quenched after mercury uptake, Figure 1.31(b).

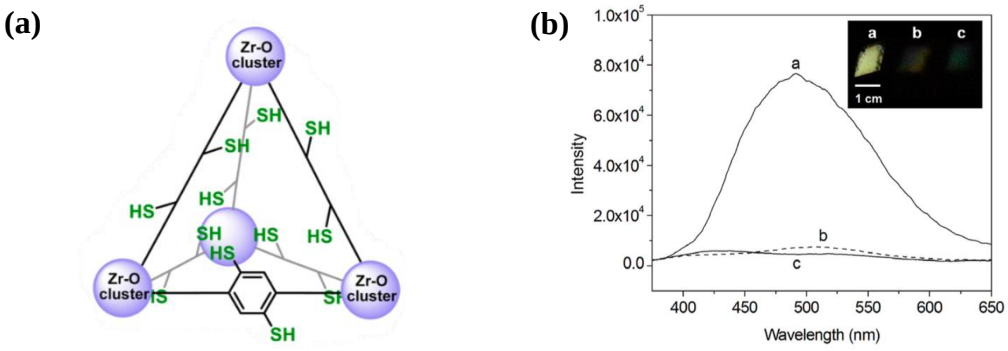

Figure 1.31 (a) A tetrahedral cage of UiO-66-$(SH)_2$ showing thiol groups protruding into the pores. **(b)** Solid state emission spectra of UiO-66-$(SH)_2$ samples: (a) as-synthesised sample; (b) post-treatment with aqueous solution of $HgCl_2$; (c) post-treatment with Hg(0) vapor. The inset shows photographs of samples a−c under 365 nm UV radiation.[65]

1.5. Post-Synthetic Modification of MOFs

1.5.1. Definition, Significance and Post-Synthetic Modification Classification

In recent years, the field of post-synthetic modification (PSM) has gained a lot of attention within the MOF community.[66, 67] PSM is defined as a process by which a pre-formed MOF is transformed into a new MOF *via* crystal-to-crystal transformation. PSM is of interest as it can allow for the formation of MOFs which cannot be formed by direct synthesis. Simple functional groups such as amines and halides can be incorporated in the pores by reacting the functionalised linkers with the metal centres in the MOF syntheses. More reactive functional groups however, are difficult to incorporate in the pores as they may coordinate to the metal centres thus taking part in the SBU formation. This can lead to a MOF with different topology. Furthermore, some functional groups are intolerant towards the synthetic conditions used in MOF syntheses. These limitations can be addressed by utilising PSM as an alternative route to obtain functionalised MOFs. Additionally, MOFs that are formed *via* PSM typically have different physical/chemical properties from the starting MOFs. These include surface area, porosity and affinity towards certain gases. Thus, it is possible to tune the properties of MOFs *via* PSM by introducing specific functionalities into the pores.

PSM can be classified according to the methods by which the transformations take place. The most common methods are described below, and the schematic representation of each method is shown in Figure 1.32:

a) *Covalent PSM*: this is the most studied method of PSM, and involves the covalent modification of a linker ligand.

b) *Dative PSM*: this method involves the coordination of a metal ion to a ligand.

c) *Inorganic PSM*: this method involves the modification of the SBUs and includes the modification of the metal ions or the exchange of a linker with a different one.

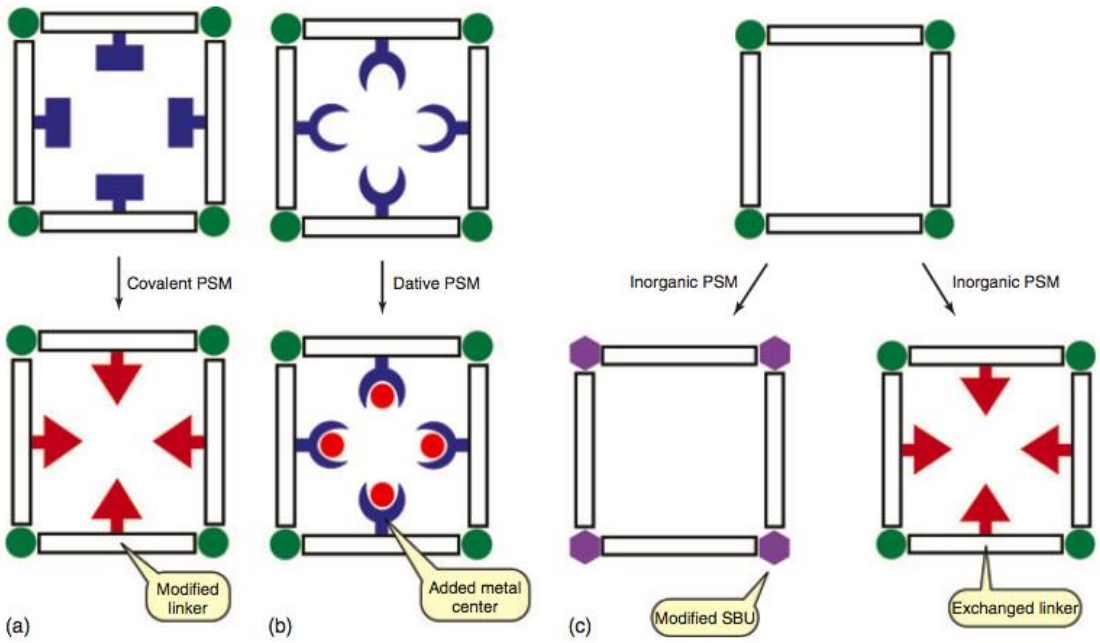

Figure 1.32 Schematic representation of the three categories of PSM; (a) covalent PSM, (b) dative PSM and (c) inorganic PSM.[68]

Due to space limitation, this review is mainly focussed on covalent PSM although dative and inorganic PSMs are also presented to a lesser extent. To date, there are a variety of covalent PSM reactions that have been reported by different research groups. These include amide coupling, imine condensation, *N*-alkylation, urea formation, salicylaldehyde condensation, click reactions, and bromination.[5, 69-74] The scope of PSM reactions is vast, due to different transformations that can be applied to a specific functional group. For instance, most of the PSM reactions mentioned earlier are carried out on an amino group which demonstrates the versatility of this group towards PSM.

1.5.2. PSM Characterisation

There are various characterisation techniques that can be used to determine the effectiveness of a PSM reaction. One of the requirements in order to be deemed successful is that a MOF has to maintain its crystallinity upon PSM. The most common method to investigate the crystallinity of a MOF is powder X-ray diffraction (PXRD). The PXRD pattern of a MOF upon PSM should normally be similar to that for the starting MOF. However, in the case of flexible MOFs such as [M(OH)BDC] MIL-53, (M = Al, Cr, Fe, Ga, In) PSM can induce a change in the pore shape, which is reflected by the change in the PXRD patterns. Another method that can be used to examine the

structure of a MOF upon PSM is single crystal X-ray diffraction. Although this technique can be useful for validating the topology of the PSM product, this method is limited to MOFs with single crystals. Furthermore, in some cases, the scattering of electron densities caused by disorder can prevent full information of the chemical entities present in the PSM product.

Nuclear magnetic resonance (NMR) spectroscopy is employed by MOF chemists to examine the chemical transformations that may have occurred upon PSM. For example, ^{1}H NMR spectroscopy is commonly used to gauge the percentage conversion of a functional group into a different group. Prior to an NMR measurement, a MOF is typically digested in an acid or a base solution together with an NMR solvent. Care has to be taken in order to ensure that no additional reaction occurred on the PSM product within the NMR solution.

In some cases, solid state NMR is employed to address the issue of possible reactions of NMR solvent with a PSM product. Nonetheless, solution NMR is generally preferred over solid state NMR as the latter often provides ambiguous information due to broad signals. Qualitative analysis of a PSM product can also be carried out using Fourier transform infrared (FTIR) spectroscopy. This technique is carried out on a solid sample, thus eliminating the possible interference due to NMR solvent in the case of solution NMR.

For PSM processes that involve substitution of metal centres (or coordination of metal ions), various characterisation methods have been used to provide information of the metal ions and their environments. These include atomic absorption spectroscopy (AAS), inductively coupled plasma atomic emission spectroscopy (ICP-AES), energy-dispersive X-ray spectroscopy (EDX), X-ray photoelectron spectroscopy and extended X-ray fine structure (EXAFS) spectroscopy.

The physical properties of a PSM product such as surface area, pore size and porosity can be examined using gas sorption measurements. In some cases, these criteria can be validated *via* computational methods much as Grand Canonical Monte Carlo (GCMC) and Density Functional Theory (DFT).[57]

1.5.3. Early Reports of PSM

The idea of modifying a MOF pore surface to tailor its properties for different applications was first suggested by Hoskins and Robson in 1989.[13] Nonetheless, the experimental work was not reported until 1999, when Lee *et al*. described the PSM of a hydroxyl functionalised MOF [Ag(**L**^{1})]OTf.[75] The reaction involved transforming the hydroxyl group into an ester, Scheme 1.1, with the complete conversion determined *via* ^{1}H NMR and IR spectroscopy. They reported that the framework structure remained the same after the PSM reaction.

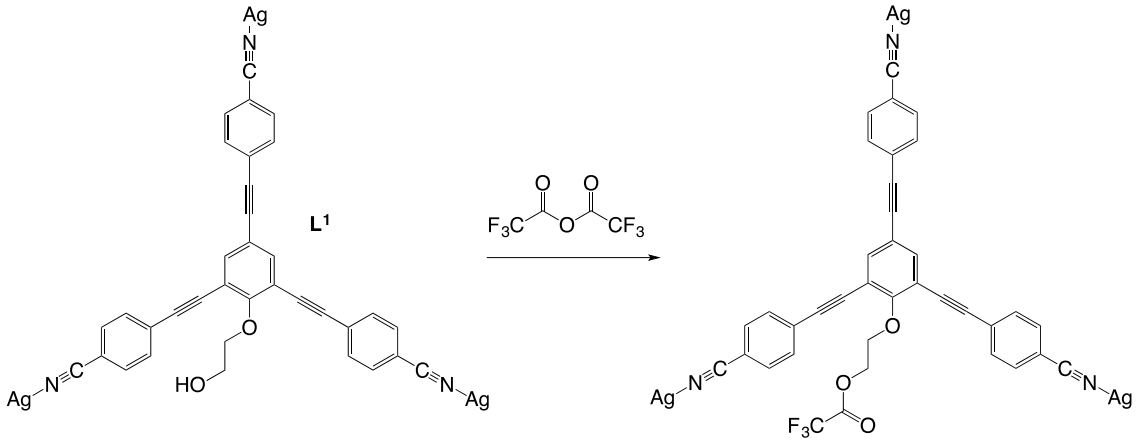

Scheme 1.1 Schematic representation of the conversion of a hydroxyl group into an ester within [Ag(**L**^{1})]OTf.[75]

In 2000, Kim *et al*. prepared a homochiral MOF [Zn_3O(**L**^{2})$_6$], D-POST-1 with pyridyl groups protruding into the pores.[76] The pyridyl groups underwent *N*-alkylation with iodomethane to form *N*-methyl pyridinium ions, Scheme 1.2, as evidenced by ^{1}H NMR analysis. They reported that the pore size of D-POST-1 can be tuned by varying the degree of *N*-alkylation of the pyridyl groups. For example, the pore volume of D-POST-1 was reduced by 14% and 60% upon *N*-alkylation with iodomethane and 1-iodohexane, respectively. The quantity of counterions that can be included in the pores also decreases as the pore volume becomes smaller.

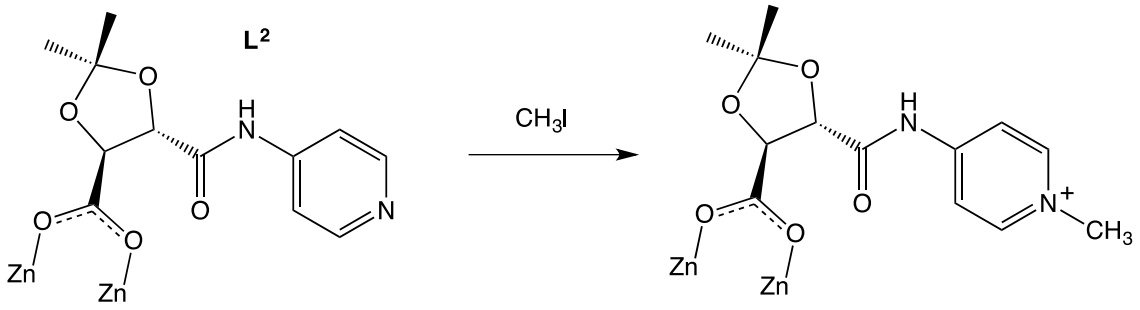

Scheme 1.2 Schematic representation of the conversion of a pyridyl group into *N*-methyl pyridinium ion within D-POST-1.[76]

The work on inorganic PSM was first reported by Williams *et al*. in 1999.[77] They demonstrated that the terminal water molecules in $[Cu_3(BTC)_2]$, HKUST-1, which are coordinated to copper metal centres, can be substituted by pyridine, Scheme 1.3. The substitution reaction was accompanied by the colour change of the crystal from dark blue to green. Williams *et al*. also anticipated that substitution of copper centres with other metals such as rhodium may allow the incorporation of catalytic sites in the framework.

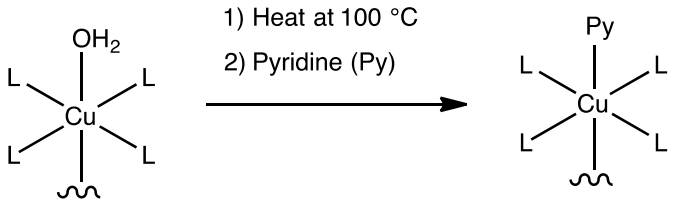

Scheme 1.3 The substitution of a terminal water molecule with pyridine in HKUST-1.[77]

1.5.4. PSM on Amino Group

MOFs with amino functionalised linkers have been widely studied in the field of PSM due to the large number of reactions that can be carried out on this functional group. One of the most studied reactions is the conversion of an amine into an amide upon treatment with an acid anhydride or acid chloride, Scheme 1.4. First introduced by Cohen *et al*. in 2007,[78] the reaction was initially studied on zinc-based MOFs although since then aluminium, gadolinium, iron, chromium and zirconium systems have also been investigated.[79-83]

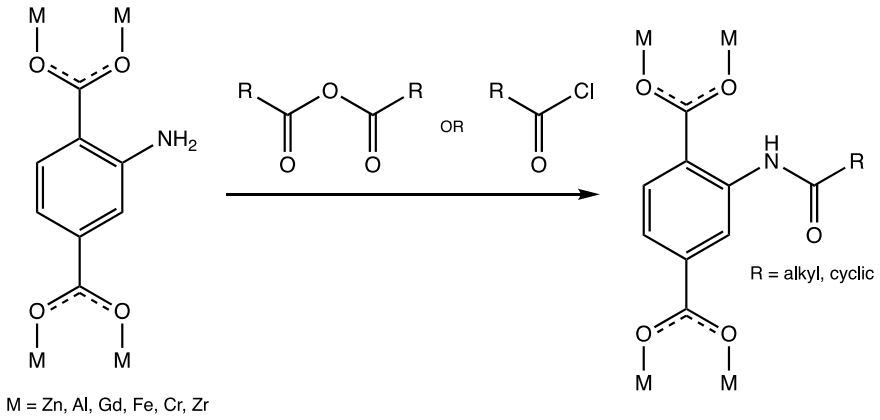

Scheme 1.4 Schematic representation of the conversion of an amine into amide group upon treatment with acid anhydrides or acid chlorides.

One of the factors which dictates the degree of conversion is the size of the R group. Generally, the larger/longer the group, the lower the conversion. For example, Cohen *et al.* observed greater than 90% conversions of IRMOF-3 into the corresponding amides [Zn_4O(BDC-NHC(O)R)$_3$], upon treatment with RCO_2COR (R = Me, Et, Pr, Bu and C_5H_{11}).[49] However, lower conversions were observed when longer alkyl R groups were present in the reagents (46% when R = C_9H_{19} and 20% when R = $C_{16}H_{33}$).

Another factor that has a significant impact on percentage conversion is the aperture size. In general, MOFs with large pore apertures can allow bulkier reagents to diffuse in the pores compared to MOFs with smaller apertures. For instance, Cohen *et al*. compared the conversion of $–NH_2$ into $–NHC(O)C_9H_{19}$ in three different MOFs with different aperture sizes (UMCM-1-NH_2 = 32 Å, IRMOF-3 = 9.6 Å, DMOF-1-NH_2 = 7.5 Å).[69] Highest conversion was achieved with UMCM-1-NH_2 (89%), followed by IRMOF-3 (46%) and DMOF-1-NH_2 (34%).

The significance of aperture size on the degree of conversion was further demonstrated by Burrows and co-workers. Three different MOFs ([Zn_4O(BPDC-NH_2)$_3$], UMCM-1-NH_2 and IRMOF-3) were reacted with ferrocenecarboxylic anhydride to form ferrocenyl amide functionalised MOFs, Scheme 1.5.[84] As anticipated, the highest conversion (100%) was achieved in the MOF with the largest aperture, [Zn_4O(BPDC-NH_2)$_3$], followed by UMCM-1-NH_2 (17-31%) and IRMOF-3 (5%). Temperature also has a significant impact in the degrees of conversion. For example, for the [Zn_4O(BPDC-NH_2)$_3$] system, although complete conversion was achieved whilst

performing the reaction at 100 °C, no conversion was observed when the reaction was carried out at room temperature.

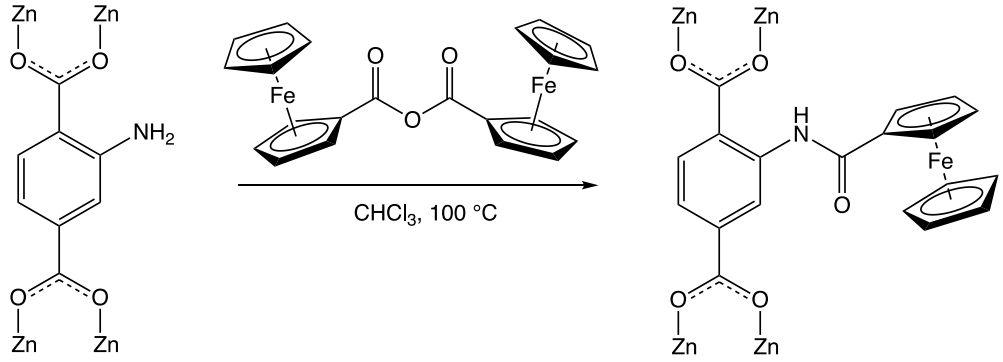

Scheme 1.5 Schematic representation of PSM of IRMOF-3 with ferrocenecarboxylic anhydride to form a ferrocenyl amide-functionalised MOF.[84]

One interesting feature of PSM is the possibility of introducing multiple functional groups in sequential steps. This process is referred to as *tandem PSM* and can be achieved in two different ways.

The first of these involves performing second PSM reaction on a modified MOF obtained upon a PSM reaction. For example, Cohen *et al*. reported a complete conversion of IRMOF-3 into [Zn_4O(BDC-NHC(O)CH=CHMe)$_3$] by reacting the amino group with crotonic anhydride, Scheme 1.6.[74] A second PSM reaction was carried out on [Zn_4O(BDC-NHC(O)CH=CHMe)$_3$] with bromine to form [Zn_4O(BDC-NHC(O)CH=CHMe)$_{3-x}$(BDC-NHC(O)CHBrCHBrMe)$_x$].

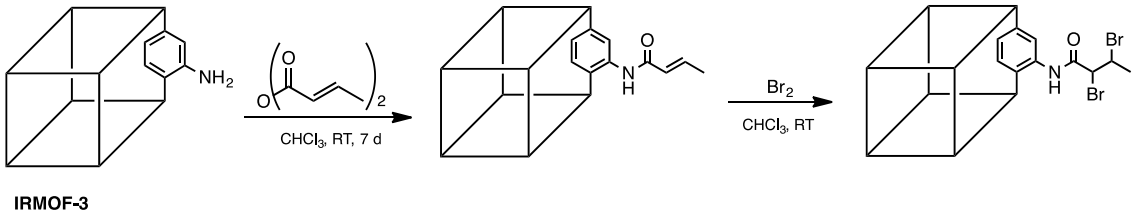

Scheme 1.6 Tandem PSM of IRMOF-3 showing the conversion of an amino group into -NHC(O)CH=CHMe which was then treated with bromine.[74]

Incomplete conversion in a PSM reaction opens up the possibility of undertaking a second PSM reaction on the product. In other words, unreacted functional groups can be further modified by a subsequent PSM reaction leading to pores with multiple functionalities. An example of this type of reaction is the incomplete reaction between IRMOF-3 and crotonic acid to form [Zn_4O(BDC-NH_2)$_{3-x}$(BDC-NHC(O)CH=CHMe)$_x$] which still contains unreacted amino groups, Scheme 1.7. The remaining amino groups

were subsequently reacted with acetic anhydride to form an overall framework of composition $[Zn_4O(BDC\text{-}NHC(O)CH{=}CHMe)_{3-x}(BDC\text{-}NHC(O)Me)_x]$.

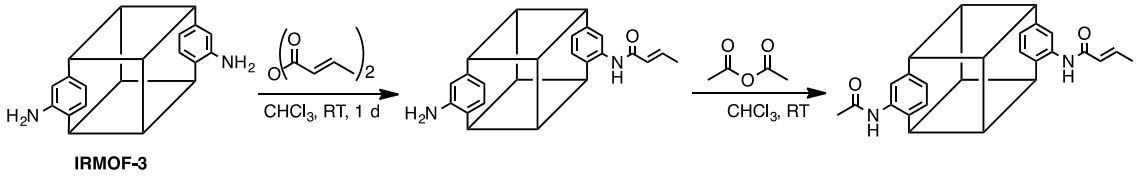

Scheme 1.7 Tandem PSM of IRMOF-3 showing the incomplete conversion of an amino group into -NHC(O)CH=CHMe in the first step. The second step involves the consecutive conversion of the amino group into an amide upon treatment with acetic anhydride.[74]

Farrusseng *et al*. produced a library of twenty-four functionalised MOFs using a tandem PSM procedure.[85] The first step involved converting the amino group in five different MOFs into an azide, Scheme 1.8. The azide group was then reacted with different alkynes *via* "click chemistry" to form MOFs with different functionalities protruding into the pores. The degrees of conversion varied according to the topology of the MOFs. High conversions were achieved with three-dimensional MOFs (DMOF-NH_2, CAU-1, and MIL-101(Fe)-NH_2) whereas lower conversions were observed with one dimensional MOFs (MIL-68(In)-NH_2 and MIL-53(Al)-NH_2). Farrusseng *et al*. proposed that the lower conversions were due to the slow diffusion of the reactants to the centre of the crystallites although in the case of flexible MIL-53(Al)-NH_2, pore contraction may be a factor. Further work on MIL-68-NH_2 shows that the alignment of the amino group within the pores may limit the access of reactants to the amino group.[86]

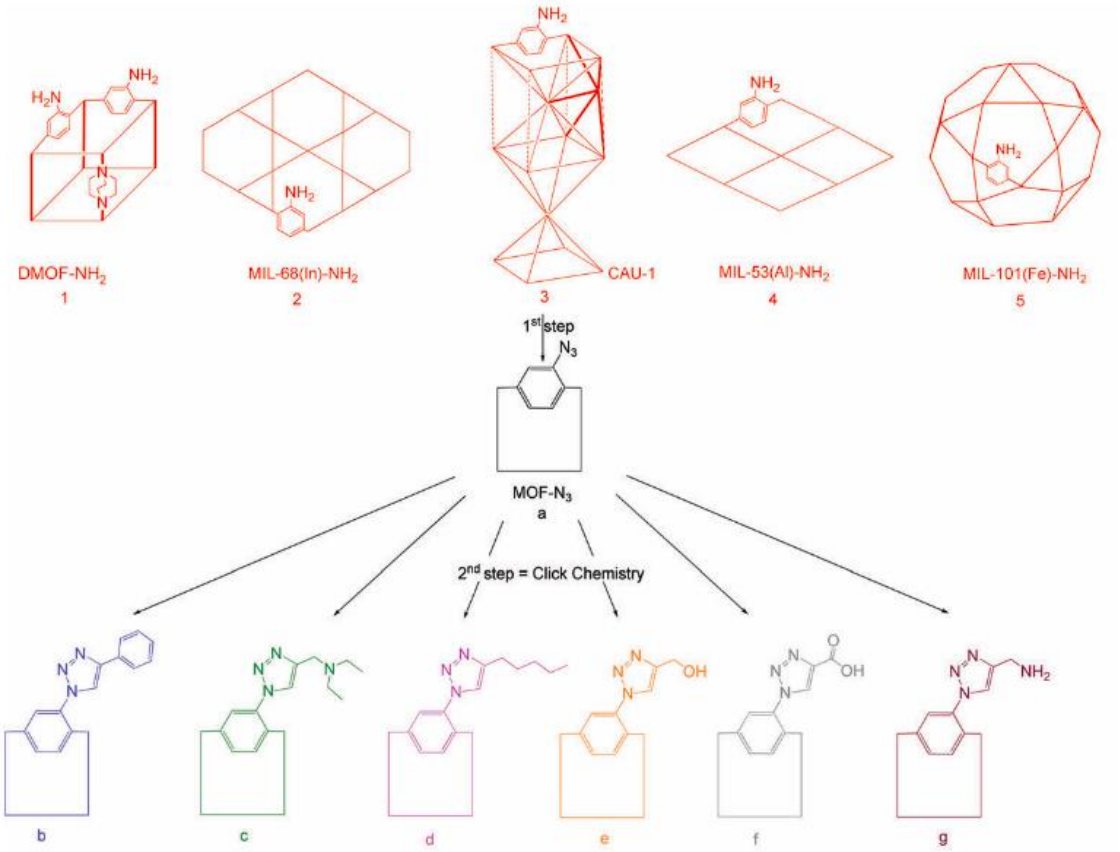

Scheme 1.8 Tandem PSM involving "click chemistry" in five different MOFs. First step: ^{t}BuONO, Me_3SiN_3. Second step: RC_2H, $Cu(NCMe)_4PF_6$. [85]

In 2014, Liu *et al.* reported a PSM procedure involving carbon-carbon bond-forming Mizoroki-Heck reaction with the aim of introducing different alkenyl functionalities.[87] The MOF used in this reaction, MIL-101(Cr)-$N_2^+BF_4^-$, can be prepared *in situ* by suspending MIL-101(Cr)-NH_2 in an acidic aqueous solution of HBF_4 followed by slow addition of $NaNO_2$, Scheme 1.9(a).[88] The Mizoroki-Heck reaction was carried out by reacting MIL-101(Cr)-$N_2^+BF_4^-$ with different alkenyl derivatives with the presence of a palladium catalyst. The degrees of conversion varied in the range of 29 – 76%, with the highest conversion achieved with the least bulky substituent. A tandem PSM reaction was carried out on one of the modified MOFs, MIL-101(Cr)-OH, with the aim to convert the terminal hydroxyl into a thiol group, Scheme 1.9(b). The presence of the thiol group was verified by elemental analysis, and the MOF itself was shown to have a high affinity towards Hg(II). This work by Liu *et al*. is an example of a multi-step tandem covalent PSM followed by a dative PSM, the latter step involving Hg(II) binding to the thiol group.

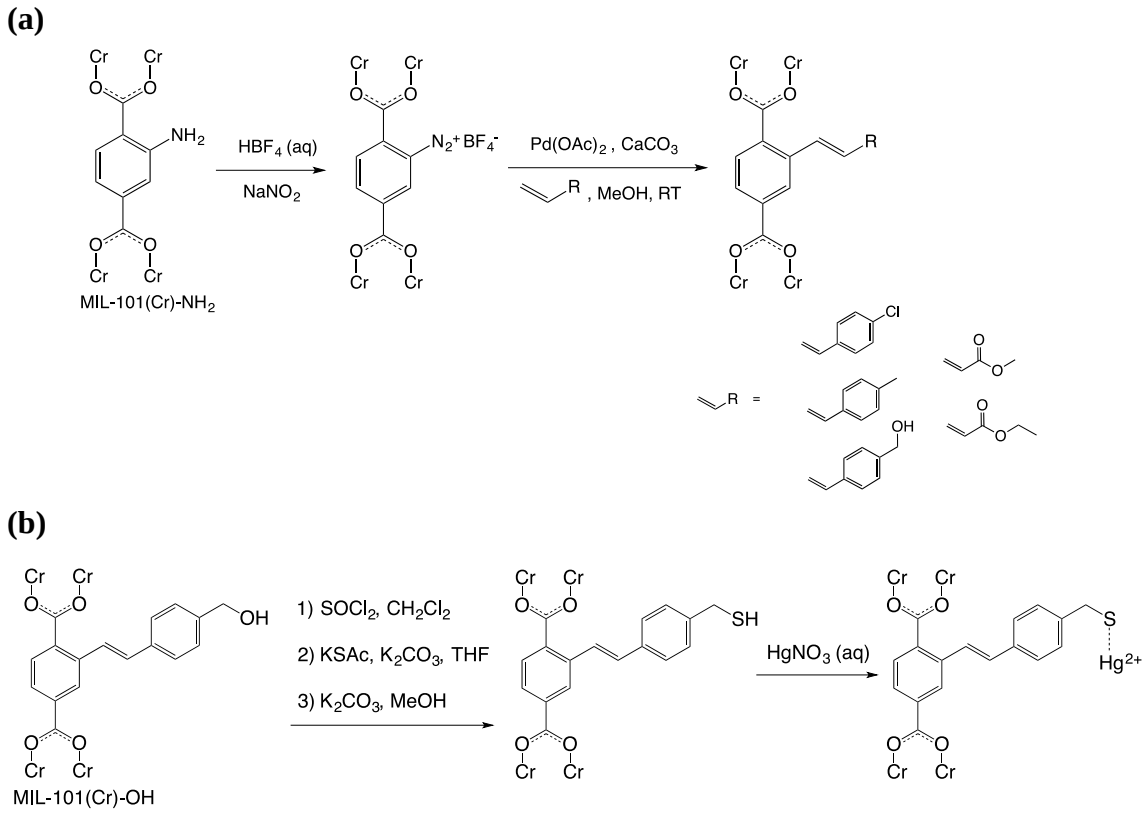

Scheme 1.9 (a) Tandem PSM of MIL-101(Cr)-NH_2 showing the conversion of an amino group into different alkenyl moieties. **(b)** Tandem PSM of MIL-101(Cr)-OH showing the conversion of a hydroxyl group into thiol.[87, 88]

Recently, there has been a growing interest in carrying out reactions on guest molecules encapsulated within the pores of MOFs. For example, Burrows *et al.* prepared a MOF with an amino-containing guest molecule in the pores $[Zn_3I_6(TPT)_2]\cdot(ATP\text{-}NH_2)$, (TPT = 2,4,6-tris(4-pyridyl)-1,3,5-triazine and ATP-NH_2 = aminotriphenylene) and reacted the amino groups with diketene, Scheme 1.10.[89] The quantitative conversion of the amino groups into *β*-amidoketone groups was evidenced by ^{1}H NMR spectroscopy analysis and single crystal X-ray crystallography.

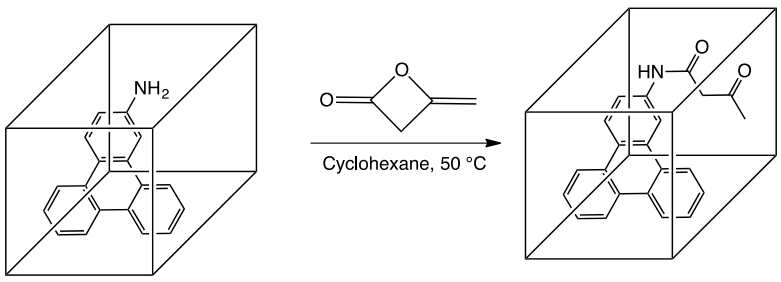

Scheme 1.10 Schematic representation of PSM of a guest molecule encapsulated within the pore of a MOF.[89]

1.5.5. PSM on Non-Amino Groups

MOFs bearing different functional groups such as aldehyde, halide and alkene have also been studied for PSM.[90-92] One of the most studied aldehyde-bearing MOFs, $Zn(C_4H_3N_2O)_2$, ZIF-90, underwent imine condensation reaction without the loss of crystallinity upon PSM reaction.[90] First reported by Yaghi *et al.* in 2008, the reaction involved treating ZIF-90 with ethanolamine to functionalise the pores with pendant hydroxyl group, Scheme 1.11. The aldehyde can also be reduced into hydroxyl group by treating the MOF with $NaBH_4$.

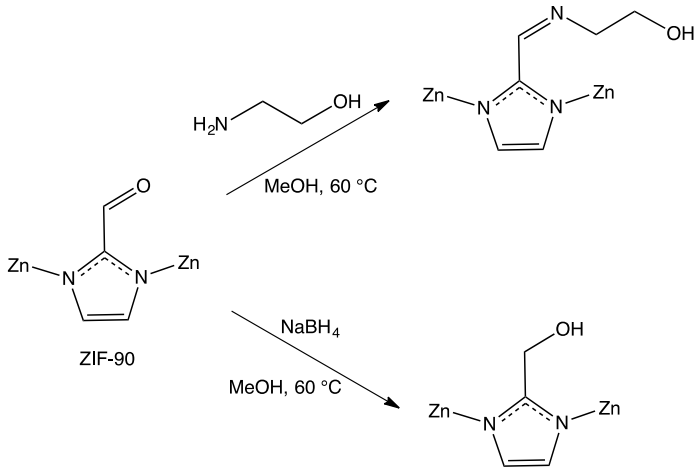

Scheme 1.11 PSM of ZIF-90 with ethanolamine and $NaBH_4$.[90]

In a recent work by Ghosh *et al.*, the aldehyde in ZIF-90 was converted into dicyanovinyl group, a fluorescent tag, upon treatment with malononitrile, Scheme 1.12.[93] The dicyanovinyl moiety selectively binds with cyanide ion *via* nucleophilic addition reaction which was evidenced by a significant fluorescence quenching of the MOF.

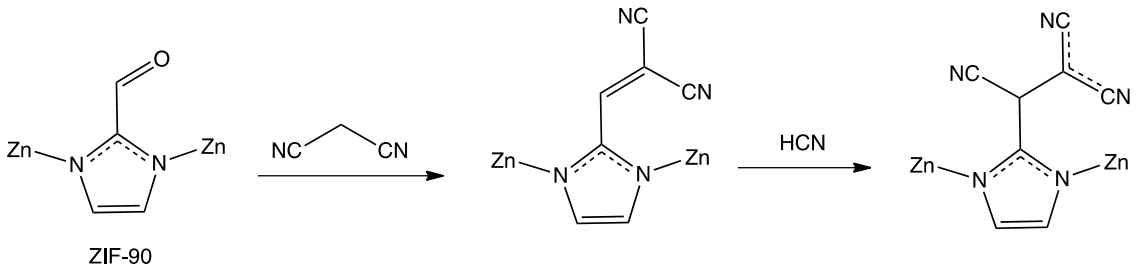

Scheme 1.12 PSM of ZIF-90 with malononitrile and subsequent reaction with HCN.[93]

Cohen *et al.* reported the cyanation of UiO-66-Br by treating the MOF with copper cyanide, Scheme 1.13.[91] They emphasised the merit of carrying out the reaction using microwave irradiation over conventional heating. While 43% conversion was achieved

by carrying out the reaction using conventional heating (140 °C for 24 hours), higher degree of conversion (90%) and faster reaction could be achieved by microwave irradiation (170 °C for 10 min).

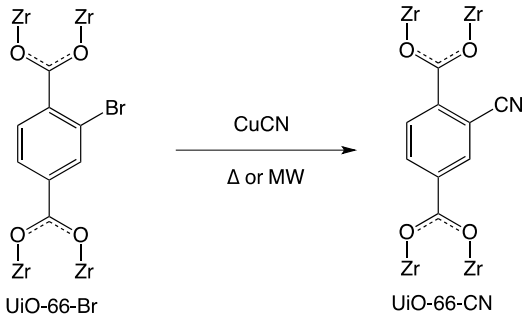

Scheme 1.13 PSM of UiO-66-Br with CuCN to form UiO-66-CN.[91]

Rieger *et al.* synthesised an allyl-functionalised MOF, UiO-66-AL (AL = 2-allyl-1,4-benzenedicarboxylate) and subjected the MOF to two different tandem PSM procedures.[92] The first tandem reaction involved the nucleophilic addition of Br_2 to the C=C double bond which resulted in alkyl bromides protruding into the pores, Scheme 1.14(a). The alkyl bromides were then converted into alkyldiamines *via* nucleophilic substitution with NH_3. The second tandem reaction involved treating UiO-66-AL with dimethyldioxirane to functionalise the pores with epoxides, Scheme 1.14(b). Ring opening reaction was then carried out on the epoxides to form a MOF functionalised with alkanolamines.

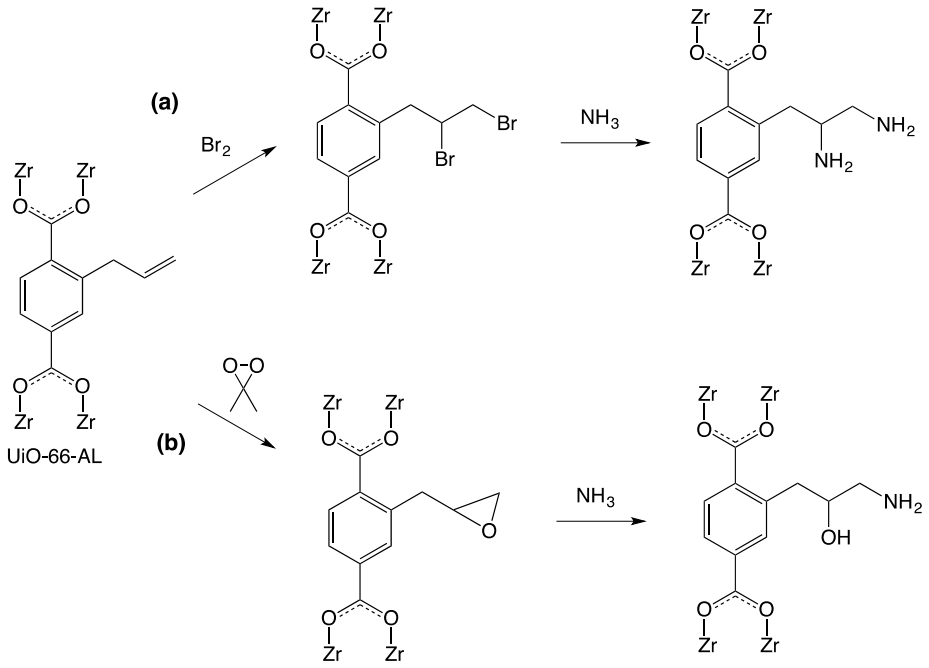

Scheme 1.14 Tandem PSM of UiO-66-AL showing the conversion of an allyl group into **(a)** alkyldiamine and **(b)** alkanolamine.[92]

One of the factors that contributes to the low degrees of conversion in some PSM processes is pore blocking by substituents in the MOF cavities. The pore blocking effect can be reduced by employing a mixed-ligand MOF (MIXMOF), Scheme 1.15. A MIXMOF is a MOF which consists of two or more different ligands in its framework. The different ligands have the same structural role towards the overall framework.

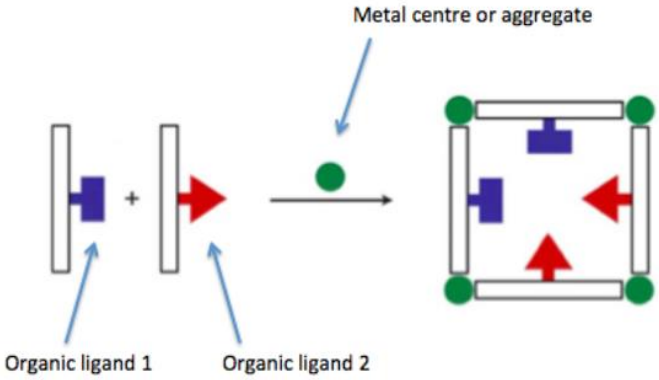

Scheme 1.15 Formation of a MIXMOF *via* direct synthesis.[94]

Burrows *et al*. reported the use of a MIXMOF with the aim to increase the degree of conversion. They synthesised an aldehyde-functionalised MOF [$Zn_4O(BPDC\text{-}CHO)_3(H_2O)_2$] and converted the aldehyde group into hydrazone with 60% conversion, Scheme 1.16.[95] The incomplete conversion was due to the pore blocking caused by the bulky hydrazone moieties. Nonetheless, 90% conversion was achieved whilst carrying out the reaction using a MIXMOF containing fewer aldehyde groups [$Zn_4O(BPDC\text{-}OMe)_{2.7}(BPDC\text{-}CHO)_{0.3}$].

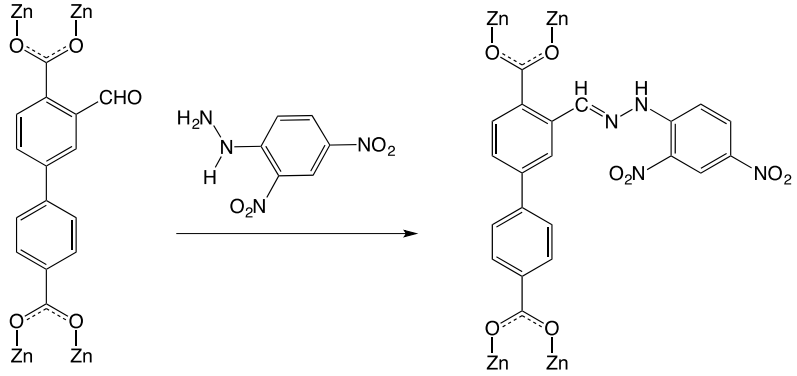

Scheme 1.16 Conversion of an aldehyde group into hydrazone in [$Zn_4O(BPDC\text{-}CHO)_3(H_2O)_2$].[95]

The use of bulky substituents can limit a PSM process to occur only on a MOF crystal surfaces rather than in the pores. For example, Mirkin *et al*. demonstrated the grafting of DNA on the surface of UiO-66-N_3 *via* PSM.[96] The DNA functionalised MOF was obtained by a click reaction between the azide group with dibenzylcyclooctyne (DBCO)

appended to dye-labelled DNA, Scheme 1.17, to facilitate the characterisation of the modified sample. Confocal microscopy showed that the product was highly fluorescent, due to the presence of the dye-labelled DNA on the MOF surface. However, the PSM reaction only occurred on the MOF surface due to the large size of the DNA substituent.

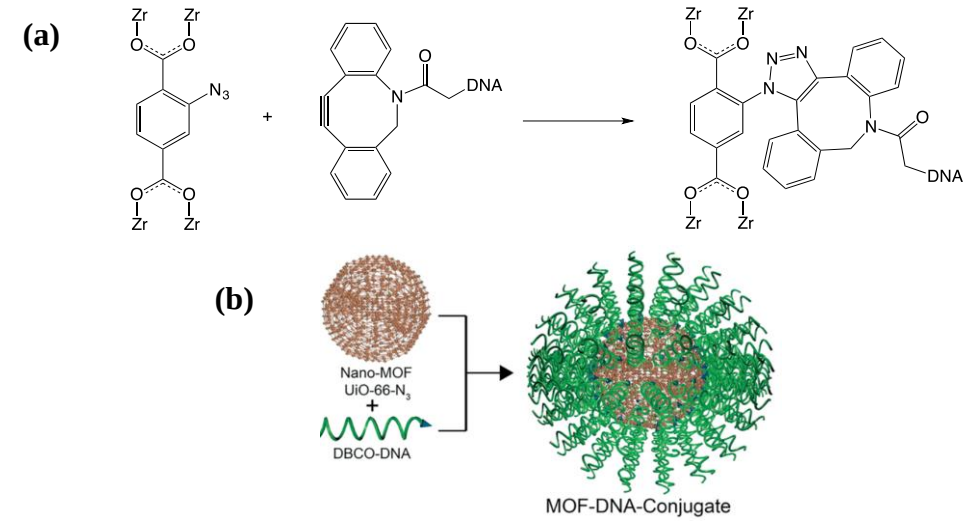

Scheme 1.17 Schematic representation of **(a)** the click reaction between an azide group with DBCO appended with DNA and **(b)** the grafting of DNA on the surface of UiO-66-N_3 *via* PSM.[96]

The PSM reactions described hitherto involved the modification of pendant groups attached to the ligand backbones. In the past few years, there has been an increase in the studies related to the direct modification of the aromatic rings. For example, Stock *et al.* first reported the use of electrophilic aromatic substitution to directly introduce nitro groups onto the BDC linker in MIL-101(Cr).[97] The reaction involved nitrating MIL-101(Cr) with concentrated nitric acid and sulfuric acid to form MIL-101(Cr)-NO_2, Scheme 1.18. The nitro-functionalised MOF was shown to undergo further PSM with tin(II) chloride in ethanol to form MIL-101-NH_2 and the amino group was subsequently converted into a urea derivative by reacting MIL-101-NH_2 with ethyl isocyanate.

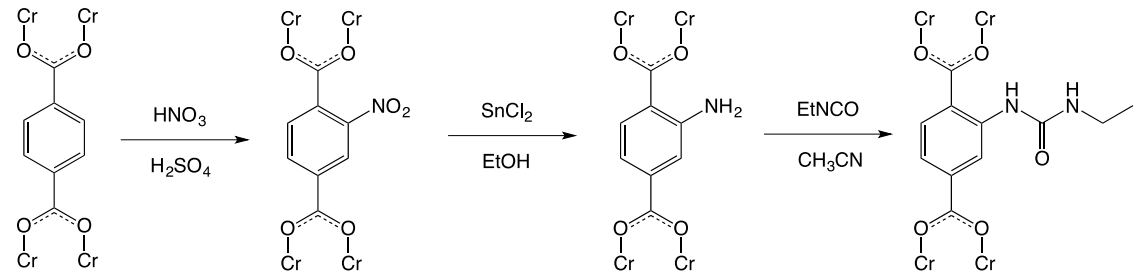

MIL-101(Cr)

Scheme 1.18 Schematic representation of a tandem PSM of MIL-101(Cr) to form a urea-functionalised MIL-101(Cr).[97]

Forgan *et al.* synthesised two MOFs, $[M_6O_4(OH)_4(EDB)_6]$ (M = Zr, Hf; EDB = 4,4′-ethynylenedibenzoate) which are isostructural to UiO-66.[36] The MOFs contain reactive alkyne unit in the ligand backbone which was investigated for PSM. The alkyne unit was shown to undergo bromination with the reaction occurring in a single-crystal to single-crystal manner, Scheme 1.19. Forgan *et al.* also demonstrated similar observation upon treating the MOFs with I_2 vapour.

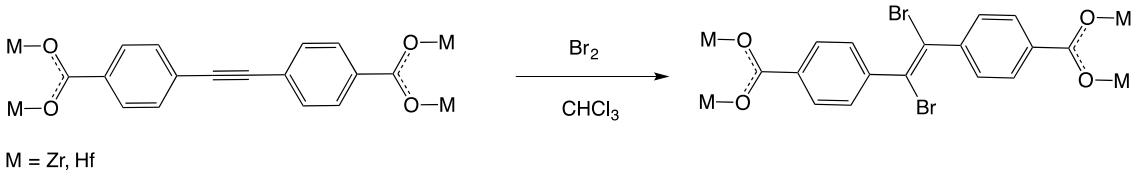

Scheme 1.19 Schematic representation of the bromination of $[M_6O_4(OH)_4(EDB)_6]$.[36]

1.5.6. Post-Synthetic Exchange

As described in Section 1.5.1, PSM can also be carried out by substituting a ligand in a pre-formed MOF by a new ligand. In order for this process to work, both ligands need to have the same structural role in the framework. Commonly referred to as post-synthetic exchange (PSE), this process is regarded as a mild method of introducing different functionalities in MOF pores. In 2014, Cohen *et al.* reported a PSE process in UiO-66 where the BDC linkers were replaced by BDC-$(OH)_2$ (BDC-$(OH)_2$ = 2,3-dihydroxy-1,4-benzenedicarboxylate) to form a MOF with dihydroxy group protruding into the pores, Scheme 1.20.[98] The PSE process was carried out by treating UiO-66 powder in a solution of BDC-$(OH)_2$ for 2 days at 85 °C. The degree of conversion can be controlled by varying the concentration of BDC-$(OH)_2$ in the solution.

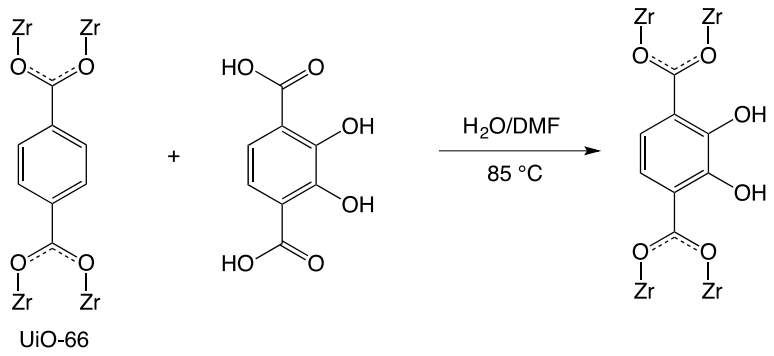

Scheme 1.20 Schematic representation of post-synthetic exchange in UiO-66.[98]

PSE can also be employed to increase the pore dimensions of MOFs. For example, Rosi *et al.* demonstrated that *in situ* ligand exchange with progressively longer dicarboxylate ligands could be performed on $[Zn_8(AD)_4(BDC)_6O_2]$ Bio-MOF-101, (AD = adeninate) to form products with progressively larger mesoporous cavities, Scheme 1.21.[99] The modified MOFs were shown to exhibit permanent mesoporosity and pore sizes ranging from ~2.1−2.9 nm and surface areas ranging from 2704 to 4410 m^2/g.

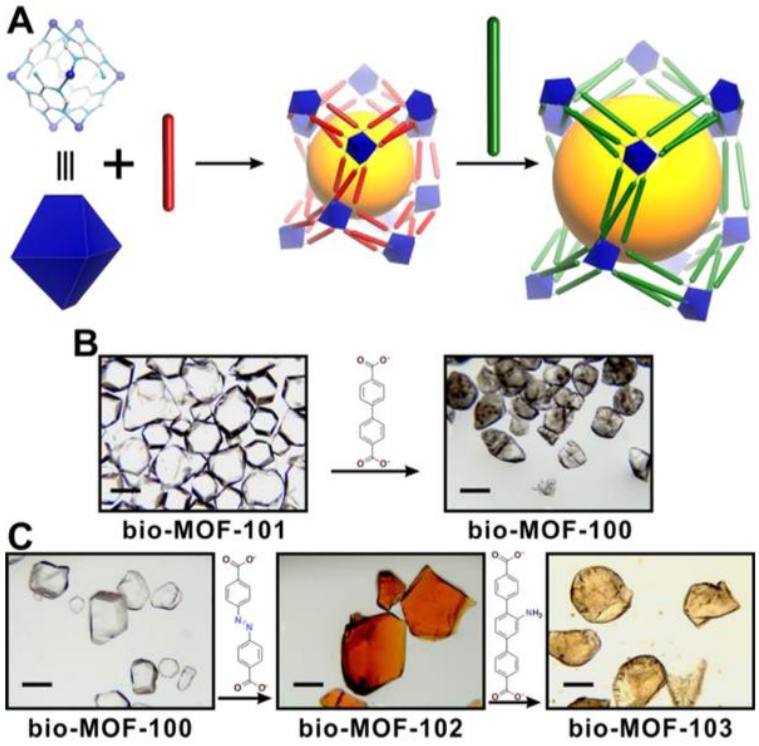

Scheme 1.21 (A) Scheme depicting pore expansion strategy *via* PSE. **(B)** As-synthesised Bio-MOF-101 was converted into Bio-MOF-100 *via* ligand exchange with BPDC. **(C)** BPDC in Bio-MOF-100 was replaced with ABDC to yield Bio-MOF-102 and subsequent conversion of Bio-MOF-102 into Bio-MOF-103 by the replacement of ABDC with NH_2-TPDC.[99]

In a recent publication, Rosi *et al*. reported that PSE can be used to produce structurally heterogeneous MOF crystals with porosity gradients.[100] For example, they demonstrated that the conversion of $[Zn_8(AD)_4(ABDC)_6O_2]$ Bio-MOF-102, (ABDC = azobenzene-4,4′-dicarboxylate) into $[Zn_8(AD)_4(ABDC)_{6-x}(TPDC\text{-}NO_2)_xO_2]$ Bio-MOF-102/106, ($TPDC\text{-}NO_2$ = 2′-nitro-1,1′:4′,1″-terphenyl-4,4″-dicarboxylate) proceeded gradually from the surface of the crystal to the crystal core, producing a product with descending porosity gradients, Scheme 1.22. As a proof of concept, the size-selective incorporation of a gold thiolate nanocluster, $Au_{133}(SR)_{52}$, was undertaken and microspectrophotometric results revealed that the clusters reside exclusively on the MOF surface.

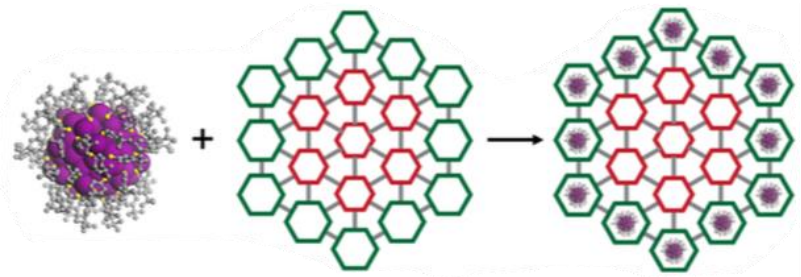

Scheme 1.22 Schematic representation of "ideal" $Au_{133}(SR)_{52}$ incorporation on the crystal surface of Bio-MOF-102/106.[100]

PSE process is not only limited to the exchange of linkers within a MOF, but it also applies to the exchange of metal ions in SBUs. For example, Cohen *et al.* reported that some of the zirconium ions in UiO-66 can be substituted with titanium cations to form a mixed-metal MOF, Scheme 1.23.[101] The substitution reaction was performed by treating UiO-66 powder with different titanium salts for 5 days at 85 °C. The degrees of substitution, which were determined by ICP-MS, varied depending on the titanium salts used in the reaction.

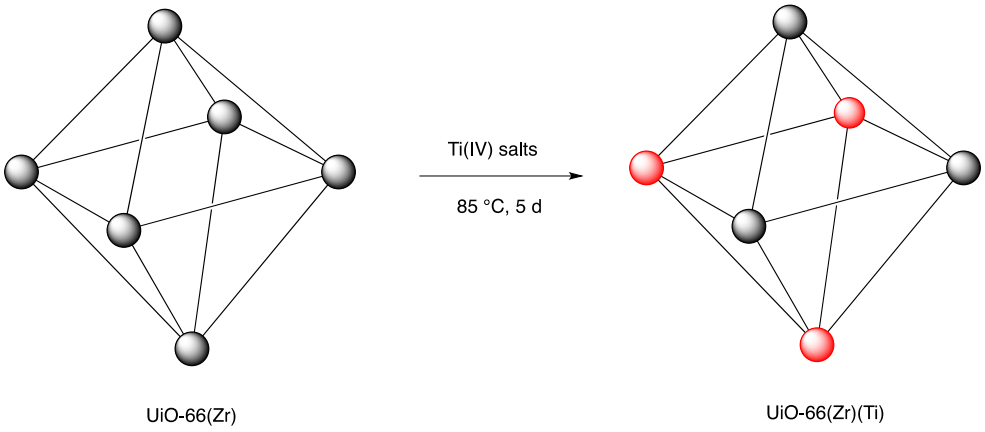

Scheme 1.23 Schematic representation of the formation of a mixed-metal MOF UiO-66(Zr)(Ti) *via* PSE process. Ti(IV) salts: $TiCp_2Cl_2$ (Cp: η^5-cyclopentadienyl), $TiCl_4(THF)_2$ or $TiBr_4$. Grey balls: Zr, red balls: Ti.[101]

1.5.7. PSM *via* Photochemical, Thermal and Electrochemical Treatment

The PSM reactions described thus far involved the addition of reagents to initiate the modification processes. An alternative procedure for carrying out a PSM reaction is *via* photochemical treatment. This procedure has gained a lot of interest among MOF chemists as it is considered to be a simple and 'green' method in producing functionalised materials. Photochemical treatment is commonly used in MOF chemistry as a deprotection method to expose reactive functional groups in the pores. In the

context of PSM, this process is commonly known as post-synthetic deprotection (PSD). For example, Cohen *et al*. reported the use of UV light to transform nitrobenzyl into hydroxyl groups to obtain a MOF with hydroxyl groups protruding into the pores, UiO-66-CAT (CAT = catechol), Scheme 1.24.[98] Nitrobenzyl groups are widely used as photocleavable protecting groups for alcohols. UiO-66-CAT is difficult to obtain *via* direct synthesis due to the reactive nature of the hydroxyl groups which could take part in the SBU formation. Upon PSM, the exposed hydroxyl groups could be metalated with Fe(II) and Cr(III) with the metal loading quantified by energy-dispersed X-ray (EDX) spectroscopy. The Cr-metalated MOF was shown to effectively catalyse the oxidation of alcohols into ketones.

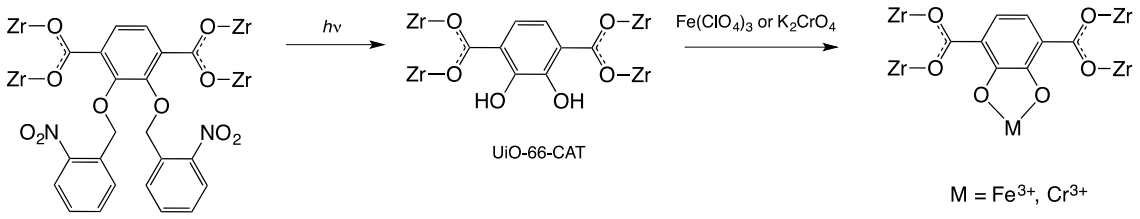

Scheme 1.24 Schematic representation of the formation of UiO-66-CAT *via* PSD and subsequent coordination with Fe^{3+} and Cr^{3+}.[98]

Bradshaw *et al.* reported the direct hydroxylation of the aromatic ring in UiO-66 using hydroxyl radicals, Scheme 1.25.[102] They investigated three different methods to generate the hydroxyl radicals (UV-A irradiation of commercial TiO_2 photocatalyst, UV-A irradiation of composite γ-Fe_2O_3@SiO_2@TiO_2 and UV-C irradiation of H_2O_2) and showed that the degrees of hydroxylation varied (40-77%) according to the methods used.

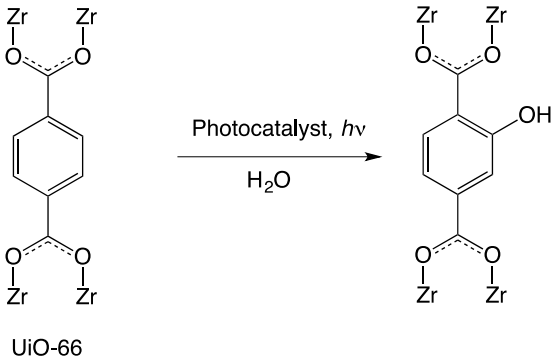

Scheme 1.25 Schematic representation of the direct hydroxylation of UiO-66 *via* the photogeneration of hydroxyl radicals.[102]

Thermal treatment has also been employed in PSM studies. For example, Richardson *et al.* synthesised an allyloxy-functionalised MOF, $[Zn_4O(BDC\text{-}ALY)_3]$ (BDC-ALY =

2,5-bis(allyloxy)-1,4-benzenedicarboxylate) and showed that the allyoxy moiety underwent Claisen rearrangement upon heating in DMF or DEF, Scheme 1.26.[103] The rearrangement of atoms on the BDC-ALY ligand was shown to have an impact on the product surface area, with the modified MOF having a higher surface area compared to the starting MOF.

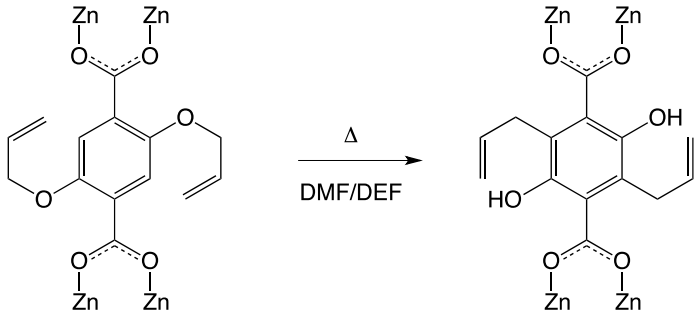

Scheme 1.26 Schematic representation of Claisen rearrangement in $[Zn_4O(BDC\text{-}ALY)_3]$.[103]

Thermal treatment can induce a change in the connectivity of the ligands within a MOF, by joining two pendant groups together. For example, Stock *et al.* reported that the pendent carboxylic acids in MIL-53(Al)-CO_2H could undergo condensation to form acid anhydrides, by heating the MOF under reduced pressure, Scheme 1.27.[104]

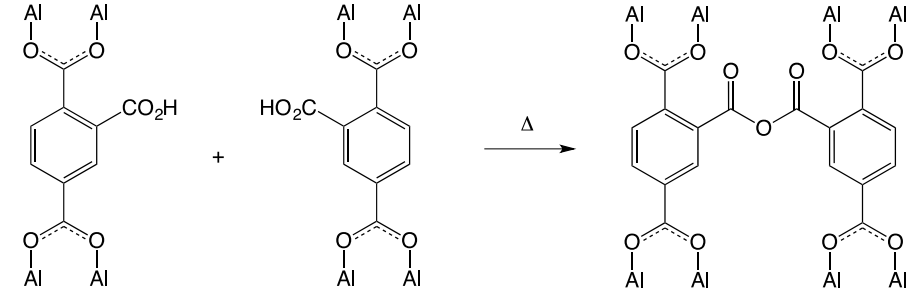

Scheme 1.27 The condensation of carboxylic acids to form acid anhydride in MIL-53(Al)-CO_2H.[104]

Thermal treatment has also been employed to produce MOFs with organocatalytic moieties protruding into the pores. For example, Telfer *et al.* synthesised a MOF containing *tert*-butoxycarbonyl (BOC) protecting groups in its pores $[Zn_4O(\mathbf{1})_3]$, IRMOF-Pro-Boc, Scheme 1.29.[105] The presence of the bulky BOC groups prevents framework interpenetration and thus, results in a framework that can incorporate relatively large substrates. The BOC groups were subjected to post-synthetic deprotection (PSD), whereby the thermolabile groups were removed by heating at

165 °C to expose proline moieties, which were shown to catalyse asymmetric aldol reactions.

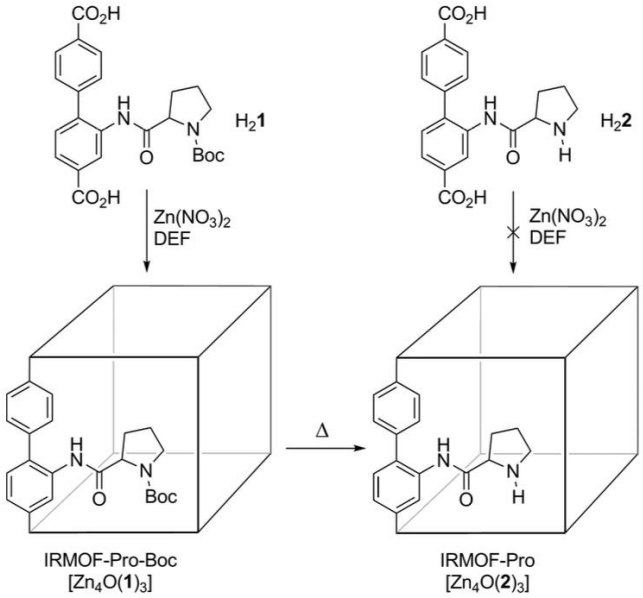

Scheme 1.29 Schematic representation of the post-synthetic deprotection (PSD) of *tert*-butoxycarbonyl (BOC) protecting groups to form proline-functionalised MOF, $[Zn_4O(\mathbf{2})_3]$, IRMOF-Pro *via* thermal treatment.[105]

Electrochemical transformations within MOFs have also been studied in the area of PSM. These transformations can involve redox processes on either the SBUs or the ligands. An example of the latter is the work by Wang *et al.* in which they reported a hydroquinone-quinone redox reaction in $[Zn_4O(TPDC\text{-}(OH)_2)_3]$ UiO-68-$(OH)_2$, (TPDC-$(OH)_2$ = 2′,5′-dihydroxy-*p*-terphenyl-4,4″-dicarboxylate), Scheme 1.30.[106] The oxidation of the diol to quinone was achieved by treating the MOF with a solution of iodobenzene diacetate. The transformation was fully reversible and occurred from the outer surface of the crystal and gradually diffused inwards. Wang *et al.* anticipated the application of this redox-switchable MOF in memory storage and nanoscale electronic devices.

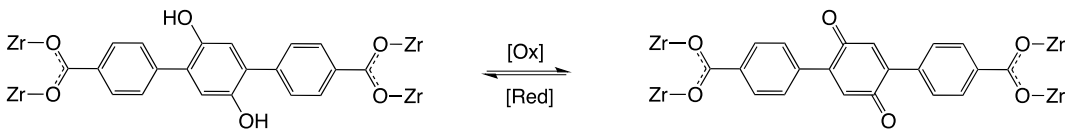

Scheme 1.30. Schematic representation of the redox triggered transformation of hydroquinone-quinone reaction in UiO-68-$(OH)_2$.[106]

1.6. Aims

The research described in this thesis is built upon two work packages concerning MOFs. The aim of the first work package is to investigate new PSM reaction pathways, with a view to expand the available routes to obtaining functionalised MOFs that are not accessible *via* direct synthesis. The chemical and physical properties of the modified MOFs such as BET surface area, CO_2 uptake capacity and CO_2 over N_2 selectivity will be investigated and compared with those for the starting MOFs. The effect of PSM towards flexible MOFs will also be studied. This research is described in Chapter 2 and 3.

Although there has been considerable interest surrounding the incorporation of drug molecules into MOFs, other biologically active species have received less attention. These include insect pheromones, which are extensively used in the agricultural industry for crop protection. Therefore, the aim of the second work package is to investigate the potential of MOFs in hosting insect pheromones. In this study, the factors which contribute to higher pheromone loadings in MOFs will be investigated. The end goal of this project is to develop materials that could provide controlled and highly targeted release of insect pheromones for pest control. This research is presented in Chapter 4.

1.7. References

1. B. Li, H. M. Wen, W. Zhou and B. L. Chen, *J. Phys. Chem. Lett.*, 2014, **5**, 3468.
2. P. Horcajada, C. Serre, M. Vallet-Regi, M. Sebban, F. Taulelle and G. Ferey, *Angew. Chem. Int. Ed.*, 2006, **45**, 5974.
3. A. D. Burrows, M. Jurcic, L. L. Keenan, R. A. Lane, M. F. Mahon, M. R. Warren, H. Nowell, M. Paradowski and J. Spencer, *Chem. Commun.*, 2013, **49**, 11260.
4. S. L. James, *Chem. Soc. Rev.*, 2003, **32**, 276.
5. H. Furukawa, N. Ko, Y. B. Go, N. Aratani, S. B. Choi, E. Choi, A. O. Yazaydin, R. Q. Snurr, M. O'Keeffe, J. Kim and O. M. Yaghi, *Science*, 2010, **329**, 424.
6. O. K. Farha, I. Eryazici, N. C. Jeong, B. G. Hauser, C. E. Wilmer, A. A. Sarjeant, R. Q. Snurr, S. T. Nguyen, A. Yazaydın and J. T. Hupp, *J. Am. Chem. Soc.*, 2012, **134**, 15016.
7. Z. Wang and S. M. Cohen, *Angew. Chem. Int. Ed.*, 2008, **120**, 4777.
8. O. M. Yaghi and H. Li, *J. Am. Chem. Soc.*, 1995, **117**, 10401.
9. H. Schrmidbaur, W. Bublak, B. Huber, G. Reber and G. Müller, *Angew. Chem. Int. Ed.*, 1986, **25**, 1089.
10. J. F. Modder, K. Vrieze, A. L. Spek, G. Challa and G. Van Koten, *Inorg. Chem.*, 1992, **31**, 1238.
11. D. Venkataraman, G. B. Gardner, S. Lee and J. S. Moore, *J. Am. Chem. Soc.*, 1995, **117**, 11600.
12. S. R. Batten, N. R. Champness, X.-M. Chen, J. Garcia-Martinez, S. Kitagawa, L. Öhrström, M. O'Keeffe, M. P. Suh and J. Reedijk, *Pure Appl. Chem.*, 2013, **85**, 1715.
13. B. F. Hoskins and R. Robson, *J. Am. Chem. Soc.*, 1989, **111**, 5962.
14. M. Fujita, Y. J. Kwon, S. Washizu and K. Ogura, *J. Am. Chem. Soc.*, 1994, **116**, 1151.
15. M. Eddaoudi, D. B. Moler, H. Li, B. Chen, T. M. Reineke, M. O'Keeffe and O. M. Yaghi, *Acc. Chem. Res.*, 2001, **34**, 319.
16. H. Li, M. Eddaoudi, T. L. Groy and O. M. Yaghi, *J. Am. Chem. Soc.*, 1998, **120**, 8571.
17. D. J. Tranchemontagne, J. L. Mendoza-Cortés, M. O'Keeffe and O. M. Yaghi, *Chem. Soc. Rev.*, 2009, **38**, 1257.
18. A. D. Burrows, M. Jurcic, M. F. Mahon, S. Pierrat, G. W. Roffe, H. J. Windle and J. Spencer, *Dalton Trans.*, 2015, **44**, 13814.
19. J. M. Rueff, O. Perez, V. Caignaert, G. Hix, M. Berchel, F. Quentel and P. A. Jaffrès, *Inorg. Chem.*, 2015, **54**, 2152.
20. J. V. Knichal, W. J. Gee, A. D. Burrows, P. R. Raithby, S. J. Teat and C. C. Wilson, *Chem. Commun.*, 2014, **50**, 14436.
21. D. Feng, K. Wang, Z. Wei, Y. P. Chen, C. M. Simon, R. K. Arvapally, R. L. Martin, M. Bosch, T. F. Liu, S. Fordham, D. Yuan, M. A. Omary, M. Haranczyk, B. Smit and H. C. Zhou, *Nat. Commun.*, 2014, **5**, 1.
22. H. Li, M. Eddaoudi, M. O'Keeffe and O. M. Yaghi, *Nature*, 1999, **402**, 276.
23. M. Eddaoudi, J. Kim, N. Rosi, D. Vodak, J. Wachter, M. O'Keeffe and O. M. Yaghi, *Science*, 2002, **295**, 469.
24. H. Deng, C. J. Doonan, H. Furukawa, R. B. Ferreira, J. Towne, C. B. Knobler, B. Wang and O. M. Yaghi, *Science*, 2010, **327**, 846.
25. J. H. Cavka, S. Jakobsen, U. Olsbye, N. Guillou, C. Lamberti, S. Bordiga and K. P. Lillerud, *J. Am. Chem. Soc.*, 2008, **130**, 13850.
26. H. Furukawa, Y. B. Go, N. Ko, Y. K. Park, F. J. Uribe-Romo, J. Kim, M. O'Keeffe and O. M. Yaghi, *Inorg. Chem.*, 2011, **50**, 9147.

27. H. Furukawa, K. E. Cordova, M. O'Keeffe and O. M. Yaghi, *Science*, 2013, **341**, 1230444.
28. K. Koh, A. G. Wong-Foy and A. J. Matzger, *Angew. Chem. Int. Ed.*, 2008, **47**, 677.
29. M. Kondo, M. Shimamura, S. I. Noro, S. Minakoshi, A. Asami, K. Seki and S. Kitagawa, *Chem. Mater.*, 2000, **12**, 1288.
30. D. N. Dybtsev, H. Chun and K. Kim, *Angew. Chem. Int. Ed.*, 2004, **43**, 5033.
31. K. S. Park, Z. Ni, A. P. Côté, J. Y. Choi, R. Huang, F. J. Uribe-Romo, H. K. Chae, M. O'Keeffe and O. M. Yaghi, *Proc. Natl. Acad. Sci. U.S.A.*, 2006, **103**, 10186.
32. A. Phan, C. J. Doonan, F. J. Uribe-Romo, C. B. Knobler, M. O'Keeffe and O. M. Yaghi, *Acc. Chem. Res.*, 2010, **43**, 58.
33. N. Stock and S. Biswas, *Chem. Rev.*, 2012, **112**, 933.
34. R. Banerjee, H. Furukawa, D. Britt, C. Knobler, M. O'Keeffe and O. M. Yaghi, *J. Am. Chem. Soc.*, 2009, **131**, 3875.
35. A. Rabenau, *Angew. Chem. Int. Ed.*, 1985, **24**, 1026.
36. R. J. Marshall, S. L. Griffin, C. Wilson and R. S. Forgan, *J. Am. Chem. Soc.*, 2015, **137**, 9527.
37. Y. Chen, C. Yang, X. Wang, J. Yang, K. Ouyang and J. Li, *J. Mater. Chem. A*, 2016, **4**, 10345.
38. O. M. Yaghi, H. Li and T. L. Groy, *J. Am. Chem. Soc.*, 1996, **118**, 9096.
39. J. Y. Choi, J. Kim, S. H. Jhung, H.-K. Kim, J.-S. Chang and H. K. Chae, *Bull. Korean Chem. Soc.*, 2006, **27**, 1523.
40. M. Schlesinger, S. Schulze, M. Hietschold and M. Mehring, *Microporous Mesoporous Mater.*, 2010, **132**, 121.
41. U. Müller, H. Puetter, M. Hesse and H. Wessel, *WO 2005/049892*, 2005, BASF Aktiengesellschaft.
42. I. Richter, M. Schubert and U. Müller, *WO 2007/131955*, 2007, BASF SE.
43. A. Pichon, A. Lazuen-Garay and S. L. James, *CrystEngComm*, 2006, **8**, 211.
44. W. Yuan, J. O'Connorb and S. L. James, *CrystEngComm*, 2010, **12**, 3515.
45. L.-G. Qiu, Z.-Q. Li, Y. Wu, W. Wang, T. Xu and S. Jiang, *Chem. Commun.*, 2008, 3642.
46. K. Sumida, D. L. Rogow, J. A. Mason, T. M. McDonald, E. D. Bloch, Z. R. Herm, T.-H. Bae and J. R. Long, *Chem. Rev.*, 2012, **112**, 724.
47. Y. X. Zhou, Y. Z. Chen, Y. Hu, G. Huang, S. H. Yu and H. L. Jiang, *Chem. Eur. J.*, 2014, **20**, 14976.
48. N. C. Jeong, B. Samanta, C. Y. Lee, O. Farha and J. Hupp, *J. Am. Chem. Soc.*, 2012, **134**, 51.
49. K. K. Tanabe, Z. Wang and S. M. Cohen, *J. Am. Chem. Soc.*, 2008, **130**, 8508.
50. O. K. Farha, A. Yazaydın, I. Eryazici, C. D. Malliakas, B. G. Hauser, M. G. Kanatzidis, S. T. Nguyen, R. Q. Snurr and J. T. Hupp, *Nat. Chem.*, 2010, **2**, 944.
51. A. P. Nelson, O. K. Farha, K. L. Mulfort and J. T. Hupp, *J. Am. Chem. Soc.*, 2009, **131**, 458.
52. Y.-P. He, Y.-X. Tan and J. Zhang, *Inorg. Chem.*, 2012, **51**, 11232.
53. K. Sing, *Colloids Surf., A*, 2001, **187-188**, 3.
54. S. Lowell, J. E. Shields, M. A. Thomas and M. Thommes, *Characterization of Porous Solids and Powders: Surface Area, Pore Size and Density*, Springer Science & Business Media, 2004.
55. S. Brunauer, L. S. Deming, W. E. Deming and E. Teller, *J. Am. Chem. Soc.*, 1940, **62**, 1723.
56. Y-S. Bae, A. Ö. Yazaydin and R. Q. Snurr, *Langmuir*, 2010, **26**, 5475.
57. K. S. Walton and R. Q. Snurr, *J. Am. Chem. Soc.*, 2007, **129**, 8552.

58. A. J. Fletcher, K. M. Thomas and M. J. Rosseinsky, *J. Solid State Chem.*, 2005, **178**.
59. P. D. C. Dietzel, V. Besikiotis and R. Blom, *J. Mater. Chem.*, 2009, **19**, 7362.
60. T. M. McDonald, D. M. D'Alessandro, R.Krishnac and J. R. Long, *Chem. Sci.*, 2011, **2**, 2022.
61. P. W. Seo, B. N. Bhadra, I. Ahmed, N. A. Khan and S. H. Jhung, *Sci. Rep.*, 2016, **6**, 34462.
62. E. Haque, J. W. Jun and S. H. Jhung, *J. Hazard. Mater.*, 2011, **185**, 507.
63. X. Zhu, B. Li, J. Yang, Y. Li, W. Zhao, J. Shi and J. Gu, *ACS Appl. Mater. Interfaces*, 2015, **7**, 223.
64. C. Wang, X. Liu, J. P. Chen and K. Li, *Sci. Rep.*, 2015, **5**.
65. K-K. Yee, N. Reimer, J. Liu, S-Y. Cheng, S-M. Yiu, J. Weber, N. Stock and Z. Xu, *J. Am. Chem. Soc.*, 2013, **135**, 7795.
66. K. K. Tanabe and S. M. Cohen, *Chem. Soc. Rev.*, 2011, **40**, 498.
67. R. J. Marshall and R. S. Forgan, *Eur. J. Inorg. Chem.*, 2016, **2016**, 4310.
68. A. D. Burrows, in *Encyclopedia of Inorganic and Bioinorganic Chemistry*, John Wiley & Sons, 2014, pp. 1.
69. Z. Wang, K. K. Tanabe and S. M. Cohen, *Inorg. Chem.*, 2009, **48**, 296.
70. T. Haneda, M. Kawano, T. Kawamichi and M. Fujita, *J. Am. Chem. Soc.*, 2008, **130**, 1578.
71. E. Dugan, Z. Wang, M. Okamura, A. Medina and S. M. Cohen, *Chem. Commun.*, 2008, 3366.
72. M. J. Ingleson, J. P. Barrio, J. B. Guilbaud, Y. Z. Khimyak and M. J. Rosseinsky, *Chem. Commun.*, 2008, 2680.
73. B. Gui, X. Meng, H. Xu and C. Wang, *Chin. J. Chem* . 2016, **34**, 186.
74. Z. Wang and S. M. Cohen, *Angew. Chem. Int. Ed.*, 2008, **47**, 4699.
75. Y.-H. Kiang, G. B. Gardner, S. Lee, Z. Xu and E. B. Lobkovsky, *J. Am. Chem. Soc.*, 1999, **121**, 8204.
76. J. S. Seo, D. Whang, H. Lee, S. I. Jun, J. Oh, Y. J. Jeon and K. Kim, *Nature*, 2000, **404**, 982.
77. S. S.-Y. Chui, S. M.-F. Lo, J. P. H. Charmant, A. G. Orpen and I. D. Williams, *Science*, 1999, **283**, 1148.
78. Z. Wang and S. M. Cohen, *J. Am. Chem. Soc.*, 2007, **129**, 12368.
79. J. G. Nguyen and S. M. Cohen, *J. Am. Chem. Soc.*, 2010, **132**, 4560.
80. J. S. Costa, P. Gamez, C. A. Black, O. Roubeau, S. J. Teat and J. Reedijk, *Eur. J. Inorg. Chem.*, 2008, **2008**, 1551.
81. K. M. Taylor-Pashow, J. Della Rocca, Z. Xie, S. Tran and W. Lin, *J. Am. Chem. Soc.*, 2009, **131**, 14261.
82. A. Modrow, D. Zargarani, R. Herges and N. Stock, *Dalton Trans.*, 2012, **41**, 8690.
83. S. J. Garibay and S. M. Cohen, *Chem. Commun.*, 2010, **46**, 7700.
84. J. E. Halls, A. Hernan-Gomez, A. D. Burrows and F. Marken, *Dalton Trans.*, 2012, **41**, 1475.
85. M. Savonnet, E. Kockrick, A. Camarata, D. Bazer-Bachi, N. Bats, V. Lecocq, C. Pinel and D. Farrusseng, *New J. Chem.*, 2011, **35**, 1892.
86. L. L. Keenan, H. Amer Hamzah, M. F. Mahon, M. R. Warren and A. D. Burrows, *CrystEngComm*, 2016, **18**, 5710.
87. T. Liu, J. X. Che, Y. Z. Hu, X. W. Dong, X. Y. Liu and C. M. Che, *Chem. Eur. J.*, 2014, **20**, 14090.
88. D. Jiang, L. L. Keenan, A. D. Burrows and K. J. Edler, *Chem. Commun.*, 2012, **48**, 12053.

89. W. J. Gee, L. K. Cadman, H. Amer Hamzah, M. F. Mahon, P. R. Raithby and A. D. Burrows, *Inorg. Chem.*, 2016, **55**, 10839.
90. W. Morris, C. J. Doonan, H. Furukawa, R. Banerjee and O. M. Yaghi, *J. Am. Chem. Soc.*, 2008, **130**, 12626.
91. M. Kim, S. J. Garibay and S. M. Cohen, *Inorg. Chem.*, 2011, **50**, 729.
92. A. Kronast, S. Eckstein, P. T. Altenbuchner, K. Hindelang, S. I. Vagin and B. Rieger, *Chem. Eur. J.*, 2016, **22**, 12800.
93. A. Karmakar, N. Kumar, P. Samanta, A. V. Desai and S. K. Ghosh, *Chem. Eur. J.*, 2016, **22**, 864.
94. A. D. Burrows, *CrystEngComm*, 2011, **13**, 3623.
95. A. D. Burrows, C. G. Frost, M. F. Mahon and C. Richardson, *Angew. Chem. Int. Ed.*, 2008, **47**, 8482.
96. W. Morris, W. E. Briley, E. Auyeung, M. D. Cabezas and C. A. Mirkin, *J. Am. Chem. Soc.*, 2014, **136**, 7261.
97. S. Bernt, V. Guillerm, C. Serre and N. Stock, *Chem. Commun.*, 2011, **47**, 2838.
98. H. Fei, J. Shin, Y. S. Meng, M. Adelhardt, J. Sutter, K. Meyer and S. M. Cohen, *J. Am. Chem. Soc.*, 2014, **136**, 4965.
99. T. Li, M. T. Kozlowski, E. A. Doud, M. N. Blakely and N. L. Rosi, *J. Am. Chem. Soc.*, 2013, **135**, 11688.
100. C. Liu, C. J. Zeng, T. Y. Luo, A. D. Merg, R. C. Jin and N. L. Rosi, *J. Am. Chem. Soc.*, 2016, **138**, 12045.
101. M. Kim, J. F. Cahill, H. Fei, K. A. Prather and S. M. Cohen, *J. Am. Chem. Soc.*, 2012, **134**, 18082.
102. J. Aguilera-Sigalat, A. Fox-Charles and D. Bradshaw, *Chem. Commun.*, 2014, **50**, 15453.
103. L. Tshering, S. O. Hunter, A. Nikolich, E. Minato, C. M. Fitchett, D. M. D'Alessandro and C. Richardson, *CrystEngComm*, 2014, **16**, 9158.
104. N. Reimer, B. Gil, B. Marszalek and N. Stock, *CrystEngComm*, 2012, **14**, 4119.
105. D. J. Lun, G. I. Waterhouse and S. G. Telfer, *J. Am. Chem. Soc.*, 2011, **133**, 5806.
106. B. Gui, X. Meng, Y. Chen, J. Tian, G. Liu, C. Shen, M. Zeller, D. Yuan and C. Wang, *Chem. Mater.*, 2015, **27**, 6426.

2. Post-Synthetic Modification of MOFs: Aza-Michael Reaction

The aza-Michael reaction is a type of conjugate addition in which a nitrogen nucleophile adds to the β-carbon of an electron-deficient alkene (Michael acceptor) to afford a β-amino carbonyl compound, Scheme 2.1.[1] This reaction is regarded as a versatile method for constructing new C–N bonds, and it generally requires a Lewis acid such as $Bi(OTf)_3$ and SmI_2 to catalyse it.[2, 3]

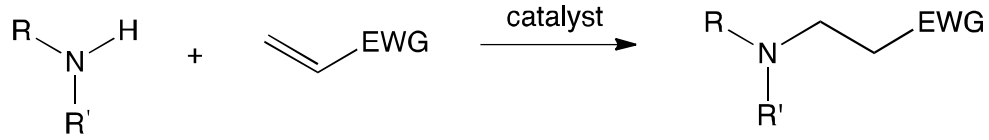

Scheme 2.1 General scheme for the aza-Michael reaction. R = alkyl, aryl; R' = H, alkyl, aryl; EWG = COH, COR, CO_2R, $CONR_2$, CN, SO_2R, SOR, NO_2. EWG = electron withdrawing group.[1]

The reaction mechanism for the aza-Michael reaction involving a secondary amine and acrylonitrile as the Michael acceptor is exemplified in Scheme 2.2.

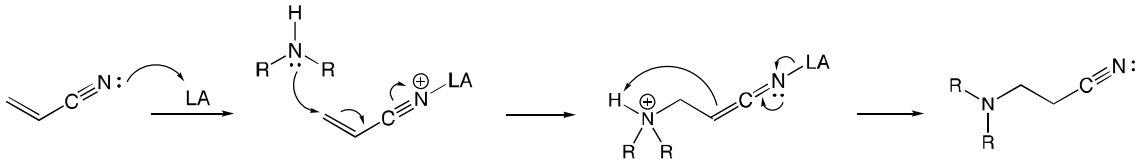

Scheme 2.2 Reaction mechanism for the reaction of a secondary amine and acrylonitrile. LA = Lewis acid catalyst.

As outlined in Section 1.4.1, MOFs have been extensively studied in the field of catalysis. In this context, Nguyen *et al.* reported the role of $[Cu_3(BTC)_2]$, HKUST-1, (BTC = 1,3,5-benzenetricarboxylate), Figure 2.1, as an efficient heterogeneous catalyst for the aza-Michael reaction.[4] They studied the reaction of benzylamine with ethyl acrylate to form ethyl 2-(benzylamino)acetate using HKUST-1 as a catalyst. The reaction proceeded under mild conditions, with 89% conversion to the β-amino carbonyl compound by employing 5 mol% of the MOF catalyst. The catalytic activity of this MOF originates from the $Cu_2(CO_2)_4$ SBU, which contains coordinatively unsaturated Cu(II) metal centres that form the catalytic active sites.

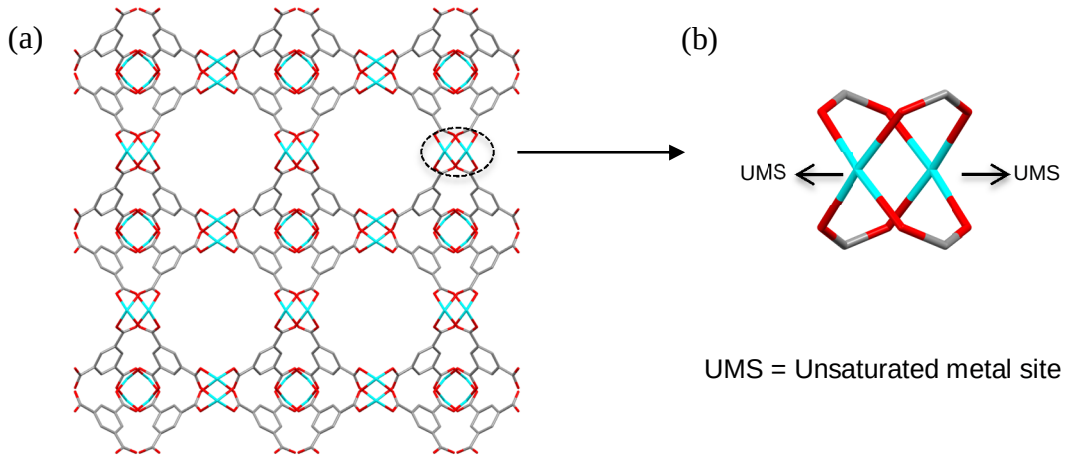

Figure 2.1 (a) Framework of HKUST-1 viewed along [100] direction. **(b)** SBU of activated HKUST-1 showing unsaturated metal sites (UMS). Cu: cyan, C: grey, O: red.[5]

More recent studies have shown that the aza-Michael reaction can proceed without the aid of a catalyst. Wang *et al.* demonstrated that azoles could react readily with a range of β, γ-unsaturated α-keto esters to afford new C–N bond adducts, Scheme 2.3.[6] They postulated that hydrogen bonding between the NH moiety of the azoles and the carbonyl oxygen facilitates the conjugate addition reaction, thus eliminating the need to employ a catalyst.

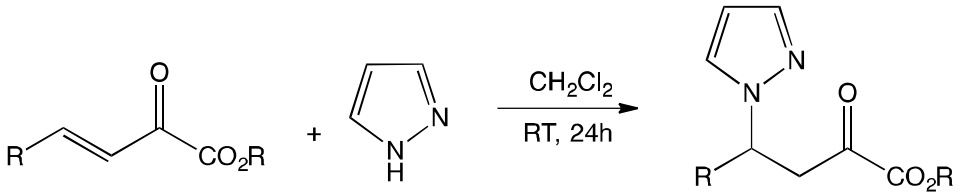

Scheme 2.3 Catalyst-free aza-Michael addition of pyrazole to β, γ-unsaturated α-keto esters.

De *et al.* reported that aza-Michael additions could be achieved in highly polar protic solvents without any promoting agent, but that the choice of the solvent is crucial in determining the products obtained.[7] The reaction involves the nucleophilic addition of aromatic amines into methyl acrylate or methyl vinyl ketone, which leads to the formation of the respective monoadduct or the diadduct depending on the solvent employed in the reaction.

2.1. Preliminary Reactions of UiO-66-NH_2 with Acrylonitrile: An Investigation of Reaction Conditions on PSM Percentage Conversions

As mentioned previously, HKUST-1 has been shown to act as a catalyst for the aza-Michael reaction. Based on this finding, it was decided to investigate if the aza-Michael reaction could be carried out on a MOF framework *via* a PSM reaction instead of

performing the reaction in the pores. $[Zr_6O_4(OH)_4(BDC\text{-}NH_2)_6]$, UiO-66-$NH_2$, was selected as the candidate MOF for these preliminary reactions due to its high chemical stability in different solvents and its large pore channels.[8, 9] The aperture size is also crucial in PSM chemistry, as MOFs with large apertures allow easier diffusion of the reactants in and by-products out of the framework. In this context, UiO-66-NH_2 has an aperture size of 6.9 Å which is large enough for diffusion of small reactants. Additionally, it possesses free amino groups protruding in the pores which afford potential for the PSM reactions to occur on the MOF framework.

Acrylonitrile was chosen as a Michael acceptor for the preliminary reactions with UiO-66-NH_2 due to its relatively small size. The reactions were carried out with no catalyst employed. This approach is advantageous in the context of PSM chemistry, as the absence of catalyst reduces the possibility of pore blockage.

2.1.1. Solvent Effects on PSM Reactions

UiO-66-NH_2 was synthesised based on the previously reported procedure.[8] The as-synthesised MOF was rinsed and soaked in MeOH for 3 days, replacing the solvent with fresh MeOH every 24 hours. Subsequently, yellow UiO-66-NH_2 powder was collected *via* centrifugation, dried under reduced pressure and further used in the PSM reactions. The proposed preliminary reaction is shown in Scheme 2.4. A range of solvents were screened, from polar protic to polar aprotic liquids. In all cases, reactions were conducted for 24 hours by refluxing the reaction mixtures in respective solvents. The results are summarised in Table 2.1.

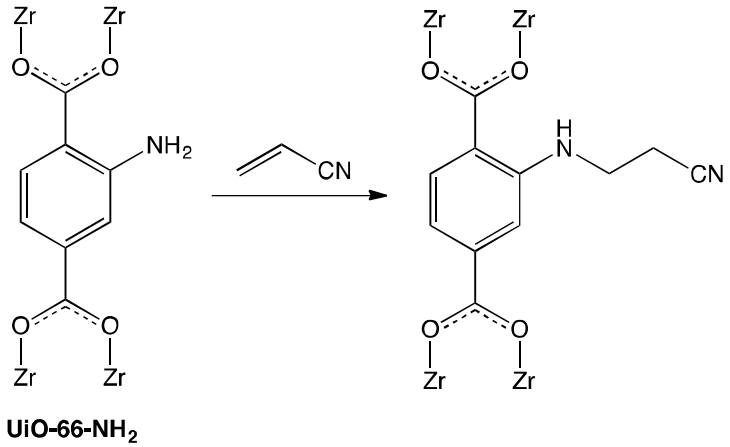

Scheme 2.4 General scheme for the PSM reaction between UiO-66-NH_2 with acrylonitrile.

Solvent	% conversion	Product
Water	38	$[Zr_6O_4(OH)_4(BDC\text{-}NH_2)_{3.72}(BDC\text{-}NHCH_2CH_2CN)_{2.28}]$
Hexafluoroisopropanol	5	$[Zr_6O_4(OH)_4(BDC\text{-}NH_2)_{5.7}(BDC\text{-}NHCH_2CH_2CN)_{0.3}]$
2,2,2-Trifluoroethanol	4	$[Zr_6O_4(OH)_4(BDC\text{-}NH_2)_{5.8}(BDC\text{-}NHCH_2CH_2CN)_{0.2}]$
Ethanol	0	$[Zr_6O_4(OH)_4(BDC\text{-}NH_2)_6]$
Acetic acid (Glacial)		
Chloroform		
Tetrahydrofuran		

Table 2.1. Solvents used in preliminary PSM reactions and the respective percentage conversions.

Conversion from the amino into cyanoethyl groups was successful, with the highest conversion (38%) achieved whilst using H_2O as the solvent. The choice of solvents used in the preliminary reactions stemmed from the work by De *et al.* in which they observed excellent conversions whilst employing highly polar protic solvents (H_2O, hexafluoroisopropanol (HFIP) and 2,2,2-trifluoroethanol (TFE)).[7] In this work, different observations were noted whilst carrying out the reactions on a MOF framework. H_2O was shown to be the optimum solvent whereas similar reactions in HFIP and TFE gave low conversions of amino to cyanoethyl groups. The ^1H NMR spectrum of the digested PSM product for the reaction in H_2O is shown in Figure 2.2.

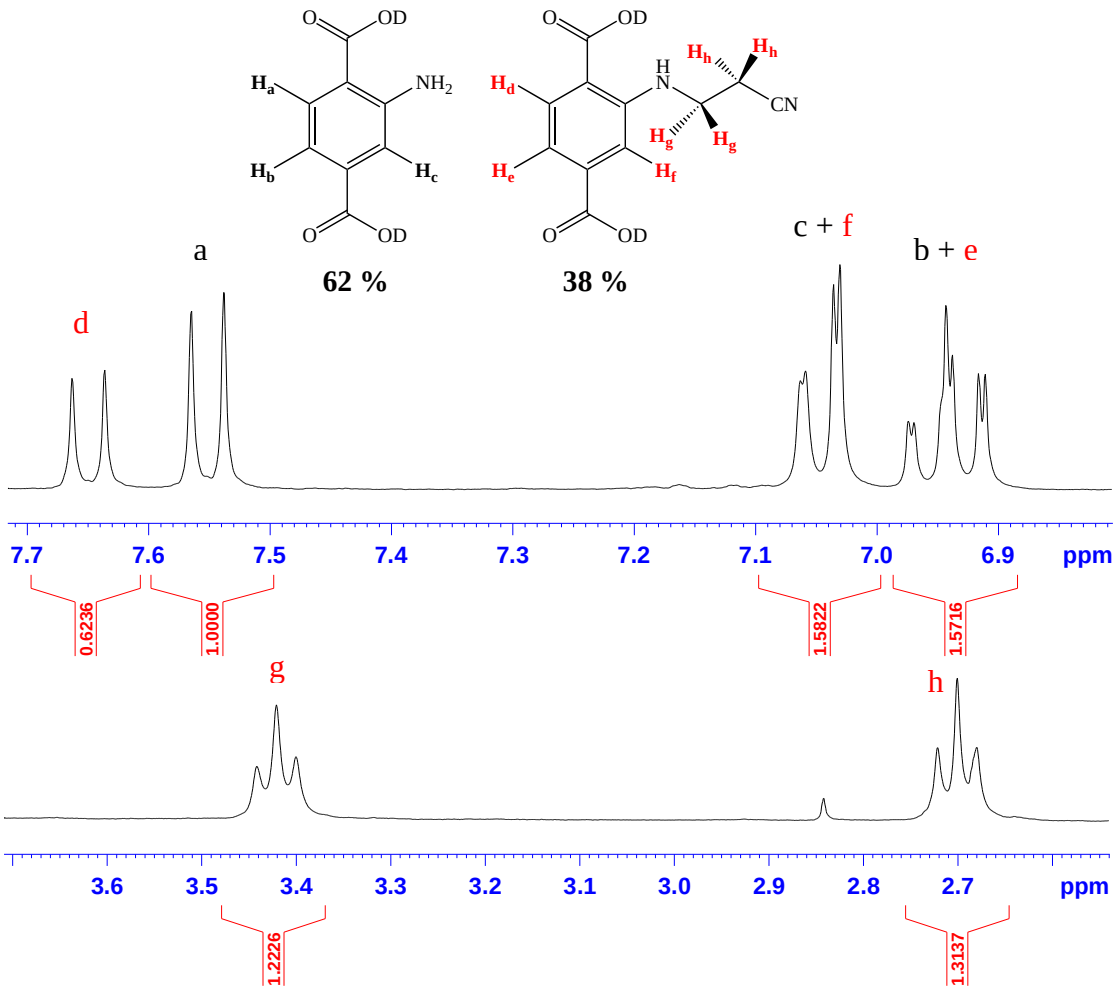

Figure 2.2. ^{1}H NMR spectrum for the digested PSM product for the reaction between UiO-66-NH_2 and acrylonitrile at 100 °C for 24 hours with H_2O as the solvent. Top: aromatic region; bottom: aliphatic region.

The ^{1}H NMR spectrum of the digested PSM product was obtained by treating the sample in NH_4F/D_2O with DMSO-d_6. The PSM percentage conversion was calculated by comparing the integrals at δ 7.55 ppm and δ 7.65 ppm which correspond to aryl protons from D_2BDC-NH_2 and D_2BDC-$NHCH_2CH_2CN$, respectively. The aliphatic region shows the emergence of two sets of triplets at δ 2.70 ppm and δ 3.43 ppm which respectively correspond to the β- and α-hydrogens to the nitrogen atom of D_2BDC-$NHCH_2CH_2CN$.

The conventional method of digesting UiO-66 and its derivatives is by using HF, as the fluoride anion helps cleave the bond between zirconium and the carbonyl oxygen of the ligand. In this work, a new digestion method was developed in which NH_4F was used instead of HF to avoid the hazards associated with hydrofluoric acid. Hintz *et. al.* reported the use of CsF for the digestion of UiO-66-NH_2, $[Cr_3O(OH)(OH_2)_2(BDC)_3]$ MIL-101(Al)-NH_2, and [Al(OH)(BDC-NH_2)] MIL-53(Al)-NH_2.[10] Nonetheless, to date, there

are no prior reports on the use of NH_4F for the digestion of UiO-66 systems.

The structural integrity of UiO-66-NH_2 framework upon PSM reaction in H_2O was examined by powder X-ray diffraction (PXRD). As shown in Figure 2.3, the PXRD pattern of the PSM product is similar to the starting MOF, UiO-66-NH_2, which indicates that the framework integrity was maintained and the PSM reaction did not alter the crystallinity of the PSM product. The PXRD pattern of the sample is broad due to the size of the MOF microparticles.

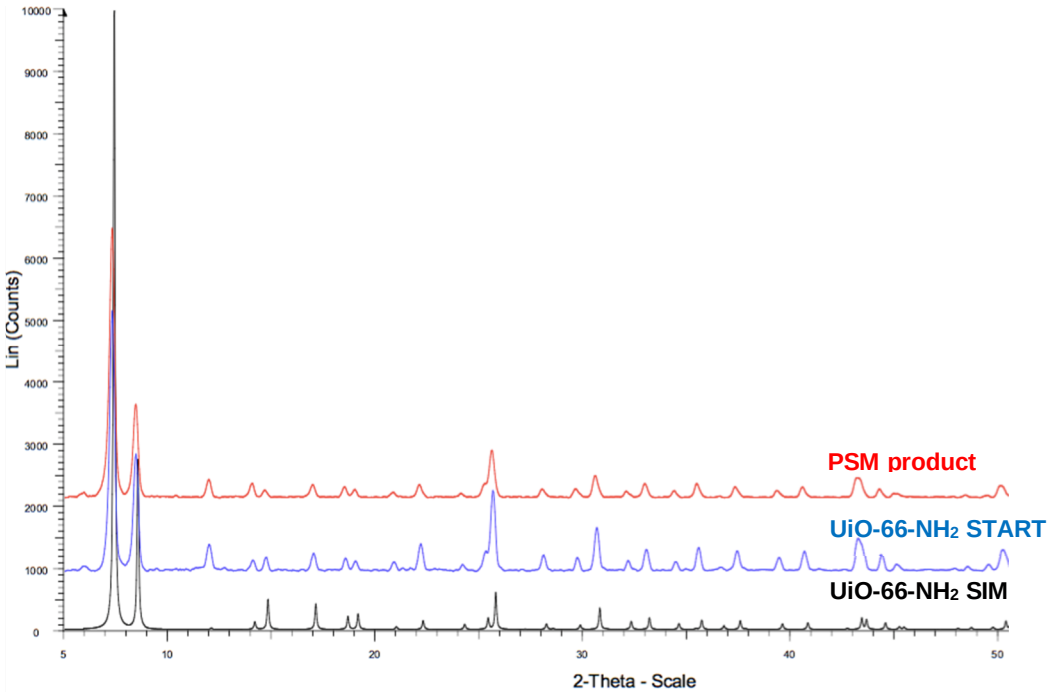

Figure 2.3. Black: Simulated PXRD pattern of UiO-66-NH_2. Blue: PXRD pattern of starting MOF, UiO-66-NH_2. Red: PXRD pattern of PSM product upon reaction in H_2O.

2.1.2. Reaction Time, Environment and Temperature Effects on PSM Reactions

The reaction time was also investigated with the aim of improving the percentage conversion of the amino group into the cyanoethyl group. Prior to PSM reactions, UiO-66-NH_2 powder was washed with water by centrifugation over 3 days with the solvent replaced every 24 hours. The MOF was then left to react with acrylonitrile in H_2O at 100 °C for 1, 3, 5, 7 and 12 days. The PSM percentage conversions for each experiment are summarised in Table 2.2.

Reaction time (days)	% conversion	Chemical formula
1	38	$[Zr_6O_4(OH)_4(BDC\text{-}NH_2)_{3.72}(BDC\text{-}NHCH_2CH_2CN)_{2.28}]$
3	43	$[Zr_6O_4(OH)_4(BDC\text{-}NH_2)_{3.42}(BDC\text{-}NHCH_2CH_2CN)_{2.58}]$
5	50	$[Zr_6O_4(OH)_4(BDC\text{-}NH_2)_{3.0}(BDC\text{-}NHCH_2CH_2CN)_{3.0}]$
7		
12		

Table 2.2. Reaction times and the respective percentage conversions of amino into cyanoethyl groups.

These results reveal that the percentage conversion increases with time but reaches a plateau after 5 days with 50% conversion.

Different reaction environments were also assessed with the aim to further increase the PSM conversion. Instead of employing 'open system' reactions by refluxing the reactants in H_2O, the reactions were carried out in a 'closed system' using an autoclave as the reaction vessel. One of the advantages of carrying out reactions in autoclaves is the possibility of increasing the reaction temperature above the solvent boiling point. Another plausible reason for carrying out the reactions in a 'closed system' is to overcome acrylonitrile's low boiling point (77 °C). 100% conversion was achieved after leaving the reaction in an autoclave at 120 °C for 2 days. This reaction yielded a PSM product with the formula $[Zr_6O_4(OH)_4(BDC\text{-}NHCH_2CH_2CN)_6]$, **1a**. The reaction also proceeded rapidly with 78% conversion after 1 day. It is proposed that the increased PSM conversion was due to the closed environment created by the autoclave in which acrylonitrile vapours could not diffuse out of the vessel.

The ^1H NMR spectrum for the digested PSM product **1a**, Figure 2.4, shows two sets of triplets at δ 2.71 ppm and δ 3.42 ppm which correspond to the β- and α-protons to the secondary nitrogen of $D_2BDC\text{-}NHCH_2CH_2CN$. The peaks at δ 6.95, 7.05 and 7.65 ppm correspond to the protons from the aromatic ring of $D_2BDC\text{-}NHCH_2CH_2CN$.

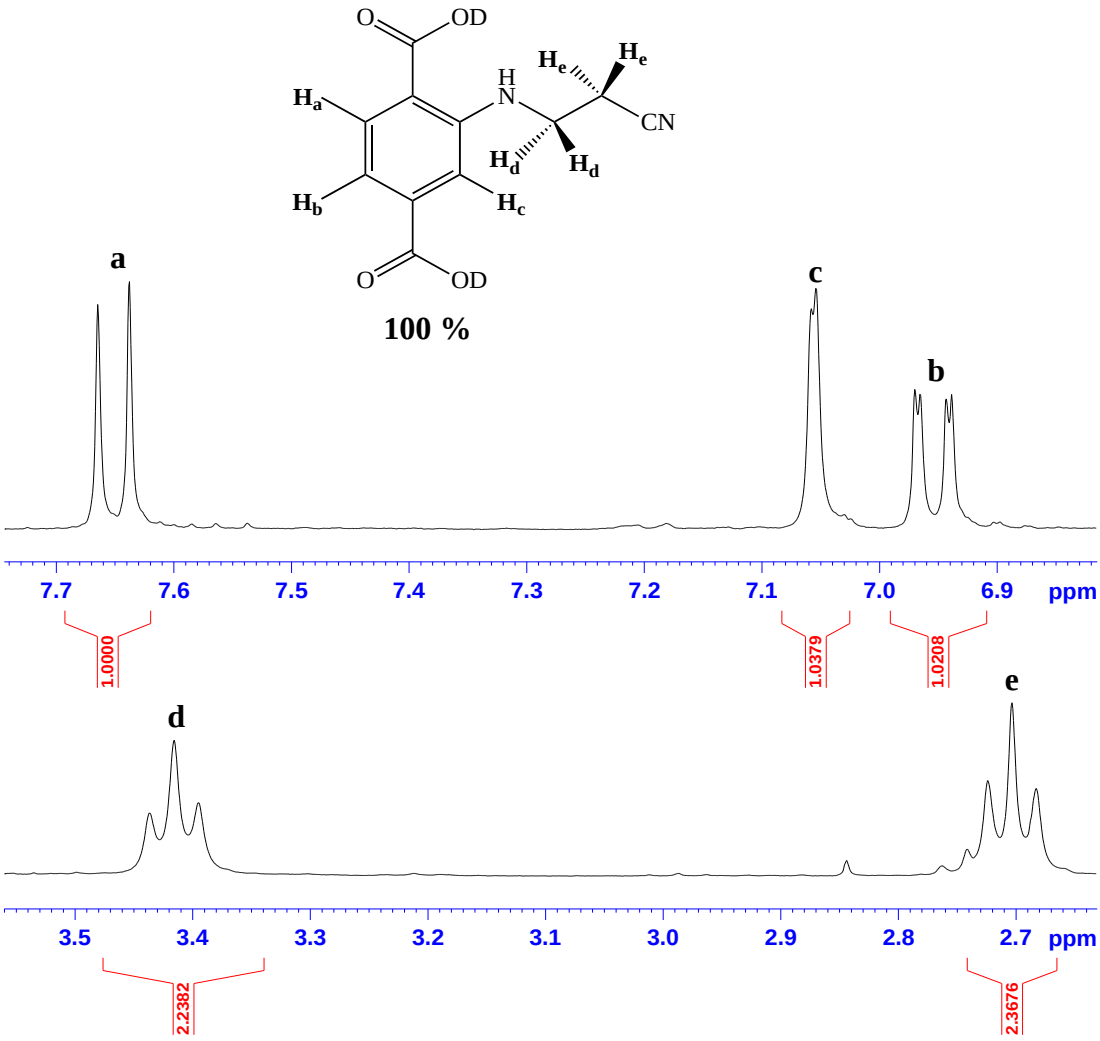

Figure 2.4. Aromatic (top) and aliphatic (bottom) regions of ^{1}H NMR spectrum of digested PSM product **1a**.

The negative ESI mass spectrum of the digested product **1a** confirms the singularly deprotonated anion of H_2BDC-NHCH$_2$CH$_2$CN at *m*/*z* = 233.0561 (predicted [M-H]$^-$ = 233.0562). The second addition of acrylonitrile into UiO-66-NHCH$_2$CH$_2$CN to form the di-adduct UiO-66-N(CH$_2$CH$_2$CN)$_2$ was ruled out as there is no evidence of the presence of signals which correspond to H_2BDC-N(CH$_2$CH$_2$CN)$_2$.

Fourier Transform Infrared (FTIR) Spectroscopy was also used to confirm the identity of the PSM product. This method has its own merit in comparison to solution NMR spectroscopy. In the latter case, there is a possibility of side reactions occurring between digested PSM products with the NMR solvent. In contrast, the FTIR spectrum was recorded on solid samples which eliminates this issue. The FTIR spectrum for **1a**, Figure

2.5, shows a broad peak at 3364 cm^{-1} which corresponds to N-H stretching of the modified framework. Furthermore, the presence of C≡N stretching at 2161 cm^{-1} indicates that the amino groups were successfully converted into cyanoethyl groups. This peak was not observed in the FTIR spectrum for the starting MOF, UiO-66-NH_2. The strong peaks at 1572 and 1388 cm^{-1} correspond to carbonyl stretching of the MOF framework.

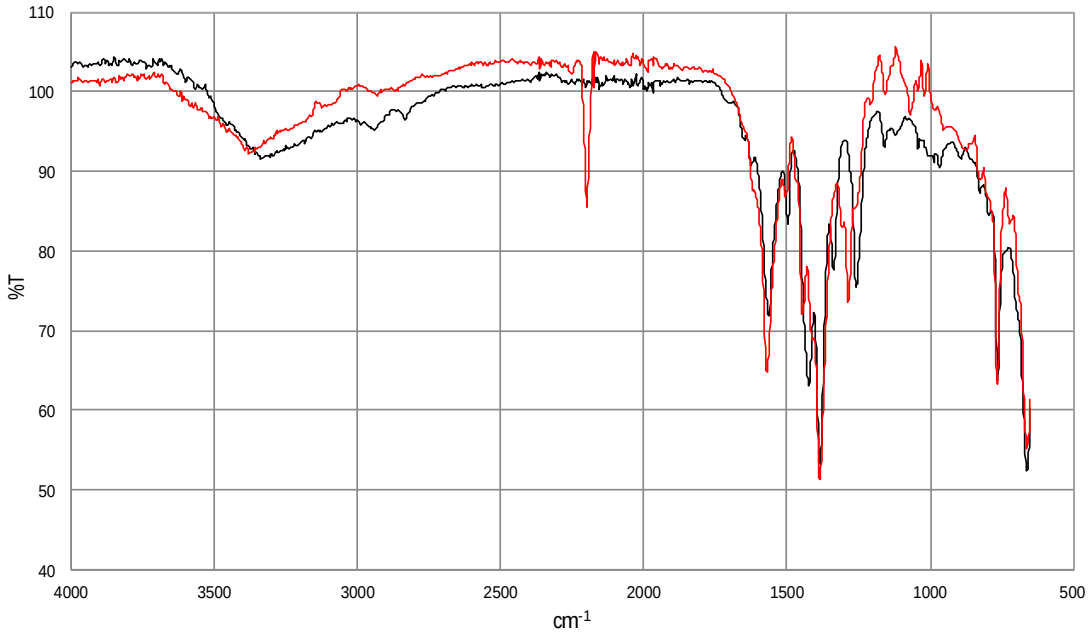

Figure 2.5. Black: FTIR spectrum of UiO-66-NH_2. Red: FTIR spectrum of $[Zr_6O_4(OH)_4(BDC\text{-}NHCH_2CH_2CN)_6]$, **1a.**

The high similarity between the PXRD pattern of **1a** and the starting MOF, UiO-66-NH_2 indicates that the structural integrity of the MOF was retained upon PSM, Figure 2.6. This result illustrates the robustness of the UiO-66 framework, in which increasing the reaction temperature has no effect on the crystallinity of the MOF structure.

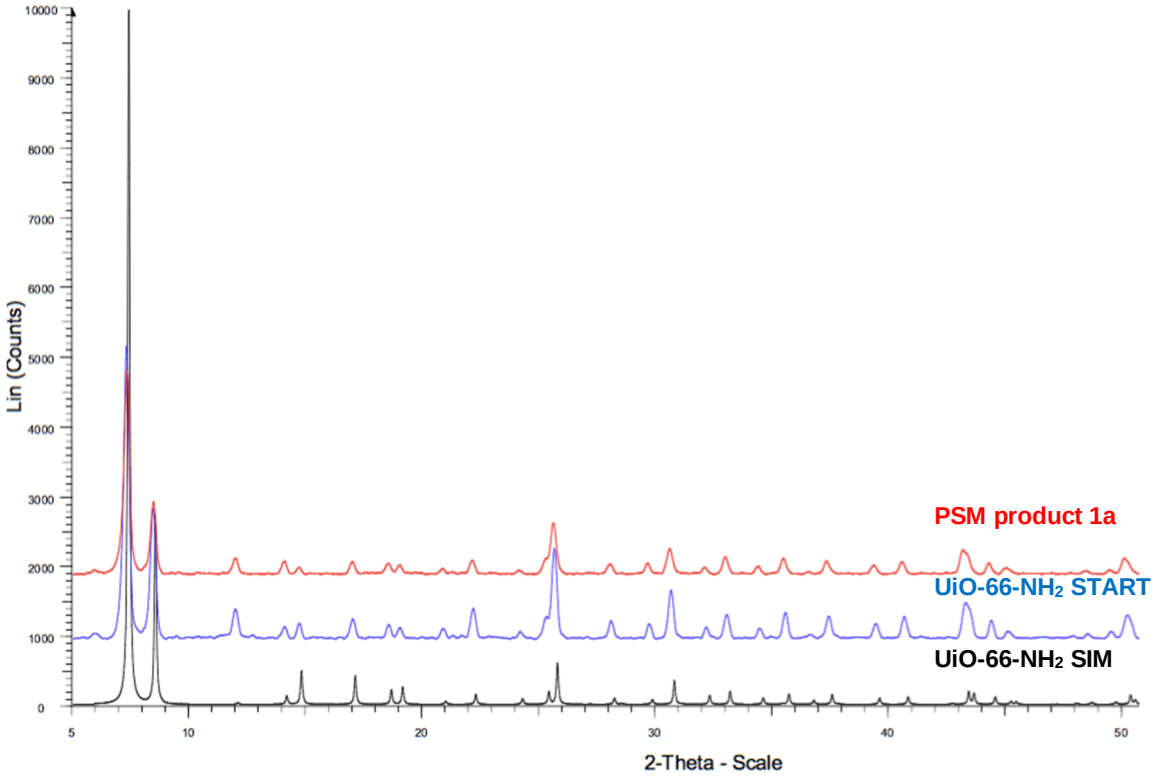

Figure 2.6. Black: Simulated PXRD pattern of UiO-66-NH_2. Blue: PXRD pattern of starting MOF, UiO-66-NH_2. Red: PXRD pattern of PSM product **1a**.

2.2. Scope of the aza-Michael Reaction on UiO-66-NH_2

In order to investigate the versatility of the aza-Michael reaction on UiO-66-NH_2, a variety of electron-deficient olefins, Figure 2.7, were assessed as Michael acceptors in this study. One reason for expanding the scope of this reaction is to introduce different functionalities into the pores of the parent MOF, UiO-66. Inclusion of oxygen-containing functional groups was a specific target, in order to explore the use of derivatised MOFs for CO_2 sorption studies which will be described in Section 2.5.2. The general reaction scheme showing the optimised reaction conditions is depicted in Scheme 2.5.

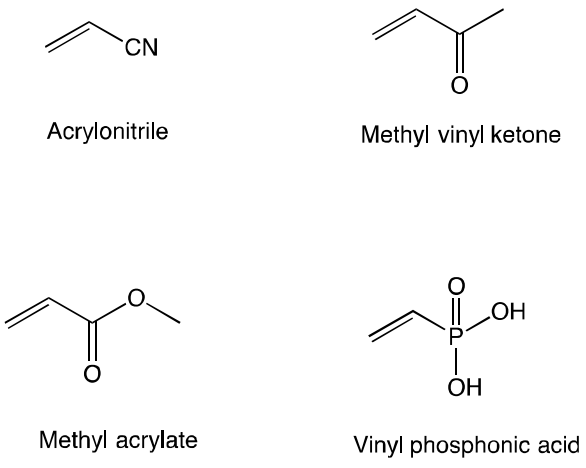

Figure 2.7. Michael acceptors used in the PSM reactions.

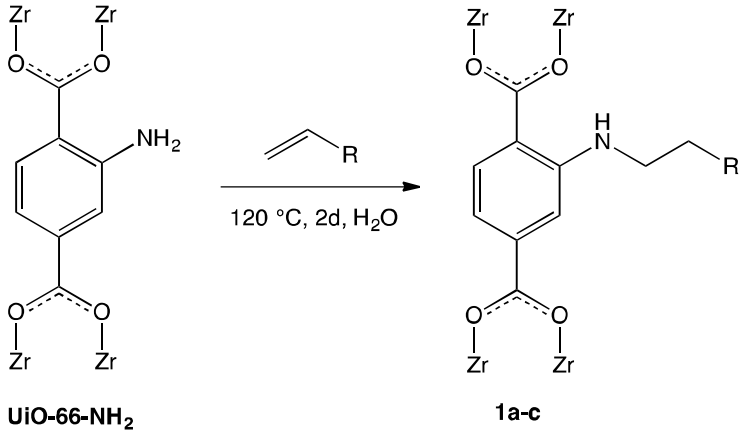

Scheme 2.5. Optimised PSM reaction scheme between UiO-66-NH_2 with electron deficient alkenes RC_2H_2. R = CN (**1a**), CO_2CH_3 (**1b**), $COCH_3$ (**1c**).

In addition to acrylonitrile, successful conversions from the amino to the respective β-amino carbonyl compounds were achieved by using methyl acrylate and methyl vinyl ketone. The results are described in the following section. Vinyl phosphonic acid was also employed as a potential Michael acceptor but the reaction yielded amorphous powders as evidenced by PXRD and hence was not explored any further.

2.2.1. PSM Reaction of UiO-66-NH_2 with Methyl Acrylate

The PSM reaction of UiO-66-NH_2 with methyl acrylate was carried out using the optimised conditions shown in Scheme 2.5. The percentage conversion of amino into the β-amino ester groups ($NHCH_2CH_2CO_2CH_3$) was gauged by ^1H NMR spectroscopy, Figure 2.8. The digestion conditions were similar to that used for PSM product **1a**, namely using a mixture of NH_4F/D_2O with DMSO-d_6.

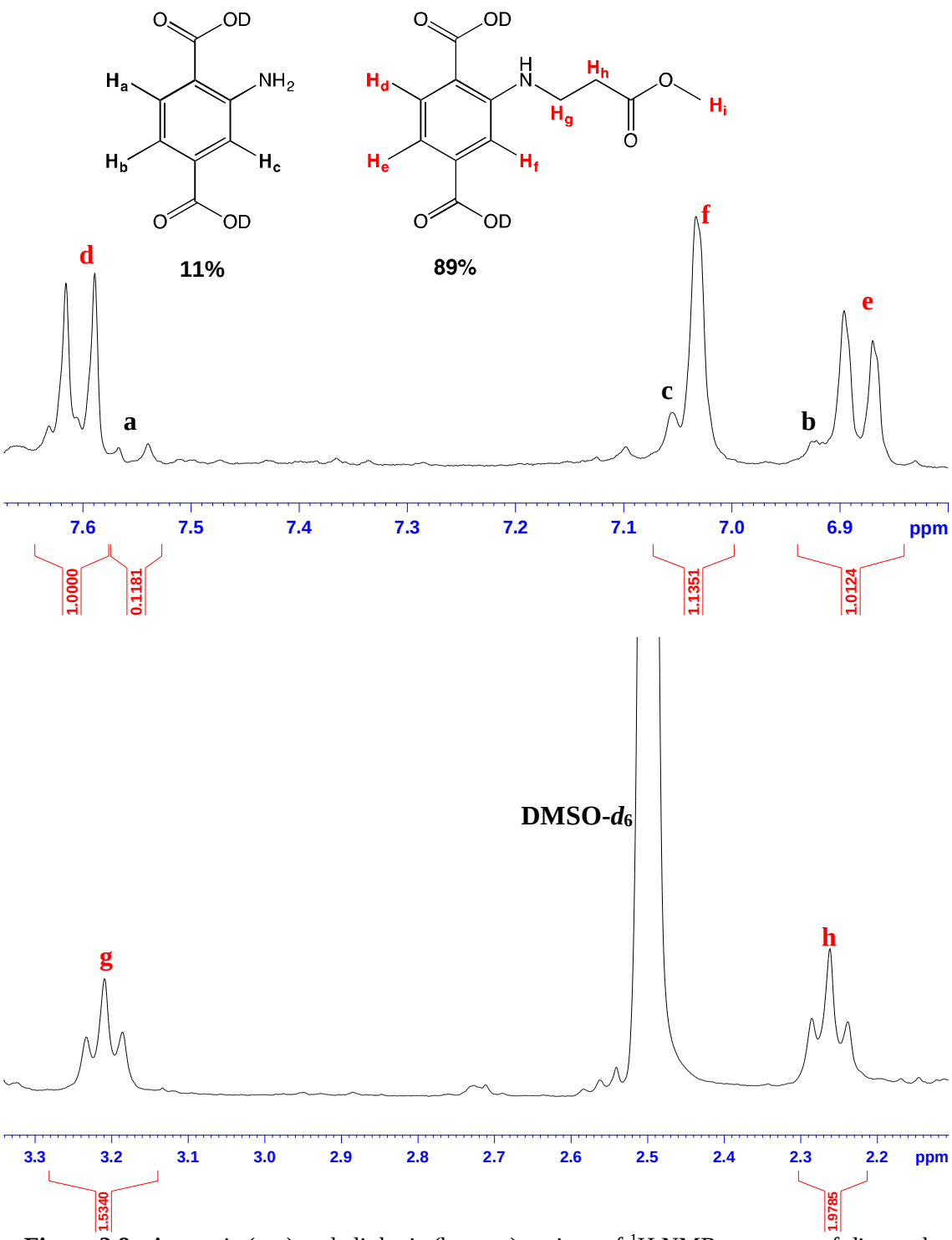

Figure 2.8. Aromatic (top) and aliphatic (bottom) regions of ^{1}H NMR spectrum of digested PSM product **1b**.

The presence of new peaks at δ 6.88, 7.03 and 7.61 ppm which correspond to aromatic protons of D_2BDC-$NHCH_2CH_2CO_2CH_3$ indicates that the PSM reaction was successful. Furthermore, two sets of triplets at δ 2.27 and 3.21 ppm can be seen in the spectrum, which correspond to the β- and α-protons to the secondary nitrogen of D_2BDC-$NHCH_2CH_2CO_2CH_3$, respectively. The singlet peak which corresponds to the terminal methyl protons H_i, could not be identified. The H_i peak was thought to be obscured by

the dominant HDO peak used in the digestion, thus making the task in locating it impossible. Comparing the integrals of the protons at δ 7.61 and 7.55 ppm, the percentage conversion was 89% and the formula of the product can be expressed as $[Zr_6O_4(OH)_4(BDC\text{-}NH_2)_{0.66}(BDC\text{-}NHCH_2CH_2CO_2CH_3)_{5.34}]$, **1b**.

The negative ESI mass spectrum of the digested PSM product **1b** confirmed the presence of singularly deprotonated anion of $H_2BDC\text{-}NHCH_2CH_2CO_2CH_3$ at m/z = 266.0661 (predicted $[M\text{-}H]^-$ = 266.06646).

FTIR spectroscopy of **1b** showed a weak peak at 3364 cm^{-1}, Figure 2.9, which corresponds to the N-H stretching of $UiO\text{-}66\text{-}NHCH_2CH_2CO_2CH_3$. The presence of ester groups on the modified framework was confirmed by the ester C=O stretch at 1712 cm^{-1}.

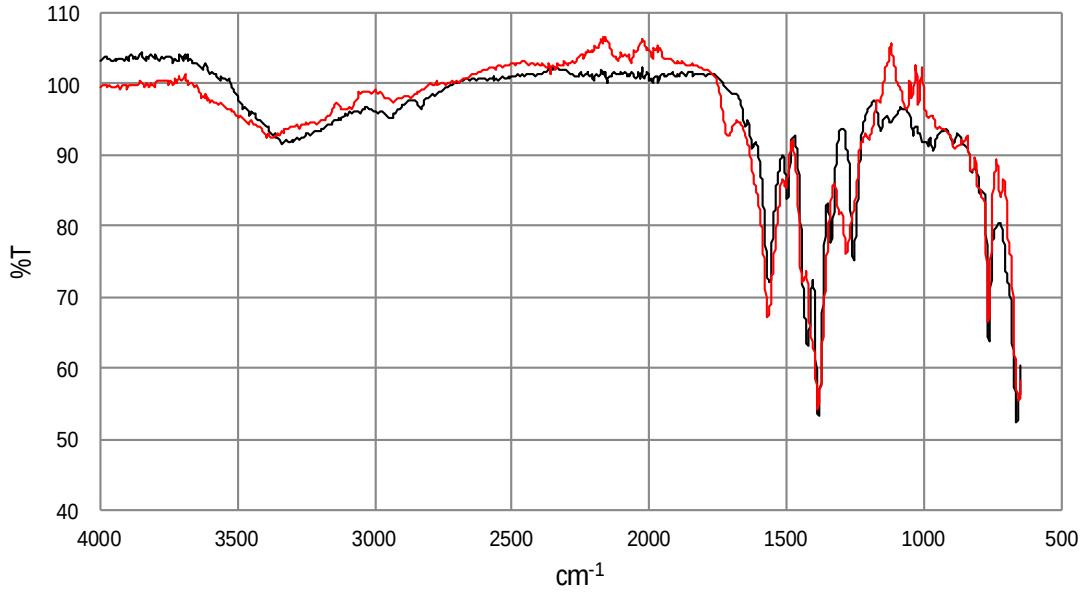

Figure 2.9. Black: FTIR spectrum of $UiO\text{-}66\text{-}NH_2$. Red: FTIR spectrum of $[Zr_6O_4(OH)_4(BDC\text{-}NH_2)_{0.66}(BDC\text{-}NHCH_2CH_2CO_2CH_3)_{5.34}]$, **1b.**

The structural integrity of **1b** was assessed by PXRD, Figure 2.10. Due to the high similarities of the PXRD patterns of $UiO\text{-}66\text{-}NH_2$ and PSM product **1b**, it was concluded that the framework remained intact and retained its crystallinity upon PSM reaction. Furthermore, this result indicates that the framework of $UiO\text{-}66\text{-}NH_2$ is robust towards methyl acrylate.

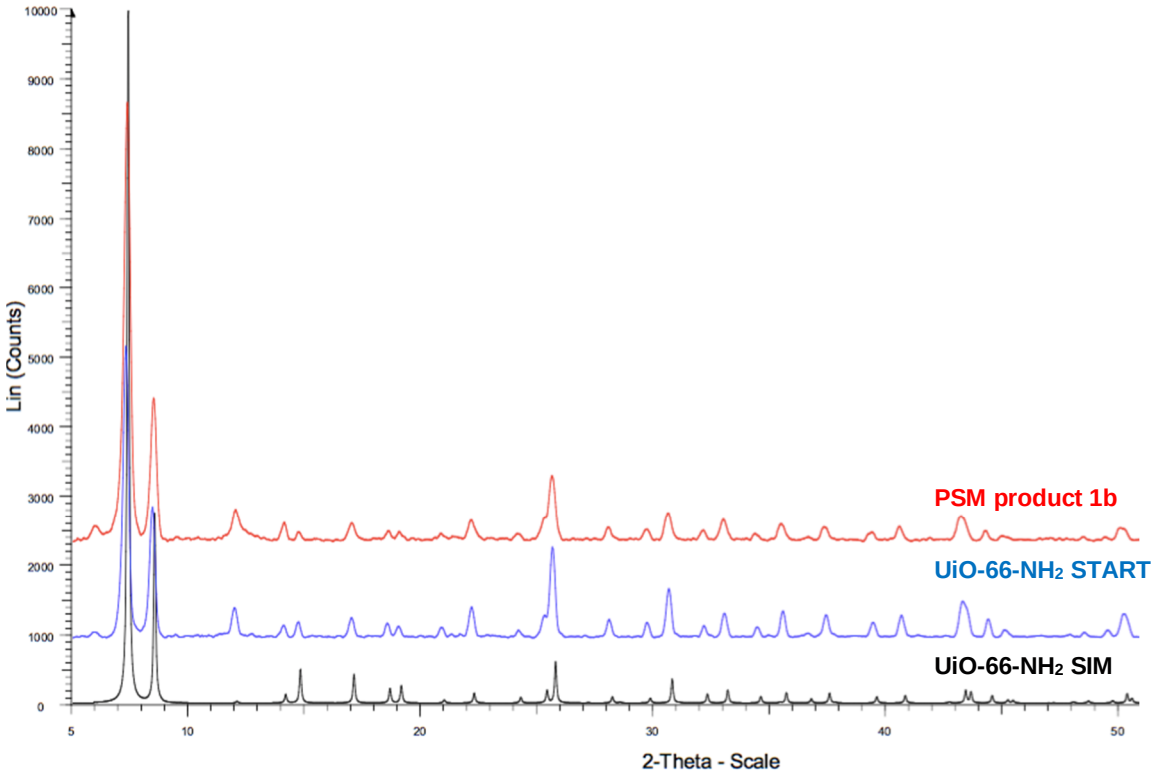

Figure 2.10. Black: Simulated PXRD pattern of UiO-66-NH_2. Blue: PXRD pattern of the starting MOF, UiO-66-NH_2. Red: PXRD pattern of PSM product **1b**.

2.2.2. PSM Reaction of UiO-66-NH_2 with Methyl Vinyl Ketone

The PSM reaction with methyl vinyl ketone was carried out using the same reaction conditions as outlined in Scheme 2.5. Apart from aromatic proton peaks which correspond to the starting MOF UiO-66-NH_2, new sets of peaks can be seen in the downfield region of the digested PSM product, **1c**, Figure 2.11.

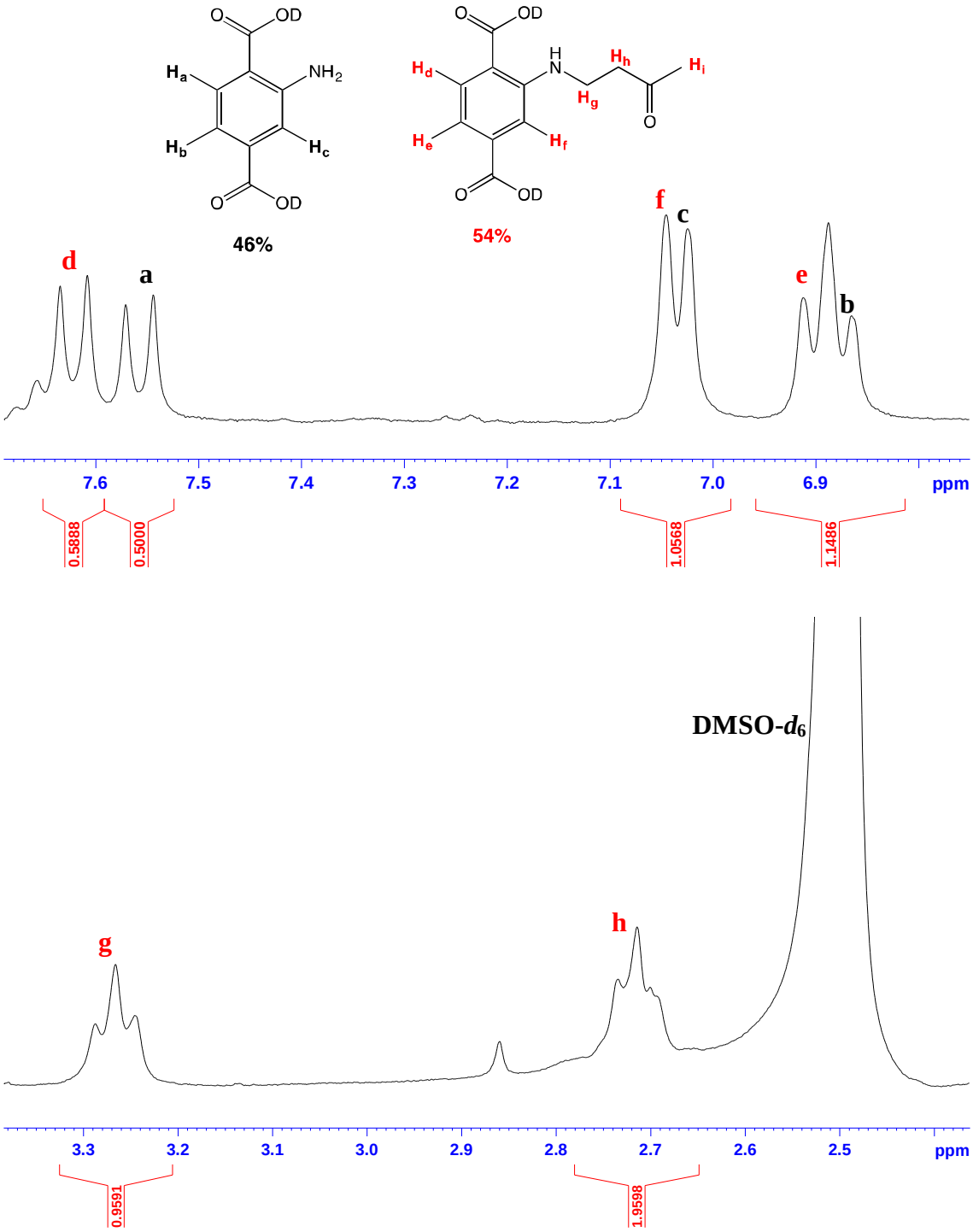

Figure 2.11 Aromatic (top) and aliphatic (bottom) regions of ^{1}H NMR spectrum of digested PSM product **1c**.

These peaks correspond to the aromatic protons of D_2BDC-NHCH$_2$CH$_2$COCH$_3$. Furthermore, the presence of two sets of triplets at δ 2.72 and 3.27 ppm which correspond to β- and α-protons to the secondary nitrogen of D_2BDC-NHCH$_2$CH$_2$COCH$_3$ indicates that the functional groups were successfully grafted on the MOF framework. The integral of the triplet at δ 2.72 ppm is larger than expected, due to some degree of overlapping with DMSO-d_6 solvent used in the digestion. There is also a small peak at δ 2.69 ppm which originates from the protons of DMF solvent used in the synthesis of the starting

MOF, UiO-66-NH_2. Extensive washing of UiO-66-NH_2 with MeOH and H_2O was carried out prior to using the MOF for PSM reactions but, in some cases, residual DMF solvent can still be seen in the ^1H NMR spectra. The singlet peak which corresponds to the terminal methyl protons H_i, could not be identified as the peak was thought to be obscured by the dominant HDO peak in similar vein to **1b**. Based on the integrals at δ 7.57 ppm and δ 7.62 ppm, it can be concluded that the PSM reaction proceeded with 54% conversion from amino to the β-amino ketone groups ($NHCH_2CH_2COCH_3$). The chemical formula for the PSM product **1c** can therefore be expressed as $[Zr_6O_4(OH)_4(BDC\text{-}NH_2)_{2.76}(BDC\text{-}NHCH_2CH_2COCH_3)_{3.24}]$.

The FTIR spectrum of the solid sample **1c** shows a broad peak at 3367 cm^{-1}, Figure 2.12, which corresponds to the N-H stretching of UiO-66-$NHCH_2CH_2COCH_3$. The presence of ketone functional groups on the modified framework was confirmed by the ketone C=O stretch at 1710 cm^{-1}.

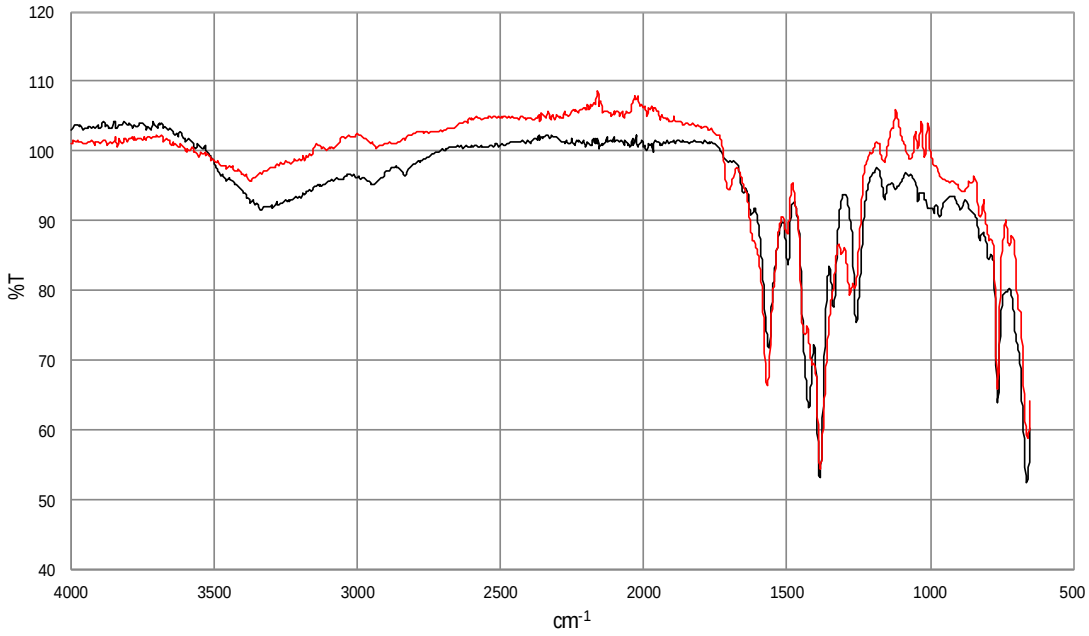

Figure 2.12 Black: FTIR spectrum of UiO-66-NH_2. Red: FTIR spectrum of $[Zr_6O_4(OH)_4(BDC\text{-}NH_2)_{2.76}(BDC\text{-}NHCH_2CH_2COCH_3)_{3.24}]$, **1c.**

Figure 2.13 shows the PXRD patterns of the starting MOF, UiO-66-NH_2 with PSM product **1c**, illustrating the high similarities between the two MOFs. The retention in peak positions in the PXRD pattern for **1c** indicates that the framework was retained throughout PSM reaction.

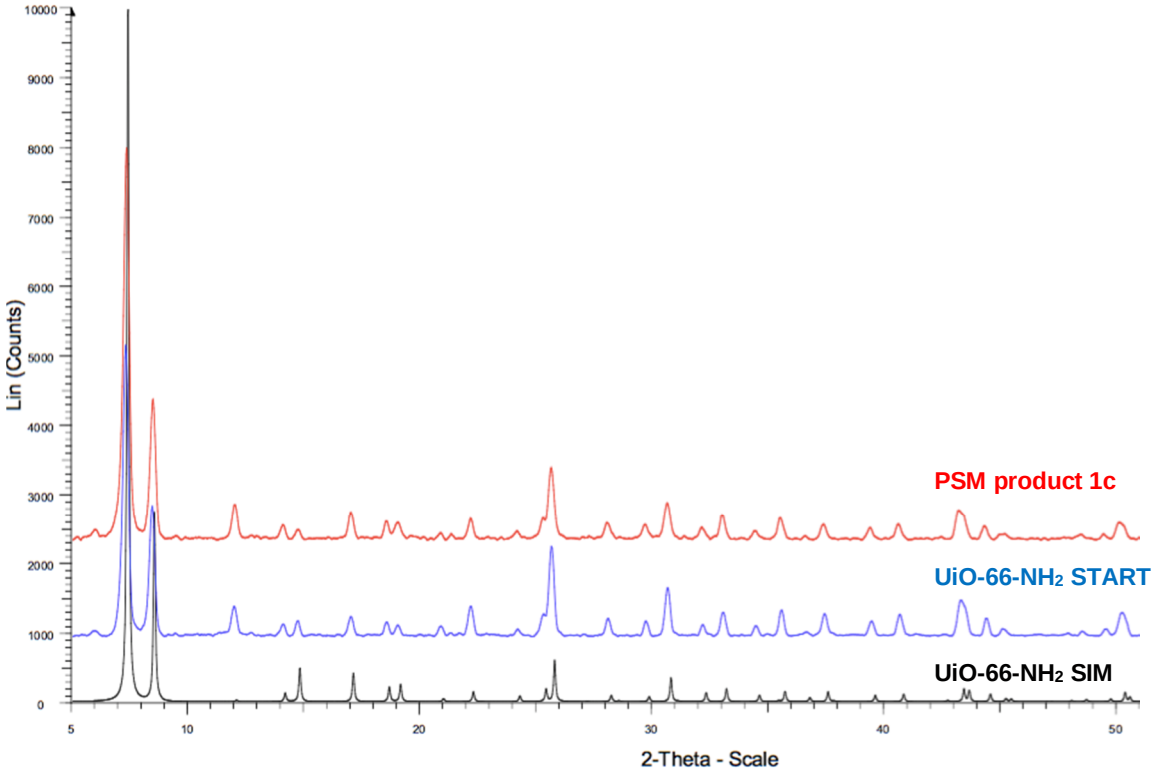

Figure 2.13. Black: Simulated PXRD pattern of UiO-66-NH_2. Blue: PXRD pattern of starting MOF, UiO-66-NH_2. Red: PXRD pattern of PSM product **1c**.

Based on the results reported thus far, it is clear that the type of Michael acceptors used in the PSM reactions have a significant effect on the PSM percentage conversions, Table 2.3. The difference in percentage conversions can be rationalised by the effect of electron withdrawing groups (EWG) in each Michael acceptors used in this study. For example, the −C≡N group in acrylonitrile is strongly deactivating, thus making the terminal alkene in acrylonitrile susceptible towards nucleophilic addition with –NH_2. In comparison, the ester group in methyl acrylate is less deactivating, leading to a lower conversion of –NH_2 into the β-amino ester groups (89%) (**1b**). A similar explanation can be applied to the least reactive aza-Michael acceptor, methyl vinyl ketone, in which the lowest conversion (54%) was observed (**1c**).

Compound	Michael acceptor	EWG	% conversion	Chemical formula
1a	Acrylonitrile, CH_2CH_2CN	$-C\equiv N$	100	$[Zr_6O_4(OH)_4(BDC\text{-}NHCH_2CH_2CN)_6]$
1b	Methyl acrylate, $CH_2CH_2CO_2CH_3$	$-CO_2CH_3$	89	$[Zr_6O_4(OH)_4(BDC\text{-}NH_2)_{0.66}(BDC\text{-}NHCH_2CH_2CO_2CH_3)_{5.34}]$
1c	Methyl vinyl ketone, $CH_2CH_2COCH_3$	$-COCH_3$	54	$[Zr_6O_4(OH)_4(BDC\text{-}NH_2)_{2.76}(BDC\text{-}NHCH_2CH_2COCH_3)_{3.24}]$

Table 2.3 The effect of EWG on PSM percentage conversions.

2.3. Tandem PSM Reaction of UiO-66-$NHCH_2CH_2CN$, 1a, with Sodium Azide: Incorporation of Tetrazole in UiO-66 Framework

As described in Section 2.1.2, the amino groups in UiO-66-NH_2 could successfully be converted into cyanoethyl groups (UiO-66-$NHCH_2CH_2CN$) with 100% conversion. In order to access whether the cyano groups in the MOF could be transformed into different functional groups, a further PSM reaction was carried out. A range of organic reactions were screened, of which the most promising was the conversion of cyano groups into 5-substituted tetrazoles. The tandem PSM reaction for the conversion of UiO-66-NH_2 into a MOF containing two different functionalities (cyanoethyl and 5-substituted tetrazoles) is shown in Scheme 2.6.

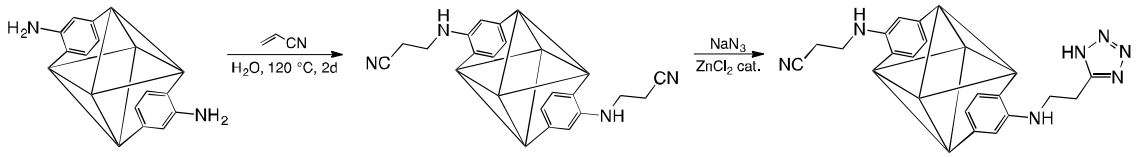

Scheme 2.6. Tandem PSM reaction of UiO-66-NH_2 forming a MOF containing two different functionalities. The UiO-66 framework is shown as an octahedral cage for clarity.

2.3.1. Investigation on Optimum Reaction Conditions

In this study, different solvents (MeCN, DMF, H_2O, EtOH, *n*-PrOH and *n*-BuOH) were screened with the aim of obtaining the highest conversion from cyano to 5-substituted tetrazoles. Prior to PSM reactions, UiO-66-$NHCH_2CH_2CN$ powder was rinsed with the respective solvents. All reactions were carried out by heating the reaction mixture under reflux for 24 hours. The reactions were quenched by rinsing the PSM products by centrifugation with the respective solvents. Detailed experimental procedures can be

found in Section 2.9.5. The conversion from cyano to 5-substituted tetrazoles was achieved by using *n*-BuOH as the solvent. In contrast, no conversion was observed when MeCN, DMF, H_2O, EtOH, *n*-PrOH were used in the reactions.

The successful conversion from cyano to 5-substituted tetrazoles in *n*-BuOH was confirmed by ^1H NMR spectroscopy of the digested PSM product **1d**, Figure 2.14. New sets of peaks (δ 6.92, 7.08 and 7.61 ppm) were observed in the aromatic region, in addition to the peaks which correspond to the aromatic protons of D_2BDC-$NHCH_2CH_2CN$ (δ 6.96, 7.06 and 7.65 ppm). The new peaks correspond to the protons from the aromatic ring of D_2BDC-$NHCH_2CH_2CN_4H$, (CN_4H = 5-substituted tetrazole). A triplet peak which corresponds to the β-protons to the secondary nitrogen of D_2BDC-$NHCH_2CH_2CN_4H$, H_j can be clearly seen at δ 3.0 ppm. The triplet peak of the neighbouring α-protons, H_i is only partly visible due to overlap by the more dominant H_d peak. Comparing the integrals at δ 3.0 ppm and δ 6.86 ~ 7.01 ppm, the percentage conversion from cyano to 5-substituted tetrazoles was calculated as being approximately 21%. The calculated conversion gives the formula for **1d** as $[Zr_6O_4(OH)_4(BDC\text{-}NHCH_2CH_2CN)_{4.74}(BDC\text{-}NHCH_2CH_2CN_4H)_{1.26}]$.

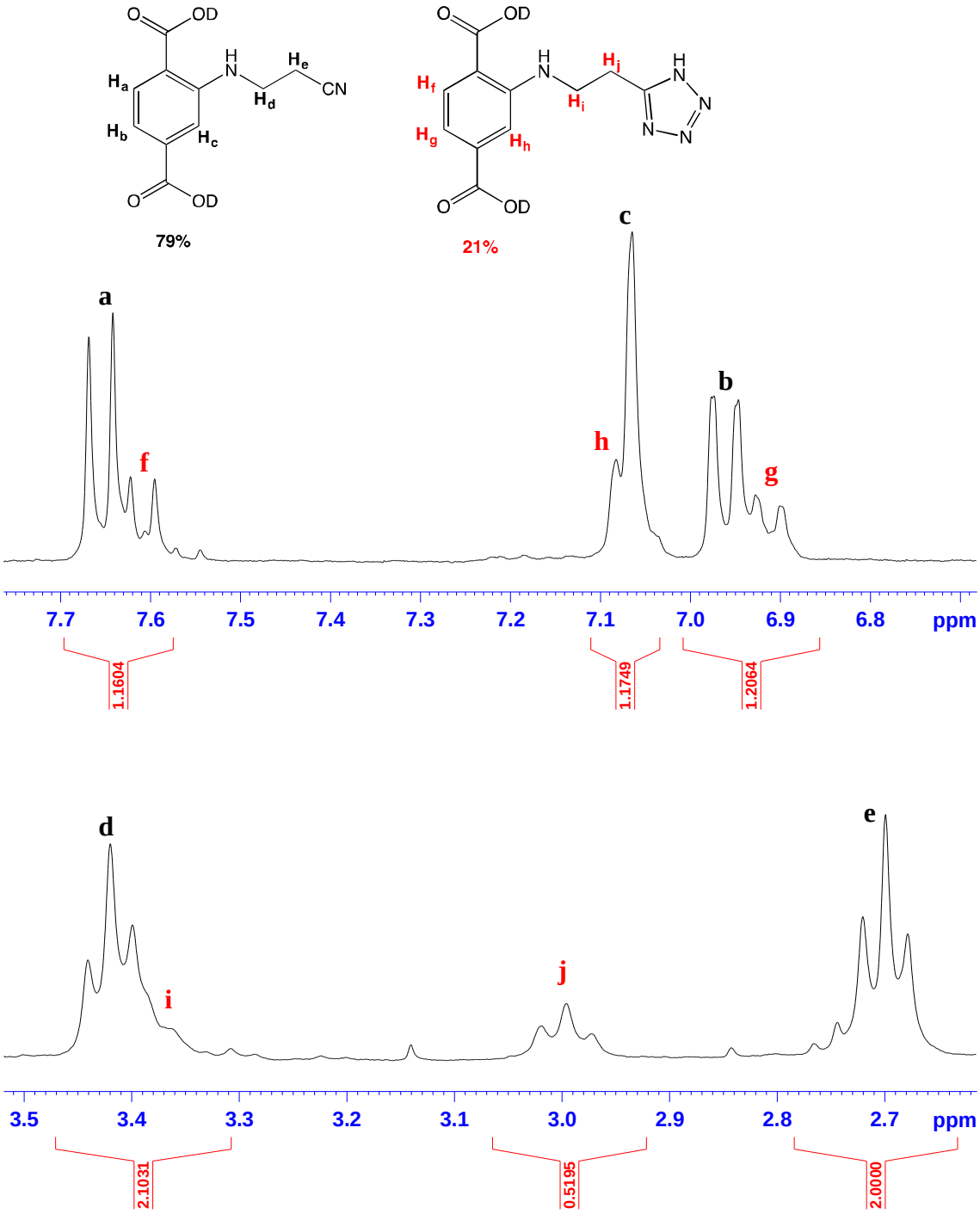

Figure 2.14 Aromatic (top) and aliphatic (bottom) regions of ^{1}H NMR spectrum of digested PSM product **1d**.

The negative ESI mass spectrum of the digested product **1d** confirmed the singularly deprotonated anion of $H_2BDC\text{-}NHCH_2CH_2CN_4H$ at *m*/*z* = 276.0727 (predicted $[M\text{-}H]^-$ = 276.0733).

In order to investigate the structural integrity of the PSM product, PXRD was carried out on the solid sample **1d**. The sample was extensively rinsed with *n*-BuOH prior to the

PXRD measurement and the pattern of the *n*-BuOH-rinsed sample, **1d (*n*-BuOH)** shows additional peaks at 2θ 31.5, 34.5, 36.0 and 47.5 in addition to peaks that correspond to the UiO-66 framework, Figure 2.15. This indicates that more than one crystalline material is present in **1d (*n*-BuOH)**. The presence of unreacted starting materials (*i.e.* NaN_3 and $ZnCl_2$) in **1d (*n*-BuOH)** were ruled out as the PXRD patterns for both reactants are different to the unknown peaks observed in the PXRD pattern for **1d (*n*-BuOH)**. Attempts to identify the unknown crystalline material was unsuccessful, although it was thought that they might originate from a zinc salt. This assumption is due to the fact that no additional organic compounds were observed in the ^{1}H NMR spectrum of digested **1d**, which implies that the by-product must be an inorganic compound. With the aim of eliminating the crystalline by-product in **1d**, the solid sample was rinsed with H_2O. This proved effective, as the PXRD pattern of the H_2O-rinsed sample, **1d (H_2O)** shows disappearance of the by-product's peaks. The ^{1}H NMR spectrum of the solid sample **1d (H_2O)** digested in NH_4F/D_2O with DMSO-d_6 was similar to that for **1d (*n*-BuOH)** shown in Figure 2.14. This indicates that the calculated conversion of cyano to 5-substituted tetrazoles was not affected by the rinsing method.

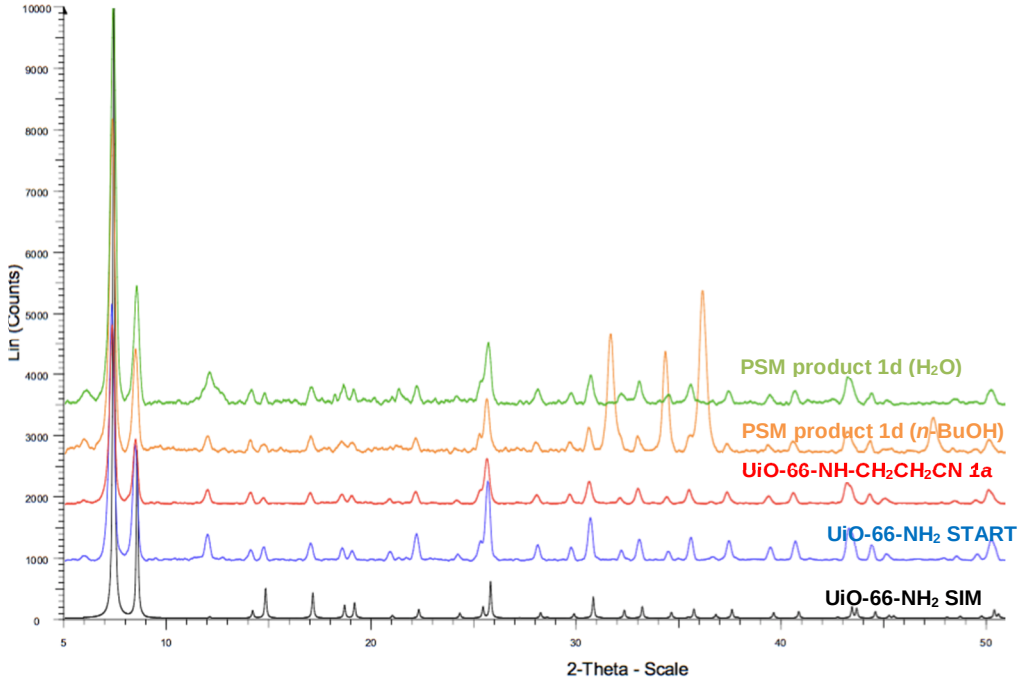

Figure 2.15. Black: Simulated PXRD pattern of UiO-66-NH_2. Blue: PXRD pattern of starting MOF, UiO-66-NH_2. Red: PXRD pattern of UiO-66-NH-CH_2CH_2CN **1a**. Orange: PXRD pattern of *n*-BuOH rinsed sample **1d**. Green: PXRD pattern of H_2O rinsed sample **1d**.

Different experimental procedures were carried out to investigate whether it was possible to increase the percentage conversion of cyano into 5-substituted tetrazoles. One of these involved employing a mixture of *n*-BuOH and H_2O as the solvent, as H_2O was shown to

dissolve the unknown by-product. Nonetheless, no reaction occurred in this solvent system as evidenced by ^{1}H NMR spectroscopy. As described earlier, using neat H_2O also leads to no conversion of the cyano groups. Increasing the amount of $ZnCl_2$ catalyst in the reaction and increasing the reaction time also had no effect on the percentage conversion.

Based on these findings, it was concluded that the optimum conditions for the conversion from cyano into 5-substituted tetrazoles were by leaving the reaction mixture for a day under reflux in *n*-BuOH, Scheme 2.7. As shown previously in Figure 2.14, under these reaction conditions, the conversion from cyano into 5-substituted tetrazoles was approximately 21%. This was the maximum conversion that could be achieved for this system, possibly because the presence of cyano and 5-substituted tetrazoles in the pores causes pore blocking.

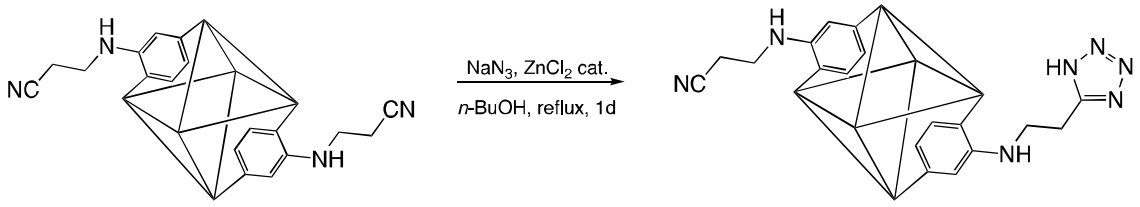

Scheme 2.7. Schematic representation of the conversion of cyano groups into 5-substituted tetrazoles showing the optimum reaction conditions.

The FTIR spectrum of the solid sample **1d**, $[Zr_6O_4(OH)_4(BDC\text{-}NHCH_2CH_2CN)_{4.74}(BDC\text{-}NHCH_2CH_2CN_4H)_{1.26}]$ was similar to that for **1a**, $[Zr_6O_4(OH)_4(BDC\text{-}NHCH_2CH_2CN)_6]$, Figure 2.16. There was a broad peak at 3367 cm^{-1}, which corresponds to the secondary amine stretching. The C≡N stretching from the unmodified C≡N groups can still be seen at 2087 cm^{-1}. The tetrazole absorption bands could not be located due to the presence of other dominant peaks associated with the framework's backbone.

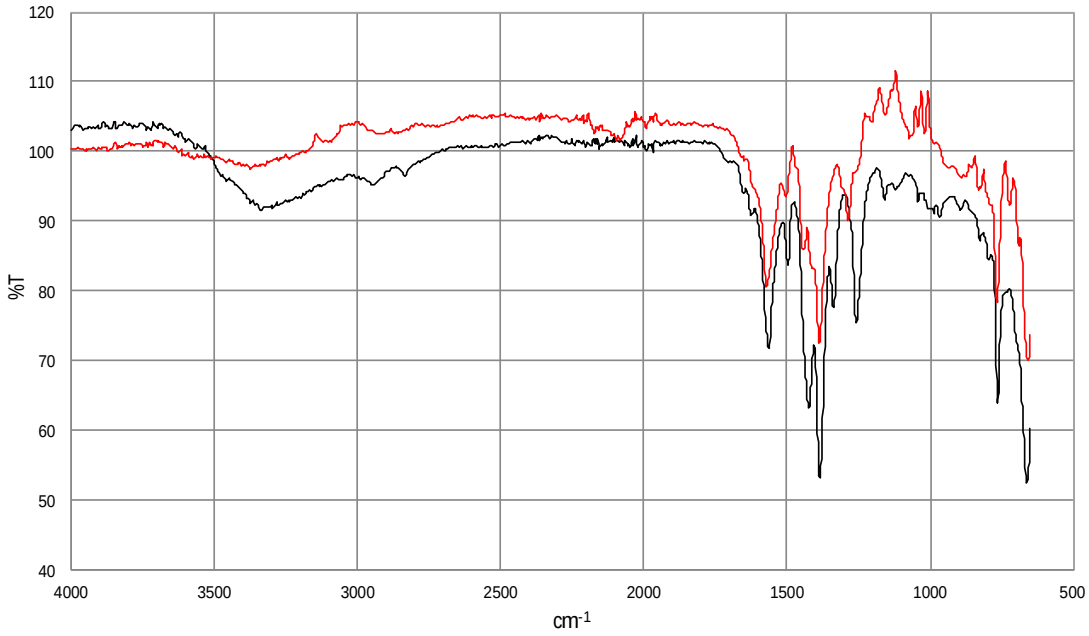

Figure 2.16. FTIR spectrum of $[Zr_6O_4(OH)_4(BDC\text{-}NHCH_2CH_2CN)_{4.74}(BDC\text{-}NHCH_2CH_2CN_4H)_{1.26}]$, **1d.**

2.4. Thermogravimetric Analysis of PSM Products, 1a-1d.

The thermal stability of the PSM products, **1a-1d** were assessed by thermogravimetric analysis (TGA), Figure 2.17. All samples were rinsed with H_2O prior to the TGA measurements. An initial mass loss (up to 120 °C) was seen in all products which is attributed to H_2O solvent in the pores and on the solid surface. The second mass loss (120 °C – 470 °C) may be attributed to residual DMF solvent in the pores and/or the dehydroxylation of the $Zr_6O_4(OH)_4$ nodes to form $Zr_6O_6(OH)_x$ (x = 3, 2, 1, 0). The UiO-66 series are known to undergo a complete dehydroxylation reaction at 300 °C.[11] Traditionally, a plateau region in a TGA profile represents the range of temperature that can be used to produce the porous form of a MOF. In this work, due to the subtle mass loss in the 120 °C – 470 °C region, 120 °C was chosen as the activation temperature of **1a-1d**. A rapid weight loss can be seen at 470 °C, which implies the decomposition of the framework. A similar observation was also noted for the TGA of UiO-66-NH_2, in which framework decomposition occurred at approximately 470 °C. This result implies that PSM did not alter the framework integrity of UiO-66-NH_2.

The TGA data also gives an insight into the amount of solvent (H_2O molecules) that reside in the pores of the MOFs. For each $Zr_6O_4(OH)_4$ unit, UiO-66-NH_2 has ten, **1a** has seven, **1b** has eight, **1c** has nine and **1d** has one H_2O molecule/molecules. This result indicates

that the number of H_2O molecules decreases as the percentage conversion increases. Furthermore, **1d** has the least number of H_2O molecules as the presence of the bulky tetrazole groups in the pores may limit the space available for H_2O molecules. On the other hand, UiO-66-NH_2 has the highest amount of H_2O molecules and this may be attributed to the large free space in the pores and the hydrogen bonding between the amino groups in UiO-66-NH_2 and H_2O molecules.

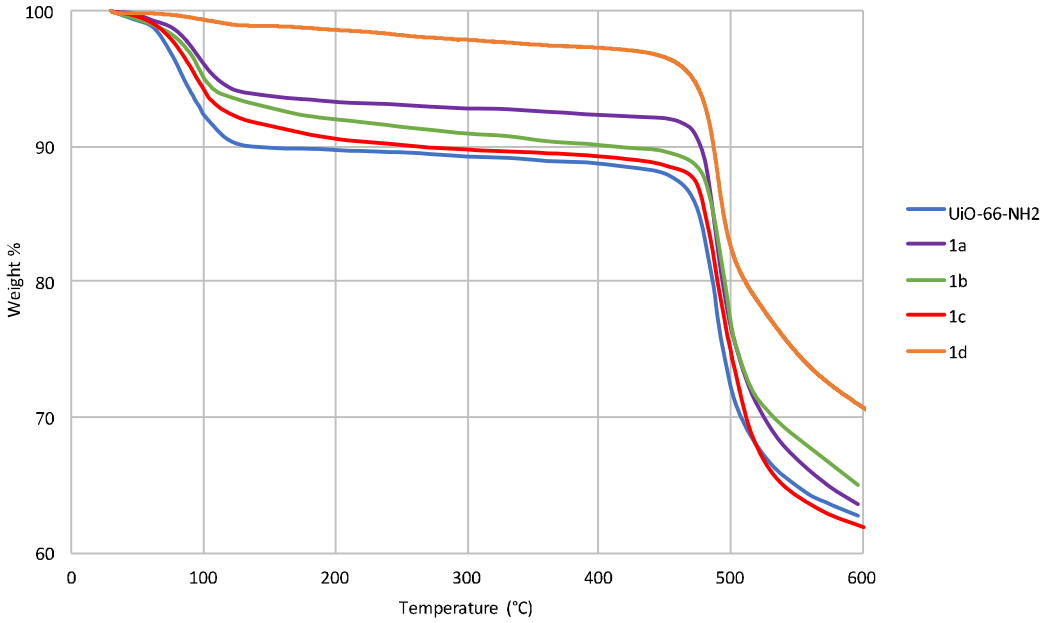

Figure 2.17. TGA of UiO-66-NH_2 and PSM products, **1a-1d**. The samples were heated from 30 °C to 600 °C at a rate of 20 K/min under a flow of argon gas (20 mL/min).

2.5. Gas Sorption Studies

2.5.1. BET Surface Areas of PSM Products, 1a-d

In order to investigate the porosity of PSM products, **1a-d**, N_2 adsorption measurements were carried out at 77 K. Prior to the measurements, the samples were activated at 120 °C for 12 hours. 120 °C is the conventional activation temperature for UiO-66 (and its derivatives) that has been used by different research groups.[12-14] Moreover, TGA experiments confirm that H_2O is lost at this temperature. The PXRD patterns of the activated samples were similar to those recorded prior to activation, which indicates that the activation conditions do not alter the crystallinity of **1a-d**. The N_2 adsorption isotherms for UiO-66-NH_2 and **1a-d** are shown in Figure 2.18.

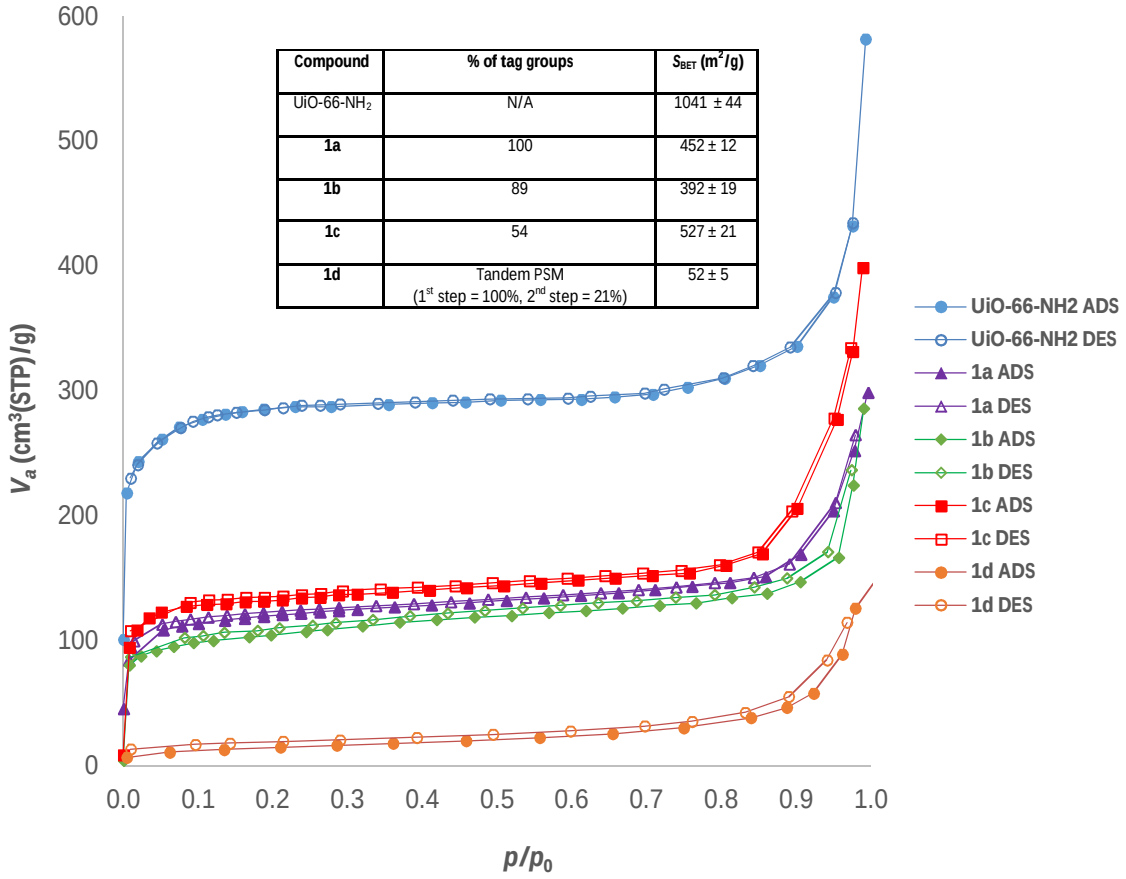

Figure 2.18. The N_2 adsorption isotherms for UiO-66-NH_2 and PSM products, **1a-d**, at 77 K and the respective BET surface areas.

The BET surface area for UiO-66-NH_2 obtained in this work (S_{BET} = 1041 m^2/g) is similar to the values reported in the literature, which confirms the reproducibility of the surface area measurement and also the efficiency of the activation conditions used in this work. The PSM products, **1a-c** were shown to exhibit type I isotherm with each product showing lower degrees of porosity than the starting MOF, UiO-66-NH_2. However, this observation can be rationalised by the mass increase caused by the tag groups in the pores which lead to the reduction in the BET surface areas (m^2/g). The percentage conversion also had an impact on the BET surface area. In general, the higher the percentage conversion, the lower the surface area. This is due to the reduced amount of N_2 adsorption sites as well as pore blocking effect caused by the tag groups. For example, the surface area for **1b** (S_{BET} = 392 m^2/g) is lower than **1c** (S_{BET} = 527 m^2/g), in part due to the higher percentage of tag groups in **1b**.

Another factor that influences the surface area of a PSM product is the size of the tag groups and the associated steric hindrance potential. In general, the bulkier the groups,

the lower the surface area of a MOF. In some cases, the size effect is more pronounced than the effect caused by the degree of percentage conversion. For example, due to the higher percentage of tag groups in **1a** (100%) compared to **1b** (89%), one would expect that the surface area for the former would be lower than the latter if only the effect of percentage conversion was taken into account. Nonetheless, as shown in Figure 2.18, **1b** exhibits lower surface area than **1a** due to the greater effect of the pore blocking caused by the larger tag group, $-NHCH_2CH_2CO_2CH_3$ in **1b** compared to that in **1a**, $-NHCH_2CH_2CN$.

The effect of pore blocking is exemplified further by the essentially non-porous nature of **1d**, which shows a type II isotherm. Although two different functional groups (Section 2.3.1, Scheme 2.7) were successfully grafted in the pores of UiO-66-NH_2 *via* tandem PSM, the introduction of these groups has resulted in a substantial loss of porosity.

2.5.2. CO_2 and N_2 Adsorption of PSM Products, 1a-d, at 273 K

As stated in Section 2.2, one of the aims of this work was to investigate the CO_2 loadings of the PSM products, Figure 2.19, and also to probe the effects of the tag groups on the CO_2 uptake.

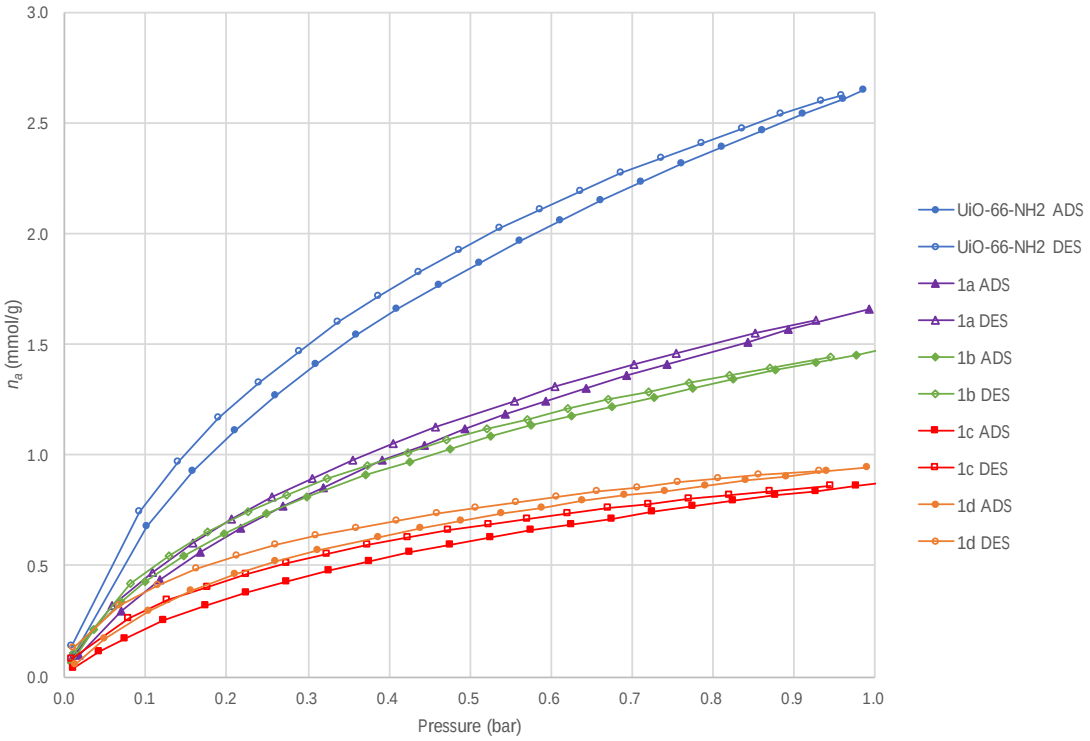

Figure 2.19. The CO_2 adsorption isotherms for UiO-66-NH_2 and PSM products, **1a-d**, at 273 K.

The CO_2 uptake for the PSM products, **1a-1d** are lower than that for the starting material, UiO-66-NH_2. This reflects, once again, the pore blocking caused by the tag groups which limit the diffusion of CO_2 molecules in **1a-1d**. Furthermore, the absence of the CO_2-philic –NH_2 group in the pores of **1a-1d** may also impart to the lower CO_2 uptake capacities. Interestingly, the CO_2 loading for **1a** is higher than that for **1b** at high pressure (1 bar) although the loadings are similar at low pressure (0.1 bar), Table 2.4. This is probably due to the smaller tag group in **1a** (–$NHCH_2CH_2CN$) which at higher pressure, permits the CO_2 molecules to diffuse more effectively into the pores in comparison to **1b** which has a larger tag group protruding into the pores (–$NHCH_2CH_2CO_2CH_3$).

Unexpectedly, the CO_2 loading of **1d** is somewhat higher than that for **1c** despite the former being essentially non-porous. One possible reason for this observation may be the strong interaction of CO_2 molecules with the tetrazole moieties present in the pores and on the crystal surface. MOFs with nitrogen-rich environment such as tetrazole- and triazole-functionalised MOFs have been shown to have high affinity towards CO_2.[15, 16] In the case of **1d**, although the sample is essentially non-porous due to the pore blocking of the tag groups in the pores, the sample still shows a decent amount of CO_2 uptake due to the presence of CO_2-philic tetrazole moieties in the pores and on the crystal surface.

The N_2 adsorption measurements were also carried out at 273 K, Figure 2.20, to determine the selectivity of CO_2 over N_2 for each PSM product. The results are summarised in Table 2.4.

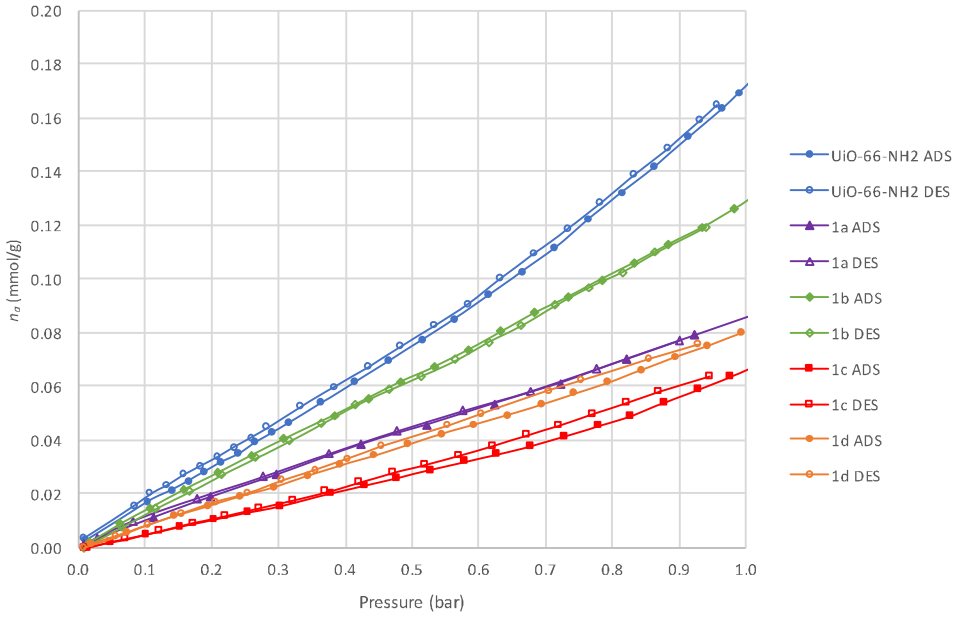

Figure 2.20. The N_2 adsorption isotherms for UiO-66-NH_2 and PSM products, **1a-d**, at 273 K.

Sample	CO_2 (mmol/g)		N_2 (mmol/g)		Selectivity (CO_2/N_2)	
	1 bar	0.1 bar	1 bar	0.1 bar	1 bar	0.1 bar
UiO-66-NH_2	2.645	0.679	0.169	0.019	16	36
1a	1.655	0.437	0.087	0.011	19	40
1b	1.481	0.425	0.126	0.015	12	28
1c	0.879	0.252	0.068	0.005	13	50
1d	0.944	0.297	0.080	0.012	12	25

Table 2.4. The CO_2 and N_2 adsorption data for UiO-66-NH_2 and PSM products, **1a-d**, at 0.1 and 1 bar at 273 K. The selectivity of CO_2 over N_2 of the material was calculated from the single gas isotherms by dividing the CO_2 uptake by that of N_2 at a specific pressure (0.1 or 1 bar).

All PSM products, **1a-1d** show lower N_2 uptake than that for the starting MOF, UiO-66-NH_2. The reason for this observation is similar with that reported previously with the CO_2 adsorption isotherms, in which pore blocking causes a decrease in gas diffusion and adsorption. Nonetheless, in terms of CO_2 selectivity over N_2, **1a** shows subtle increase in selectivity at 1 and 0.1 bar. The increase is even more pronounced for **1c** at 0.1 bar with the selectivity reaching 50. At present, the reason for this increase in unclear although it is thought that the tag group ($–NHCH_2CH_2COCH_3$) may contribute to the higher selectivity of CO_2 over N_2 in **1c**.

To date, $[Zn(PYR)_2(SiF_6)]$ SIFSIX-3-Zn, (PYR = pyrazine), Figure 2.21, holds the record for the highest CO_2/N_2 selectivity among MOF materials with the selectivity reaching 1539 (1 bar, 298 K).[17] This MOF consists of zinc ions coordinated to PYR ligands in two dimensions. These 2-D layers are pillared by $SiF_6^{2–}$ anions which results in a 3-D primitive cubic topological framework with one-dimensional square channels aligned by a periodic array of $SiF_6^{2–}$ pillars. The remarkably high CO_2/N_2 selectivity in SIFSIX-3-Zn is thought to be due to the presence of small channels (3.84 Å), which helps with the strengthening of the electrostatic interactions provided by the array of $SiF_6^{2–}$ anions.

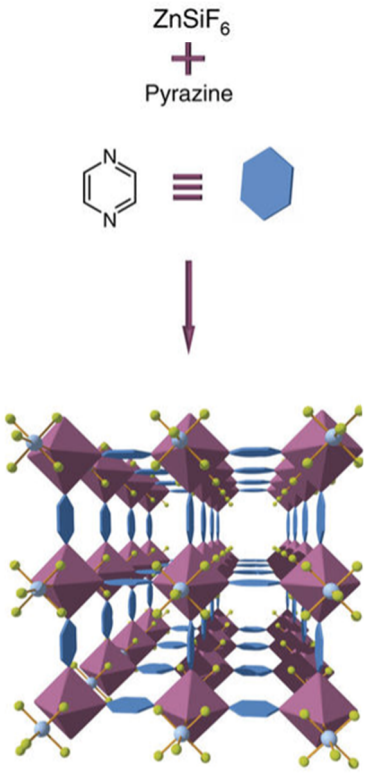

Figure 2.21. Schematic representation of the formation of SIFSIX-3-Zn.[17]

2.6. Summary

A new single step PSM reaction has been developed in which the primary amino group in UiO-66-NH_2 was converted into a range of secondary amines bearing different functional groups (UiO-66-$NHCH_2CH_2CN$, UiO-66-$NHCH_2CH_2CO_2CH_3$ and UiO-NH-$CH_2CH_2COCH_3$) *via* a catalyst-free aza-Michael reaction. The reaction was achieved by reacting UiO-66-NH_2 with three different alkenes appended to different electron withdrawing groups (EWG), CH_2=CHR (R = CN, CO_2CH_3, $COCH_3$).

Initially, the reaction of UiO-66-NH_2 with CH_2=CHCN to form UiO-66-$NHCH_2CH_2CN$ was used to investigate the optimum reaction conditions for maximum percentage conversion. Complete conversion was achieved whilst carrying out the reaction solvothermally in H_2O at 120 °C for 2 days. Using the same reaction conditions, the reaction was then extended to different alkenes, CH_2=$CHCO_2CH_3$ and CH_2=$CHCOCH_3$ to form UiO-66-$NHCH_2CH_2CO_2CH_3$ and UiO-66-$NHCH_2CH_2COCH_3$, respectively. The degrees of conversion were governed by the strength of the EWGs attached to the alkenes with the stronger EWG resulted in higher conversion. In other words, highest conversion

(100%) was achieved whilst using CH_2=CHCN as the reactant followed by CH_2=$CHCO_2CH_3$ (89%) and CH_2=$CHCOCH_3$ (54%).

The PSM products show similar PXRD patterns with that for the starting MOF, UiO-66-NH_2 which indicates that the framework integrity and crystallinity were maintained upon PSM. The N_2 sorption measurements at 77 K showed that the PSM products still possess some degrees of porosity despite the introduction of tag groups in the pores. The BET surface areas for the PSM products are lower than for UiO-66-NH_2, reflecting mass increase and pore blocking effects caused by the tag groups. The CO_2 sorption properties of the PSM products were assessed and it was concluded that the introduction of the tag groups led to the observed decrease in CO_2 loadings. Nonetheless, PSM product **1a** showed a subtle increase in CO_2 selectivity over N_2 at low and high pressure in comparison to UiO-66-NH_2. PSM product **1c** on the other hand, showed the highest increase of CO_2 over N_2 selectivity at 0.1 bar.

A tandem PSM reaction was successfully performed on UiO-66-$NHCH_2CH_2CN$ in which the MOF was treated with NaN_3 and $ZnCl_2$ catalyst in *n*-BuOH. This reaction resulted in the partial conversion of the cyano group into 5-substituted tetrazole (21%). PXRD analysis of the PSM product (**1d**) revealed that the crystallinity was retained, albeit the reaction also yielded an unknown crystalline by-product which was successfully eliminated by thorough rinsing with H_2O. The successful inclusion of 5-substituted tetrazole *via* tandem PSM came at the expense of a reduction in porosity of the PSM product. Nonetheless, **1d** still shows a significant uptake of CO_2, most likely due to the strong interactions of CO_2 molecules and the tetrazole moieties.

A new digestion method was developed for UiO-66 materials in which NH_4F was used instead of HF to avoid the hazards associated with the latter.

2.7. Future Work

The aza-Michael PSM reaction on UiO-66-NH_2, in the absence of a catalyst developed herein can be extended to different MOFs that possess high stability towards H_2O and alcohol-based solvents such as the MIL-101-NH_2 and MIL-53-NH_2 systems. The results obtained for these systems can then be compared to that reported in this thesis, in order to determine if similar observations could be deduced.

The range of functionalised MOFs accessible *via* this PSM reaction could be extended by employing alkenes attached to different EWGs such as ethenesulfonic acid (CH_2=$CHSO_3H$) and acryloyl chloride (CH_2=CHCOCl), with a view to further understand the effect of EWGs on PSM conversions. The resulting –SO_3H functionalised MOF may in turn be used for Cd(II) removal studies.[18]

Tandem PSM could also be performed on PSM products **1b** and **1c** which may lead to MOFs with multiple or different functional groups protruding into the pores.

The reactions reported herein, as well as those proposed, merit investigation under microwave assisted PSM to see if reaction times and percentage conversions could be further enhanced.

It is anticipated that the CO_2 loadings would be augmented by employing MOFs with larger pore sizes than that in UiO-66-NH_2 such as MIL-101-NH_2. This should reduce the effect of pore blockage caused by tag groups in the pores, and yield higher percentage conversions.
Further investigation on the CO_2 and N_2 sorption properties of PSM product **1c** may be required to understand the factors for its higher CO_2 over N_2 selectivity in comparison to UiO-66-NH_2 and other PSM products.

2.8. General Experimental Procedures

2.8.1. Powder X-Ray Diffraction

Powder X-ray diffraction (PXRD) patterns for all samples were recorded on a Bruker AXS D8 Advance diffractometer with copper K_α radiation (wavelength, $\lambda = 1.5406$ Å) at 298 K. The beam slit was set to 1 mm, detector slit set to 0.2 mm and anti-scattering slit set to 1 mm. Samples were dried in ambient conditions and ground to a powder using a pestle and mortar. The powders were then packed onto a flat plate and measured over a 2θ range of 5 - 60°. The step size was 0.024° with the scan speed set to 0.3 s per step.

2.8.2. ^{1}H NMR Spectroscopy

^{1}H NMR spectrometry carried out on the digested MOFs was recorded at 298 K on a Bruker Avance 300 MHz Ultrashield NMR spectrometer. All ^{1}H NMR spectra were referenced to the residual protio peaks at δ 2.50 ppm for DMSO-d_6. Samples were dried

at 100 °C for 15 minutes prior to digestion. A typical MOF digestion was carried out by adding 10 mg of a crystalline sample into 0.4 mL of DMSO-d_6 and 0.2 mL of a stock solution of NH_4F in D_2O (4.14 M). The mixture was sonicated until the solid had completely dissolved. In some cases, a trace amount of white solid presumably NH_4F salt precipitated out of the solution. The white solid was removed by filtering the solution prior to ^1H NMR measurement.

2.8.3. Mass Spectroscopy

Mass spectrometry was carried out on digested MOF solutions diluted in EtOH, using a Bruker micrOTOF electrospray ionisation time-of-flight (ESI-TOF) mass spectrometer.

2.8.4. FTIR Spectroscopy

FTIR spectrometry was carried out on solid samples using a PerkinElmer Spectrum 100 spectrometer mounted on a diamond/gem platform.

2.8.5. Thermogravimetric Analysis

TGA was carried out on the solid samples using a Setaram Setsys Evolution 16/18 thermogravimetric analyser. The samples were heated from 30 °C to 600 °C at a rate of 20 K/min under a flow of argon gas (20 mL/min).

2.8.6. Gas Sorption Measurements

A typical gas sorption measurement was carried out by loading an approximately 20 mg of MeOH rinsed sample into a pre-weighed sample tube. The sample was then heated at 120 °C for 12 hours on a BELSORP Mini-II (BEL Japan) gas sorption analyser. The sample tube was re-weighed to obtain a consistent mass of the activated sample prior to the gas adsorption measurement. To determine the specific surface area, N_2 sorption isotherm was recorded at 77 K. The temperature was kept constant using a liquid nitrogen bath. The specific surface area was calculated based on the Brunauer-Emmett-Teller (BET) method in the P/P_0 range of 0.05 - 0.10. CO_2 and N_2 adsorption isotherms were also recorded at 273 K. The selectivity of CO_2 over N_2 of the material was calculated from the single gas isotherms by dividing the CO_2 uptake by that of N_2 at a specific pressure (0.1 or 1.0 bar).

2.9. Synthetic Procedures

Unless specified, all reagents and solvents used in this work were purchased from commercial sources (Sigma Aldrich/Fisher Scientific) and were used without further purification.

2.9.1. Synthesis of UiO-66-NH_2, $[Zr_6O_4(OH)_4(BDC\text{-}NH_2)_6]$

The synthesis was modified from a procedure reported by Garibay and Cohen.[8] In a typical reaction, $H_2BDC\text{-}NH_2$ (190 mg, 1.05 mmol) along with $ZrCl_4$ (243 mg, 1.05 mmol) and DMF (12 mL) were loaded into a Teflon lined autoclave. The solution was stirred until the reactants had completely dissolved. The autoclave was placed in an oven and heated at 120 °C for 24 hours. The resulting yellow powder was rinsed and centrifuged with MeOH (6000 rpm for 15 minutes) to remove unreacted $H_2BDC\text{-}NH_2$ and residual DMF in the pores. The washing procedure was repeated over 3 days with the solvent replaced every 24 hours. Finally, the UiO-66-NH_2 powder was dried under vacuum at 120 °C for 12 hours.

2.9.2. Synthesis of UiO-66-$NHCH_2CH_2CN$ (100%), $[Zr_6O_4(OH)_4(BDC\text{-}NHCH_2CH_2CN)_6]\cdot 7H_2O$, 1a

The starting material, UiO-66-NH_2, was synthesise according to the procedure described in Section 2.9.1. Prior to PSM reaction, the UiO-66-NH_2 powder was washed with H_2O by centrifugation over 3 days with the solvent replaced every 24 hours. The powder was then left to dry under ambient conditions. The PSM reaction was carried out by adding UiO-66-NH_2 powder (117 mg, ca. 0.4 mmol eq. of NH_2) and acrylonitrile (0.10 mL, 1.6 mmol, 4 eq.) into a Teflon lined autoclave containing 7 mL H_2O. The autoclave was sealed and heated at 120 °C for 2 days. Upon cooling to ambient temperature, the autoclave was opened and the resulting yellow powder was rinsed and centrifuged with H_2O. The washing procedure was repeated over 3 days with the solvent replaced every 24 hours. The PSM product was then left to dry under ambient conditions.

2.9.3. Synthesis of UiO-66-$NHCH_2CH_2CO_2CH_3$ (89%), $[Zr_6O_4(OH)_4(BDC\text{-}NH_2)_{0.66}(BDC\text{-}NHCH_2CH_2CO_2CH_3)_{5.34}]\cdot 8H_2O$, 1b

The starting material, UiO-66-NH_2, was synthesise according to the procedure described in Section 2.9.1. Prior to PSM reaction, the UiO-66-NH_2 powder was washed with H_2O by centrifugation over 3 days with the solvent replaced every 24 hours. The powder was then left to dry under ambient conditions. The PSM reaction was carried out by adding

UiO-66-NH_2 powder (117 mg, ca. 0.4 mmol eq. of NH_2) and methyl acrylate (0.14 mL, 1.6 mmol, 4 eq.) into a Teflon lined autoclave containing 7 mL H_2O. The autoclave was sealed and heated at 120 °C for 2 days. Upon cooling to ambient temperature, the autoclave was opened and the resulting yellow powder was rinsed and centrifuged with H_2O. The washing procedure was repeated over 3 days with the solvent replaced every 24 hours. The PSM product was then left to dry under ambient conditions.

2.9.4. Synthesis of UiO-66-$NHCH_2CH_2COCH_3$ (54%), $[Zr_6O_4(OH)_4(BDC\text{-}NH_2)_{2.76}(BDC\text{-}NHCH_2CH_2CO_2CH_3)_{3.24}]\cdot 9H_2O$, 1c

The starting material, UiO-66-NH_2, was synthesise according to the procedure described in Section 2.9.1. Prior to PSM reaction, the UiO-66-NH_2 powder was washed with H_2O by centrifugation over 3 days with the solvent replaced every 24 hours. The powder was then left to dry under ambient conditions. The PSM reaction was carried out by adding UiO-66-NH_2 powder (117 mg, ca. 0.4 mmol eq. of NH_2) and methyl vinyl ketone (0.13 mL, 1.6 mmol, 4 eq.) into a Teflon lined autoclave containing 7 mL H_2O. The autoclave was sealed and heated at 120 °C for 2 days. Upon cooling to ambient temperature, the autoclave was opened and the resulting yellow powder was rinsed and centrifuged with H_2O. The washing procedure was repeated over 3 days with the solvent replaced every 24 hours. The PSM product was then left to dry under ambient conditions.

2.9.5. Synthesis of UiO-66-$NHCH_2CH_2CN_4H$ (21%), $[Zr_6O_4(OH)_4(BDC\text{-}NHCH_2CH_2CN)_{4.74}(BDC\text{-}NHCH_2CH_2CN_4H)_{1.26}]\cdot H_2O$, 1d

The starting material, UiO-66-NH_2, was synthesise according to the procedure described in Section 2.9.1. Prior to PSM reaction, the UiO-66-NH_2 powder was washed with H_2O by centrifugation over 3 days with the solvent replaced every 24 hours. The powder was then left to dry under ambient conditions. The first PSM reaction was carried out by adding UiO-66-NH_2 powder (117 mg, ca. 0.4 mmol eq. of NH_2) and acrylonitrile (0.10 mL, 1.6 mmol, 4 eq.) into a Teflon lined autoclave containing 7 mL H_2O. The autoclave was sealed and heated at 120 °C for 2 days. Upon cooling to ambient temperature, the autoclave was opened and the resulting yellow powder was rinsed and centrifuged with H_2O. The washing procedure was repeated over 3 days with the solvent replaced every 24 hours. The sample was then left to dry under ambient conditions. In preparation for tandem PSM reaction, the sample was first rinsed and centrifuged with *n*-BuOH. The

washing procedure was repeated over 3 days with the solvent replaced every 24 hours. Tandem PSM reaction was carried out by suspending the *n*-BuOH rinsed sample (69 mg, ca. 0.2 mmol eq. of CN) in *n*-BuOH (10 mL) in a round bottom flask, followed by the addition of NaN_3 (16 mg, 0.24 mmol, 1.2 eq.) and $ZnCl_2$ catalyst (27 mg, 0.2 mmol, 1 eq.). The reaction mixture was stirred vigorously and heated under reflux for 24 hours. The reaction was quenched by cooling the reaction mixture to ambient temperature and rinsing the resulting yellow solid with fresh *n*-BuOH. The washing procedure was repeated over 3 days with the solvent replaced every 24 hours. The sample was then left to dry under ambient conditions.

2.10. References

1. J. L. Vicario, D. Badía, L. Carrillo, J. Etxebarria, E. Reyes and N. Ruiz, *Org. Prep. Proced. Int.*, 2005, **37**, 513.
2. R. Varala, M. M. Alam and S. R. Adapa, *Synlett*, 2003, 720.
3. I. Reboule, R. Gil and J. Collin, *Tetrahedron Lett.*, 2005, **46**, 7761.
4. L. T. L. Nguyen, T. T. Nguyen, K. D. Nguyen and N. T. S. Phan, *Appl. Catal., A*, 2012, **425–426**, 44.
5. S. S.-Y. Chui, S. M.-F. Lo, J. P. H. Charmant, A. G. Orpen and I. D. Williams, *Science*, 1999, **283**, 1148.
6. J. Wang, P.-F. Li, S. H. Chan, A. S. C. Chan and F. Y. Kwong, *Tetrahedron Lett.*, 2012, **53**, 2887.
7. K. De, J. Legros, B. Crousse and D. Bonnet-Delpon, *J. Org. Chem.*, 2009, **74**, 6260.
8. S. J. Garibay and S. M. Cohen, *Chem. Commun.*, 2010, **46**, 7700.
9. J. H. Cavka, S. Jakobsen, U. Olsbye, N. Guillou, C. Lamberti, S. Bordiga and K. P. Lillerud, *J. Am. Chem. Soc.*, 2008, **130**, 13850.
10. H. Hintz and S. Wuttke, *Chem. Mater.*, 2014, **26**, 6722.
11. R. Ameloot, M. Aubrey, B. M. Wiers, A. P. Gómora-Figueroa, S. N. Patel, N. P. Balsara and J. R. Long, *Chem. Eur. J.*, 2013, **19**, 5533.
12. Z. Hu, K. Zhang, M. Zhang, Z. Guo, J. Jiang and D. Zhao, *ChemSusChem*, 2014, **7**, 2791.
13. A. Kronast, S. Eckstein, P. T. Altenbuchner, K. Hindelang, S. I. Vagin and B. Rieger, *Chem. Eur. J.*, 2016, **22**, 12800.
14. C. Wang, X. Liu, J. P. Chen and K. Li, *Sci. Rep.*, 2015, **5**.
15. D.-M. Chen, J.-Y. Tian, M. Chen, C.-S. Liu and M. Du, *ACS Appl. Mater. Interfaces*, 2016, **8**, 18043.
16. S. Seth, G. Savitha and J. N. Moorthy, *Inorg. Chem.*, 2015, **54**, 6829.
17. P. Nugent, Y. Belmabkhout, S. D. Burd, A. J. Cairns, R. Luebke, K. Forrest, T. Pham, S. Q. Ma, B. Space, L. Wojtas, M. Eddaoudi and M. J. Zaworotko, *Nature*, 2013, **495**, 80.
18. Y. Wang, G. Q. Ye, H. H. Chen, X. Y. Hu, Z. Niu and S. Q. Ma, *J. Mater. Chem.*, 2015, **3**, 15292.

3. Post-Synthetic Modification of MOFs: Mannich Reaction

The Mannich reaction involves the combination of an amine with an aldehyde, usually formaldehyde, together with an α-CH-acidic compound (a nucleophile), Scheme 3.1.[1] In some cases, the Mannich reaction is carried out in two steps to prevent the nucleophile from reacting with formaldehyde.

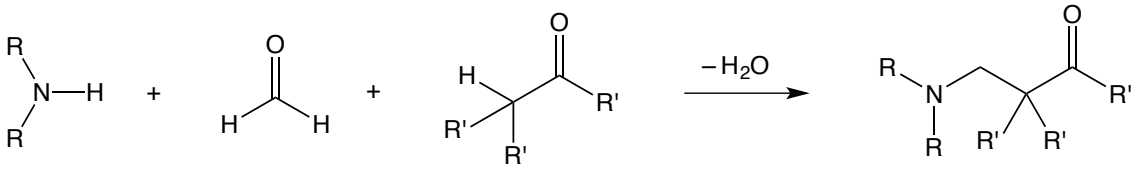

Scheme 3.1. General scheme for the Mannich reaction. R, R' = H, alkyl, aryl.[1]

The α-CH-acidic compounds are generally enolisable carbonyl compounds such as ketones and esters. The development of this reaction has seen other nucleophiles such as nitroalkanes,[2] acetylenes[3] and electron-rich heterocycles (pyrroles[4], furan[5] and thiophene[6]) being employed as alternatives to the α-CH-acidic compounds. This is illustrated for pyrrole in Scheme 3.2.

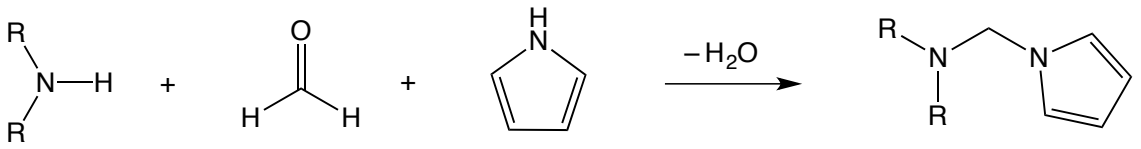

Scheme 3.2. Schematic representation of a Mannich reaction with pyrrole as a nucleophile. R, R' = H, alkyl, aryl.

A survey of the literature did not reveal any studies on the Mannich reactions on MOF frameworks, although studies of MOFs as catalysts for Mannich reactions have previously been reported.[7, 8] Hence, the aim of this work was to explore the possibility of carrying out post-synthetic Mannich reactions on MOF frameworks. Since the Mannich reaction is versatile, in the sense that different functional groups can be incorporated on the MOF framework by using a range of nucleophiles, another aim of this work was to use the modified MOFs for applications such as gas storage and heavy metal capture.

3.1. The Mannich Reaction on $[Zr_6O_4(OH)_4(BDC\text{-}NH_2)_6]$, UiO-66-$NH_2$

As mentioned in Section 2.1.1, $[Zr_6O_4(OH)_4(BDC\text{-}NH_2)_6]$, UiO-66-$NH_2$, has been widely studied in the field of PSM mainly due to its high chemical stability and other attractive properties such as large pore windows (6.9 Å) and high crystallinity. Furthermore, UiO-66-NH_2 possesses free amino groups protruding into the pores which are available for PSM reactions. Figure 3.1 shows the SBU and network structure of UiO-66, the parent MOF of UiO-66-NH_2. The crystal structure of UiO-66-NH_2 cannot be produced due to the absence of its crystallographic data in the literature.

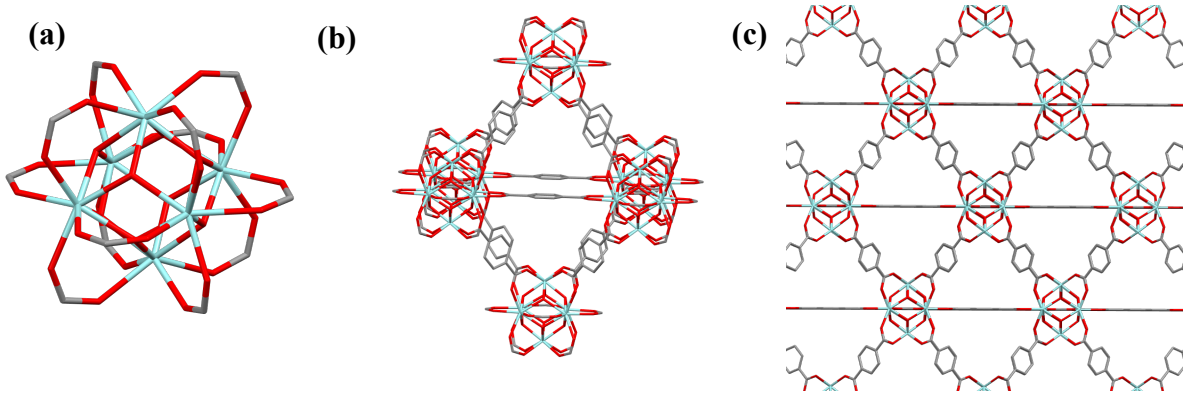

Figure 3.1. (a) SBU of UiO-66. **(b)** Triangular apertures in UiO-66. **(c)** Framework of UiO-66. Zr: cyan, C: grey, O: red. Hydrogen atoms are omitted for clarity.[9]

Due to the attractive features stated beforehand, UiO-66-NH_2 was chosen as a candidate for the Mannich reactions, on the basis of the proposed general reaction shown in Scheme 3.3.

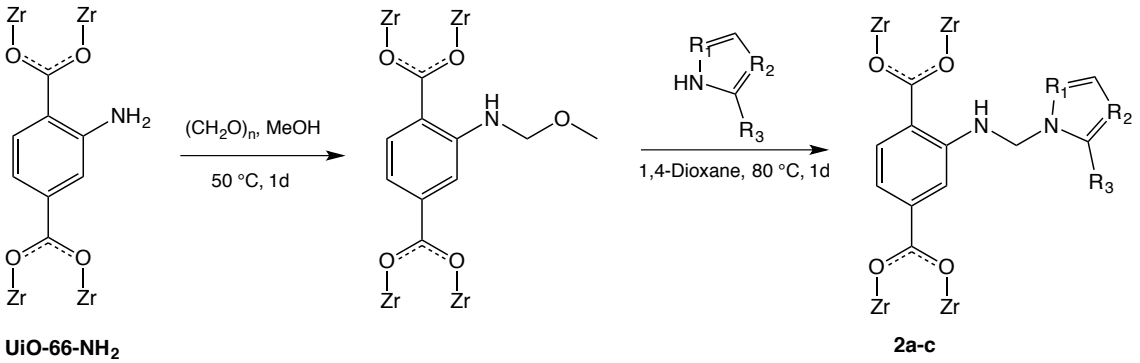

UiO-66-NH_2 **2a-c**

Scheme 3.3. General procedure for the conversion of UiO-66-NH_2 into azole-functionalised MOFs. **2a**; R_1 = N, R_2 = CH, R_3 = H. **2b**; R_1 = CH, R_2 = N, R_3 = H. **2c**; R_1 = CH, R_2 = N, R_3 = SH.

In this Mannich reaction, the conversion takes place in two separate steps. The first step involves the formation of methoxymethyl hemiaminal groups by the reaction of the amino groups with paraformaldehyde and MeOH. The reaction was carried out at 50 °C to facilitate the solubilisation of paraformaldehyde in MeOH. The methoxymethyl hemiaminal groups are subsequently converted into a range of α-amino azoles *via* nucleophilic substitution in the second step. 1,4-dioxane was used as a solvent in the second step of the reaction due to the precedence of this solvent in Mannich reactions. The overall process was carried out in two steps to avoid the side-reaction of paraformaldehyde with the nucleophiles.

Pyrazole, imidazole and 2-mercaptoimidazole were the selected nucleophiles as these compounds possess functional groups that are attractive for different applications. For example, pyrazole and imidazole contain nitrogen atoms which are favourable for selective CO_2 adsorption. 2-Mercaptoimidazole on the other hand, contains a thiol group which has a high affinity towards soft metal centres such as Hg(II).

The majority of the Mannich reactions reported to date require Lewis acid catalysts.[10, 11] It is notable that those reported herein proceeded without the aid of a catalyst, which eliminates the typical work-up associated with catalyst removal from the pores of the MOF. The possibility of pore blocking which could impede the reaction rate was also avoided by employing catalyst-free conditions.

The reaction mechanism for the Mannich reaction involving imidazole as the nucleophile is exemplified in Scheme 3.4.

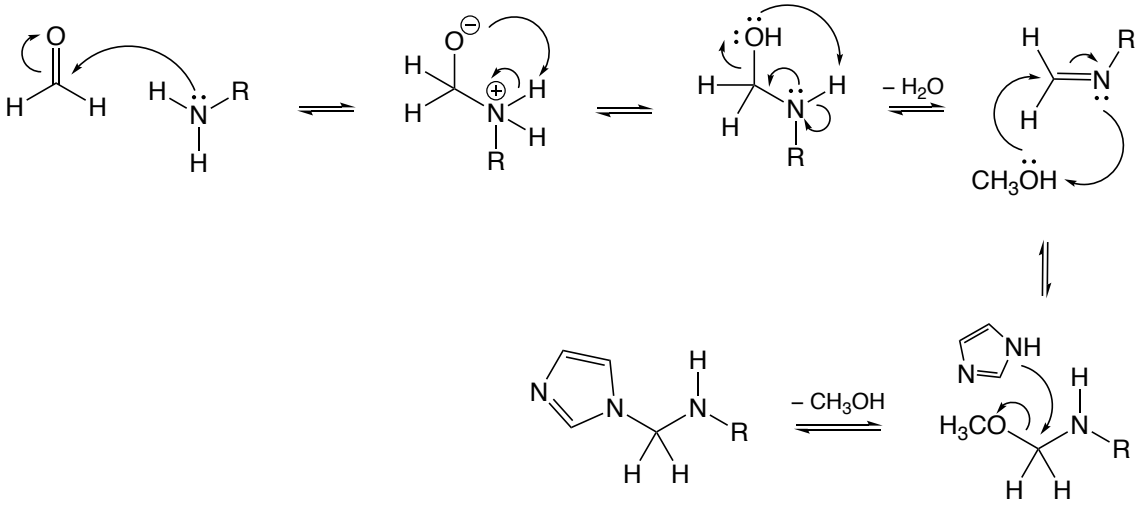

Scheme 3.4. The reaction mechanism for the Mannich reaction involving imidazole as the nucleophile.

3.1.1. The Mannich Reaction on UiO-66-NH_2: Pyrazole as the Nucleophile

One of the earliest reports on using pyrazole as a nucleophile in the Mannich reaction was documented by Hüttel and Jochum in 1952.[12] They reported that a range of nitrogen-substituted compounds could be formed by the reaction of secondary amines with formaldehyde and pyrazole in neutral solution. In the work reported herein, the Mannich reaction of UiO-66-NH_2 with pyrazole as the nucleophile was carried out based on the reaction conditions shown in Scheme 3.5.

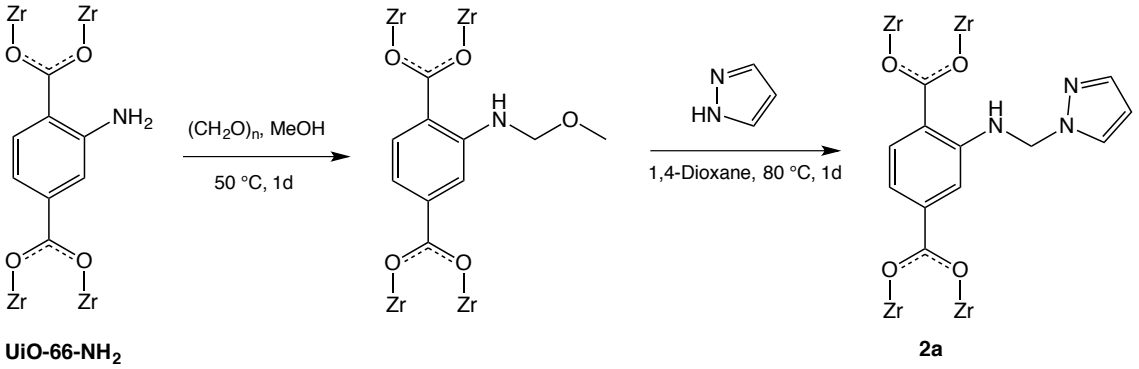

Scheme 3.5 The Mannich reaction of UiO-66-NH_2 using pyrazole as the nucleophile.

UiO-66-NH_2 was synthesised following the previous report by Cohen and co-workers.[13] In a typical procedure, $ZrCl_4$ and H_2BDC-NH_2 were dissolved in DMF in a Teflon-lined autoclave and heated at 120 °C for 24 hours. The resulting microcrystalline powder was then soaked and washed with MeOH for 3 days, replacing the solvent with fresh solvent every 24 hours before isolating the powder by centrifugation. In a typical PSM reaction, UiO-66-NH_2 was treated with paraformaldehyde and MeOH at 50 °C for 1 day. The intermediate was then washed with 1,4-dioxane (three times) to remove any residual paraformaldehyde and MeOH in the pores or on the solid surface. This powder was subsequently treated with pyrazole in 1,4-dioxane at 80°C for 1 day before quenching the reaction by rinsing the sample with fresh 1,4-dioxane. The product was soaked in 1,4-dioxane for 3 days, replacing the solvent with fresh solvent every 24 hours, before isolation by centrifugation. Prior to characterisation, the samples were left to dry in air for 2 hours to obtain free-flowing powders. The detailed experimental procedures can be found in Section 3.9.2.

The effectiveness of the PSM reaction in terms of the percentage conversion of amino groups into α-amino pyrazole (–$NHCH_2C_3H_3N_2$) was gauged by ^{1}H NMR spectroscopy, Figure 3.2. The ^{1}H NMR spectrum was obtained by digesting the PSM product, **2a** in NH_4F/D_2O with DMSO-d_6. The spectrum shows a number of new peaks in addition to the peaks which correspond to the aromatic protons of the starting MOF, UiO-66-NH_2.

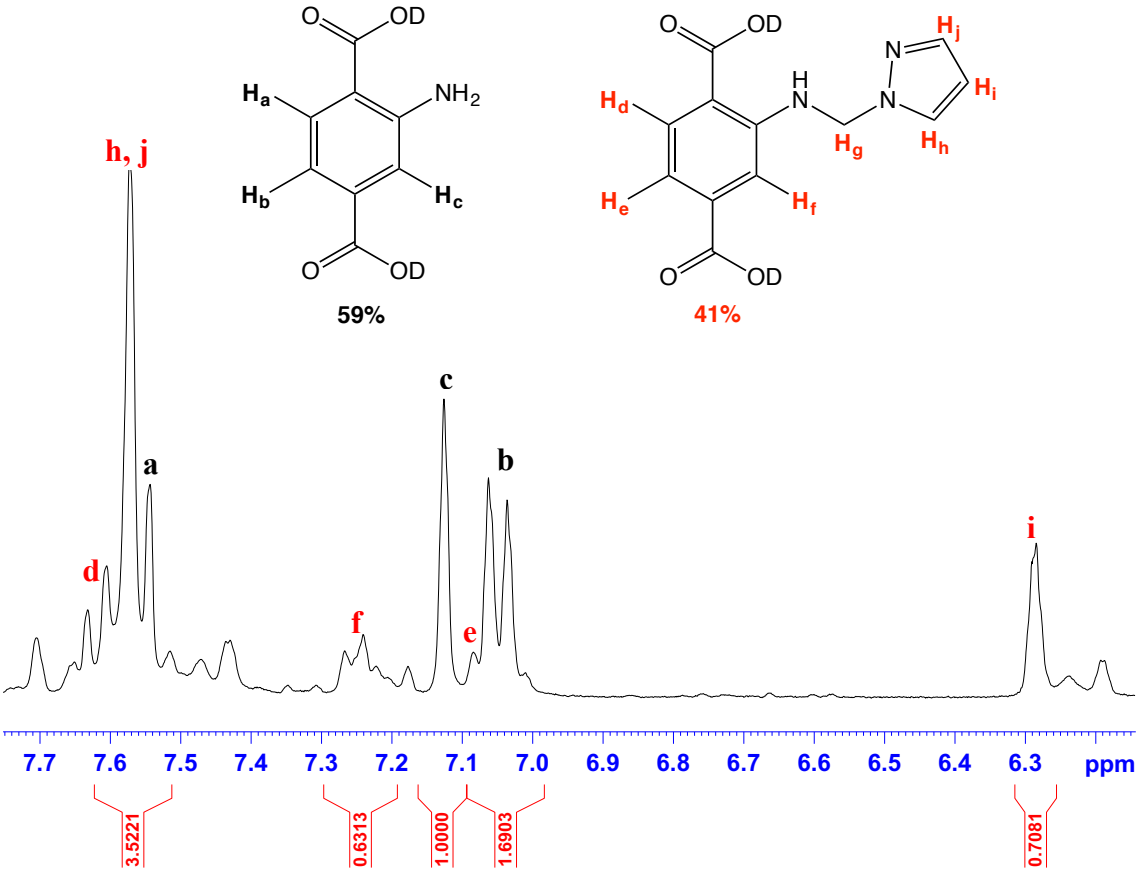

Figure 3.2. Aromatic region of ^{1}H NMR spectrum of digested PSM product **2a**.

The aromatic protons of D_2BDC-$NHCH_2C_3H_3N_2$ can be observed at δ 7.08, 7.25 and 7.62 ppm. The peaks overlap with the aromatic peaks of either D_2BDC-NH_2 or signals attributed to unknown by-products. The presence of the pyrazole ring on the digested framework of **2a** was confirmed by the peaks at δ 6.28 ppm (H_i) and δ 7.57 ppm (H_h and H_j) which correspond to the protons of the pyrazole ring. The peak attributed to the α-CH_2 protons of D_2BDC-$NHCH_2C_3H_3N_2$, H_g, could not be located, most likely due to being obscured by the dominant HDO peak used in the digestion.

In addition to the α-amino pyrazole species (UiO-66-$NHCH_2C_3H_3N_2$), this reaction clearly produced some by-products as evidenced by the ^{1}H NMR spectrum of digested **2a**, Figure 3.2. Attempts to remove these *via* thorough rinsing with different solvents were

unsuccessful. The identity of these by-products could not be reliably confirmed and it is unclear if they are part of the framework or independent species that reside in the pores.

However, one possible by-product that may form *via* this reaction is pyrazole-1-methanol, Figure 3.3. This can arise as a product from the reaction between paraformaldehyde and pyrazole. Although every effort was made to remove unreacted paraformaldehyde by thorough washing after the first reaction step, residual paraformaldehyde might still be present which could considerably react with pyrazole to form pyrazole-1-methanol.

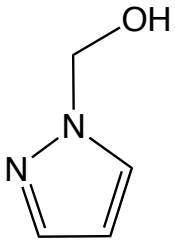

Figure 3.3. Chemical structure of pyrazole-1-methanol.

To probe this hypothesis, pyrazole-1-methanol was synthesised by reacting paraformaldehyde and pyrazole. The ^{1}H NMR spectrum of the product (dissolved in NH_4F/D_2O with DMSO-d_6) confirmed the identity of this material, Figure 3.4, and the peaks were compared to the unknown peaks obtained for the digested PSM product **2a**.

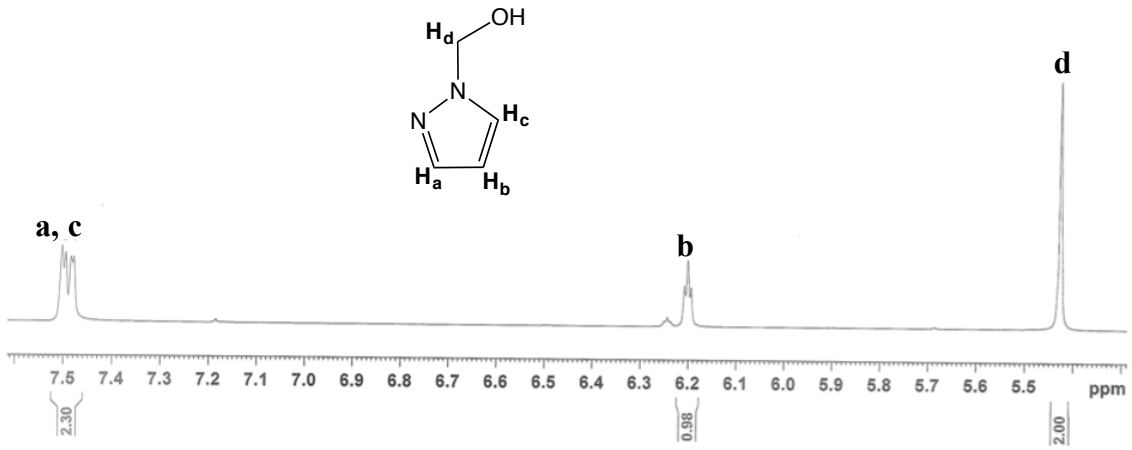

Figure 3.4 ^{1}H NMR spectrum of pyrazole-1-methanol dissolved in NH_4F/D_2O with DMSO-d_6.

Based on the comparison, the peaks at δ 6.19 ppm and δ 7.45 ~ 7.53 ppm observed in Figure 3.2 are thought to correspond to the protons from pyrazole-1-methanol. It was also thought possible that the methoxymethyl hemiaminal ($–NHCH_2OCH_3$) groups may still

be present in the PSM product **2a** due to their incomplete conversion into the α-amino pyrazole (–$NHCH_2C_3H_3N_2$) groups and that these might be giving rise to some of the unassigned by-product resonances observed in **2a**. However, the presence of –$NHCH_2OCH_3$ groups could not be confirmed *via* ^{1}H NMR spectroscopy most likely because they undergo hydrolysis in the digestion solution (NH_4F/D_2O with DMSO-d_6) leading back to the formation of D_2BDC-NH_2.

Overall however, ignoring the by-products, the percentage conversion from –NH_2 into –$NHCH_2C_3H_3N_2$ groups was calculated as being approximately 41%, by comparing the integrals at δ 7.13 and δ 6.28 ppm. The calculated conversion gives the formula for **2a** as $[Zr_6O_4(OH)_4(BDC\text{-}NH_2)_{3.54}(BDC\text{-}NHCH_2C_3H_3N_2)_{2.46}]$. Attempt to increase the degree of conversion by carrying out the PSM reaction at higher temperature was unsuccessful, with the PSM product possessing the same percentage conversion with that for **2a** (41%).

The negative ESI mass spectrum of the digested product **2a** confirms the presence of the deprotonated anion of H_2BDC-$NHCH_2C_3H_3N_2$ and H_2BDC-NH_2 at m/z = 260.0664 (predicted $[M\text{-}H]^-$ = 260.0671) and m/z = 180.0308 (predicted $[M\text{-}H]^-$ = 180.0375), respectively.

The N-H stretching band of the secondary amine group of the modified framework, UiO-66-$NHCH_2C_3H_3N_2$ can be seen at 3372 cm^{-1} on the FTIR spectrum of **2a**, Figure 3.5 (red plot). The C-H and C=C bending of the pyrazole ring are typically observed in the 620 ~ 1600 cm^{-1} region. However, these peaks could not be unambiguously located on the FTIR spectrum of **2a** due to the presence of other dominant peaks associated with the framework's backbone.

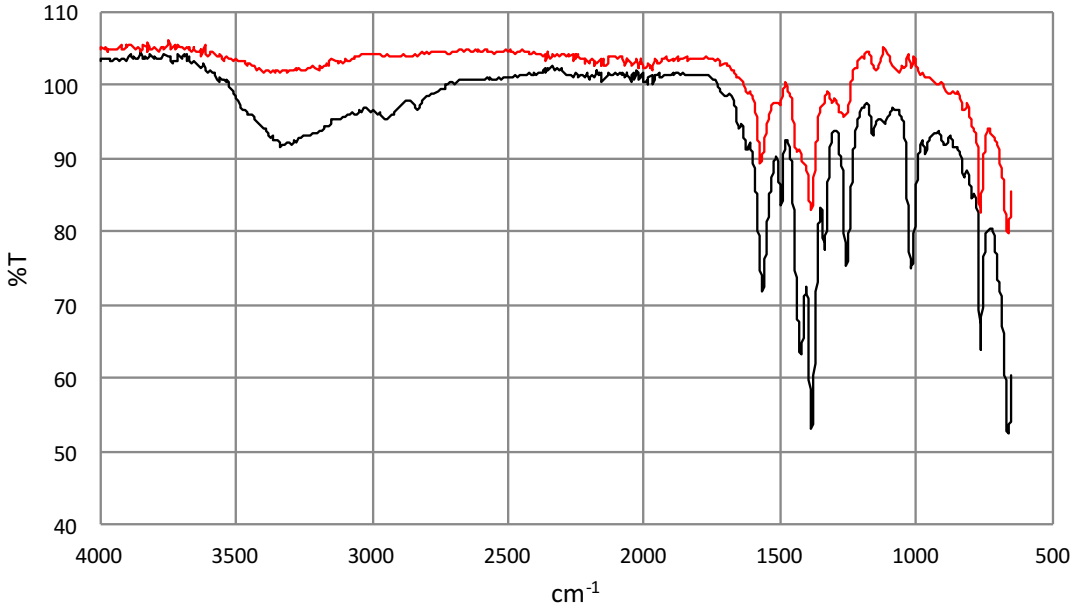

Figure 3.5. Black: FTIR spectrum of UiO-66-NH_2. Red: FTIR spectrum of $[Zr_6O_4(OH)_4(BDC\text{-}NH_2)_{3.54}(BDC\text{-}NHCH_2C_3H_3N_2)_{2.46}]$, **2a**.

Figure 3.6 shows the PXRD patterns of the starting MOF, UiO-66-NH_2, with PSM product **2a**, illustrating the high similarities between the two MOFs. The retention of Bragg peak positions from the parent MOF in the PXRD pattern for **2a** indicates that the framework was maintained upon the PSM reaction. Furthermore, since no additional peaks are observed in the **2a** trace, it can be concluded that the by-products in **2a** (if they are independent species and not part of the framework) are amorphous.

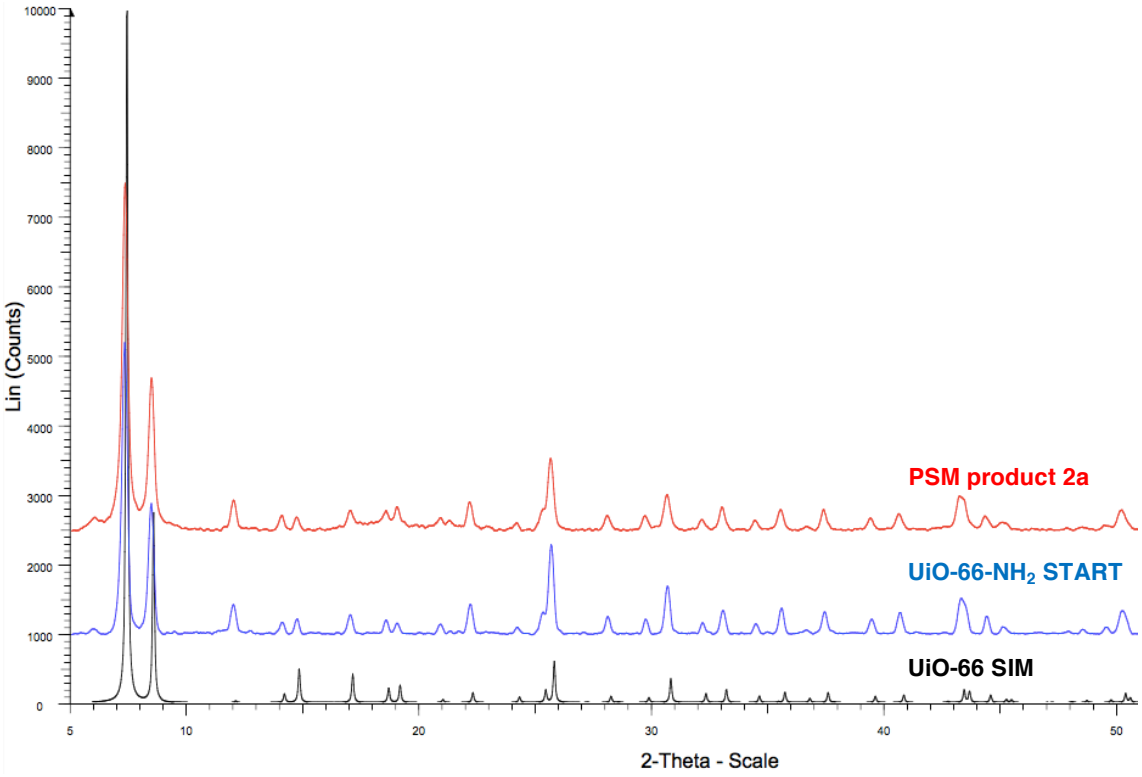

Figure 3.6. Black: Simulated PXRD pattern calculated from the UiO-66 crystal structure.[9] Blue: PXRD pattern of starting MOF, UiO-66-NH_2. Red: PXRD pattern of PSM product, **2a**.

3.1.2. The Mannich Reaction on UiO-66-NH_2: Imidazole as the Nucleophile

The Mannich reaction of UiO-66-NH_2 with imidazole as the nucleophile was carried out based on the reaction conditions shown in Scheme 3.6.

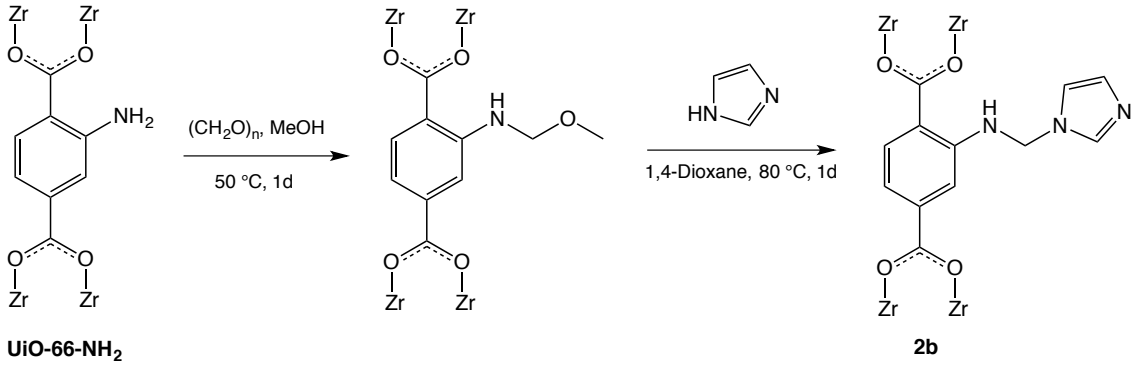

Scheme 3.6 The Mannich reaction of UiO-66-NH_2 using imidazole as the nucleophile.

The reaction was successful, with the amino groups completely (100%) converted into the α-amino imidazole ($–NHCH_2C_3H_3N_2$) groups, Figure 3.7.

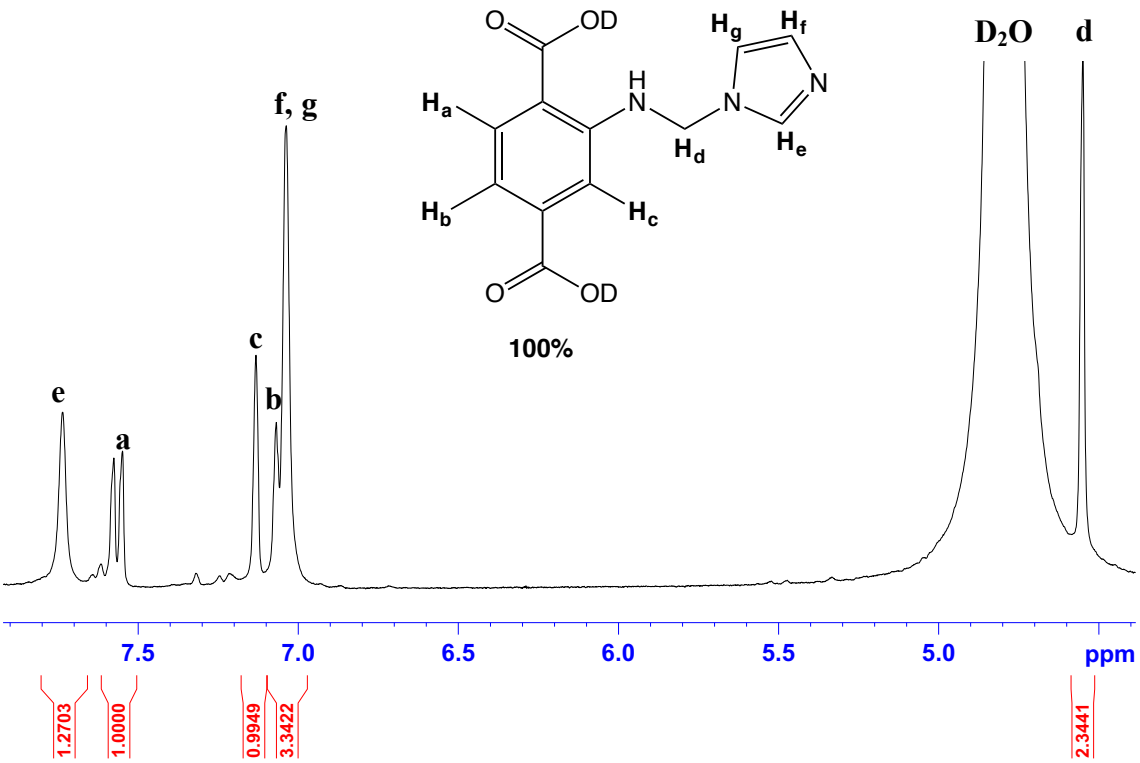

Figure 3.7. ^{1}H NMR spectrum of digested PSM product $[Zr_6O_4(OH)_4(BDC\text{-}NHCH_2C_3H_3N_2)_6]$, **2b**.

This was confirmed by the disappearance of the peaks which correspond to the aromatic protons of the starting MOF, UiO-66-NH_2. Instead, new peaks at δ 7.07, 7.14 and 7.56 ppm were observed which correspond to the protons from the aromatic ring of $D_2BDC\text{-}NHCH_2C_3H_3N_2$ (H_b, H_c and H_a, respectively). Furthermore, the presence of the imidazole ring can be confirmed by the presence of two singlets in the aromatic region (δ 7.03 and 7.75 ppm). The signal at δ 7.03 ppm corresponds to two protons from the imidazole ring, H_f and H_g, which overlaps with the peak from one of the aryl protons, H_b (δ 7.07 ppm). The singlet at δ 7.75 ppm was attributed to the remaining proton peak of the imidazole ring, H_e. The signal attributed to the α-CH_2 protons, H_d can be seen at δ 4.56 ppm but was overlapped with the broad HDO peak used in the digestion. The chemical formula of this PSM product can be expressed as $[Zr_6O_4(OH)_4(BDC\text{-}NHCH_2C_3H_3N_2)_6]$, **2b**.

The positive ESI mass spectrum of the digested product **2b** also confirmed the presence of the protonated cation of $H_2BDC\text{-}NHCH_2C_3H_3N_2$ at m/z = 262.0824 (predicted $[M+H]^+$ = 262.0828).

The FTIR spectrum of **2b** showed a broad peak at 3335 cm^{-1}, Figure 3.8 (red plot), which corresponds to the secondary N-H stretching band of UiO-66-$NHCH_2C_3H_3N_2$. The presence of imidazole ring on the modified framework could not be inferred *via* FTIR spectroscopy due to the presence of framework's backbone peaks which dominate the 600 – 1700 cm^{-1} region.

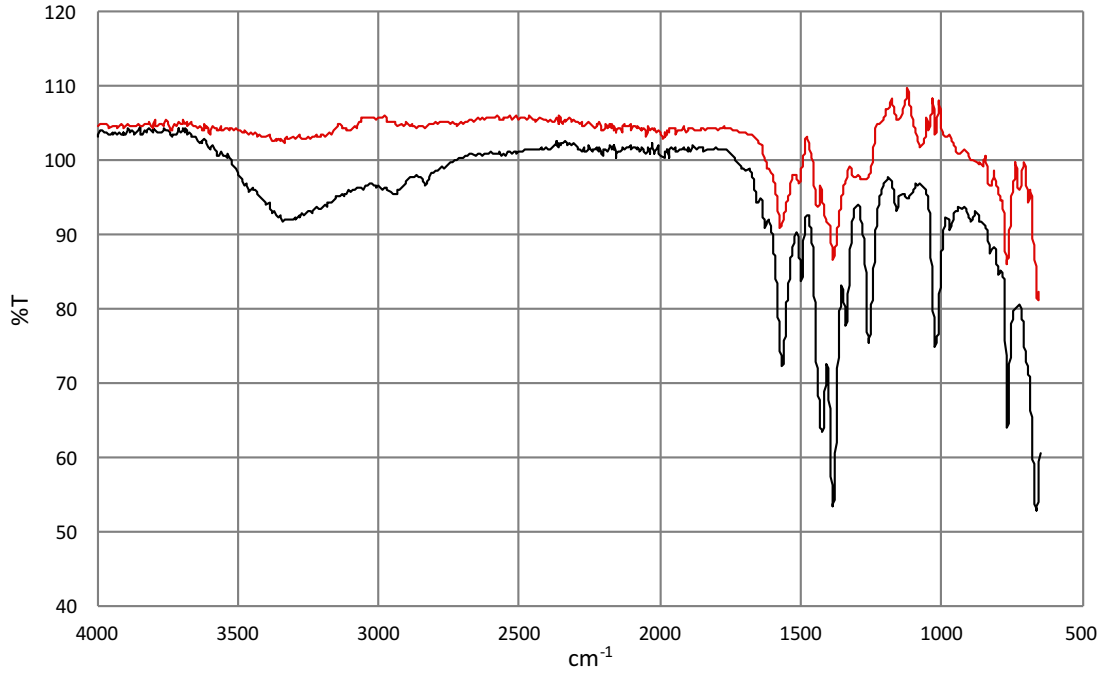

Figure 3.8. Black: FTIR spectrum of UiO-66-NH_2. Red: FTIR spectrum of $[Zr_6O_4(OH)_4(BDC\text{-}NHCH_2C_3H_3N_2)_6]$, **2b**.

The structural integrity of **2b** was assessed by PXRD, Figure 3.9. Due to the high similarities of the PXRD patterns of the starting MOF, UiO-66-NH_2, and PSM product **2b**, it was concluded that the framework had remained intact and retained its crystallinity upon the PSM reaction, in a similar manner to that observed for **2a**.

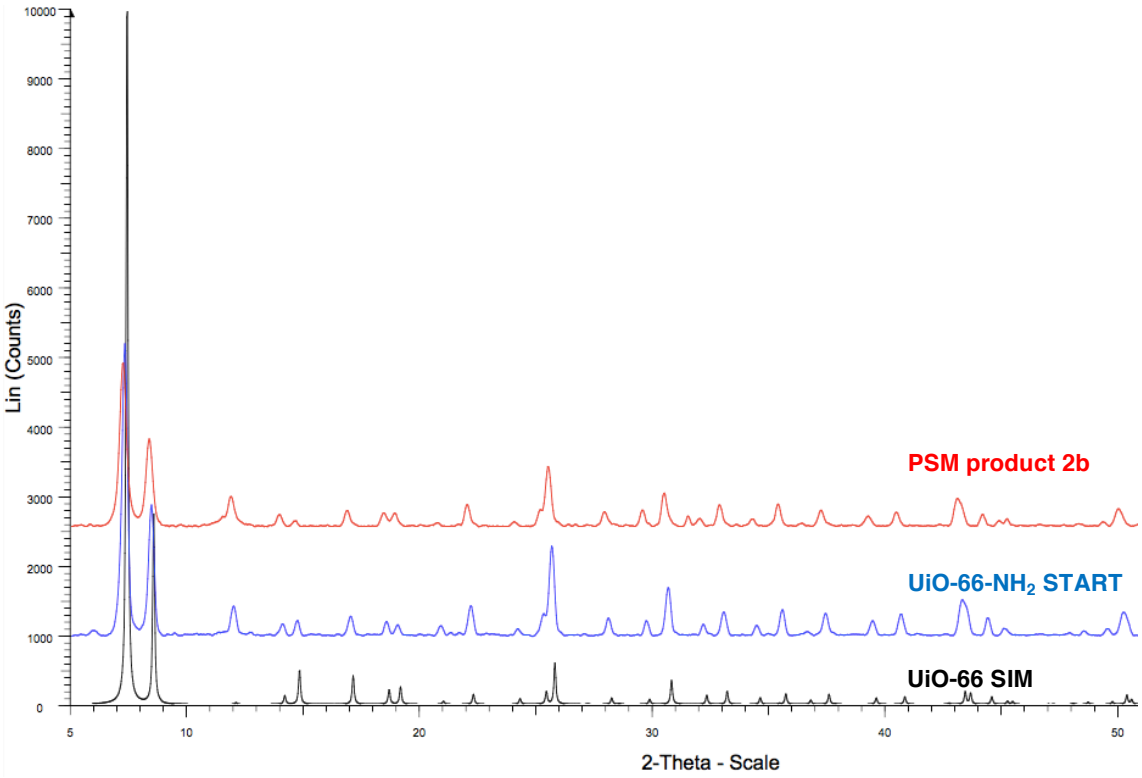

Figure 3.9. Black: Simulated PXRD pattern calculated from the UiO-66 crystal structure.[9] Blue: PXRD pattern of starting MOF, UiO-66-NH_2. Red: PXRD pattern of PSM product, **2b**.

3.1.3. The Mannich Reaction on UiO-66-NH_2: 2-Mercaptoimidazole as the Nucleophile

In a similar manner to the synthesis of **2a** and **2b**, the Mannich reaction of UiO-66-NH_2 with the nucleophile 2-mercaptoimidazole was carried out using the reaction conditions outlined in Scheme 3.7.

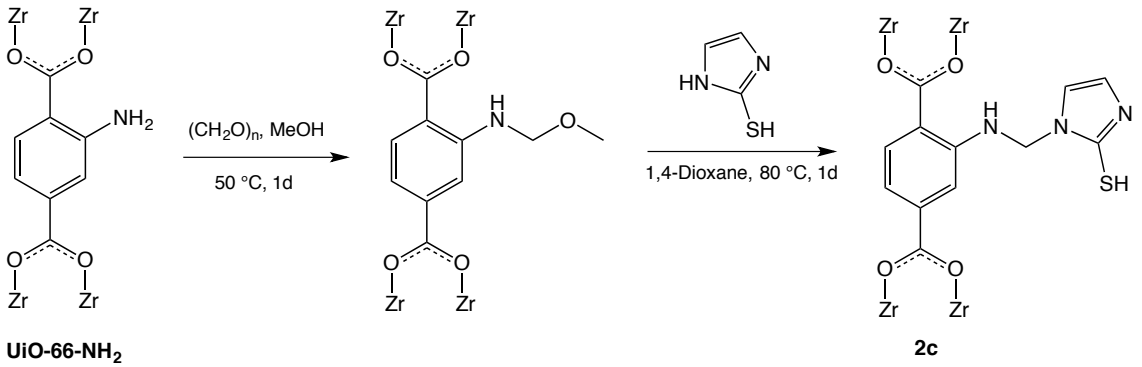

Scheme 3.7. The Mannich reaction of UiO-66-NH_2 using 2-mercaptoimidazole as the nucleophile.

The ^{1}H NMR spectrum of the digested PSM product, **2c** shows the presence of new peaks in addition to the aromatic proton peaks which correspond to the starting MOF, UiO-66-NH_2, Figure 3.10.

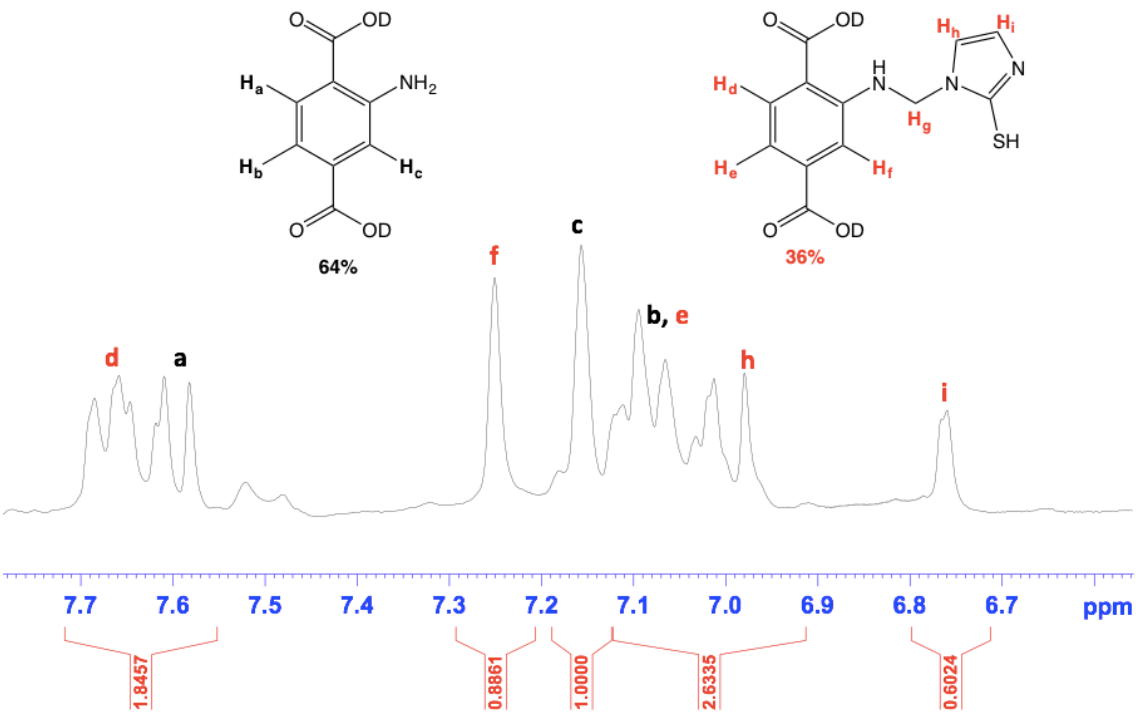

Figure 3.10. Aromatic region of ^{1}H NMR spectrum of digested PSM product **2c**.

The peaks attributed to the aromatic protons of D_2BDC-$NHCH_2C_3H_2N_2SH$ (H_d, H_e, and H_f) can be observed at δ 7.68, 7.08 and 7.26 ppm, respectively, although these peaks overlap with others from by-products to some extent. The presence of new peaks at δ 6.76 and 6.98 ppm which correspond to H_i and H_h, respectively, indicates that the 2-mercaptoimidazole ring was successfully grafted on the MOF framework. The singlet peak which corresponds to the α-CH_2 protons of D_2BDC-$NHCH_2C_3H_2N_2SH$, H_g, could not be identified as the peak was thought to be obscured by the dominant HDO peak from the digestion solvent.

In parallel to the observations for **2a** described in Section 3.1.1, the by-products are thought to be unreacted methoxymethyl hemiaminal (D_2BDC-$NHCH_2OCH_3$) species and/or (2-mercapto-1*H*-imidazol-1-yl)methanol. The latter could be formed by the reaction of residual paraformaldehyde and 2-mercaptoimidazole. The presence of unreacted 2-mercaptoimidazole in **2c** was ruled out, however, as the typical ^{1}H NMR peaks corresponding to it were absent from the spectrum for digested **2c**.

The percentage conversion from $-NH_2$ into $-NHCH_2C_3H_2N_2SH$ groups was calculated as being approximately 36%, by comparing the integrals at δ 7.16 and δ 6.76 ppm. The calculated conversion gives the formula for **2c** as $[Zr_6O_4(OH)_4(BDC\text{-}NH_2)_{3.84}(BDC\text{-}NHCH_2C_3H_2N_2SH)_{2.16}]$.

The negative ESI mass spectrum of the digested product **2c** confirms the presence of the deprotonated anion of $H_2BDC\text{-}NHCH_2C_3H_2N_2SH$ and $H_2BDC\text{-}NH_2$ at m/z = 292.0400 (predicted $[M\text{-}H]^-$ = 292.0392) and m/z = 180.0308 (predicted $[M\text{-}H]^-$ = 180.0375), respectively.

A broad peak at 3372 cm^{-1}, Figure 3.11 (red plot), in the FTIR spectrum of the solid sample **2c** corresponds to the N-H stretching band of $UiO\text{-}66\text{-}NHCH_2C_3H_2N_2SH$. Thiol groups are known to characteristically display a weak S-H stretching band in the 2550 ~ 2600 cm^{-1} IR region. However, this band was not observed in the FTIR spectrum of **2c** and is probably due to the low percentage of 2-mercaptoimidazole (thiol groups) in **2c**.

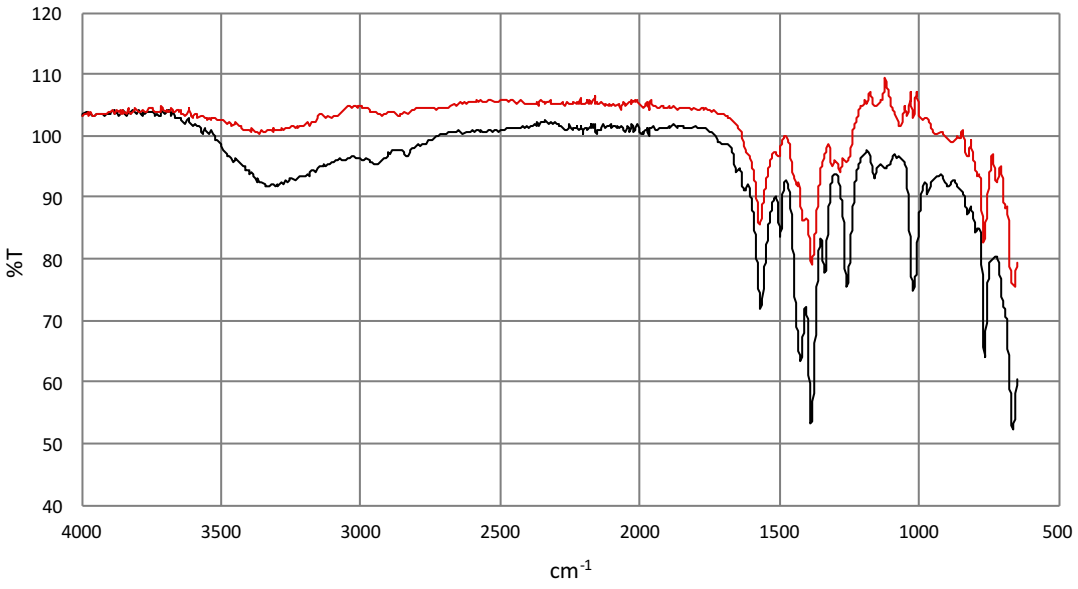

Figure 3.11. Black: FTIR spectrum of $UiO\text{-}66\text{-}NH_2$. Red: FTIR spectrum of $[Zr_6O_4(OH)_4(BDC\text{-}NH_2)_{3.84}(BDC\text{-}NHCH_2C_3H_2N_2SH)_{2.16}]$, **2c**.

PXRD on **2c** allows one to conclude that the parent framework remains intact and retains its crystallinity upon PSM reaction, Figure 3.12.

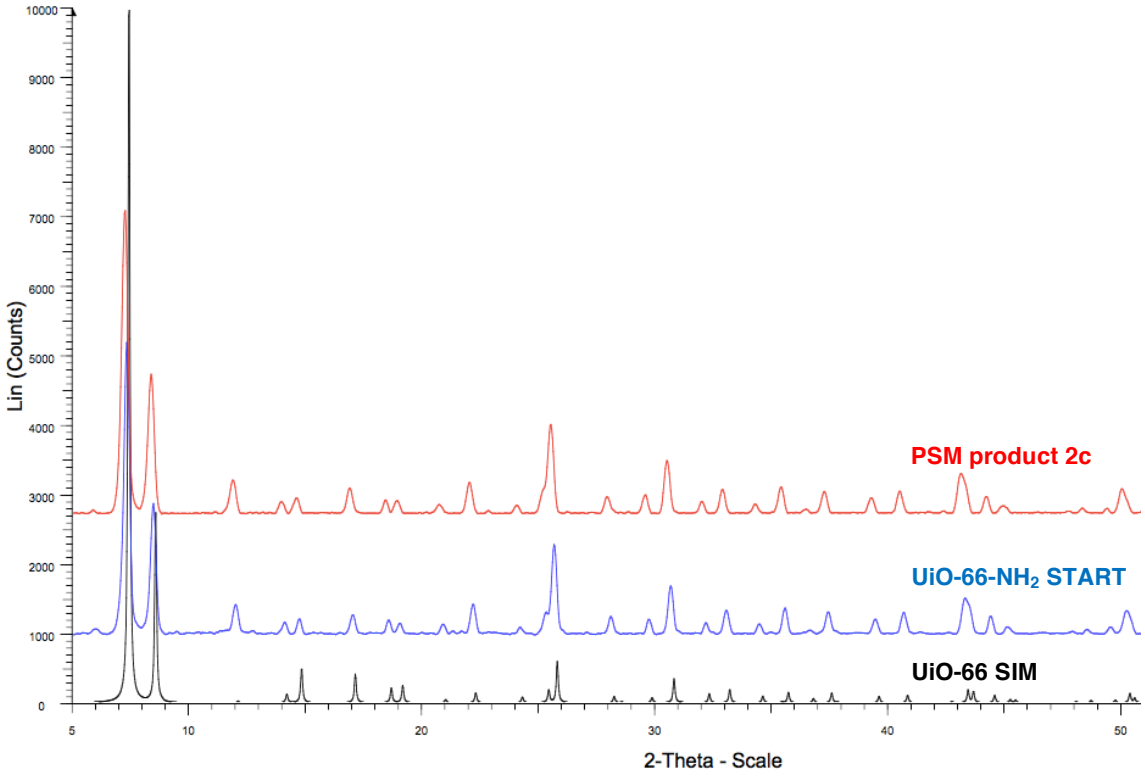

Figure 3.12. Black: Simulated PXRD pattern calculated from the UiO-66 crystal structure.[9] Blue: PXRD pattern of starting MOF, UiO-66-NH_2. Red: PXRD pattern of PSM product, **2c**.

As stated at the beginning of this chapter (Section 3.1), one of the aims of this work was to assess the Hg(II) uptake in the thiol containing PSM product. In order to probe the effect of different –$NHCH_2C_3H_2N_2SH$ loadings on Hg(II) uptake, a derivatised thiol-containing MOF was synthesised based on the reaction conditions shown in Scheme 3.7. This alternative reaction was performed such that the temperature for the conversion of –$NHCH_2OCH_3$ into –$NHCH_2C_3H_2N_2SH$ groups was reduced from 80 °C to 50 °C. It was postulated that this would lead to a lower –$NHCH_2C_3H_2N_2SH$ loading, which would affect the Hg(II) uptake.

The ^{1}H NMR spectrum of the digested PSM product **2d** shows the presence of the modified group (–$NHCH_2C_3H_2N_2SH$), Figure 3.13.

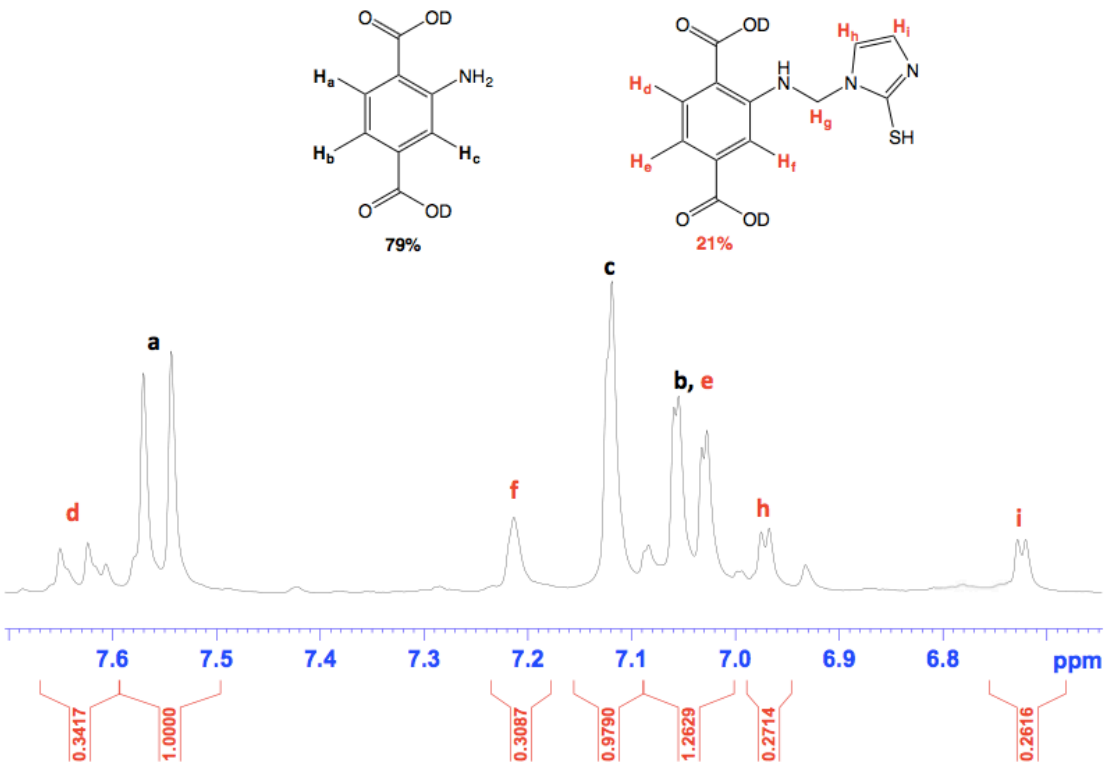

Figure 3.13. Aromatic region of ^{1}H NMR spectrum of digested PSM product **2d**.

The percentage conversion from –NH_2 into –$NHCH_2C_3H_2N_2SH$ groups was calculated as being approximately 21%, by comparing the integrals at δ 7.13 and δ 6.73 ppm. The calculated conversion gives the formula for **2d** as $[Zr_6O_4(OH)_4(BDC\text{-}NH_2)_{4.74}(BDC\text{-}NHCH_2C_3H_2N_2SH)_{1.26}]$. This result confirms that the reaction temperature has a significant impact on percentage conversion *i.e.* higher conversion was achieved at higher reaction temperature as seen for PSM product **2c** (36%) compared to **2d** (21%).

3.1.4. Comparison of Percentage Conversions in PSM Products, 2a-2c.

Based on the results presented thus far, it can be concluded that the identity of the nucleophile used in the Mannich PSM reaction has a significant impact on the percentage conversions, Table 3.1.

Compound	Nucleophile	% conversion	Chemical formula
2a	Pyrazole	41	$[Zr_6O_4(OH)_4(BDC\text{-}NH_2)_{3.54}(BDC\text{-}NHCH_2C_3H_3N_2)_{2.46}]$
2b	Imidazole	100	$[Zr_6O_4(OH)_4(BDC\text{-}NHCH_2C_3H_3N_2)_6]$
2c	2-Mercaptoimidazole	36	$[Zr_6O_4(OH)_4(BDC\text{-}NH_2)_{3.84}(BDC\text{-}NHCH_2C_3H_2N_2SH)_{2.16}]$

Table 3.1. The effect of nucleophiles on PSM percentage conversions. The reactions were carried out using the conditions shown in Scheme 3.3. Compound **2d** was not included in this table as the reaction conditions used to produce this sample differ from that for **2a-2c**.

The differences can be partly rationalised by the strength of nucleophiles used in this study. For example, imidazole is a better nucleophile than pyrazole partly due to its higher basicity.[14] For this reason, imidazole is more susceptible than pyrazole towards nucleophilic substitution with $–NHCH_2OCH_3$ thus leading to a higher conversion for the former. The steric impact of the nucleophile also appears to have some influence on percentage conversion. For instance, only 36% conversion was achieved when a larger substituent, 2-mercaptoimidazole, was used as the nucleophile. This can be explained by more restricted diffusion of 2-mercaptoimidazole (compared to smaller size pyrazole and imidazole) into the pores of the MOF. (Size of substituents = imidazole: 6.6 Å x 6.6 Å, pyrazole: 6.6 Å x 6.6 Å, 2-mercaptoimidazole: 8.4 Å x 6.6 Å. UiO-66-NH_2 channels: 6.9 Å).

3.1.5. Thermogravimetric Analysis of PSM Products, 2a-2d.

The TGA profiles of PSM products, **2a-2d** show the mass change with respect to temperature, Figure 3.14. Prior to TGA measurements, all samples were washed with 1,4-dioxane and left to dry in air for 2 hours to obtain free-flowing powders.

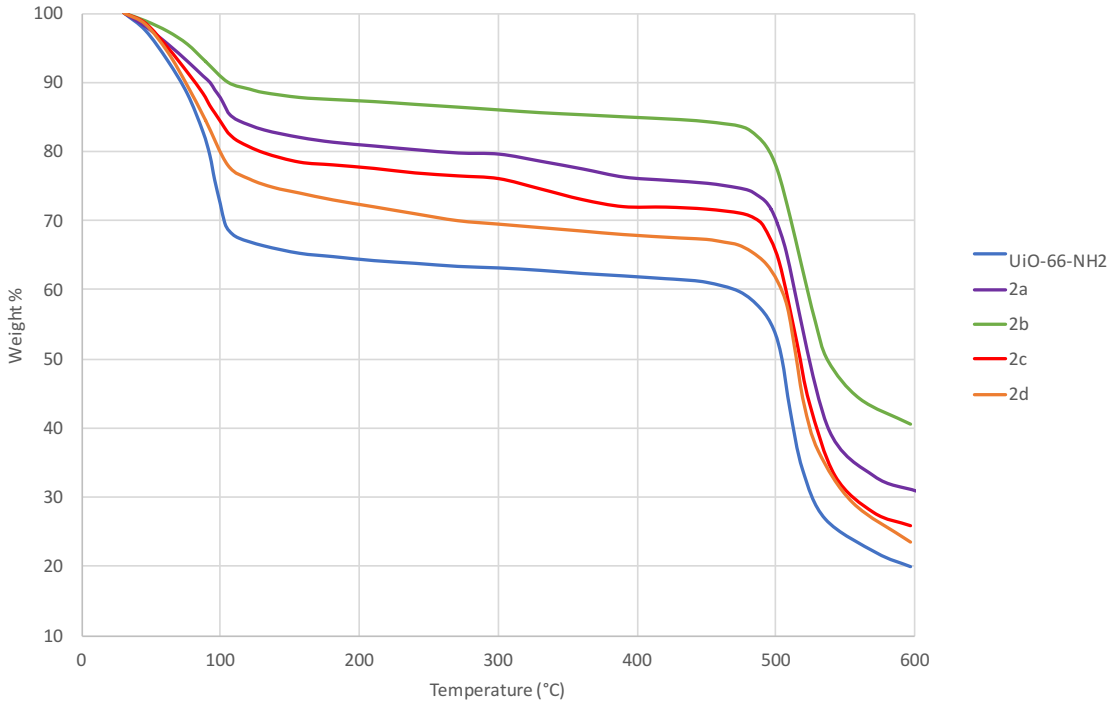

Figure 3.14. TGA of UiO-66-NH_2 and PSM products, **2a**-**2d**. The samples were heated from 30 °C to 600 °C at a rate of 20 K/min under a flow of argon gas (20 mL/min).

In the case of UiO-66-NH_2, the initial mass loss (up to 110 °C) represents the amount of 1,4-dioxane that is in the pores. A second mass change can be observed in the range 110 – 470 °C which may be attributed to residual DMF solvent in the pores and/or the dehydroxylation of the $Zr_6O_4(OH)_4$ nodes to form $Zr_6O_6(OH)_x$ ($x = 3, 2, 1, 0$).[15] The final mass loss at 470 °C is attributed to the decomposition of the MOF framework into a charred black solid. The TGA profiles for PSM products, **2a**-**2d** exhibit similar trend to that for UiO-66-NH_2, but in the case of **2a** and **2c**, an additional small mass loss was observed in the range 300 – 390 °C which may correspond to the decomposition of by-products.

The TGA data can also be used to determine the amount of solvent (1,4-dioxane molecules) that reside in the pores of the MOFs. Based on the TGA profiles, sample **2a** has 4.0, **2b** has 3.0, **2c** has 5.0, **2d** has 5.5 and UiO-66-NH_2 has 7.0 molecules of 1,4-dioxane for each $Zr_6O_4(OH)_4$ unit. This result implies that the amount of 1,4-dioxane in the pores increases as the percentage conversion decreases, which is intuitive, as more space available means more capacity to house guest solvent.

3.1.6. Gas Sorption Studies

3.1.6.1. BET Surface Areas of PSM Products, 2a-2d

The BET surface areas of PSM products, **2a-2d** were determined based on their N_2 adsorption isotherms, Figure 3.15. In terms of activation temperature, the TGA data for **2b** and **2c** suggested that the by-products in the pores may be successfully removed at 390 °C. Based on this finding, 390 °C was initially used as the activation temperature for **2b** and **2c** but this resulted in the PSM products losing their crystallinity and porosity. As a consequence, the PSM products were activated using the conventional activation temperature for UiO-66 and its derivatives (120 °C for 12 hours).

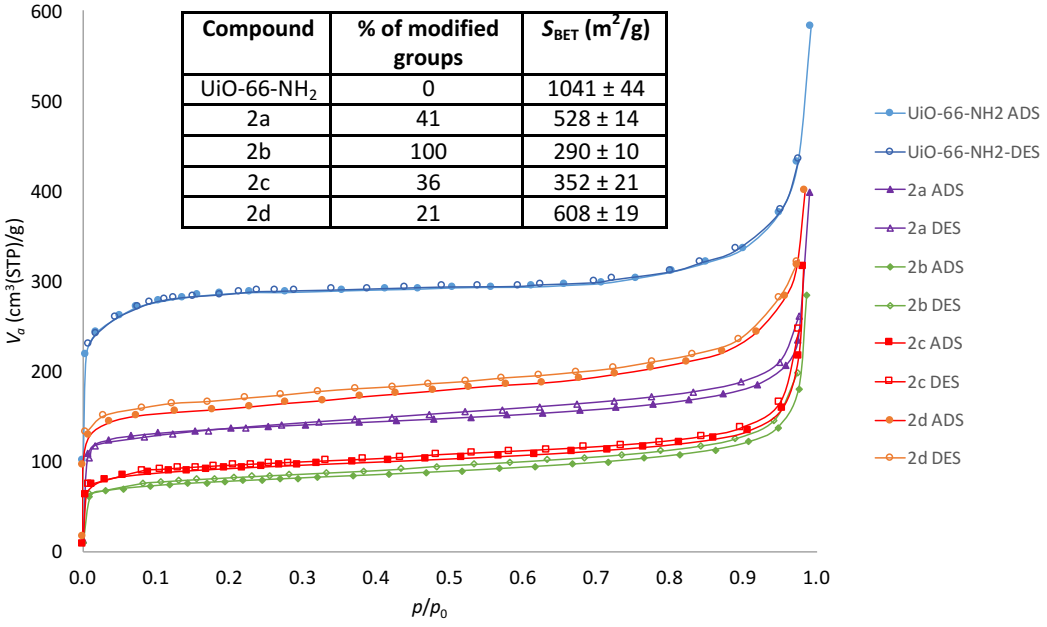

Figure 3.15. The N_2 adsorption isotherms for UiO-66-NH_2 and PSM products, **2a-2d**, at 77 K and the respective BET surface areas.

The BET surface area for UiO-66-NH_2 obtained in this work (S_{BET} = 1041 m^2/g) is similar to the values reported in the literature, which confirms the reproducibility of the surface area measurement and also the efficiency of the activation conditions used in this work.[13, 16, 17]

All PSM products exhibit a type I isotherm, indicative of microporous materials, which is expected for UiO-66 type materials. Furthermore, the samples possess lower BET surface areas than the starting MOF, UiO-66-NH_2 which was anticipated due to the additional mass originating from the modified groups.

Similar to the results observed in 2.4.1, the BET surface areas of the PSM products are governed by percentage conversion and size of the modified groups. In general, the BET surface area reduces as the percentage conversion increases. For example, $[Zr_6O_4(OH)_4(BDC\text{-}NHCH_2C_3H_3N_2)_6]$, **2b** possesses the lowest surface area (S_{BET} = 290 m^2/g) due to the highest percentage of modified groups in the pores. The effect of having larger modified groups in the pores can be exemplified by the lower BET surface area of $[Zr_6O_4(OH)_4(BDC\text{-}NH_2)_{3.84}(BDC\text{-}NHCH_2C_3H_2N_2SH)_{2.16}]$, **2c** compared to $[Zr_6O_4(OH)_4(BDC\text{-}NH_2)_{3.54}(BDC\text{-}NHCH_2C_3H_3N_2)_{2.46}]$, **2a** despite the latter possessing higher percentage of modified groups in the pores. This can be explained by the pore blocking effect caused by the larger $-NHCH_2C_3H_2N_2SH$ group in **2c**. In the case of **2c**, the size effect is more pronounced than the effect caused by percentage conversion. Another possible explanation for the lower BET surface area in **2c** is the additional pore blocking effect attributed to by-products in the pores.

3.1.6.2. CO_2 and N_2 Adsorption of PSM Products, 2a-2d, at 273 K

The CO_2 adsorption isotherms of the PSM products (at 273 K), Figure 3.16, were measured with the aim of investigating the influence of the modified groups on the CO_2 uptake capacities.

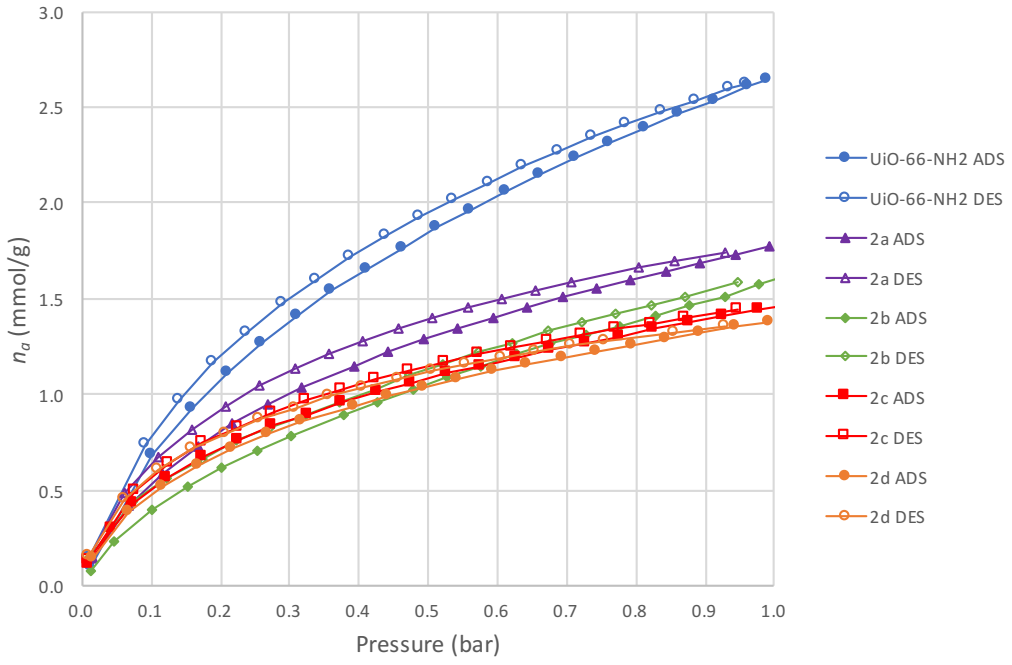

Figure 3.16. The CO_2 adsorption isotherms for UiO-66-NH_2 and PSM products, **2a-2d**, at 273 K.

All PSM products show lower CO_2 uptake capacities than that for UiO-66-NH_2. This is attributable to the reduction in free space and the lower percentage of CO_2-philic amino groups in the pores. Amongst the PSM products, $[Zr_6O_4(OH)_4(BDC\text{-}NH_2)_{3.54}(BDC\text{-}NHCH_2C_3H_3N_2)_{2.46}]$, **2a** shows the highest CO_2 uptake and this is probably due to the favourable interactions of CO_2 molecules with the nitrogen atom in the pyrazole ring. $[Zr_6O_4(OH)_4(BDC\text{-}NHCH_2C_3H_3N_2)_6]$, **2b** shows lower CO_2 uptake than that for **2a**, despite having higher percentage of imidazole groups (nitrogen atoms) in the pores. This can be explained by the pore blocking effect caused by the higher percentage of modified groups in the pores which limit the diffusion of CO_2 molecules in **2b**.

$[Zr_6O_4(OH)_4(BDC\text{-}NH_2)_{3.84}(BDC\text{-}NHCH_2C_3H_2N_2SH)_{2.16}]$, **2c** and $[Zr_6O_4(OH)_4(BDC\text{-}NH_2)_{4.74}(BDC\text{-}NHCH_2C_3H_2N_2SH)_{1.26}]$, **2d** show the lowest CO_2 uptake capacities at high pressure (1 bar) and this may be due to pore blocking caused by higher steric hindrance of the modified groups. Nonetheless, the amount/percentage of thiol groups in the pores has little impact on the CO_2 uptake capacities. This is evidenced by the relatively small difference in CO_2 uptake between **2c** and **2d**. The lowest CO_2 uptake capacity at low pressure (0.1 bar) is observed for **2b** and this once again, may be due to pore blocking effect.

In order to assess the CO_2 over N_2 selectivity of **2a-2d**, N_2 adsorption measurements were carried out at 273 K, Figure 3.17. The results are presented in Table 3.2.

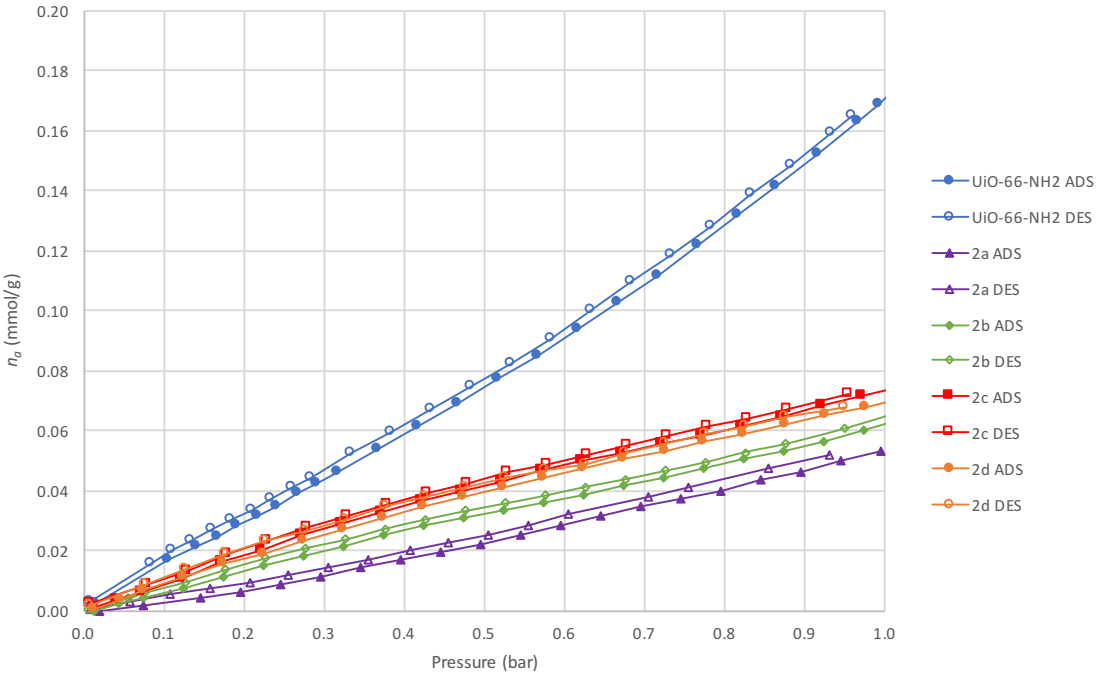

Figure 3.17. The N_2 adsorption isotherms for UiO-66-NH_2 and PSM products, **2a-2d**, at 273 K.

Sample	CO_2 (mmol/g)		N_2 (mmol/g)		Selectivity (CO_2/N_2)	
	1 bar	0.1 bar	1 bar	0.1 bar	1 bar	0.1 bar
UiO-66-NH_2	2.645	0.679	0.169	0.019	16	36
2a	1.775	0.537	0.053	0.003	33	179
2b	1.623	0.401	0.062	0.006	26	67
2c	1.470	0.486	0.073	0.009	20	54
2d	1.379	0.472	0.069	0.009	20	52

Table 3.2. The CO_2 and N_2 adsorption data for UiO-66-NH_2 and PSM products, **2a**-**2d**, at 0.1 and 1 bar at 273 K. The selectivity of CO_2 over N_2 of the material was calculated from the single gas isotherms by dividing the CO_2 uptake by that of N_2 at a specific pressure (0.1 or 1 bar).

As expected, all PSM products show lower N_2 uptake capacities than that for the starting MOF, UiO-66-NH_2. The lower N_2 uptake also leads to the PSM products exhibiting higher CO_2 over N_2 selectivity. Somewhat surprisingly, $[Zr_6O_4(OH)_4(BDC\text{-}NH_2)_{3.54}(BDC\text{-}NHCH_2C_3H_3N_2)_{2.46}]$, **2a** shows the highest increase with the selectivity reaching 33 and 179 at 1 bar and 0.1 bar, respectively. Notably, the selectivity of **2a** at 0.1 bar is ~5 times higher than that for UiO-66-NH_2. At present, the reason for this stark increase is not fully understood although it is suspected that the presence of pyrazole ring in the pores combined with moderate percentage inclusion (41%) may contribute to the higher CO_2 over N_2 selectivity.

3.1.7. Hg(II) Uptake Studies of PSM Products 2c and 2d

As stated in Section 3.1, one of the aims of this work was to investigate the Hg(II) uptake capacities in the thiol-containing PSM products, $[Zr_6O_4(OH)_4(BDC\text{-}NH_2)_{3.84}(BDC\text{-}NHCH_2C_3H_2N_2SH)_{2.16}]$ **2c** and $[Zr_6O_4(OH)_4(BDC\text{-}NH_2)_{4.74}(BDC\text{-}NHCH_2C_3H_2N_2SH)_{1.26}]$, **2d**. The Hg(II) uptake experiments were carried out by immersing the MOF samples (15 mg) in an aqueous solution of $HgCl_2$ (15 mL, 100 ppm) and the solution was stirred for 12 hours at ambient temperature. The Hg(II) treated MOFs were isolated by centrifugation and atomic emission spectroscopy (AES) was used to quantify the residual Hg(II) concentration in the supernatant.

The Hg(II) uptake capacity was calculated using Equation (1) where C_i and C_e represent the initial (100 ppm) and equilibrium (supernatant) Hg(II) concentrations, respectively. In addition to PSM products **2c** and **2d**, the Hg(II) uptake capacities of the unmodified MOFs, UiO-66 and UiO-66-NH_2, were investigated for comparison, Table 3.3 and Figure 3.18.

$$\text{Hg(II) Uptake (\%)} = \frac{(C_i - C_e)}{C_i} \times 100 \quad (1)$$

MOF	$C_{Hg(II)}$ prior to MOF treatment, C_i (ppm)	$C_{Hg(II)}$ after MOF treatment, C_e (ppm)	Hg(II) uptake (%)
UiO-66	100	89	11
UiO-66-NH_2		77	23
$[Zr_6O_4(OH)_4(BDC\text{-}NH_2)_{3.84}(BDC\text{-}NHCH_2C_3H_2N_2SH)_{2.16}]$, **2c**		50	50
$[Zr_6O_4(OH)_4(BDC\text{-}NH_2)_{4.74}(BDC\text{-}NHCH_2C_3H_2N_2SH)_{1.26}]$, **2d**		1	99

Table 3.3. The Hg(II) uptake capacities of UiO-66, UiO-66-NH_2 and PSM products **2c** and **2d**.

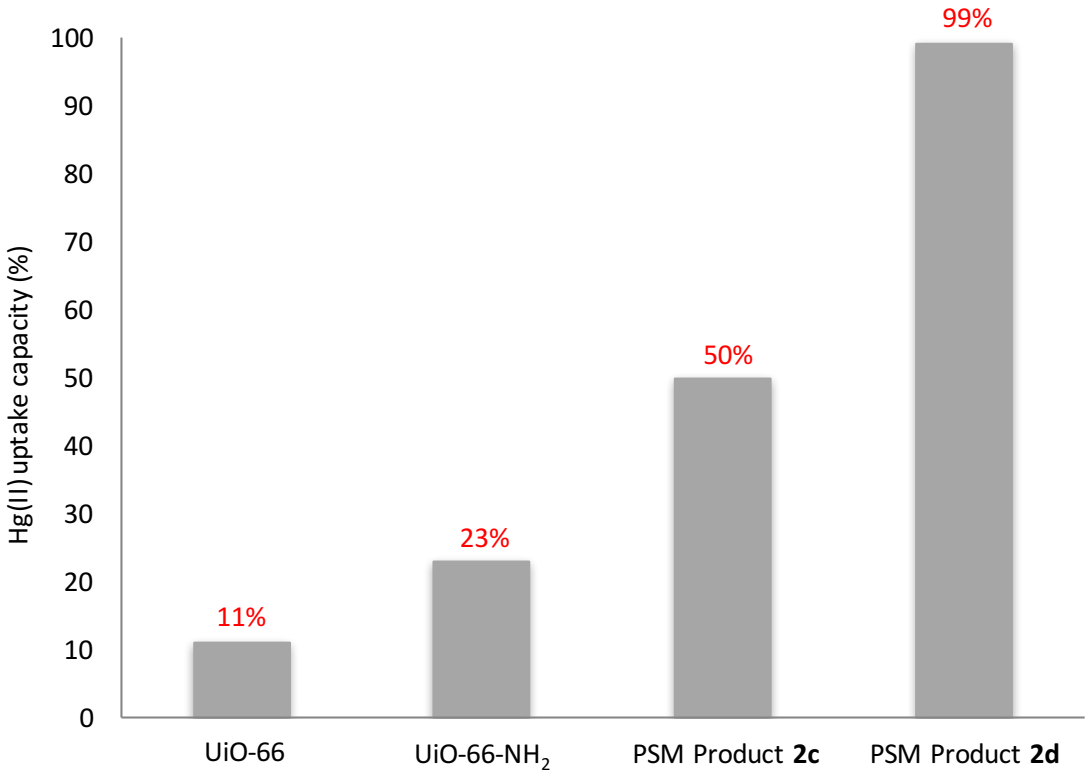

Figure 3.18. Hg(II) uptake capacities in different MOF samples.

The grafting of thiol groups in the pores of UiO-66 *via* PSM proved to be beneficial, as the Hg(II) uptake capacities greatly increased for samples **2c** and **2d**. Surprisingly, perhaps, the highest Hg(II) uptake was observed for sample **2d** although **2c** has a higher loading of thiol groups in the pores. This may be explained by the 'larger' free space in **2d** (due to lower percentage of modified groups and by-products) compared to **2c** which could allow for more Hg(II) to occupy the pores. Furthermore, the Hg(II) uptake in **2d** (99%) is comparable to that reported for UiO-66-$(SH)_2$ (~100%) (Section 1.4.3), demonstrating the potential of **2d** in real-life application.

On the other hand, the small Hg(II) uptake capacities observed in the unmodified MOFs, UiO-66 and UiO-66-NH_2 may be attributed to the large free space in the pores of these MOFs. The reason for the higher Hg(II) uptake capacity in UiO-66-NH_2 compared to UiO-66 is likely to be due to the $-NH_2$ groups though these are notably less effective than the thiol groups.

The structural integrity of **2d** upon treatment with $HgCl_2$ (aq) was assessed by PXRD, Figure 3.19. Due to the high similarities of the PXRD patterns of PSM product **2b** prior to and after treatment with $HgCl_2$ (aq), it was concluded that the framework had remained intact and retained its crystallinity upon treatment with $HgCl_2$ (aq).

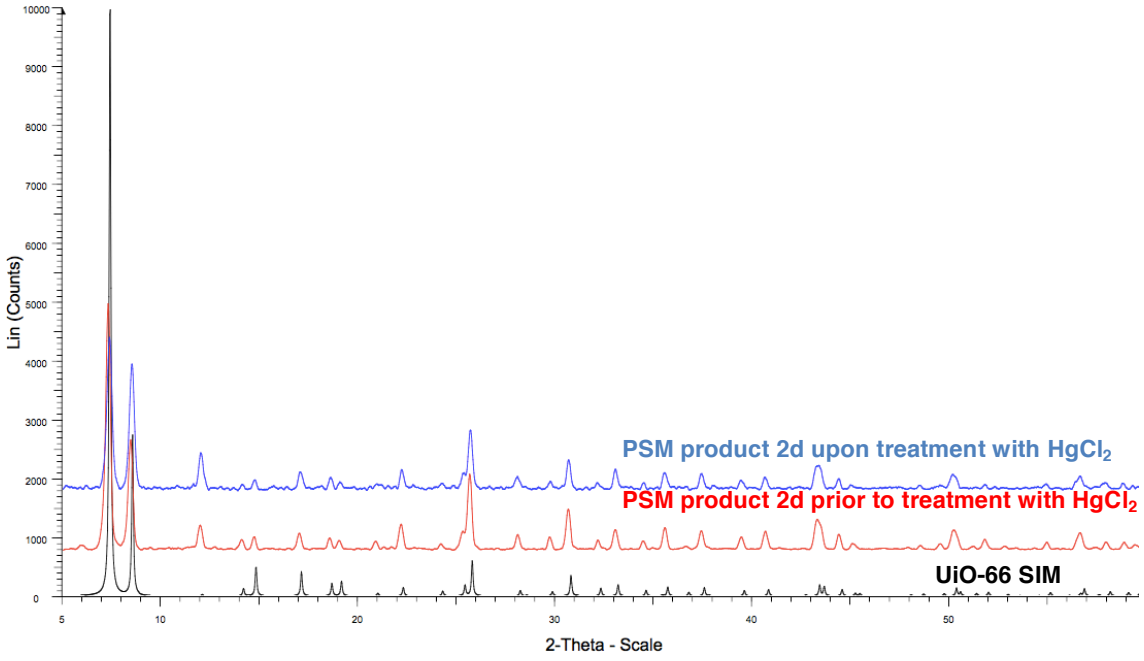

Figure 3.19. Black: Simulated PXRD pattern calculated from the UiO-66 crystal structure.[9] Red: PXRD pattern of PSM product **2d** prior to treatment with $HgCl_2$ (aq). Blue: PXRD pattern of PSM product **2d** upon treatment with $HgCl_2$ (aq).

3.2. The Mannich Reaction on $[Zn_4O(BDC\text{-}NH_2)_3]$, IRMOF-3

3.2.1. Pyrazole as the Nucleophile

In order to investigate the versatility of Mannich reaction on MOFs, $[Zn_4O(BDC\text{-}NH_2)_3]$, IRMOF-3, was used as an alternative to UiO-66-NH_2. IRMOF-3 was chosen due to its large pore channels (9.6 Å) and the presence of accessible amino groups protruding into the pores, Figure 3.20.[18] Furthermore, large crystals of IRMOF-3 are relatively easy to synthesise and this also means that the composition of the PSM product may be analysed by single crystal X-ray diffraction.

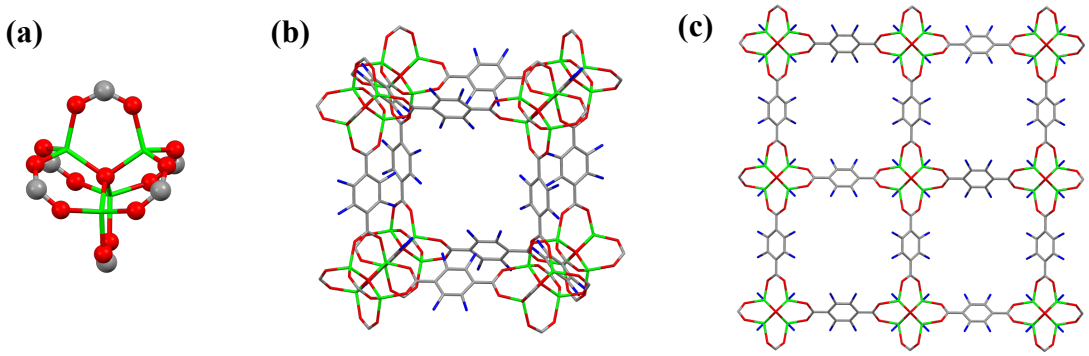

Figure 3.20. (a) SBU of IRMOF-3. **(b)** Representation of a 3-D cubic structure of IRMOF-3. **(c)** Network structure of IRMOF-3. The amino groups are disordered over four sites of the linker. Zn: light green, C: grey, O: red, N: blue.[18]

IRMOF-3 is known to have a low stability towards moisture and certain solvents particularly alcohols. Therefore, prior to PSM reaction, the stability of IRMOF-3 crystals in different solvents (toluene, 1,4-dioxane and MeOH) was investigated. The solvents used in this study were anhydrous to minimise the influence of moisture on the IRMOF-3 crystals. IRMOF-3 was synthesised according to a previously reported procedure by Kim and co-workers.[19] In a typical experiment, $Zn(NO_3)_2 \cdot 6H_2O$ and $H_2BDC\text{-}NH_2$ were dissolved in DMF in a glass vial. The vial was sealed and the reaction mixture was heated at 105 °C for 48 hours to yield pale brown cubic crystals. The crystals were then washed and soaked in the respective solvent (toluene, 1,4-dioxane or MeOH) for 3 days, replacing the solvent with fresh solvent every 24 hours before collecting the crystals by filtration.

As shown in Figure 3.21, IRMOF-3 exhibits the highest stability in toluene. This is probably due to the hydrophobic nature of toluene which lessen the effect of crystal degradation by minimising crystal exposure to moisture. Some degree of crystal degradation was observed whilst 1,4-dioxane was employed as the solvent based on the broadening of peaks and reduced peak intensities. As expected, the degree of crystal

degradation was more pronounced whilst MeOH was used as a solvent and indeed, complete crystal degradation was observed under these conditions. Based on these findings, toluene was selected as the optimum solvent for the Mannich reaction of IRMOF-3.

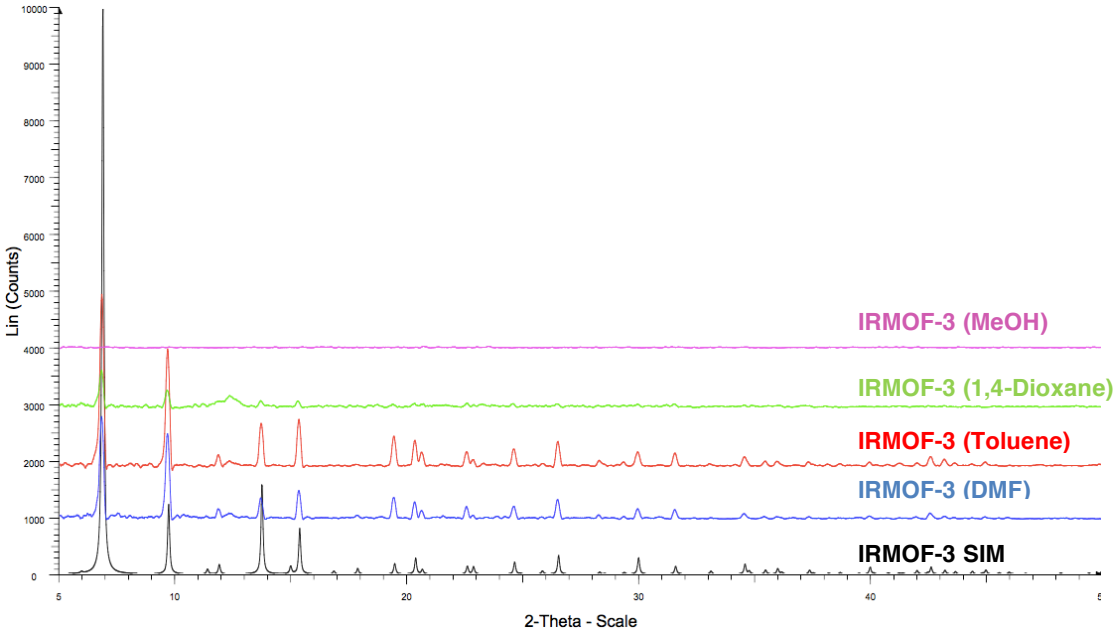

Figure 3.21. Black: Simulated PXRD pattern of IRMOF-3 calculated from the single crystal data.[18] Blue: PXRD pattern of as-synthesised IRMOF-3 in DMF. Red: PXRD pattern of IRMOF-3 in toluene. Green: PXRD pattern of IRMOF-3 in 1,4-dioxane. Pink: PXRD pattern of IRMOF-3 in methanol.

To demonstrate the applicability of Mannich reaction on IRMOF-3, the PSM reaction was carried out based on the reaction conditions outlined in Scheme 3.8.

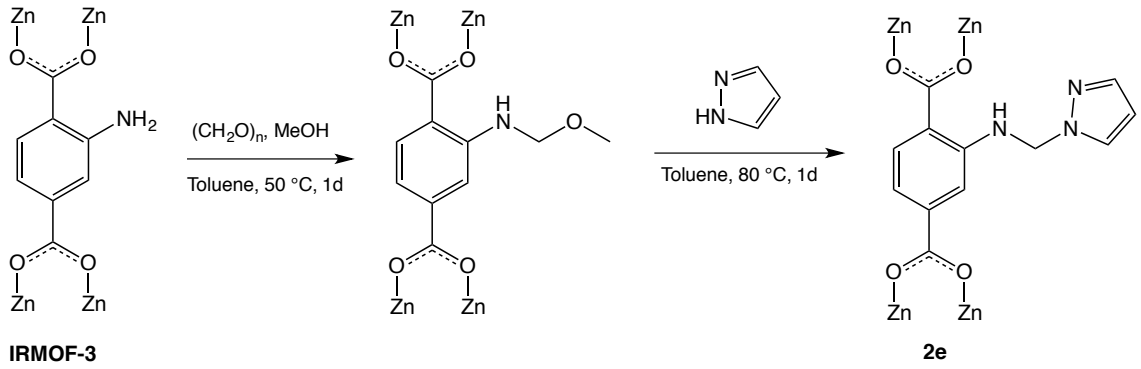

Scheme 3.8. The Mannich reaction of IRMOF-3 using pyrazole as the nucleophile.

In a typical procedure, IRMOF-3 crystals (1 eq) (rinsed beforehand with toluene) were treated with paraformaldehyde (2 eq) and MeOH (2 eq) in toluene at 50 °C for 1 day. The

intermediate product was then washed with fresh toluene (three times) to remove any residual paraformaldehyde and MeOH in the pores or on the solid surface. The crystals were subsequently treated with pyrazole in toluene at 80°C for 1 day before quenching the reaction by rinsing the crystals with fresh toluene. The crystals were soaked in toluene for 3 days, replacing the solvent with fresh solvent every 24 hours. The crystals were then isolated *via* filtration. The detailed experimental procedure can be found in Section 3.9.7.

The effectiveness of the PSM reaction in terms of the percentage conversion of amino into α-amino pyrazole (–$NHCH_2C_3H_3N_2$) was gauged by ^{1}H NMR spectroscopy. Figure 3.22 shows the spectrum that was obtained by digesting the PSM product, **2e** in DCl/D_2O with DMSO-d_6. Acid digestion was used in order to cleave the Zn-O bonds within the framework and to solubilise the MOF. This digestion procedure is common for the MOFs in the IRMOF series.[20, 21]

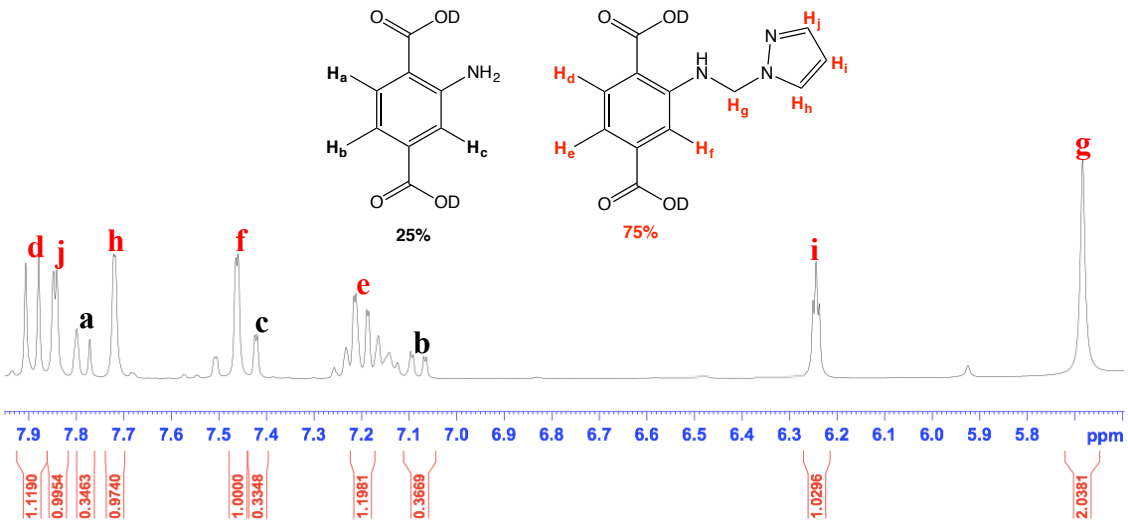

Figure 3.22 ^{1}H NMR spectrum of PSM product **2e** digested in DCl/D_2O and DMSO-d_6.

In addition to the peaks which correspond to the aryl protons of the starting MOF, $D_2BDC\text{-}NH_2$ (H_a = 7.78 ppm, H_b = 7.07 ppm and H_c = 7.42 ppm), new peaks attributed to the aryl protons of **2e** (H_d = 7.89 ppm, H_e = 7.20 ppm and H_f = 7.46 ppm) were also observed. The successful incorporation of the α-amino pyrazole (–$NHCH_2C_3H_3N_2$) groups could also be evidenced by the emergence of new peaks at δ 7.72, δ 6.25 and δ 7.85 ppm which correspond to the protons of the pyrazole ring, H_h, H_i and H_j respectively. The peak attributed to the α-CH_2 protons, H_g can be located at δ 5.68 ppm. There is also some residual toluene solvent in the digestion solution based on the peaks at δ 7.12 – 7.27 ppm. The degree of conversion of amino into α-amino pyrazole (–$NHCH_2C_3H_3N_2$) groups,

which was approximately 75%, was calculated by comparing the integrals at δ 7.46 ppm and δ 7.42 ppm. The calculated conversion gives the formula for **2e** as $[Zn_4O(BDC\text{-}NH_2)_{0.75}(BDC\text{-}NHCH_2C_3H_3N_2)_{2.25}]$.

The negative ESI mass spectrum of the digested product **2e** confirms the presence of the deprotonated anion of $H_2BDC\text{-}NHCH_2C_3H_3N_2$ and $H_2BDC\text{-}NH_2$ at m/z = 260.0669 (predicted $[M\text{-}H]^-$ = 260.0671) and m/z = 180.0308 (predicted $[M\text{-}H]^-$ = 180.0375), respectively.

The FTIR spectra of the starting MOF, IRMOF-3, and PSM product **2e** are shown in Figure 3.23. The successful conversion of primary amine ($–NH_2$) into secondary amine ($–NHCH_2C_3H_3N_2$) was evidenced by the disappearance of the $–NH_2$ stretching bands of IRMOF-3 (3123 and 3313 cm^{-1}) in the FTIR spectrum of **2e**. However, the presence of pyrazole ring on the modified framework could not be inferred *via* FTIR spectroscopy due to the presence of the framework's backbone peaks which dominate the 600 – 1700 cm^{-1} region.

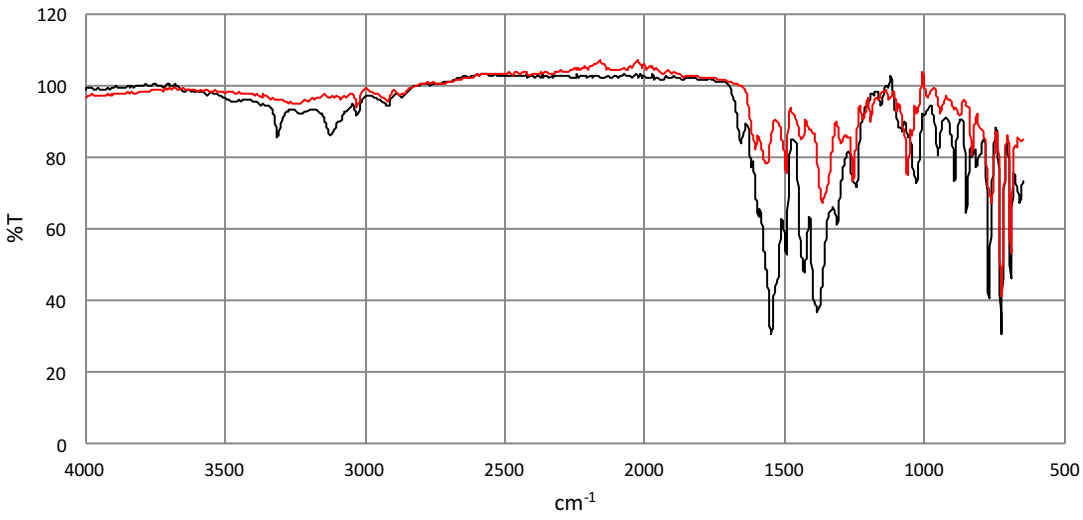

Figure 3.23. Black: FTIR spectrum of IRMOF-3. Red: FTIR spectrum of $[Zn_4O(BDC\text{-}NH_2)_{0.75}(BDC\text{-}NHCH_2C_3H_3N_2)_{2.25}]$, **2e**.

The PXRD pattern of PSM product **2e** shows the similarities in peak positions with the starting MOF, IRMOF-3, which indicates that the bulk framework structure remained unchanged upon PSM reaction, Figure 3.24. Nonetheless, a certain degree of crystal degradation was observed, as evidenced by the broadening of peaks and reduced peak

intensities. The presence of MeOH as the side product of this reaction, combined with long reaction time and high reaction temperature may cause the crystal degradation of **2e**. Attempts to analyse the components of **2e** crystallographically were hampered, due to poor diffraction quality of the crystals.

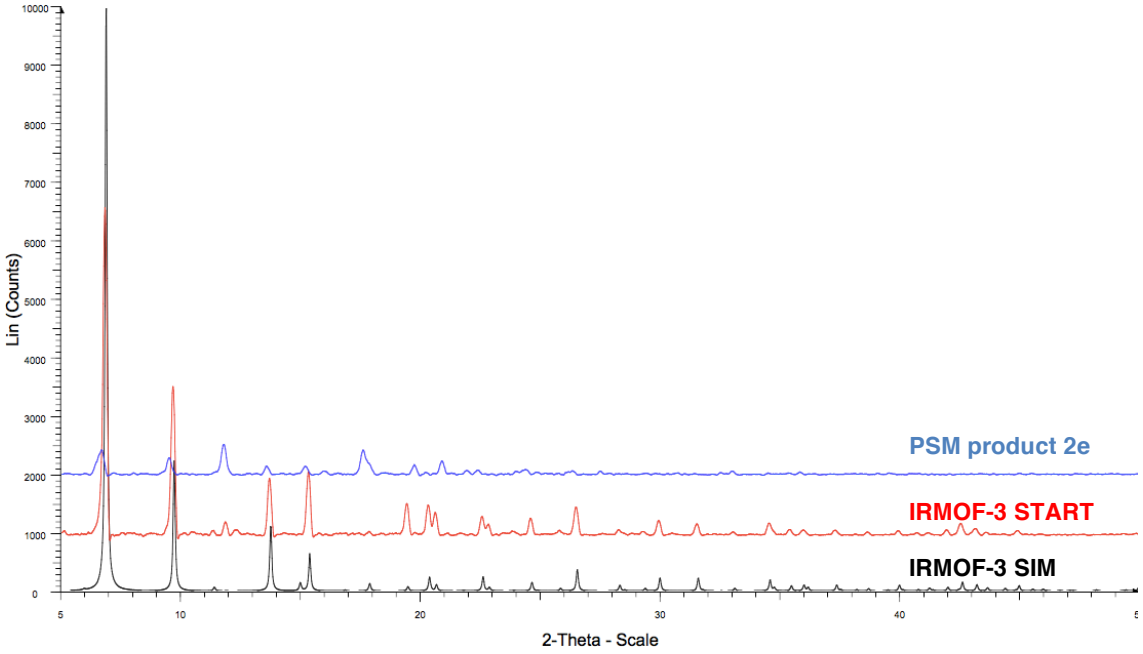

Figure 3.24. Black: Simulated PXRD pattern of IRMOF-3 calculated from the single crystal data.[18] Red: PXRD pattern of the starting MOF, IRMOF-3. Blue: PXRD pattern of PSM product **2e**.

The Mannich reactions of IRMOF-3 with imidazole and 2-mercaptoimidazole were not carried out due to the instability of IRMOF-3 crystals towards the reaction conditions used in this study, as evidenced with PSM product **2e**.

3.3. The Mannich Reaction on $[Zn_2(BDC\text{-}NH_2)_2(DABCO)]$, DMOF-1-$NH_2$

3.3.1. Pyrazole as the Nucleophile

$[Zn_2(BDC\text{-}NH_2)_2(DABCO)]$, DMOF-1-$NH_2$, is a flexible MOF which consist of zinc(II) metal centres coordinated to BDC-NH_2 ligands in two dimensions, Figure 3.25. The two-dimensional sheets are pillared by DABCO ligands to form a three-dimensional network structure. In this work, the Mannich reaction on DMOF-1-NH_2 was carried out with the aim of investigating the influence of PSM on the framework structure of a flexible MOF. Furthermore, some previous reports on the PSM of DMOF-1-NH_2 have shown that the modified frameworks were successfully analysed *via* single crystal X-ray

crystallography.[22] On this basis, crystallographic characterisation of the PSM product upon Mannich reaction would also be attempted.

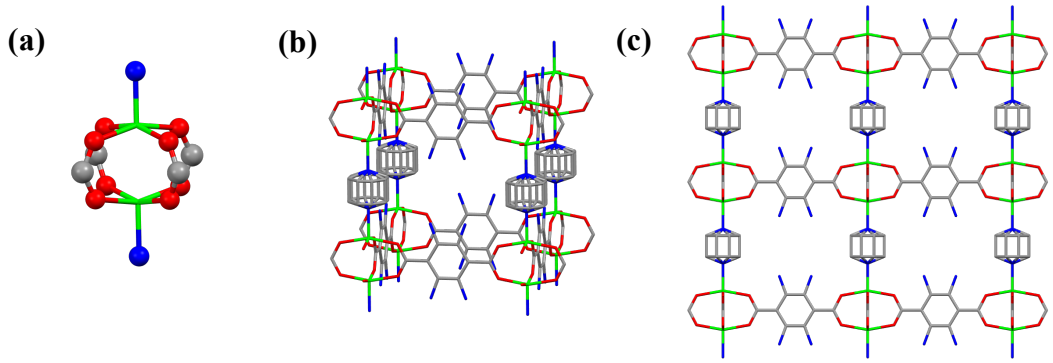

Figure 3.25. (a) SBU of DMOF-1-NH_2. **(b)** Representation of a pore in DMOF-1-NH_2. **(c)** Network structure of DMOF-1-NH_2 viewed along *a* and *b* axes**.** The amino groups are disordered over four sites of the linker. Hydrogen atoms are omitted for clarity. Zn: light green, C: grey, O: red, N: blue.[23]

DMOF-1, the parent MOF of DMOF-1-NH_2, is known to exhibit different structural features due to the flexibility of the framework. For example, Kim *et al*. demonstrated the pore geometry transition of DMOF-1 from rhomboidal (narrow pore), Figure 3.26(a), to square (open pore), Figure 3.26(b), upon removing DMF and H_2O molecules from the pores.[24] The geometry transition also depends on the nature of the solvent molecules. For example, DMOF-1 shrinks even more (exhibits narrower pores), Figure 3.26(c), when benzene is used as the solvent instead of DMF.

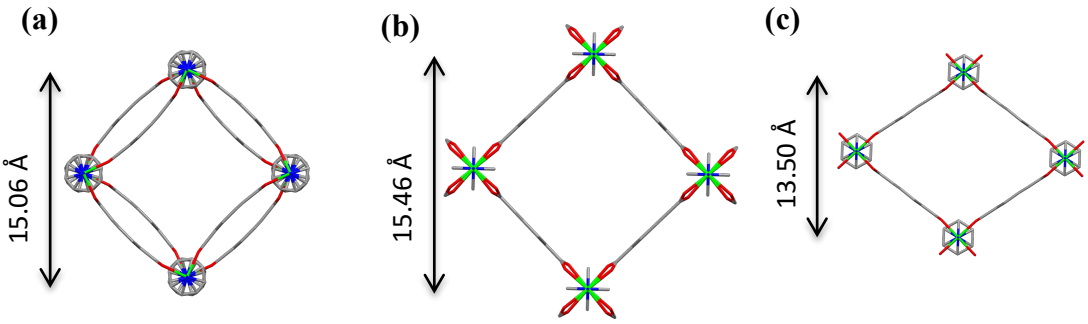

Figure 3.26. Pore structures of **(a)** $[Zn_2(BDC\text{-}NH_2)_2(DABCO)]\cdot 4DMF\cdot 0.5H_2O$ **(b)** $[Zn_2(BDC\text{-}NH_2)_2(DABCO)]$ **(c)** $[Zn_2(BDC\text{-}NH_2)_2(DABCO)]\cdot 2C_6H_6$ viewed along *c* axis. Hydrogen atoms and guest solvents are omitted for clarity. Zn: light green, C: grey, O: red, N: blue.[24]

In this work, solvent screening was carried out to investigate the effect of solvent molecules on the MOF structure prior to PSM reaction. Three different solvents (toluene, 1,4-dioxane and MeOH) were chosen due to the precedence of these solvents in the PSM

reactions on UiO-66-NH_2 and IRMOF-3. DMOF-1-NH_2 was synthesised using an analogous synthesis to that for DMOF-1, originally reported by Kim and co-workers.[24] In a typical experiment, a mixture of $Zn(NO_3)_2 \cdot 6H_2O$, $H_2BDC\text{-}NH_2$ and DABCO was suspended in DMF and heated in a glass vial at 120°C for 2 days. The resulting brown block crystals were washed and soaked in the respective solvent (toluene, 1,4-dioxane or MeOH) for 3 days, replacing the solvent with fresh solvent every 24 hours before collecting the crystals by filtration.

As shown in Figure 3.27, the PXRD pattern of the as-synthesised MOF (in DMF) is similar to that reported in the literature (narrow pore, space group = I4/*mcm*).[24] The MOF also exhibits the same pore geometry in toluene. However, DMOF-1 undergoes pore expansion (open pore, space group = P4/*mmm*) in 1,4-dioxane and MeOH as evidenced by the shifting of peak positions towards lower 2θ angle. In MeOH, some degree of crystal degradation was observed based on the broadening of peaks and reduced peak intensities. Based on these findings, toluene was chosen as the solvent for the PSM reaction as this has no effect on DMOF-1-NH_2 topology.

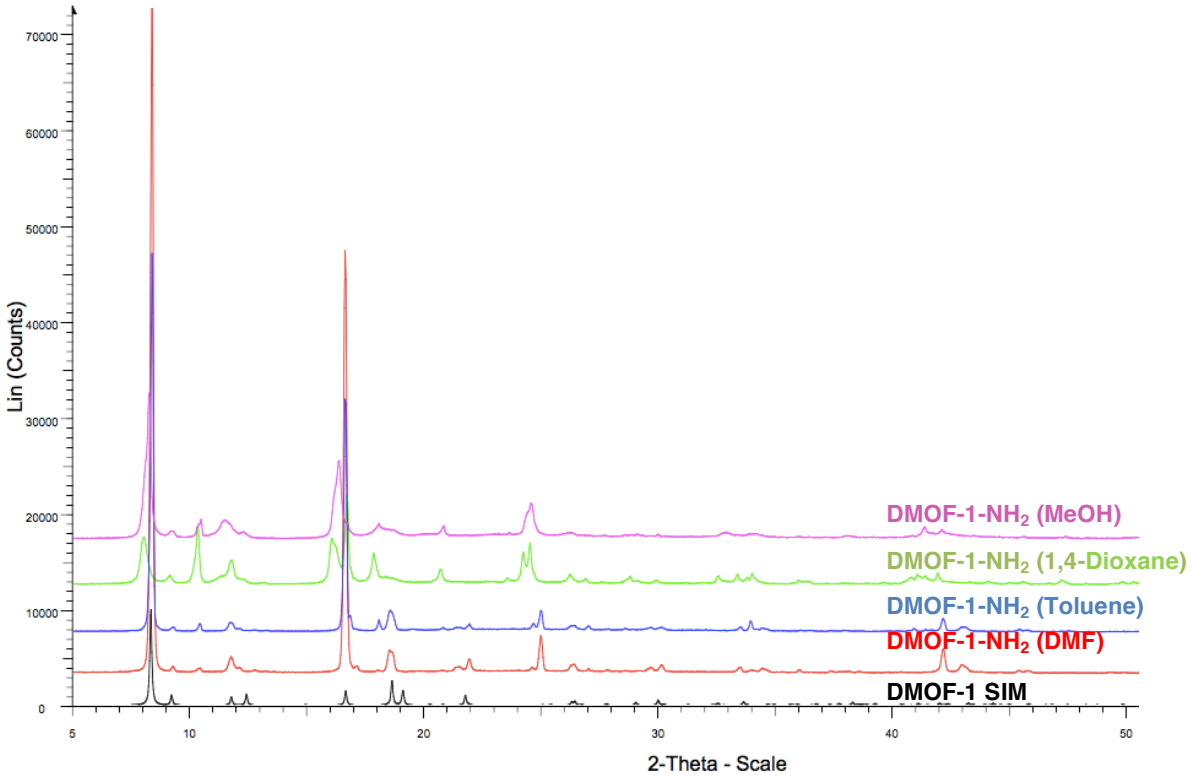

Figure 3.27. Black: Simulated PXRD pattern of DMOF-1 calculated from the single crystal data.[24] Red: PXRD pattern of as-synthesised DMOF-1-NH_2 in DMF. Blue: PXRD pattern of DMOF-1-NH_2 in toluene. Green: PXRD pattern of DMOF-1-NH_2 in 1,4-dioxane. Pink: PXRD pattern of DMOF-1-NH_2 in methanol.

To demonstrate the applicability of Mannich reaction on DMOF-1-NH_2, the PSM reaction was carried out using the reaction conditions outlined in Scheme 3.9.

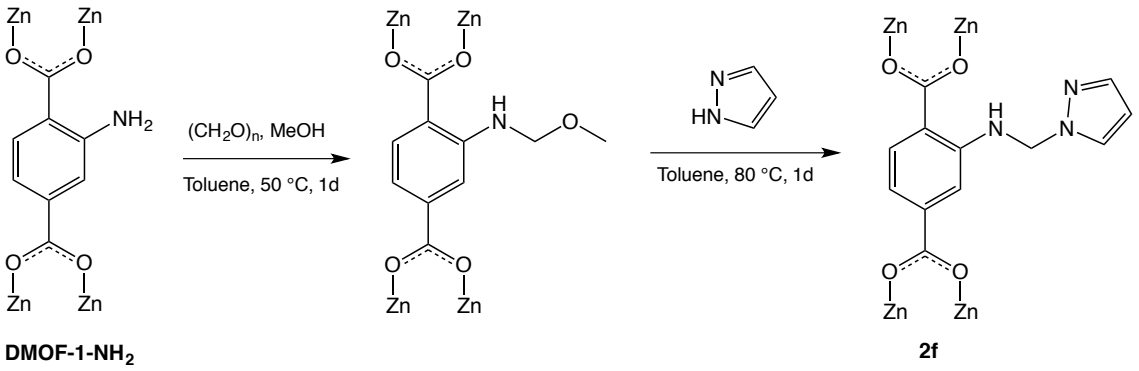

Scheme 3.9. The Mannich reaction of DMOF-1-NH_2 using pyrazole as the nucleophile.

In a typical procedure, DMOF-1-NH_2 crystals (1 eq) (rinsed beforehand with toluene) were treated with paraformaldehyde (2 eq) and MeOH (2 eq) in toluene at 50 °C for 1 day. The intermediate product was then washed with fresh toluene (three times) to remove any residual paraformaldehyde and MeOH in the pores or on the solid surface. The crystals were subsequently treated with pyrazole in toluene at 80°C for 1 day before quenching the reaction by rinsing the crystals with fresh toluene. The crystals were soaked in toluene for 3 days, replacing the solvent with fresh solvent every 24 hours. The crystals were then isolated *via* filtration. The detailed experimental procedure can be found in Section 3.9.9.

The ^{1}H NMR spectrum of the digested PSM product **2f** shows the presence of aromatic protons attributed to D_2BDC-NH_2 (H_a = 7.82 ppm, H_b = 7.13 ppm and H_c = 7.48 ppm) and D_2BDC-$NHCH_2C_3H_3N_2$ (H_d = 7.89 ppm, H_e = 7.20 ppm and H_f = 7.49 ppm), Figure 3.28.

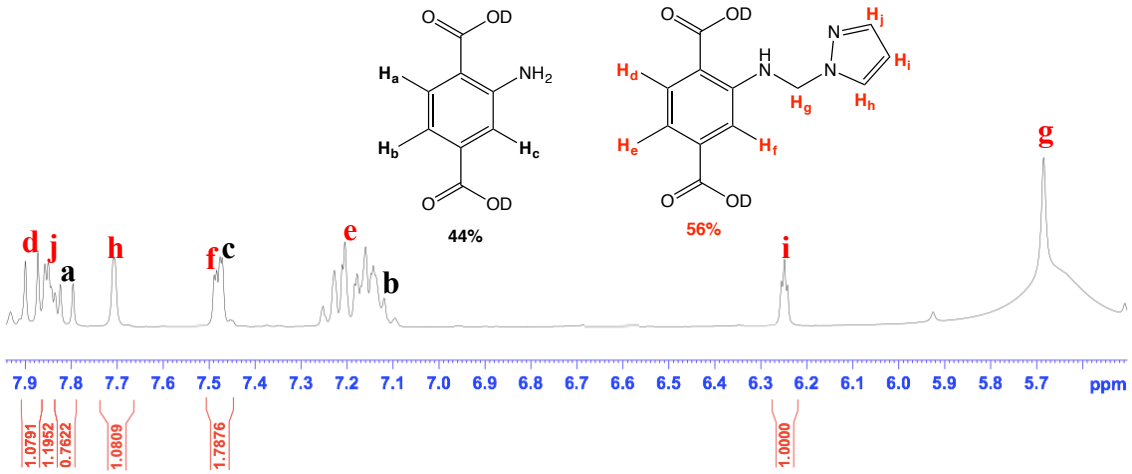

Figure 3.28 ^{1}H NMR spectrum of PSM product **2f** digested in DCl/D_2O and DMSO-d_6.

The peaks at δ 7.13 ppm (H_b) and δ 7.20 ppm (H_e) overlap with the signals from the aryl protons of residual toluene solvent. The protons of the pyrazole ring H_h, H_i and H_j can be located at δ 7.72, δ 6.25 and δ 7.85 ppm, respectively. The peak attributed to the α-CH_2 protons, H_g can be located at δ 5.68 ppm although there is some degree of overlapping between the peak and the HDO peak used in the digestion. Comparing the integrals of the protons at δ 7.48 ~ 7.49 ppm and δ 6.25 ppm, the percentage conversion of amino into α-amino pyrazole (–$NHCH_2C_3H_3N_2$) groups was calculated to be approximately 56%.

The negative ESI mass spectrum of the digested product **2f** confirms the presence of the deprotonated anion of H_2BDC-$NHCH_2C_3H_3N_2$ and H_2BDC-NH_2 at m/z = 260.0662 (predicted $[M\text{-}H]^-$ = 260.0671) and m/z = 180.0364 (predicted $[M\text{-}H]^-$ = 180.0375), respectively.

The disappearance of –NH_2 stretching bands (3287 and 3457 cm^{-1}) of DMOF-1-NH_2 in the FTIR spectrum of **2f** indicates the successful conversion of primary amine (–NH_2) into secondary amine (–$NHCH_2C_3H_3N_2$), Figure 3.29. In similar vein to **2e** (Section 3.2), the presence of pyrazole ring on the modified framework could not be inferred *via* FTIR spectroscopy due to the presence of framework's backbone peaks which dominate the 600 – 1700 cm^{-1} region.

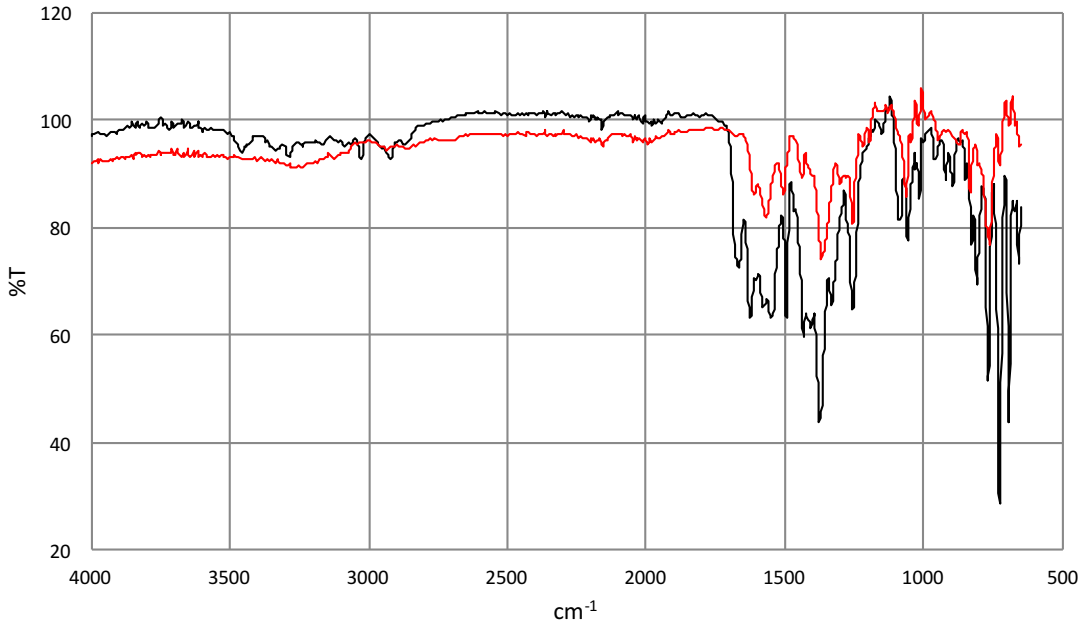

Figure 3.29. Black: FTIR spectrum of DMOF-1-NH_2. Red: FTIR spectrum of PSM product **2f**.

Figure 3.30 shows the PXRD patterns of the starting MOF, DMOF-1-NH_2, and PSM product, **2f**, illustrating the stark difference between the two materials.

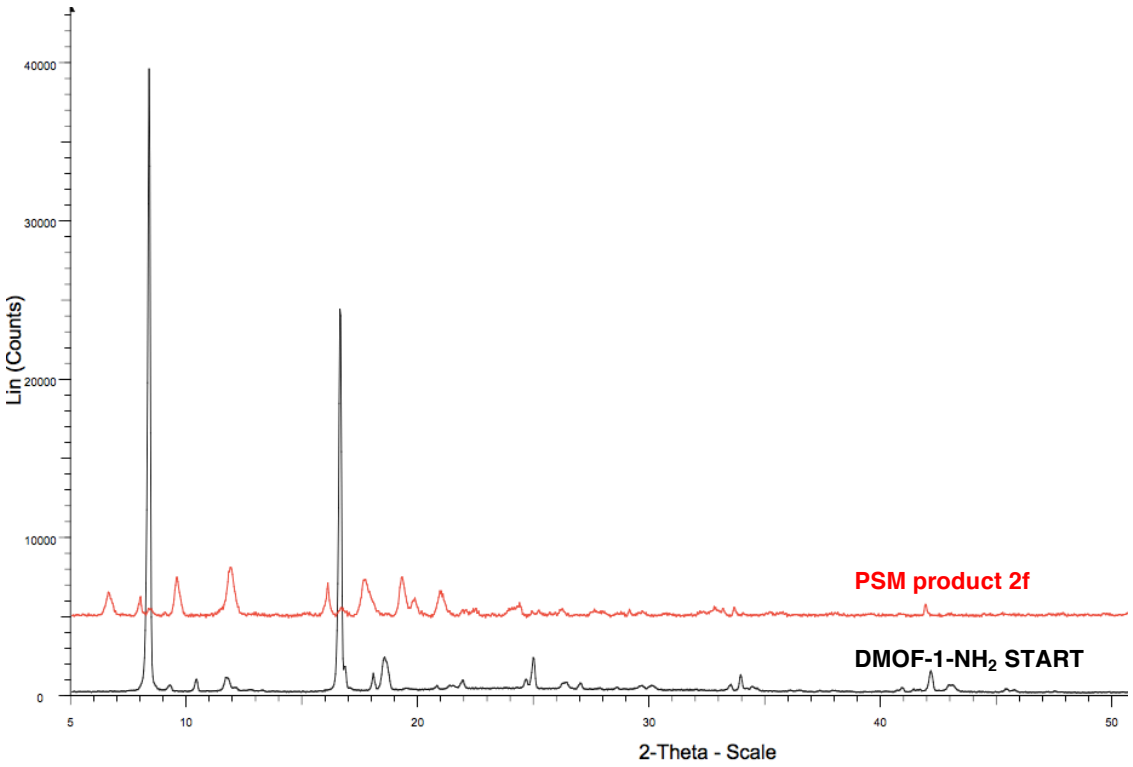

Figure 3.30. Black: PXRD pattern of the starting MOF, DMOF-1-NH_2. Red: PXRD pattern of PSM product **2f**.

The PXRD pattern of **2f** is intriguing, as it does not match with any of the PXRD patterns reported in the literature for DMOF materials. There are two weak signals observed at 2θ = 8.5 and 16.5 which may correspond to the starting MOF, DMOF-1-NH_2, or they may be attributed to an unrelated crystalline product. Nonetheless, the visual inspection of **2f** under an optical microscope reveals the presence of small colourless crystals and the absence of brown block crystals. This observation suggests that the starting MOF, DMOF-1-NH_2, underwent a complete structural change upon PSM.

The crystal structure of **2f** was successfully elucidated *via* single crystal X-ray diffraction, using the ALS synchrotron facility. Relevant details of the experiment and refinement are summarised in Table 3.4.

Empirical formula	$C_{50.72}H_{49.72}N_{8.36}O_{12}Zn_3$
Formula weight / g mol^{-1}	1164.50
Temperature / K	100(2)
Radiation / Å	Synchrotron, Beamline 11.3.1 (λ = 0.7749)
Crystal system	Trigonal
Space group	*R*-3*m*
a / Å	18.1826(7)
b / Å	18.1826(7)
c / Å	13.7312(6)
α / °	90
β / °	90
γ / °	120
Volume / $Å^3$	3931.4(3)
Z	2
Density (calculated) / g cm^{-3}	0.984
Crystal size / mm^3	0.03 × 0.03 × 0.02
Data / restraints / parameters	810 / 31 / 84
Final *R* indices [$I>=2\sigma(I)$]	R_1 = 0.0536, wR_2 = 0.1744
R indices [all data]	R_1 = 0.0613, wR_2 = 0.1811
Largest diff. peak and hole / e $Å^{-3}$	0.76 and -0.44

Table 3.4. Selected crystal data and structure refinement data for framework **2f**.

This compound crystallises in the trigonal space group *R*-3*m*. The asymmetric unit (ASU), Figure 3.31, contains one total quarter of a zinc atom (Zn1 and Zn2 have 8.3333% and 16.6667% occupancy, respectively), one twelfth of a DABCO ligand and a total of one quarter of a BDC ligand. The latter is comprised of 34:56 BDC-NH_2/BDC-$NHCH_2C_3H_3N_2$ based on the ^{1}H NMR analysis of digested **2f**.

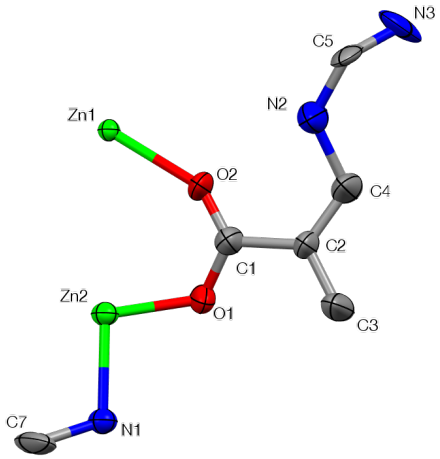

Figure 3.31. The asymmetric unit of **2f**. Ellipsoids are shown at 50% probability. Hydrogen atoms are omitted for clarity.

Atoms O1, O2, C1, C2, C3 and C4 from the dicarboxylate core are coincident with a space group mirror plane and consequently, all have half site-occupancy. The dicarboxylate ligand phenyl carbons (C2, C3 and C4) lie close to a crystallographic inversion centre which serves to generate the remainder of the linker. This means that whether the pendant group is -NH_2 or -$NHCH_2C_3H_3N_2$, it will necessarily be disordered between two positions on the phenyl ring. As N2 is common to both functionalities, it has a site occupancy of 25%. C5 and N3 were the only atoms that could be reliably located in the long pendant group. Disorder coupled with 56% PSM conversion dictate that the site occupancy of C5 and N3 atoms is in the region of 14%. The remaining atoms of the pendant group could not be reliably located owing to smearing of the electron density with increasing distance from the ligand backbone. The DABCO carbon atoms similarly exhibit disorder, which is expected given that this entity does not have 2-fold rotational symmetry along the N···N vector. Thus, C7 was refined with 50% site occupancy.

Attempts to accurately determine the structural void volume *via* the PLATON SQUEEZE algorithm were hampered, due to the PSM tag disorder and the smearing of electron density which was more diffuse with increasing distance from the ligand backbone. TGA

of **2f**, Figure 3.38, indicates a mass loss that corresponds to two toluene molecules for every three zinc centres present. Thus, this provides a formulation of **2f** as $[Zn_3(BDC\text{-}NH_2)_{1.32}(BDC\text{-}NHCH_2N_2C_3H_3)_{1.68}(C_6H_{12}N_2)]\cdot 2C_7H_8$. The extensive disorder coupled with the low level of electron density being modelled in some areas, required inclusion of anisotropic displacement parameter (ADP) restraints to fractional occupancy atoms, in order to assist convergence of the refinement.

Overall, the SBU in **2f** consists of two tetrahedral and one octahedral zinc centres, Figure 3.32. The two tetrahedral zinc atoms (Zn2) are each bonded to a DABCO ligand and three BDC ligands, the latter bridge to the octahedral zinc atom (Zn1).

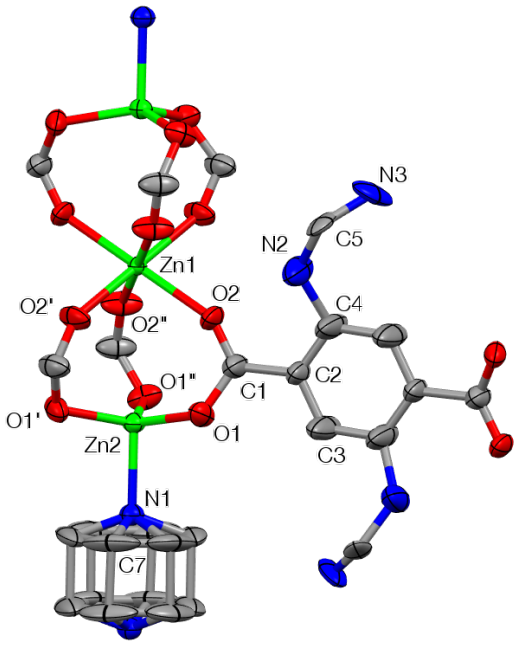

Figure 3.32. A portion of the crystal structure of $[Zn_3(BDC\text{-}NH_2)_{1.32}(BDC\text{-}NHCH_2N_2C_3H_3)_{1.68}(C_6H_{12}N_2)]\cdot 2C_7H_8$, **2f** with unprimed labelled atoms forming the asymmetric unit. All other atoms including those denoted by a primed label are generated by symmetry. O1' and O2' are related, respectively, to the atoms in the asymmetric unit, O1 and O2 by the symmetry operation *–y*, *x–y*, *z*; O1" and O2" are related, respectively, to O1 and O2 by the symmetry operation *–x+y*, *–x*, *z*. Ellipsoids are shown at 50% probability. Hydrogen atoms are omitted for clarity.

The Zn1 metal centre is in a distorted octahedral coordination environment. It is coordinated to six O2 donor atoms from six different BDC ligands. The *cis* O-Zn1-O angles demonstrate the deviations from ideal octahedral coordination for Zn1 with values ranging from 86.64(17)° to 96.36(17)°. The *trans* O-Zn1-O angles are all 180° as these oxygen atoms are symmetrically related by a 3-fold rotary inversion axis. For the same reason, the Zn1-O1 bond lengths are identical at 2.087(4) Å.

Zn2, on the other hand, exhibits a distorted tetrahedral coordination geometry. It is coordinated to three O1 donor atoms from three different BDC ligands. The oxygens are symmetrically related by a threefold rotation axis coincident with the Zn2 metal centre and N1. Therefore, the O-Zn2-O angles are identical at 116.54(12)° and the Zn2-O bond lengths are 1.913(6) Å. The Zn2-N1 distance is 2.054(9) Å and the N1-Zn2-O angles are 100.85(19)°.

The SBUs are pillared by the DABCO ligands along the *c* axis and these pillars are linked in the *ab* plane by the BDC linkers to form a three-dimensional network containing infinite one-dimensional triangular channels, Figure 3.33. The crystallographically located atoms in the derivatised PSM groups protrude into the MOF channels.

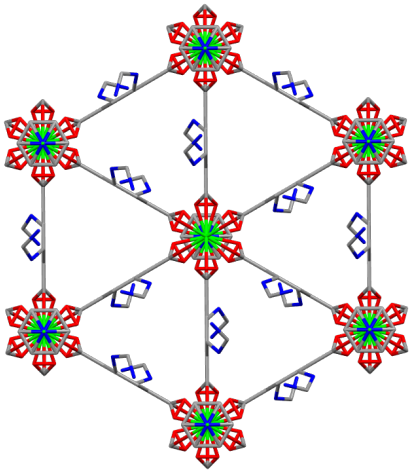

Figure 3.33. View down the crystallographic *c*-axis showing the PSM groups disordered over two sites within the channels of **2f**.

The SBU reported herein (in **2f**) has previously been observed in other MOF systems.[25, 26] For example, a three-dimensional MOF, $[Zn_3(BPDC)_3(BPY)]$, (BPDC = 4,4'-biphenyl dicarboxylate, BPY = 4,4'-bipyridine) prepared by Li and co-workers, contains zinc(II) metal centres which exhibit the same coordination geometry and identical bond distances with that for **2f**.[25]

In order to investigate the cause of the structural transformation from DMOF-1-NH_2 (tetragonal, space group = *I*4/*mcm*) into **2f** (trigonal, space group = *R*-3*m*), a series of control studies were carried out. First, DMOF-1-NH_2 crystals were subjected to the reaction conditions stated in Scheme 3.9, but without the presence of reactants (MeOH, paraformaldehyde and pyrazole). The purpose of performing this experiment was to determine if the solvent (under the reaction conditions shown in Scheme 3.9) caused the

SBU dissolution of the starting MOF, $[Zn_2(BDC\text{-}NH_2)_2(DABCO)]$, DMOF-1-$NH_2$, and subsequently initiated the formation the new framework structure. As shown in Figure 3.34, no structural change was observed after DMOF-1-NH_2 crystals were subjected to the control experiment conditions. Furthermore, the crystals were also shown to maintain their crystallinity when stored in toluene after 7 days at ambient temperature. This result, therefore, eliminates the involvement of toluene solvent in the structural transformation of DMOF-1-NH_2 into **2f**.

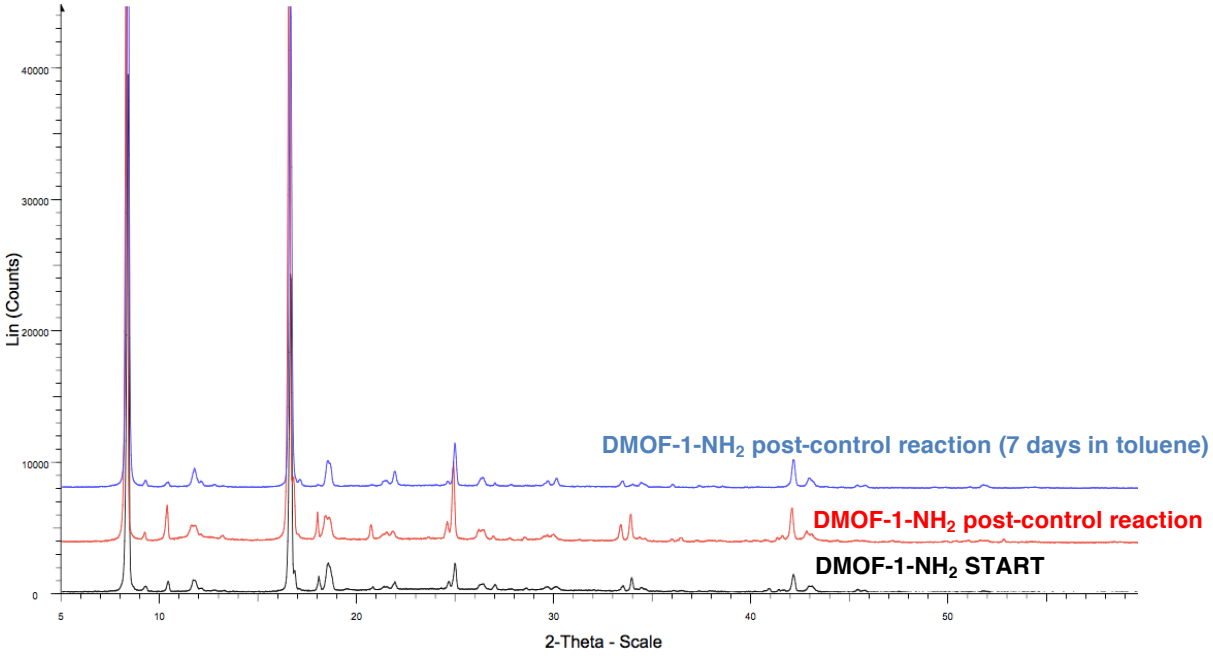

Figure 3.34. Black: PXRD pattern of the starting MOF, DMOF-1-NH_2. Red: PXRD pattern of DMOF-1-NH_2 post-control reaction. Blue: PXRD pattern of DMOF-1-NH_2 post-control reaction (stored in toluene at ambient temperature for 7 days).

A second set of control experiment was also carried out in which DMOF-1-NH_2 crystals were separately treated with paraformaldehyde, MeOH or pyrazole using the conditions shown in Scheme 3.9. The aim of these experiments was to investigate the influence of reactants on the structural change of DMOF-1-NH_2 into **2f**.

Surprisingly, the PXRD patterns of the crystals obtained after the second control experiments were similar to that for the starting MOF, DMOF-1-NH_2, Figure 3.35. This result suggests that as with the toluene solvent, the reactants also did not cause the dissolution of DMOF-1-NH_2.

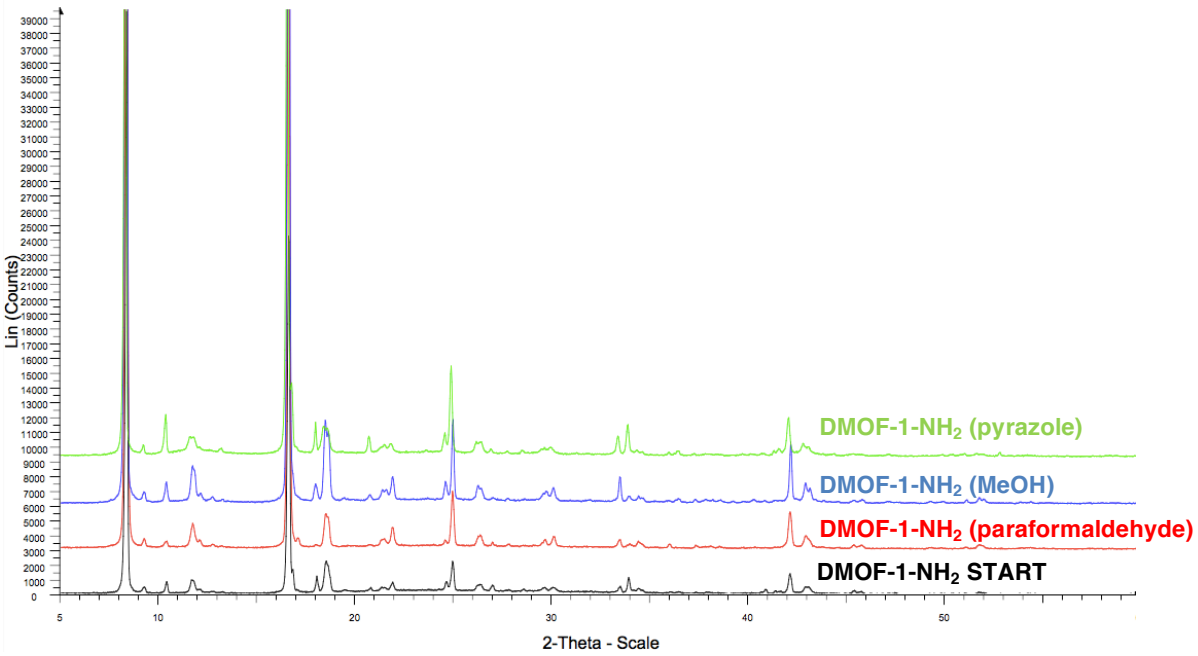

Figure 3.35. Black: PXRD pattern of the starting MOF, DMOF-1-NH_2. Red: PXRD pattern of DMOF-1-NH_2 upon reaction with paraformaldehyde. Blue: PXRD pattern of DMOF-1-NH_2 upon reaction with MeOH. Green: PXRD pattern of DMOF-1-NH_2 upon reaction with pyrazole.

Based on the results obtained thus far, it was concluded that the DMOF-1-NH_2 crystals were stable towards the solvent, reactants and the reaction conditions used in the PSM reaction. However, the methoxymethyl hemiaminal group, which was the intermediate species of this PSM reaction (Scheme 3.9), is known to have a low stability and to be prone to hydrolysis, particularly in the presence of metal ions.[27, 28] On the basis of this, it was suspected that the structural transformation may have occurred in the second step of the PSM reaction.

In an attempt to confirm this hypothesis, the second step of the PSM reaction (Scheme 3.9) was monitored under an optical microscope equipped with a camera. The reaction was modified slightly in order to be able to view the reaction under a microscope. DMOF-1-NH-CH_2OCH_3, the intermediate MOF bearing the methoxymethyl hemiaminal groups, was first prepared according to the conditions shown in Scheme 3.9. The DMOF-1-NH-CH_2OCH_3 crystals were then washed with fresh toluene, and the solvent was removed by decantation. This washing procedure was repeated three times. In a separate vial, a solution of pyrazole in toluene was prepared and transferred onto a microscopic slide. The DMOF-1-NH-CH_2OCH_3 crystals were then dispersed on the microscopic slide containing the pyrazole solution and the crystals were monitored using a microscope equipped with a camera. After approximately five minutes, the gradual dissolution of the

crystals was observed, Figure 3.36. The complete dissolution of the DMOF-1-NH-CH_2OCH_3 crystals was reached after 40 minutes. A new phase, which corresponds to the crystals of **2f**, was first observed after approximately twenty minutes (shown in red circle).

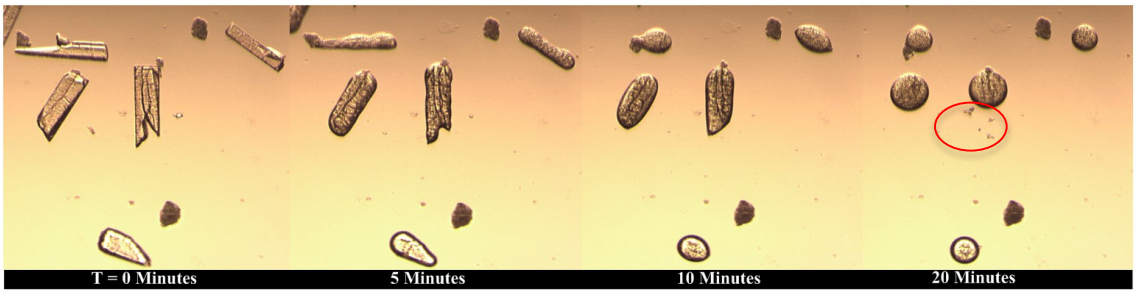

Figure 3.36. Four frames at T = 0, 5, 10 and 20 minutes of the dissolution of DMOF-1-NH-CH_2OCH_3 crystals in the presence of a solution of pyrazole in toluene. Small crystals of **2f** can be seen starting to form near the centre of the final frame (T = 20 minutes).

This result confirms the initial hypothesis that the structural transformation occurred in the second step of the PSM reaction. Furthermore, due to the fact that the structural transformation was successfully monitored under an optical microscope, this shows that the second step of the Mannich reaction (Scheme 3.9) could actually be carried out at ambient temperature instead of at 80 °C.

At present, the definitive mechanism for the dissociation of the SBUs in DMOF-1-NH-CH_2OCH_3 is unclear, although it is certain that pyrazole has a role in this process. However, one proposed reaction mechanism which leads to the dissociation of the SBUs in DMOF-1-NH-CH_2OCH_3 is shown in Figure 3.37.

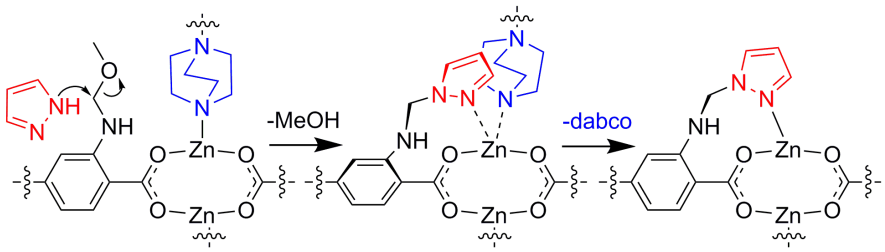

Figure 3.37. Proposed mechanism of the dissociation of the SBUs in DMOF-1-NH-CH_2OCH_3.

The amino groups within DMOF-1-NH_2 are well-positioned to undergo hydrogen bonding interactions with the adjacent carboxylate groups of the BDC-NH_2 ligand. Upon the first step of the Mannich reaction, the methoxymethyl hemiaminal species is localised in close proximity to the bridging DABCO ligands. Upon addition of pyrazole, a facile

reaction displacing methanol can occur to yield the α-amino pyrazole group. This α-amino pyrazole group is perfectly aligned to compete in an intramolecular fashion with DABCO for coordination to the Zn(II) metal centre. Displacement of DABCO breaks the three-dimensional network of DMOF-1 framework, leading to rapid delamination of the remaining two-dimensional layered structure, and ultimately triggering framework dissolution.

The TGA profile of PSM product **2f** (red) is broadly similar to that for the starting MOF, DMOF-1-NH_2 (black), despite the difference in framework structure, Figure 3.38.

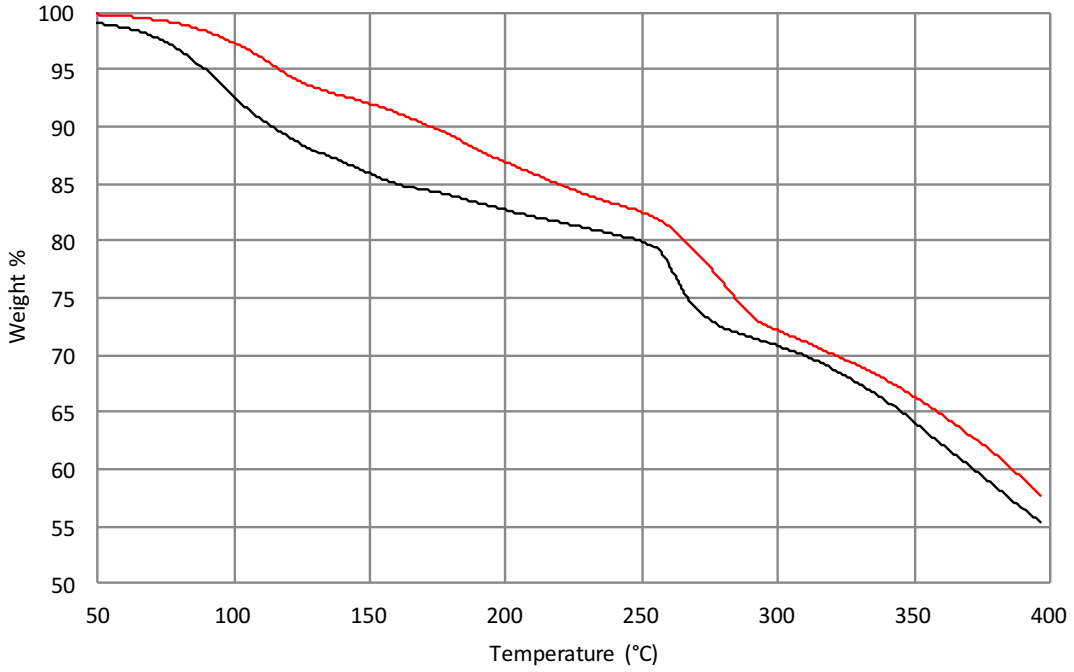

Figure 3.38. TGA of DMOF-1-NH_2 (black) and PSM products **2f** (red). The samples were heated from 30 °C to 600 °C at a rate of 20 K/min under a flow of argon gas (20 mL/min).

The initial mass loss (up to 270 °C) is attributed to the toluene molecules that are in the pores. Per Zn_2 unit, DMOF-1-NH_2 has 1.6 toluene molecules whereas for **2f**, there are 2.0 toluene molecules per Zn_3 unit. Despite the similarities in the TGA profiles, **2f** exhibits a slightly higher framework decomposition temperature (~270 °C) than that for DMOF-1-NH_2 (~260 °C).

3.3.2. Imidazole as the Nucleophile

The Mannich reaction of DMOF-1-NH_2 with imidazole as the nucleophile was performed to investigate if similar observation (framework dissolution) could be seen when a different azole is used in the PSM reaction. The reaction was carried out using the conditions shown in Scheme 3.10.

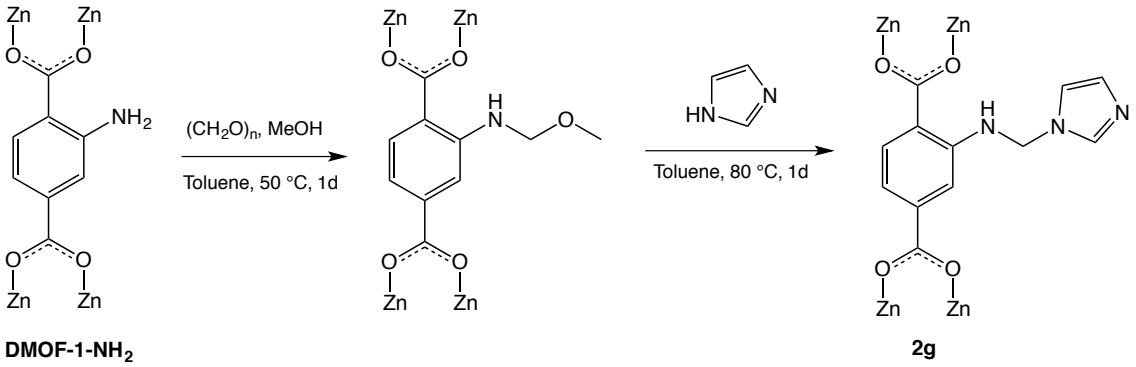

Scheme 3.10. The Mannich reaction of DMOF-1-NH_2 using imidazole as the nucleophile.

The ^{1}H NMR spectrum of the digested PSM product **2g** shows a number of new peaks in addition to the peaks which correspond to the aromatic protons of the starting MOF, DMOF-1-NH_2 (H_a = 7.91 ppm, H_b = 7.28 ppm and H_c = 7.47 ppm), Figure 3.39.

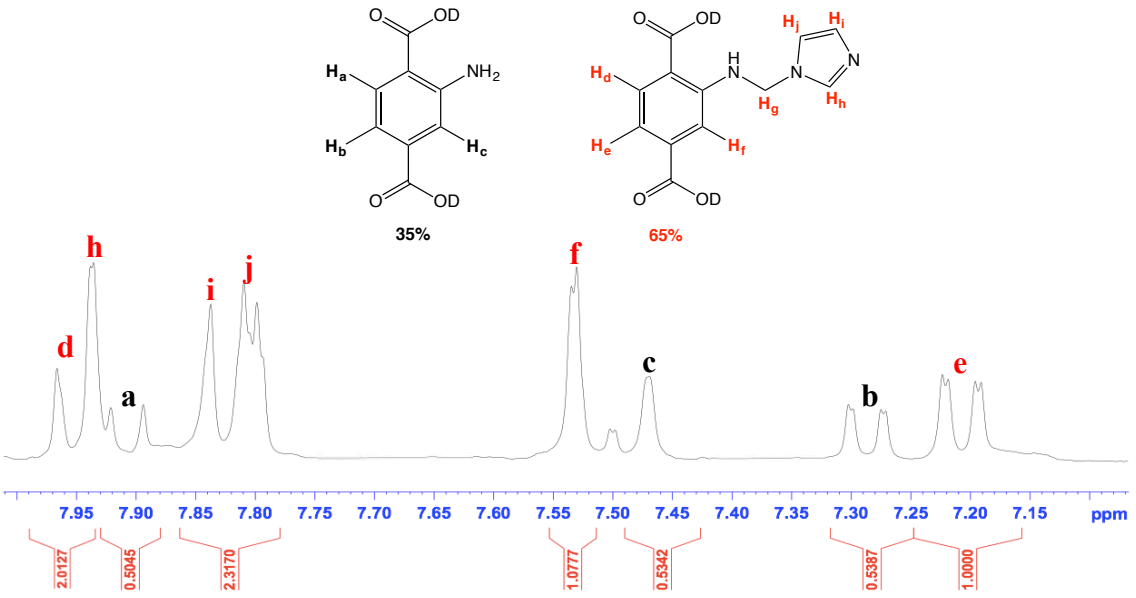

Figure 3.39. Aromatic region of ^{1}H NMR spectrum of digested PSM product **2g.**

The aromatic protons of D_2BDC-$NHCH_2C_3H_3N_2$ are observed at δ 7.95, 7.21 and 7.54 ppm which correspond to H_d, H_e and H_f, respectively. The presence of the imidazole ring on the digested framework of **2g** was confirmed by the peaks at δ 7.94 ppm, 7.84 ppm and δ 7.81 ppm which are attributed to the protons of the imidazole ring, H_h, H_i and H_j, respectively. The peak attributed to the α-CH_2 protons of D_2BDC-$NHCH_2C_3H_3N_2$, H_g, could not be located most likely due to being obscured by the dominant HDO peak used in the digestion. Comparing the integrals of the protons at δ 7.28 ppm and δ 7.21 ppm, the percentage conversion of amino into α-amino imidazole ($–NHCH_2C_3H_3N_2$) groups was calculated to be approximately 65%. The calculated conversion gives the formula for **2g** as $[Zn_2(BDC\text{-}NH_2)_{0.7}(BDC\text{-}NHCH_2C_3H_3N_2)_{1.3}(DABCO)]$.

The negative ESI mass spectrum of the digested product **2g** confirms the presence of the deprotonated anion of H_2BDC-$NHCH_2C_3H_3N_2$ and H_2BDC-NH_2 at m/z = 260.0661 (predicted $[M\text{-}H]^-$ = 260.0677) and m/z = 180.0339 (predicted $[M\text{-}H]^-$ = 180.0375), respectively.

The disappearance of $–NH_2$ stretching bands (3287 and 3457 cm^{-1}) of DMOF-NH_2 in the FTIR spectrum of **2g**, Figure 3.40, indicates the successful conversion of primary amine ($–NH_2$) into secondary amine ($–NHCH_2C_3H_3N_2$). Similar to that for **2b** (Section 3.1.2), the presence of imidazole ring on the modified framework could not be inferred *via* FTIR spectroscopy due to the presence of framework's backbone peaks which dominate the 600 – 1700 cm^{-1} region.

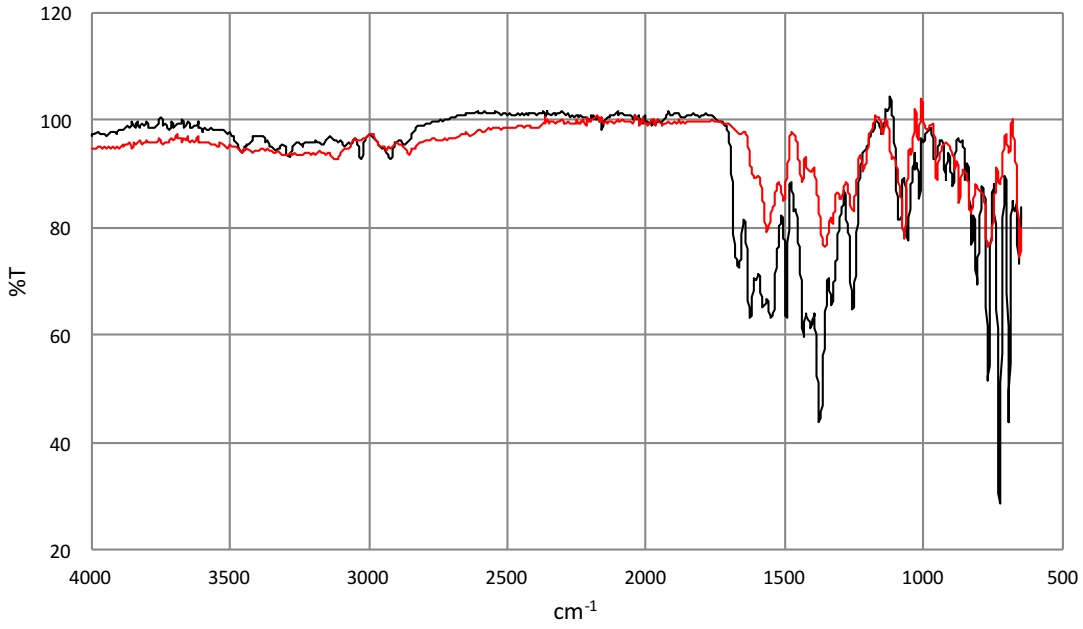

Figure 3.40. Black: FTIR spectrum of DMOF-1-NH_2. Red: FTIR spectrum of $[Zn_2(BDC\text{-}NH_2)_{0.7}(BDC\text{-}NHCH_2C_3H_3N_2)_{1.3}(DABCO)]$, **2g**.

The PXRD pattern of **2g** and the starting MOF, DMOF-1-NH_2 closely match one another, thus it is concluded that the framework was retained throughout the PSM reaction, Figure 3.41.

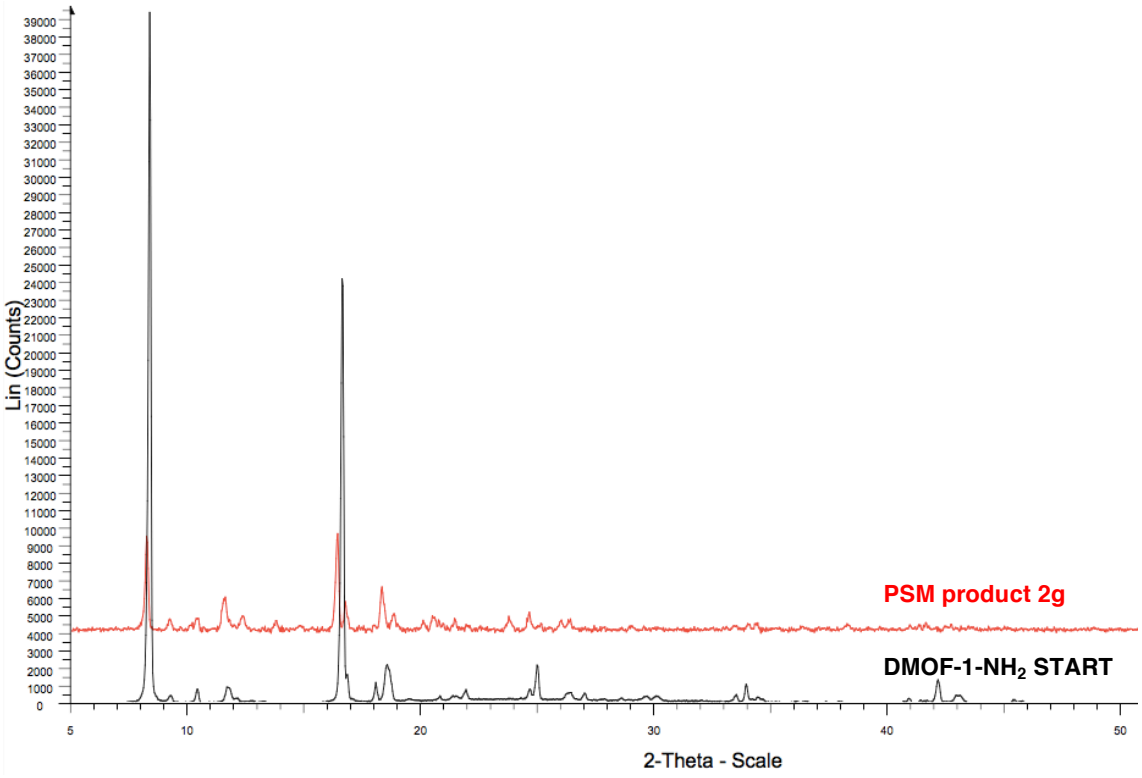

Figure 3.41. Black: PXRD pattern of the starting MOF, DMOF-1-NH_2. Red: PXRD pattern of PSM product **2g**.

Furthermore, visual inspection of **2g** confirmed the presence of only brown-block crystals and the absence of new phases. Attempts to analyse **2g** crystallographically were hampered, due to the level of crystal twinning. Nonetheless, a screening experiment suggested that there were similarities in the unit cell parameters of **2g** to those of the parent MOF, DMOF-1. The unit cell parameters for **2g** are a = 15.2955(17) Å, b = 15.2860(15) Å, c = 19.207(2) Å and the unit cell parameters for DMOF-1 are a = 15.063(2) Å, c = 19.247(5) Å.[24]

Based on the results obtained thus far, it is clear that framework dissolution did not occur whilst imidazole was used as a nucleophile. It is thought that substituting pyrazole by imidazole prevents the dissolution of the intermediate MOF, DMOF-1-NH-CH_2OCH_3, by eliminating the possibility of coordinative competition with DABCO. This is due to the positioning of the 'free' nitrogen atom in imidazole which is beyond the coordinative sphere of the Zn^{2+} ion.

Figure 3.42. illustrates the TGA profiles of PSM product **2g** (red) with the starting MOF, DMOF-1-NH_2 (black). The initial mass loss (up to 260 °C) corresponds to the toluene molecules that are in the pores. Per Zn_2 unit, DMOF-1-NH_2 has 1.6 and **2g** has 2.2 toluene molecules. The framework decomposition of **2g** starts at ~240 °C, which is approximately 20 °C lower than that for DMOF-1-NH_2.

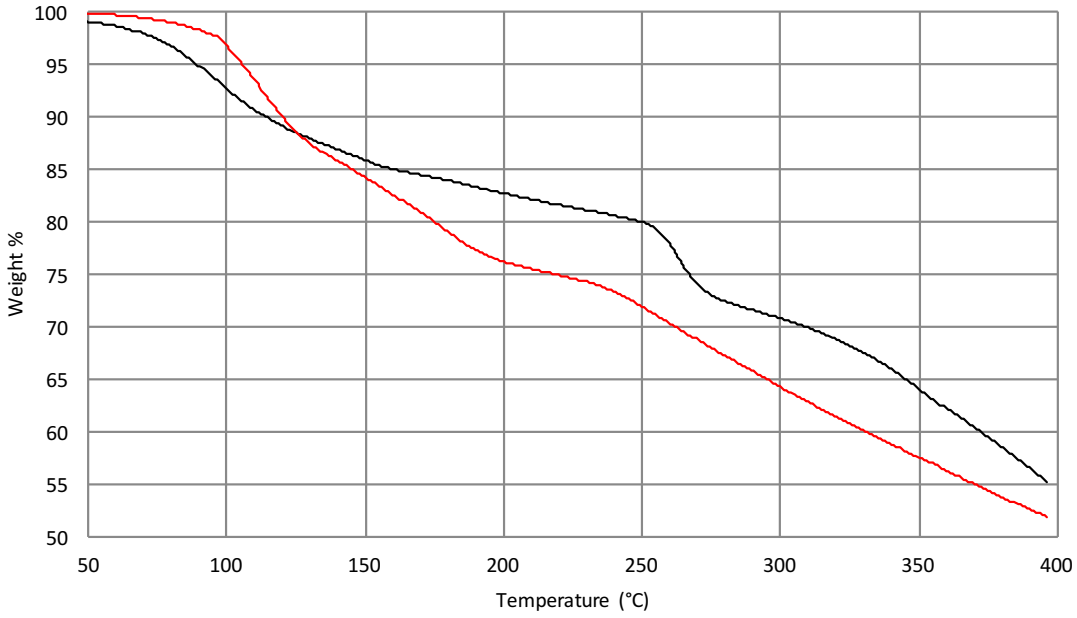

Figure 3.42. TGA of DMOF-1-NH_2 (black) and PSM products **2g** (red). The samples were heated from 30 °C to 600 °C at a rate of 20 K/min under a flow of argon gas (20 mL/min).

3.3.3. 2-Mercaptoimidazole as the Nucleophile

The Mannich reaction of DMOF-1-NH_2 with 2-mercaptoimidazole as the nucleophile was performed using the conditions shown in Scheme 3.11.

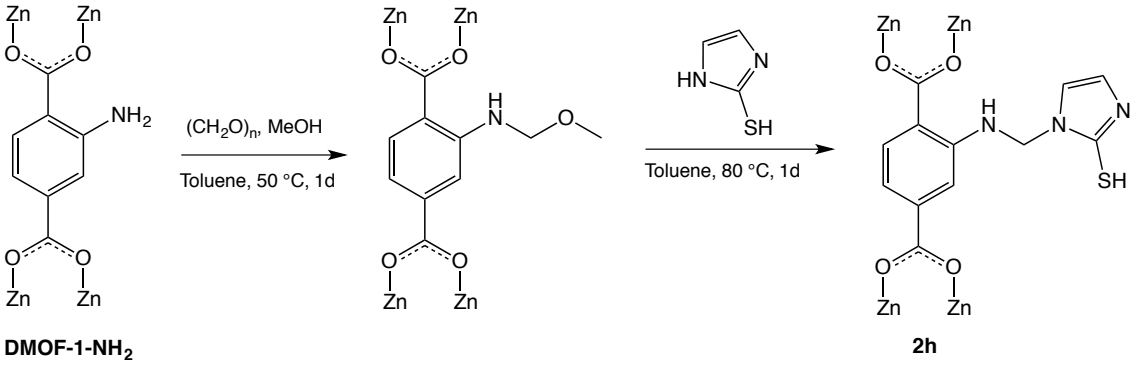

Scheme 3.11. The Mannich reaction of DMOF-1-NH_2 using 2-mercaptoimidazole as the nucleophile.

The ^{1}H NMR spectrum of the digested PSM product **2h**, Figure 3.43, shows only the peaks which correspond to the aryl protons of the starting MOF, DMOF-1-NH_2. This result indicates that the inclusion of 2-mercaptoimidazole on the MOF framework was unsuccessful with no evidence for the formation of DMOF-1-$NHCH_2CH_2N_2SH$.

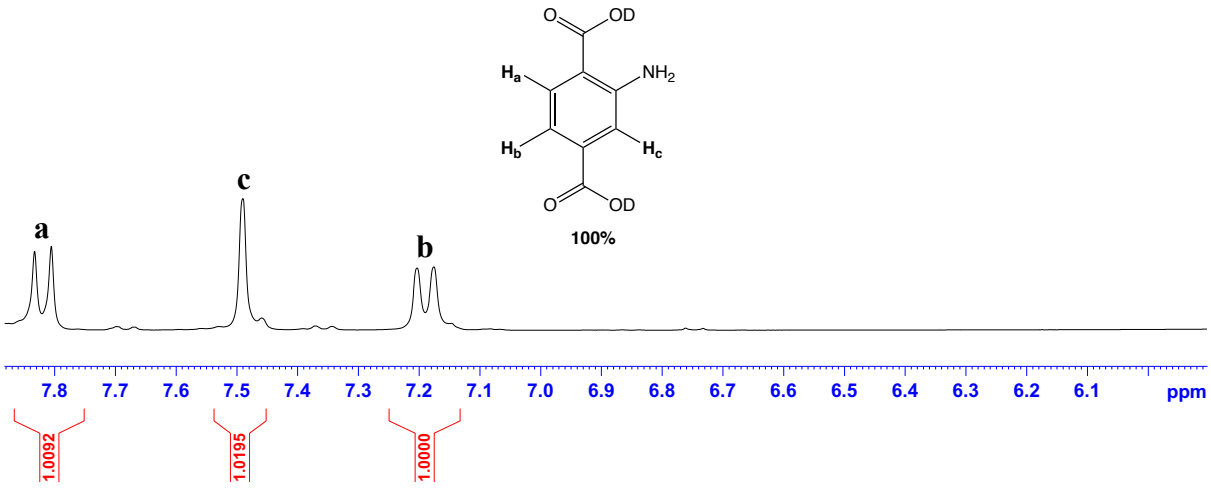

Figure 3.43. ^{1}H NMR spectrum of PSM product **2h** digested in DCl/D_2O and DMSO-d_6.

Nonetheless, the PXRD pattern of **2h** is similar to that for the starting MOF, DMOF-1-NH_2, implying that the framework was retained throughout the experiment and was not affected by the reaction conditions used in this study, Figure 3.44.

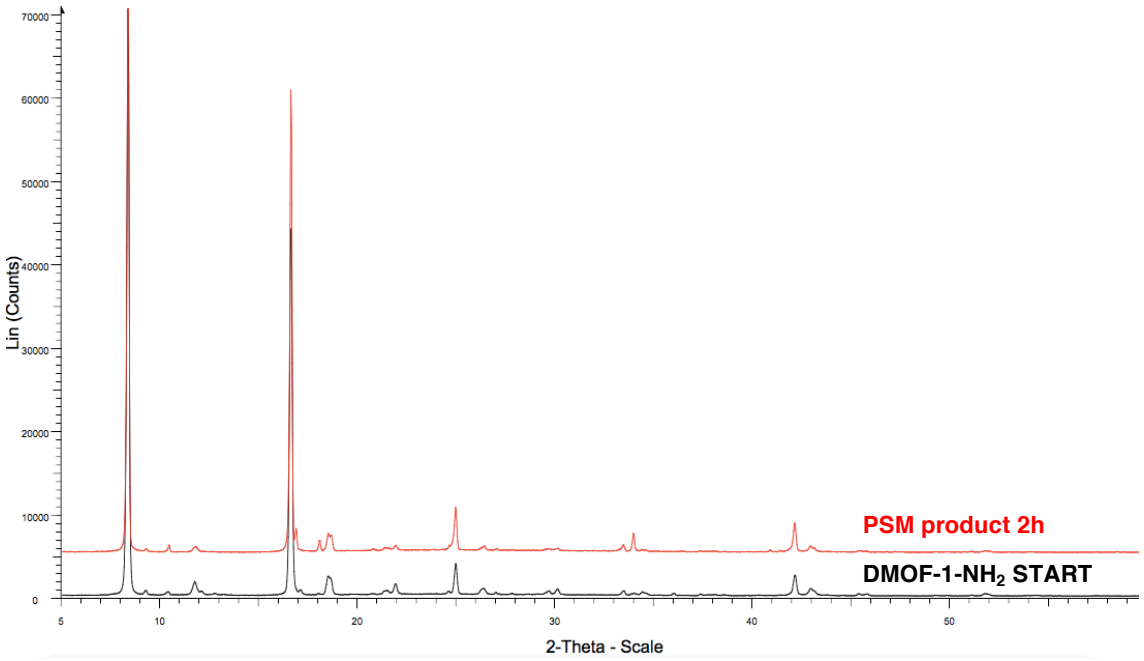

Figure 3.44. Black: PXRD pattern of the starting MOF, DMOF-1-NH_2. Red: PXRD pattern of PSM product **2h**.

The unsuccessful grafting of 2-mercaptoimidazole on the MOF framework was thought to be due to the size of 2-mercaptoimidazole, which is too big to pass through the pore window (2-mercaptoimidazole: 8.4 Å x 6.6 Å. DMOF-1-NH_2 channels: 5.3 Å x 4.8 Å).

3.4. The Mannich Reaction on [In(OH)(BDC-NH_2)], MIL-68(In)-NH_2

3.4.1. Pyrazole as the Nucleophile

[In(OH)(BDC-NH_2)], MIL-68(In)-NH_2, is a three-dimensional MOF with a Kagome-like structure. It is constructed from chains of $InO_4(OH)_2$ octahedral units, Figure 3.45(a), linked together by BDC-NH_2 ligands to form triangular (~6 Å) and hexagonal (~16 Å) one-dimensional channels, Figure 3.45(b).[29-31] One distinct feature of MIL-68(In)-NH_2 is, instead of protruding into the pores, the amino groups are in alignment with the $InO_4(OH)_2$ octahedral chains, Figure 3.45(b).

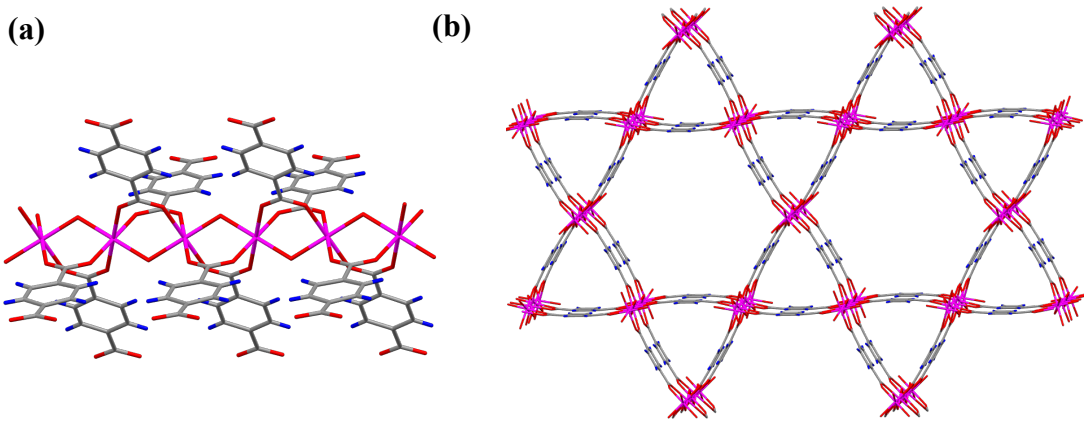

Figure 3.45. (a) View of a chain of $InO_4(OH)_2$ octahedra in MIL-68(In)-NH_2. The octahedral units are trans-connected through the hydroxyl groups to form infinite chains running along the *c* axis. Adjacent octahedra are linked to each other via the BDC-NH_2 ligands. **(b)** View of the structure of MIL-68(In)-NH_2 along the *c* axis, showing the hexagonal and triangular channels. The amino groups are in alignment with the $InO_4(OH)_2$ octahedral chains. The amino groups are disordered over four sites of the linker. In: magenta, C: grey, O: red, N: blue.[29]

MIL-68(In)-NH_2 was chosen as one of the candidates for the Mannich reaction due to several reasons. First, the reaction was performed on this MOF to investigate the accessibility of the amino groups towards the reactants used in this study. Furthermore, the precedence for successful PSM reactions on this MOF offered an insight that the Mannich reaction on this MOF may be possible.[30, 32-34] For example, Farrusseng *et al.* developed a one-pot, two-step functionalisation method of MIL-68(In)-NH_2 *via* a click reaction, Scheme 3.12. The first step involved treating MIL-68(In)-NH_2 with *tert*-butyl nitrite and trimethylsilyl azide to convert the amino groups into azides. The azides were subsequently reacted with phenylacetylene in the second step.[34]

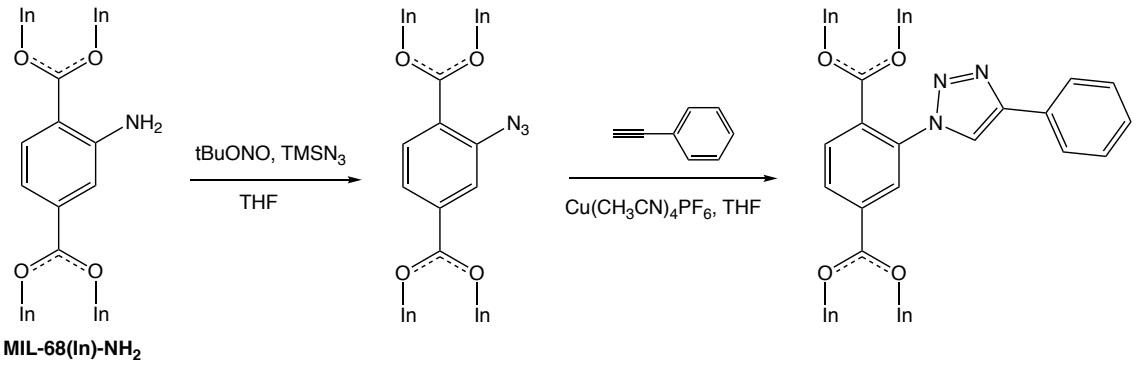

Scheme 3.12. An example of a PSM reaction on MIL-68(In)-NH_2 involving click reaction.[34]

MIL-68(In)-NH_2 is also relatively robust (stable towards moisture, alcohols and acids) and easy to synthesise. Due to these factors, MIL-68(In)-NH_2 was selected for the Mannich reaction, on the basis of the reaction scheme shown in Scheme 3.13.

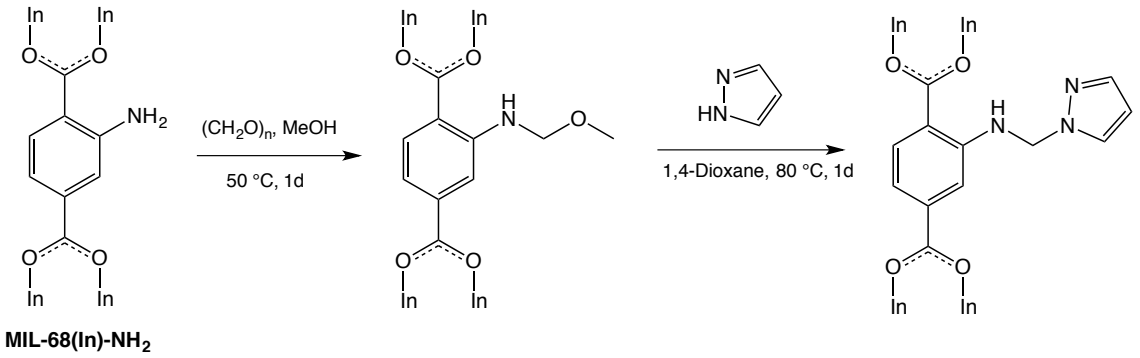

Scheme 3.13. The Mannich reaction of MIL-68(In)-NH_2 using pyrazole as the nucleophile.

MIL-68(In)-NH_2 was prepared using an analogous synthesis to that for MIL-68(In), originally reported by Loiseau and co-workers.[29] Prior to PSM reactions, MIL-68(In)-NH_2 crystals were soaked in MeOH for 3 days, replacing the solvent with fresh solvent every 24 hours before collecting the crystals by filtration. In a typical PSM procedure, MIL-68(In)-NH_2 crystals were treated with paraformaldehyde and MeOH at 50 °C for 1 day. In this reaction, MeOH was used as a reactant as well as a solvent, as MIL-68(In) is known to exhibit a high stability towards MeOH, thus eliminating the need to use a different solvent. The intermediate product was then washed three times with 1,4-dioxane to remove any residual paraformaldehyde and MeOH in the pores or on the solid surface. The crystals were subsequently treated with pyrazole at 80 °C for 1 day, before quenching the reaction by washing the sample with fresh 1,4-dioxane for 3 days, replacing the solvent with fresh solvent every 24 hours before collecting the crystals by filtration. The detailed experimental procedure can be found in Section 3.9.12.

The ^{1}H NMR spectrum of the digested PSM product **2i**, Figure 3.46, was obtained by digesting the MOF in a basic aqueous solution (NaOD/D_2O).

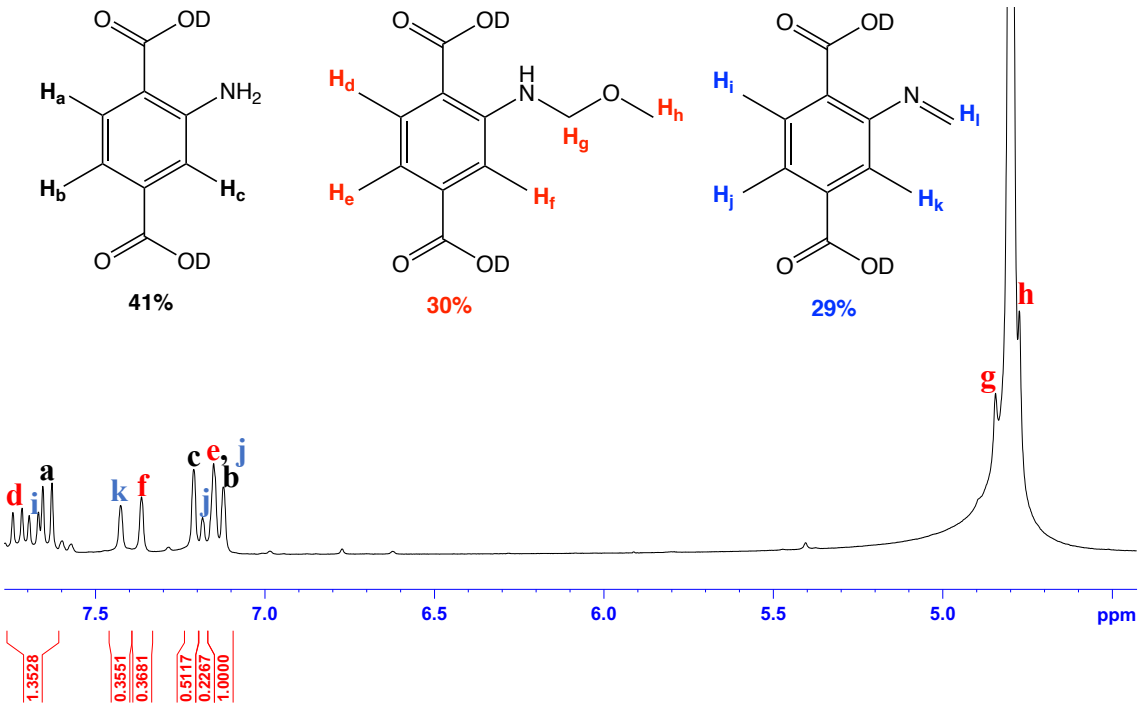

Figure 3.46. ^{1}H NMR spectrum of PSM product **2i** digested in NaOD/D_2O.

In addition to the peaks which correspond to the aromatic protons of the starting MOF, D_2BDC-NH_2 (H_a = 7.64 ppm, H_b = 7.13 ppm and H_c = 7.22 ppm), new sets of signals (H_d = 7.73 ppm, H_e = 7.15 ppm, H_f = 7.36 ppm, H_i = 7.68 ppm, H_j = 7.18 ppm and H_k = 7.43 ppm) were observed in the downfield region of the spectrum. However, the absence of peaks attributed to the protons of the pyrazole ring indicates that the PSM reaction did not afford the expected pyrazole-containing product. It is suspected that the peaks at H_d = 7.73 ppm, H_e = 7.15 ppm and H_f = 7.36 ppm may correspond to the aryl protons from the intermediate MOF, MIL-68(In)-$NHCH_2OCH_3$ (observed as D_2BDC-$NHCH_2OCH_3$ in the NMR spectrum). The peak attributed to the α-CH_2 protons, H_g and methyl terminus, H_h of D_2BDC-$NHCH_2OCH_3$ can be located at δ 4.87 ppm and δ 4.76 ppm, respectively, although these peaks are partly obscured by the peak from the HDO digestion solvent.

In addition to D_2BDC-NH_2 and D_2BDC-$NHCH_2OCH_3$, there are signals which are thought to correspond to an imine species, D_2BDC-N=CH_2. There are two ways of rationalising the formation of D_2BDC-N=CH_2. First, the imine species are formed *in situ*, upon the reaction of –NH_2 with paraformaldehyde, and subsequent elimination of water molecules, Scheme 3.14.

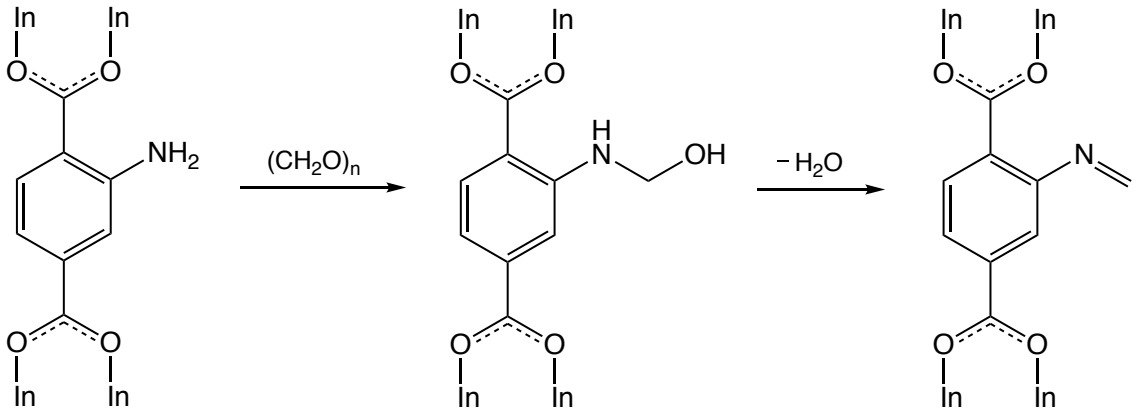

Scheme 3.14. General reaction scheme for the imine formation.

In order to confirm the initial hypothesis that the PSM product consists of unreacted –NH_2 groups, imine species –$N{=}CH_2$ and the methoxyhemiaminal species –$NHCH_2OCH_3$, a control reaction was carried out. The control reaction involved performing only the first step of the PSM reaction, Scheme 3.15, and subjecting the PSM product to ^{1}H NMR spectroscopy.

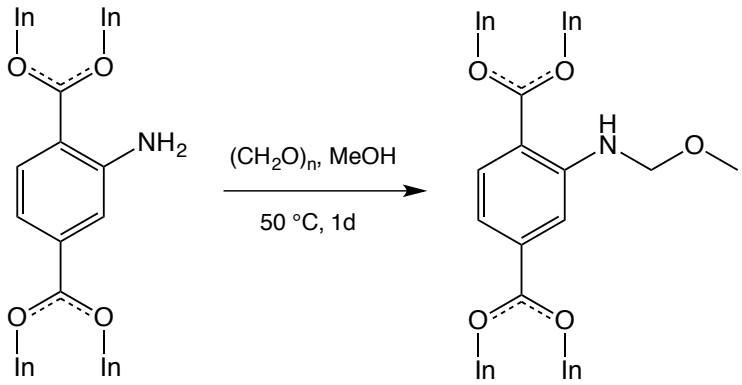

Scheme 3.15. The schematic representation of the first step of the Mannich reaction.

As anticipated, the spectrum of the digested PSM product, Figure 3.47, illustrates a high similarity with that for **2i**, Figure 3.46.

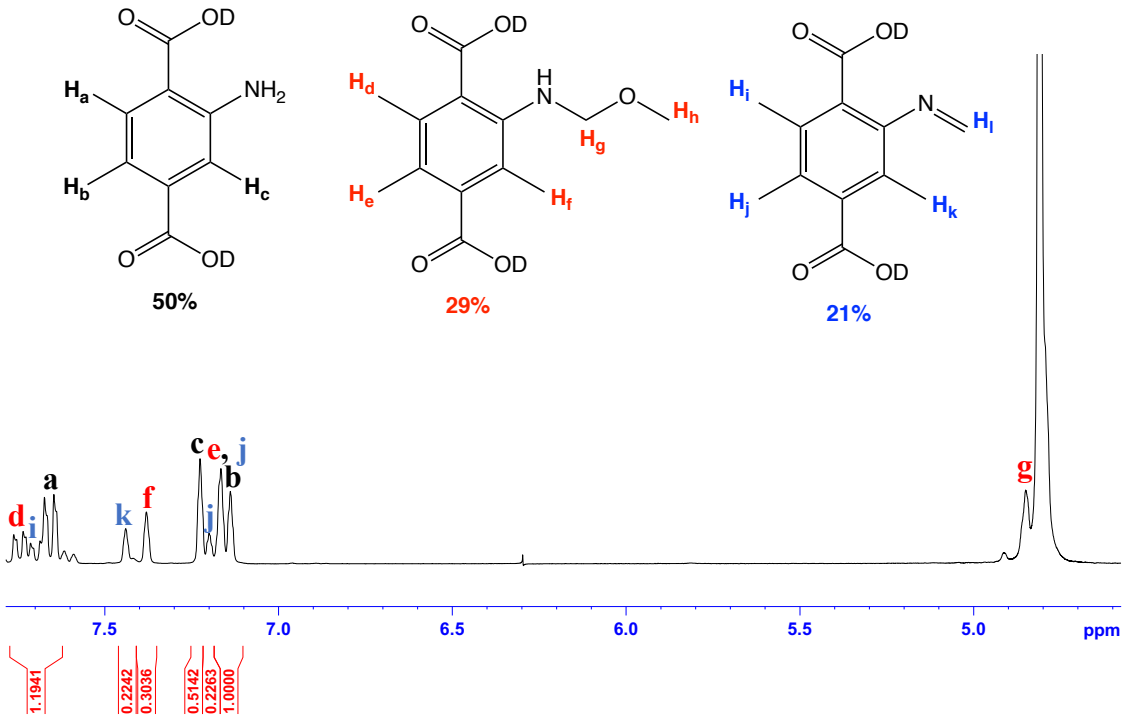

Figure 3.47. ^{1}H NMR spectrum of the digested PSM product isolated upon the first step of the Mannich reaction.

This finding validates the initial hypothesis that **2i** contains unreacted –NH_2 groups, imine species –N=CH_2 and methoxyhemiaminal species –$NHCH_2OCH_3$. It is notable that the detection of D_2BDC-$NHCH_2OCH_3$ and D_2BDC-N=CH_2 in the ^{1}H NMR spectrum of **2i** is rather unexpected, as it was anticipated that both groups would undergo hydrolysis in the digestion solution.

In terms of PSM conversion, it may be possible that the incomplete conversion of D_2BDC-N=CH_2 into D_2BDC-$NHCH_2OCH_3$ was due to pore blocking effect. As described at the beginning of this section, the amino groups in MIL-68(In)-NH_2 are aligned with the $InO_4(OH)_2$ octahedral chains (instead of protruding into the pores), and this may restrict the space available for the –$NHCH_2OCH_3$ groups.

The second possible explanation for the formation of D_2BDC-N=CH_2 is that this species is formed as a consequence of the hydrolysis of D_2BDC-$NHCH_2OCH_3$ in the digestion media. If this is indeed the case, the determination of percentage conversion would be ambiguous, as the peaks which correspond to the aryl protons of D_2BDC-NH_2 may actually originate from the product of the hydrolysis of D_2BDC-$NHCH_2OCH_3$ rather than unreacted D_2BDC-NH_2 (or mixture of both).

However, if one were to assume that D_2BDC-$NHCH_2OCH_3$ is stable towards the digestion media (hydrolysis of D_2BDC-$NHCH_2OCH_3$ did not occur), and the D_2BDC-NH_2 peaks were assumed to originate solely from unreacted $–NH_2$ groups, the percentage conversion of the $–NH_2$ group into $–NHCH_2OCH_3$ could be calculated as being approximately 59% (based on Figure 3.46). The calculated conversion therefore gives the formula for **2i** as $[In(OH)(BDC\text{-}NH_2)_{0.41}(BDC\text{-}NHCH_2OCH_3)_{0.59}]$.

As evidenced by the ^1H NMR analysis of the digested PSM product **2i**, the Mannich reaction of MIL-68(In)-NH_2 with pyrazole only afforded the intermediate product, MIL-68(In)-$NHCH_2OCH_3$. As mentioned previously, the location of the amino groups (and subsequently $–NHCH_2OCH_3$ groups) is not readily accessible to the pyrazole molecules. Furthermore, pore blocking by the $–NHCH_2OCH_3$ groups may also cause the unsuccessful inclusion of pyrazole ring on the MOF framework.

The negative ESI mass spectrum of the digested product **2i** confirms the presence of the deprotonated anion of H_2BDC-$NHCH_2OCH_3$ ($[M\text{-}H]^-$ = 224.0560), H_2BDC-$N{=}CH_2$ ($[M\text{-}H]^-$ = 192.0310) and H_2BDC-NH_2 ($[M\text{-}H]^-$ = 180.0315), Figure 3.48.

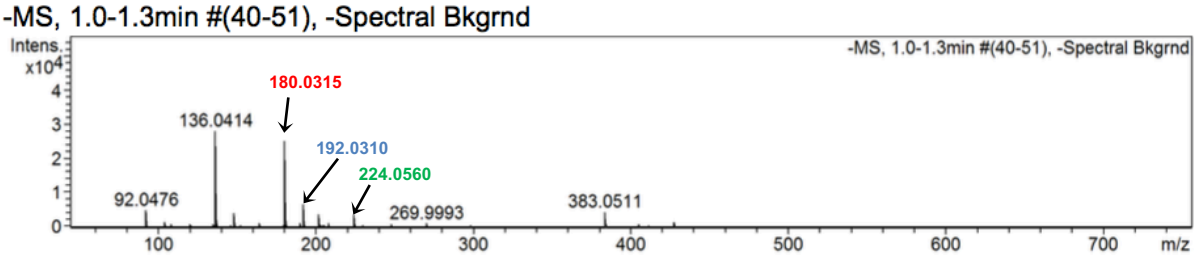

#	m/z	I	I %	Area	S/N
1	92.0476	4773	17.1	106	691.3
2	136.0414	27868	100.0	791	4233.0
3	137.0453	2390	8.6	61	365.5
4	148.0413	4122	14.8	117	695.9
5	180.0315	25055	89.9	815	5793.8
6	181.0359	2451	8.8	75	572.7
7	192.0310	6401	23.0	218	1691.7
8	202.0127	3787	13.6	133	1135.6
9	224.0560	3583	12.9	155	1407.9
10	383.0511	4433	15.9	298	1677.7

Figure 3.48. The negative ESI mass spectrum of digested PSM product **2i** showing the presence of the deprotonated anion of H_2BDC-$NHCH_2OCH_3$ (green), H_2BDC-$N{=}CH_2$ (blue), and H_2BDC-NH_2 (red).

The FTIR spectrum of **2i** (red) is somewhat similar to that for the starting MOF, MIL-68(In)-NH_2 (black), Figure 3.49. However, the presence of $–NHCH_2OCH_3$ groups in **2i** may be confirmed by the presence of ether C-O stretch (1117 cm^{-1}) (blue circle).

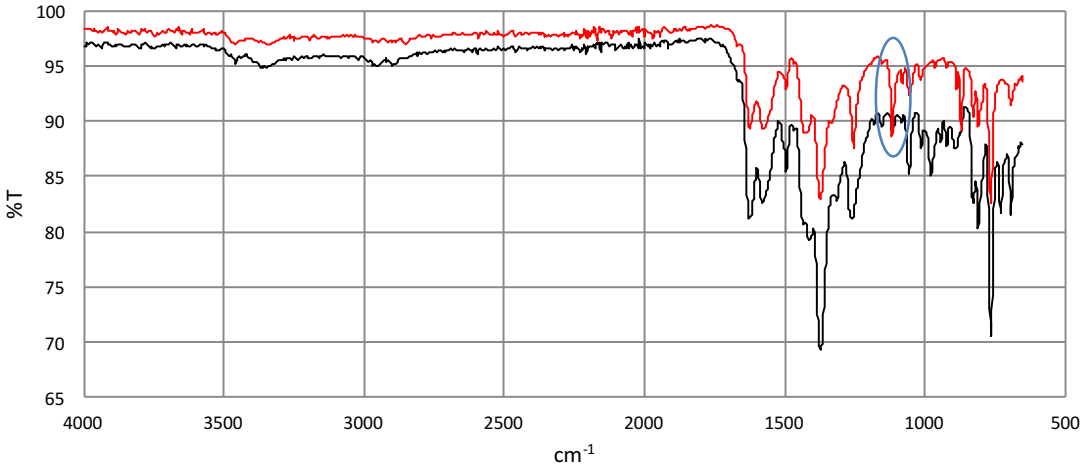

Figure 3.49. The FTIR spectrum for $[In(OH)(BDC\text{-}NH_2)_{0.41}(BDC\text{-}NHCH_2OCH_3)_{0.59}]$, **2i**.

The structural integrity of MIL-68(In)-NH_2 framework upon Mannich reaction was examined by powder X-ray diffraction (PXRD). As shown in Figure 3.50, the PXRD pattern of PSM product **2i** is similar to the starting MOF, MIL-68(In)-NH_2, which indicates that the framework integrity was maintained and the PSM reaction did not alter the crystallinity of the PSM product.

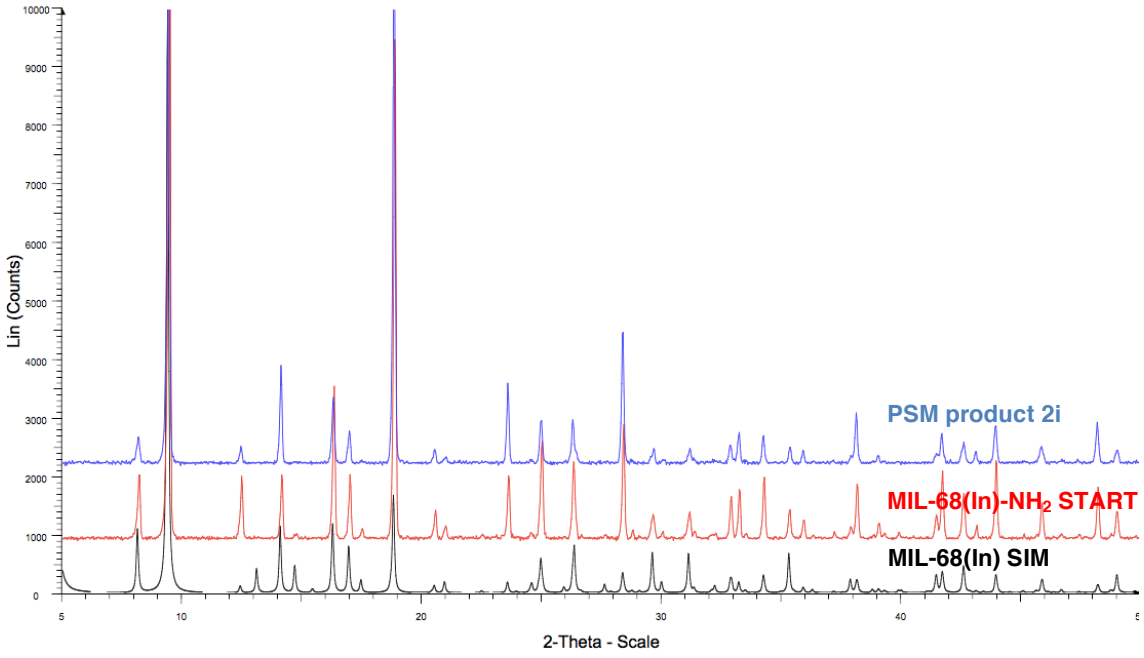

Figure 3.50. Black: Simulated PXRD pattern calculated from the MIL-68(In) crystal structure.[29] Red: PXRD pattern of starting MOF, MIL-68(In)-NH_2. Blue: PXRD pattern of PSM product, **2i**.

The crystal structure of **2i** was successfully elucidated by single crystal X-ray diffraction. Relevant details of the experiment and refinement are summarised in Table 3.5.

Empirical formula	$C_{12.38}InNO_{7.19}H_{11.76}$
Formula weight / g mol^{-1}	404.31
Temperature / K	150(10)
Radiation / Å	CuKα (λ = 1.54184)
Crystal system	Orthorhombic
Space group	*Cmcm*
a / Å	21.7325(8)
b / Å	37.6102(14)
c / Å	7.22490(19)
α / °	90
β / °	90
γ / °	90
Volume / $Å^3$	5905.4(3)
Z	12
Density (calculated) / g cm^{-3}	1.397
Crystal size / mm^3	0.126 × 0.045 × 0.035
Data / restraints / parameters	3111 / 92 / 146
Final *R* indices [*I*>=2σ (*I*)]	R_1 = 0.0396, wR_2 = 0.1087
R indices [all data]	R_1 = 0.0544, wR_2 = 0.1198
Largest diff. peak and hole / e $Å^{-3}$	0.95 and -0.87

Table 3.5. Selected crystal data and structure refinement data for framework **2i**.

The asymmetric unit (ASU) of **2i**, Figure 3.51, consists of two indium(III) metal centres with site occupancies of 0.5 and 0.25 for In1 and In2, respectively, half of a dicarboxylate ligand (based on O3) with C4, C5, C8 and C9 located at a crystallographic mirror plane, one quarter of a dicarboxylate ligand (based on O2) with C1 and C2 also located at a mirror plane. This latter moiety is also proximate to a second crystallographic mirror plane which contributes to generating the remainder. Two OH ligands (based on O1 and O5) with combined site occupancies of 0.75 are also present in the ASU. Finally, there was evidence for some diffuse solvent present in the framework. Atoms C3, C6 and C7

exhibited disorder which was modelled over two sites in 50:50, 66:34 and 66:34 ratios, respectively.

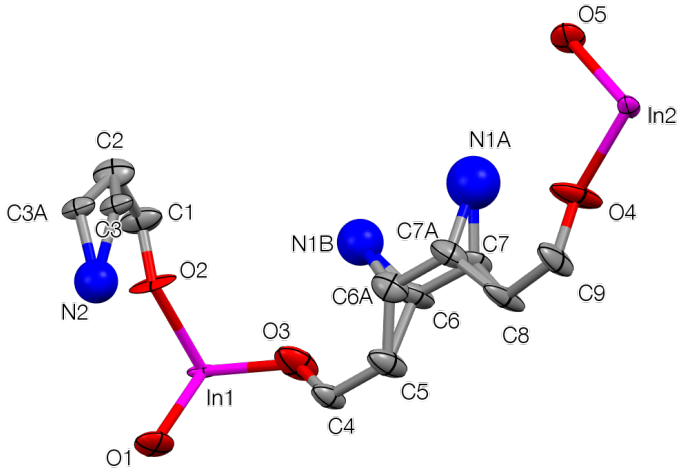

Figure 3.51. The asymmetric unit of **2i**. Ellipsoids are shown at 50% probability. Nitrogen atoms were treated isotropically.

As can be seen in Figure 3.52, the overall framework topology has not changed significantly during the reaction, from the starting MOF, MIL-68(In)-NH_2, in agreement with the PXRD data, Figure 3.50. It contains the $InO_4(OH)_2$ octahedral chains and has retained the orthorhombic space group symmetry, *Cmcm*. The unit cell parameters for **2i** are also similar to that for MIL-68(In) (a = 21.7739(6) Å, b = 37.6772(10) Å, c = 7.23300(10) Å), which is expected, due to both being isostructural to each other.

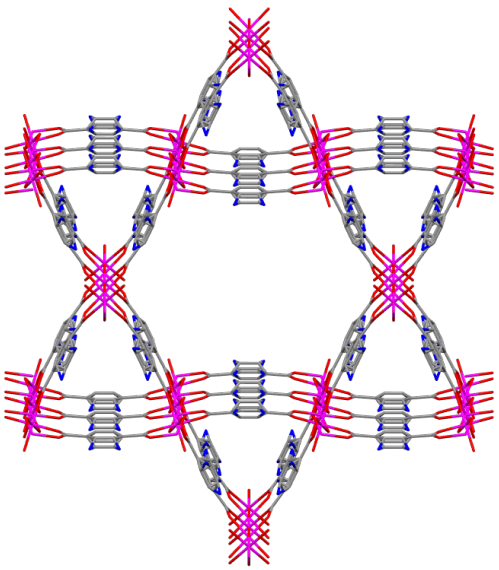

Figure 3.52. The three-dimensional crystal structure of **2i** viewed down the *c* axis. Solvent molecules are omitted for clarity.

Initial refinement (pre-PLATON SQUEEZE) rendered an *R*1 value in the region of 9.6% but with a poor weighting scheme. PLATON analysis suggested that the data might have arisen from a 3-fold pseudo-merohedral twin, and a refinement that took account of this reduced the *R*1 value to the region of 6.5%. At this point, there was no evidence of the tag, so hydrogen atoms were attached to the aromatic carbons prior to implementation of PLATON SQUEEZE. Subsequent refinement against the arising dataset from this algorithm revealed electron density maxima in the region of the aromatic hydrogens, but at a longer distance from these carbons. This could be interpreted as evidence for the nitrogen in the tags being disordered amongst the aryl carbons. Hence, the aromatic hydrogens were removed from the model, in favour of 3 isotropically refined, partial occupancy nitrogens per asymmetric unit. C-N distances were restrained to being similar given the low level of electron density at each site. Some ADP restraints were included in the refinement to assist convergence.

Figure 3.53. shows the TGA profiles of PSM product **2i** and the starting MOF, MIL-68(In)-NH_2. The initial mass loss (up to 380 °C) corresponds to the 1,4-dioxane molecules that are in the pores. Per In unit, MIL-68(In)-NH_2 has 1.7 and **2i** has 0.8 1,4-dioxane molecules. The lower amount of guest solvent in **2i** compared to that for MIL-68(In)-NH_2 is probably due to the presence of the modified groups in the pores, which limit the space for solvent molecules. The framework decomposition of **2i** starts at ~340 °C, which is approximately 40 °C lower than that for MIL-68(In)-NH_2.

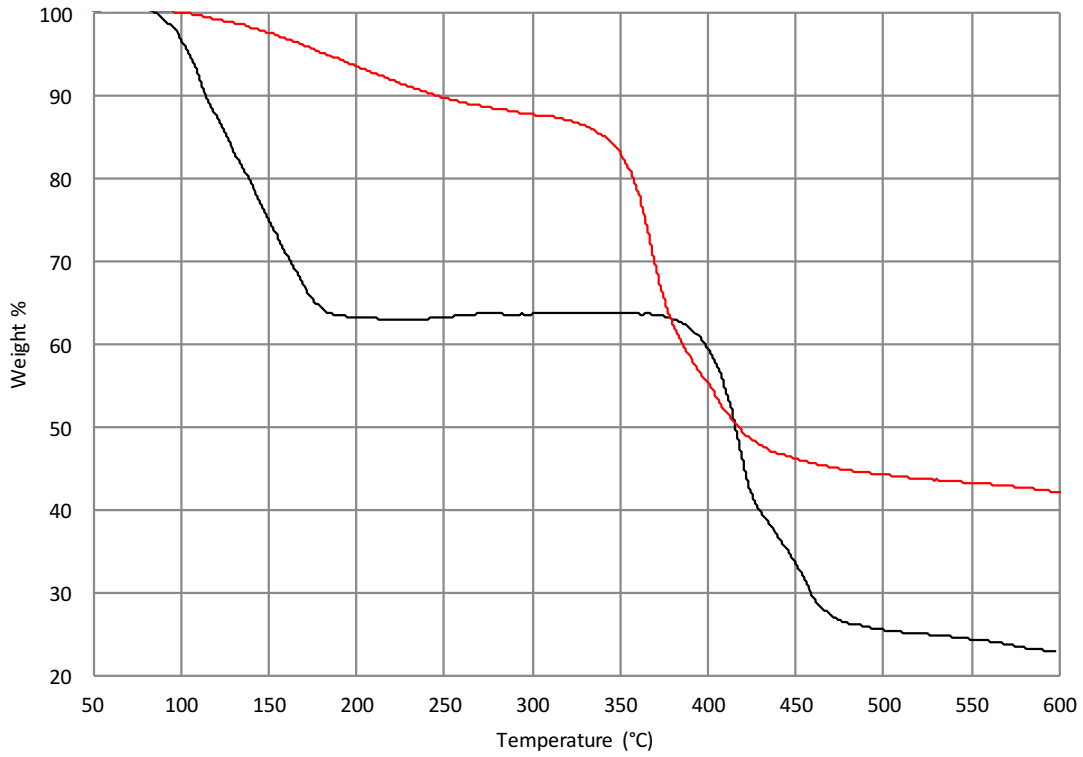

Figure 3.53. TGA of MIL-68(In)-NH_2 (black) and PSM products **2i** (red). The samples were heated from 30 °C to 600 °C at a rate of 20 K/min under a flow of argon gas (20 mL/min).

Based on the TGA results, 0.8 of a dioxane molecule per indium centre are included in the empirical formula of **2i**. Therefore, the formulation of this material can be expressed as $[In(OH)(BDC\text{-}NH_2)_{0.41}(BDC\text{-}NHCH_2OCH_3)_{0.59}]\cdot 0.8C_4H_8O_2$.

3.5. Dicarboxylic Acid Synthesis: 2-(((1*H*-pyrazol-1-yl)methyl)amino)terephthalic acid, $H_2BDC\text{-}NHCH_2N_2C_3H_3$

In order to investigate if MOFs bearing the α-amino pyrazole ($–NHCH_2C_3H_3N_2$) groups could be synthesised directly (from a mixture of a metal salt and the dicarboxylic acid, $H_2BDC\text{-}NHCH_2N_2C_3H_3$), in the first instance, the preparation of $H_2BDC\text{-}NHCH_2N_2C_3H_3$ was attempted, Scheme 3.16.

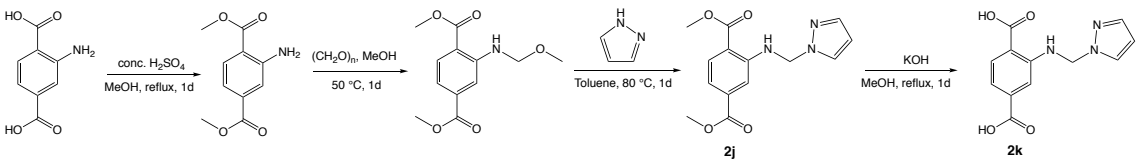

Scheme 3.16. The synthesis of 2-(((1*H*-pyrazol-1-yl)methyl)amino)terephthalic acid, $H_2BDC\text{-}NHCH_2N_2C_3H_3$.

In a typical experiment, $H_2BDC\text{-}NH_2$ was first subjected to esterification under acidic conditions. The ester, $(CH_3)_2BDC\text{-}NH_2$, which was isolated by extraction, was then treated with paraformaldehyde in MeOH for 1 day at 50 °C before removing the solvent under vacuum. The isolated solid was subsequently dissolved in toluene and treated with pyrazole for 1 day at 80 °C. Upon removing the solvent, the solid sample was dissolved in MeOH and treated with KOH for 1 day under reflux. The solution was acidified and the product was isolated by extraction and dried for several hours under high vacuum.

The first step of the reaction (the esterification of $H_2BDC\text{-}NH_2$ to form $(CH_3)_2BDC\text{-}NH_2$)) was successful, as evidenced by ^{1}H NMR spectroscopy. The conversion of $(CH_3)_2BDC\text{-}NH_2$ into $(CH_3)_2BDC\text{-}NHCH_2C_3H_3N_2$ was also successful, evidenced by the presence of the α-amino pyrazole ($–NHCH_2C_3H_3N_2$) peaks in the ^{1}H NMR spectrum of **2j**, Figure 3.17.

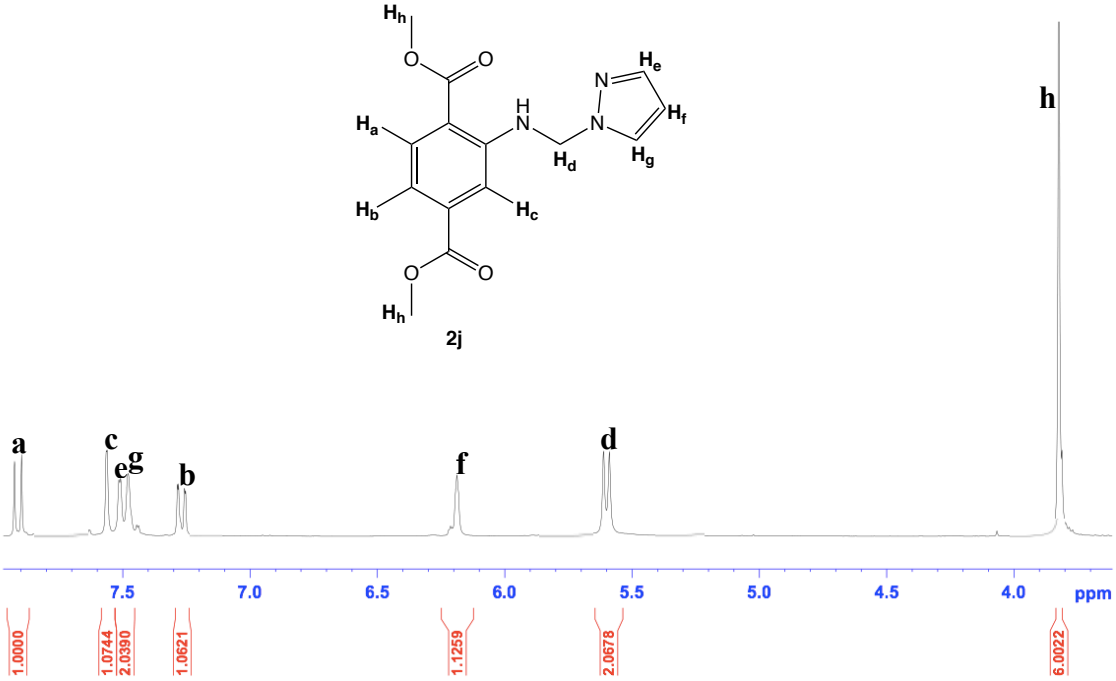

Figure 3.17. ^{1}H NMR spectrum of **2j** in DMSO-d_6.

The positive ESI mass spectrum of **2j** also confirms the presence of the sodium adduct cations of $(CH_3)_2BDC\text{-}NHCH_2C_3H_3N_2$ at m/z = 312.0994 (predicted $[M+Na]^+$ = 312.0955).

Unfortunately, the attempt to hydrolyse $(CH_3)_2BDC\text{-}NHCH_2C_3H_3N_2$ into $H_2BDC\text{-}NHCH_2C_3H_3N_2$ also led to the hydrolysis of the α-amino pyrazole ($–NHCH_2C_3H_3N_2$)

groups and reformation of the starting material, $H_2BDC\text{-}NH_2$ as evidenced by the ^1H NMR spectrum of **2k**, Figure 3.18.

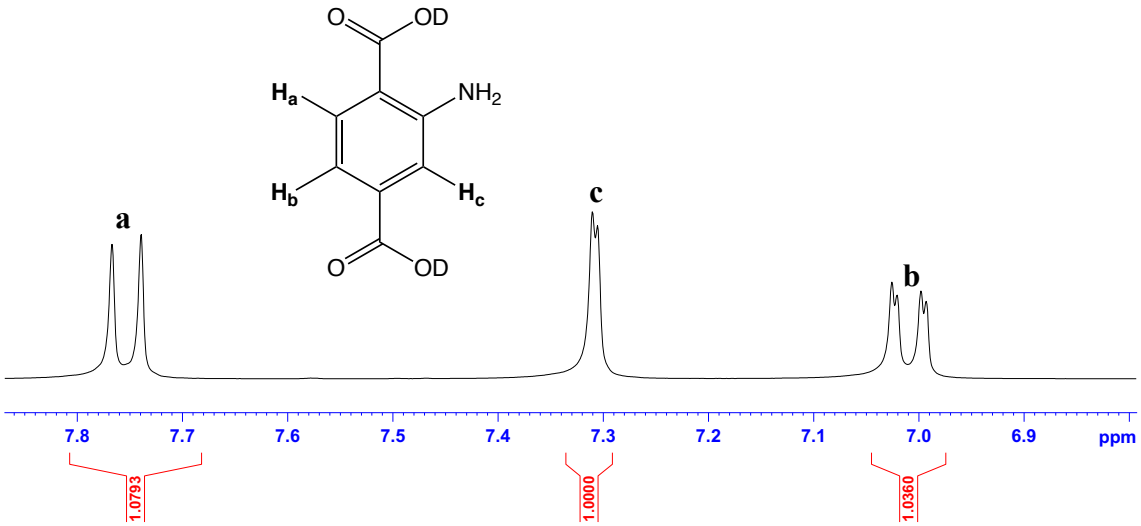

Figure 3.18. Aromatic region of the ^1H NMR spectrum of **2k** in DMSO-d_6.

This finding indicates that the synthesis of $H_2BDC\text{-}NHCH_2C_3H_3N_2$ could not be achieved by this route due to the instability of the α-amino pyrazole ($–NHCH_2C_3H_3N_2$) groups under basic conditions. Nonetheless, this result also highlights one of the advantages of PSM over direct synthesis, whereby PSM may be the only method to produce α-amino pyrazole functionalised MOFs.

3.6. Summary

The results presented herein demonstrate a new PSM reaction pathway, whereby Mannich reactions were used to convert the primary amines of UiO-66-NH_2, IRMOF-3, DMOF-1-NH_2 and MIL-68(In)-NH_2 into a range of azole-functionalised MOFs with conversions up to 100%.

In general, different observations were obtained according to the MOFs used in this study. In terms of the PSM reactions on UiO-66-NH_2, the degrees of conversion from $–NH_2$ into α-amino azoles, –NHR (R = $CH_2C_3H_3N_2$ (based on pyrazole), $CH_2C_3H_3N_2$ (based on imidazole) and $CH_2C_3H_2N_2SH$) depend on the strength and size of the nucleophiles used in this study. 100% PSM conversion was achieved with the strongest nucleophile (imidazole) whereas a lower conversion (41%) was obtained with weaker nucleophile, pyrazole. The use of a larger nucleophile, 2-mercaptoimidazole, lead to the lowest

conversion (36%) and this is most likely due to the restricted diffusion of the nucleophile into the pores of UiO-66-NH_2.

With regard to the PSM reaction on IRMOF-3, 75% conversion of $–NH_2$ into $–NHCH_2C_3H_3N_2$ was achieved whilst using pyrazole as a nucleophile. However, the successful PSM reaction comes at a cost of decreased product crystallinity as evidenced by the broadening of peaks and reduction in peak intensities in the PXRD pattern of the PSM product.

The Mannich reaction on the flexible MOF, $[Zn_2(BDC\text{-}NH_2)_2(DABCO)]$, DMOF-1-$NH_2$, using pyrazole as the nucleophile afforded a new material, formulated as $[Zn_3(BDC\text{-}NH_2)_{1.32}(BDC\text{-}NHCH_2N_2C_3H_3)_{1.68}(C_6H_{12}N_2)]$, **2f**, based on single crystal X-ray crystallography, ^{1}H NMR and TGA analyses. This structural transformation, which could be observed under an optical microscope, occurred on the intermediate MOF, DMOF-1-$NHCH_2OCH_3$. A reaction mechanism has been proposed to demonstrate the pyrazole-triggered dissolution of DMOF-1-$NHCH_2OCH_3$.

In contrast, the Mannich reaction of DMOF-1-NH_2 with imidazole afforded a PSM product bearing the same structural features with DMOF-1-NH_2 (no structural change was observed). This may suggest that substituting pyrazole for imidazole prevents the dissolution of DMOF-1-$NHCH_2OCH_3$ due to the positioning of the ‘free’ nitrogen atom within the imidazole ring which is beyond the coordinative sphere of the zinc(II) metal centre.

No conversion was observed whilst 2-mercaptoimidazole was used as a nucleophile for the DMOF-1-NH_2 system. This is likely to be due to the nucleophile size, which is too big to diffuse through the pores of DMOF-1-NH_2.

Subjecting MIL-68(In)-NH_2 to a similar PSM reaction with pyrazole, proceeded to the formation of $[In(OH)(BDC\text{-}NH_2)_{0.41}(BDC\text{-}NHCH_2OCH_3)_{0.59}]$, **2i**, as evidenced by ^{1}H NMR spectroscopy and mass spectroscopy. The inclusion of pyrazole in the pores of MIL-68(In)-NH_2 was unsuccessful probably due to the location of the amino groups (and, subsequently, the modified $–NHCH_2OCH_3$ groups) which are inaccessible to the pyrazole molecules. The effect of pore blocking by the $–NHCH_2OCH_3$ groups may also cause the unsuccessful inclusion of pyrazole ring on the MOF framework.

An attempt to synthesise the dicarboxylic acid, $H_2BDC\text{-}NHCH_2N_2C_3H_3$ as a reagent for

MOF synthesis, was unsuccessful due to the instability of the α-amino pyrazole (–$NHCH_2C_3H_3N_2$) groups under strongly basic conditions. The difficulty in obtaining the dicarboxylic acid, $H_2BDC\text{-}NHCH_2N_2C_3H_3$, highlights one of the advantages of PSM as an alternative in obtaining α-amino pyrazole functionalised MOFs as opposed to direct synthesis.

The surface areas of the modified UiO-66 materials were probed *via* N_2 gas adsorption at 77 K. The PSM products were shown to exhibit type I isotherms, indicative of microporous materials. The products also exhibited lower BET surface areas than the starting MOF, UiO-66-NH_2, due to the additional mass originating from the modified groups. In general, the BET surface area reduces as the percentage conversion increases. The presence of bulky substituent in the pores can also lower the BET surface area due to pore blocking effect.

The modified UiO-66 materials were tested for CO_2 adsorption and the selectivity over N_2 was assessed. In general, the CO_2 and N_2 adsorption of the PSM products at 273 K were lower than those for the starting MOF, UiO-66-NH_2. This is attributable to the reduction in free space in the modified MOFs. In terms of CO_2/N_2 selectivity, $[Zr_6O_4(OH)_4(BDC\text{-}NH_2)_{3.54}(BDC\text{-}NHCH_2C_3H_3N_2)_{2.46}]$, **2a**, exhibited the highest selectivity, being ~5 times higher than that for UiO-66-NH_2, at 0.1 bar.

The presence of thiol groups in $[Zr_6O_4(OH)_4(BDC\text{-}NH_2)_{3.84}(BDC\text{-}NHCH_2C_3H_2N_2SH)_{2.16}]$, **2c**, and $[Zr_6O_4(OH)_4(BDC\text{-}NH_2)_{4.74}(BDC\text{-}NHCH_2C_3H_2N_2SH)_{1.26}]$, **2d**, was exploited by using the modified MOFs for Hg(II) capture in aqueous solution. **2d** was shown to exhibit higher Hg(II) uptake despite **2c** having higher percentage of thiol groups in the pores due to larger free space in **2d** which could allow for more Hg(II) to occupy the pores.

3.7. Future Work

One of the stumbling blocks that was encountered whilst performing the PSM Mannich reactions was the difficulty in obtaining the aimed products in high purity. Most of the PSM products contained by-products and attempts to remove these *via* extensive washing were ineffective. Therefore, exploration for a more sophisticated method of purification is necessary to obtain the targeted products in higher yields. As stated in Section 1.4.1, MOF activation by supercritical CO_2 has gained a widespread interest among MOF

chemists due to its effectiveness in removing entrapped by-products and solvents from MOF pores. On this basis, this method may be used for the removal of by-products from the PSM products reported herein.

Another limitation of the PSM Mannich reactions was the long reaction times. Typically, the reactions proceeded in 3 days to form the azole-functionalised MOFs. The reaction time may be shortened by employing microwave-assisted PSM reactions as opposed to the conventional heating approach used in this study.

In terms of the characterisation of the modified MOFs, solid-state NMR spectroscopy may be useful for confirming the composition of the PSM products, and might provide a truer representation of the product ligand distributions than that evaluated *via* the solution ^{1}H NMR on the digested materials reported herein.

The scope of the PSM Mannich reactions could be expanded by performing the reactions on other MOF topologies. For example, MIL-101-NH_2 would be a good candidate due to its large pore apertures (15 and 20 Å) and high stability in different solvents and acids.[35]

The type of azoles (nucleophiles) that can be included in the MOF pores can be expanded and tailored according to the application that the modified MOF would be used in. For example, azoles bearing carboxylic acid groups such as 3*H*-imidazole-4-carboxylic acid may be included in the pores of a MOF *via* the Mannich reaction reported herein. The carboxylic acid-functionalised MOF can then be used as a metal ligating agent.

3.8. General Experimental Procedures

3.8.1. Powder X-Ray Diffraction

Powder X-ray diffraction (PXRD) patterns for all samples were recorded on a Bruker AXS D8 Advance diffractometer with copper K_α radiation (wavelength, $\lambda = 1.5406$ Å) at 298 K. The beam slit was set to 1 mm, detector slit set to 0.2 mm and anti-scattering slit set to 1 mm. Samples were dried in ambient conditions and ground to a powder using a pestle and mortar. The powders were then packed onto a flat plate and measured over a 2θ range of 5 - 60°. The step size was 0.024° with the scan speed set to 0.3 s per step.

3.8.2. Single Crystal X-Ray Diffraction

Crystal size and shapes were observed under an optical microscope (magnification up to

1000x) and a high-resolution camera (with a graduated ruler on screen with smallest divisions of 0.025 mm).

Single crystal X-ray diffraction data for $[Zn_3(BDC\text{-}NH_2)_{1.32}(BDC\text{-}NHCH_2N_2C_3H_3)_{1.68}(C_6H_{12}N_2)]\cdot 2C_7H_8$, **2f** were collected at 100 K on a Bruker Apex II diffractometer using synchrotron radiation (λ = 0.7749 Å) at Beamline 11.3.1 at the ALS Lawrence Berkeley National Laboratory.

Single crystal X-ray diffraction data for $[In(OH)(BDC\text{-}NH_2)_{0.41}(BDC\text{-}NHCH_2OCH_3)_{0.59}]\cdot 0.8C_4H_8O_2$, **2i** were collected on an Agilent SuperNova diffractometer using CuKα radiation (λ = 1.5418 Å) at 150 K.

The crystal structures were solved using SHELXS-97 and refined using full-matrix least squares in SHELXL-97.[36]

3.8.3. ^{1}H NMR Spectroscopy

^{1}H NMR spectrometry was carried out on the digested MOF samples at 298 K on a Bruker Avance 300 MHz Ultrashield NMR spectrometer. All ^{1}H NMR spectra were referenced to the residual protio peaks at δ 2.50 ppm for DMSO-d_6 with the exception of MIL-68-(In) materials, which were referenced to the residual protio peaks at δ 4.80 ppm for D_2O. Samples were dried at 100 °C for 15 minutes prior to digestion.

For the UiO-66 materials, a typical MOF digestion was carried out by adding 10 mg of a crystalline sample into 0.4 mL of DMSO-d_6 and 0.2 mL of a stock solution of NH_4F in D_2O (4.14 M). The mixture was sonicated until the solid had completely dissolved. In some cases, a trace amount of white solid presumably NH_4F salt precipitated out of the solution. The white solid was removed by filtration of the solution prior to ^{1}H NMR measurement.

For the IRMOF and DMOF materials, the MOF digestions were each carried out using approximately 10 mg of crystalline sample in 0.4 mL of DMSO-d_6 and 0.2 mL of a stock solution of 0.1 mL of 35 wt% DCl/D_2O in 3 mL DMSO. This mixture was sonicated until the solid had completely dissolved.

For the MIL-68(In) materials, the MOF digestion was carried out with approximately 10 mg of crystalline sample in 0.4 mL of D_2O and 0.2 mL of a stock solution of 0.1 mL of 30 wt% NaOD/D_2O in 3 mL D_2O. These mixtures were sonicated until the solid had

completely dissolved.

For the materials obtained during the attempted dicarboxylic acid synthesis, the samples for ^{1}H NMR analysis were prepared by dissolving 10 mg of solids in 0.6 mL of DMSO-d_6.

3.8.4. Mass Spectroscopy

Mass spectrometry was carried out on digested MOF solutions diluted in EtOH, using a Bruker micrOTOF electrospray ionisation time-of-flight (ESI-TOF) mass spectrometer.

3.8.5. Atomic Emission Spectroscopy

Atomic emission spectrometry was carried out by Mr. Alan Carver on a Perkin Elmer Model 3100 on aqueous solutions of digested MOFs.

3.8.6. FTIR Spectroscopy

FTIR spectrometry was carried out on solid samples using a Perkin Elmer Spectrum 100 spectrometer mounted on a diamond/gem platform.

3.8.7. Thermogravimetric Analysis

TGA was carried out on the solid samples using a Setaram Setsys Evolution 16/18 thermogravimetric analyser. The samples were heated from 30 °C to 600 °C at a rate of 20 K/min under a flow of argon gas (20 mL/min).

3.8.8. Gas Sorption Measurements

A typical gas sorption measurement was carried out by loading an approximately 20 mg of MeOH rinsed sample into a pre-weighed sample tube. The sample was then heated at 120 °C for 12 hours on a BELSORP Mini-II (BEL Japan) gas sorption analyser. The sample tube was re-weighed to obtain a consistent mass of the activated sample prior to the gas adsorption measurement. To determine the specific surface area, N_2 sorption isotherms were recorded at 77 K, while keeping this temperature constant using a liquid nitrogen bath. The specific surface area was calculated based on the Brunauer-Emmett-Teller (BET) method in the P/P_0 range of 0.05 - 0.10. CO_2 and N_2 adsorption isotherms were also recorded at 273 K. The selectivity of CO_2 over N_2 of the material was calculated from the single gas isotherms by dividing the CO_2 uptake by that of N_2 at a specific pressure (0.1 or 1.0 bar).

3.9. Synthetic Procedures

Unless specified, all reagents and solvents used in this work were purchased from commercial sources (Sigma Aldrich/Fisher Scientific/Alfa Aesar) and were used without further purification.

3.9.1. Synthesis of UiO-66-NH_2, $[Zr_6O_4(OH)_4(BDC\text{-}NH_2)_6]$

The synthesis was modified from a procedure reported by Garibay and Cohen.[13] In a typical reaction, $H_2BDC\text{-}NH_2$ (190 mg, 1.05 mmol) along with $ZrCl_4$ (243 mg, 1.05 mmol) and DMF (12 mL) were loaded into a Teflon-lined autoclave. The solution was stirred until the reactants had completely dissolved. The autoclave was placed in an oven and heated at 120 °C for 24 hours. The resulting yellow powder was rinsed and centrifuged with MeOH (6000 rpm for 15 minutes) to remove unreacted $H_2BDC\text{-}NH_2$ and residual DMF in the pores. The washing procedure was repeated over 3 days with the solvent replaced every 24 hours. Finally, the UiO-66-NH_2 powder was dried under vacuum at 120 °C for 12 hours. In preparation for PSM reactions, the UiO-66-NH_2 powder was washed with 1,4-dioxane by centrifugation over 3 days with the solvent replaced every 24 hours. The powder was then left to dry under ambient conditions.

3.9.2. Synthesis of UiO-66-$NHCH_2C_3H_3N_2$ (41%), $[Zr_6O_4(OH)_4(BDC\text{-}NH_2)_{3.54}(BDC\text{-}NHCH_2C_3H_3N_2)_{2.46}]\cdot 4C_4H_8O_2$, 2a

The starting material, UiO-66-NH_2, was synthesised according to the procedure described in Section 3.9.1. The PSM reaction was performed by adding UiO-66-NH_2 powder (117 mg, ca. 0.4 mmol eq. of NH_2) and paraformaldehyde (24 mg, 0.8 mmol, 2 eq.) into a glass vial containing 5 mL MeOH. The glass vial was sealed and the mixture was sonicated for 30 minutes. The vial was placed in an oven and heated at 50 °C for 1 day. The powder was then washed with 1,4-dioxane (three times) *via* centrifugation to remove any residual paraformaldehyde and MeOH in the pores or on the solid surface. The powder was subsequently treated with pyrazole (54 mg, 0.8 mmol, 2 eq.) in 1,4-dioxane at 80°C for 1 day before quenching the reaction by rinsing the sample with fresh 1,4-dioxane. The product was soaked in 1,4-dioxane for 3 days, replacing the solvent with fresh solvent every 24 hours, before isolation by centrifugation. Prior to characterisation, the sample was left to dry in air for 2 hours to obtain free-flowing powders.

3.9.3. Synthesis of UiO-66-$NHCH_2C_3H_3N_2$ (100%), $[Zr_6O_4(OH)_4(BDC\text{-}NHCH_2C_3H_3N_2)_6]\cdot 3C_4H_8O_2$, 2b

The starting material, UiO-66-NH_2, was synthesised according to the procedure described in Section 3.9.1. The PSM reaction was performed by adding UiO-66-NH_2 powder (117 mg, ca. 0.4 mmol eq. of NH_2) and paraformaldehyde (24 mg, 0.8 mmol, 2 eq.) into a glass vial containing 5 mL MeOH. The glass vial was sealed and the mixture was sonicated for 30 minutes. The vial was placed in an oven and heated at 50 °C for 1 day. The powder was then washed with 1,4-dioxane (three times) *via* centrifugation to remove any residual paraformaldehyde and MeOH in the pores or on the solid surface. The powder was subsequently treated with imidazole (54 mg, 0.8 mmol, 2 eq.) in 1,4-dioxane at 80°C for 1 day before quenching the reaction by rinsing the sample with fresh 1,4-dioxane. The product was soaked in 1,4-dioxane for 3 days, replacing the solvent with fresh solvent every 24 hours, before isolation by centrifugation. Prior to characterisation, the sample was left to dry in air for 2 hours to obtain free-flowing powders.

3.9.4. Synthesis of UiO-66-$NHCH_2C_3H_2N_2SH$ (36%), $[Zr_6O_4(OH)_4(BDC\text{-}NH_2)_{3.84}(BDC\text{-}NHCH_2C_3H_2N_2SH)_{2.16}]\cdot 5C_4H_8O_2$, 2c

The starting material, UiO-66-NH_2, was synthesised according to the procedure described in Section 3.9.1. The PSM reaction was performed by adding UiO-66-NH_2 powder (117 mg, ca. 0.4 mmol eq. of NH_2) and paraformaldehyde (24 mg, 0.8 mmol, 2 eq.) into a glass vial containing 5 mL MeOH. The glass vial was sealed and the mixture was sonicated for 30 minutes. The vial was placed in an oven and heated at 50 °C for 1 day. The powder was then washed with 1,4-dioxane (three times) *via* centrifugation to remove any residual paraformaldehyde and MeOH in the pores or on the solid surface. The powder was subsequently treated with 2-mercaptoimidazole (80 mg, 0.8 mmol, 2 eq.) in 1,4-dioxane at 80°C for 1 day before quenching the reaction by rinsing the sample with fresh 1,4-dioxane. The product was soaked in 1,4-dioxane for 3 days, replacing the solvent with fresh solvent every 24 hours, before isolation by centrifugation. Prior to characterisation, the sample was left to dry in air for 2 hours to obtain free-flowing powders.

3.9.5. Synthesis of UiO-66-$NHCH_2C_3H_2N_2SH$ (21%), $[Zr_6O_4(OH)_4(BDC\text{-}NH_2)_{4.74}(BDC\text{-}NHCH_2C_3H_2N_2SH)_{1.26}]\cdot 5.5C_4H_8O_2$, 2d

The starting material, UiO-66-NH_2, was synthesised according to the procedure described in Section 3.9.1. The PSM reaction was performed by adding UiO-66-NH_2 powder (117 mg, ca. 0.4 mmol eq. of NH_2) and paraformaldehyde (24 mg, 0.8 mmol, 2 eq.) into a glass vial containing 5 mL MeOH. The glass vial was sealed and the mixture was sonicated for 30 minutes. The vial was placed in an oven and heated at 50 °C for 1 day. The powder was then washed with 1,4-dioxane (three times) *via* centrifugation to remove any residual paraformaldehyde and MeOH in the pores or on the solid surface. The powder was subsequently treated with 2-mercaptoimidazole (80 mg, 0.8 mmol, 2 eq.) in 1,4-dioxane at 50°C for 1 day before quenching the reaction by rinsing the sample with fresh 1,4-dioxane. The product was soaked in 1,4-dioxane for 3 days, replacing the solvent with fresh solvent every 24 hours, before isolation by centrifugation. Prior to characterisation, the sample was left to dry in air for 2 hours to obtain free-flowing powders.

3.9.6. Synthesis of IRMOF-3, $[Zn_4O(BDC\text{-}NH_2)_3]$

IRMOF-3 was synthesised according to a previously reported procedure by Kim and co-workers.[19] In a typical experiment, $Zn(NO_3)_2\cdot 6H_2O$ (400 mg, 1.34 mmol) and $H_2BDC\text{-}NH_2$ (80 mg, 0.44 mmol) were dissolved in DMF (12 mL) in a glass vial. The vial was sealed and the reaction mixture was heated at 105 °C for 48 hours to yield pale brown cubic crystals. The crystals were then washed and soaked in chloroform for 3 days, replacing the solvent with fresh solvent every 24 hours before collecting the crystals by filtration. The crystals were stored in an inert atmosphere to avoid crystal degradation. Prior to PSM reactions, the IRMOF-3 crystals were washed with toluene over 3 days with the solvent replaced every 24 hours before collecting the crystals by filtration.

3.9.7. Synthesis of IRMOF-3-$NHCH_2C_3H_3N_2$ (75%), $[Zn_4O(BDC\text{-}NH_2)_{0.75}(BDC\text{-}NHCH_2C_3H_3N_2)_{2.25}]$, 2e

The starting material, IRMOF-3, was synthesised according to the procedure described in Section 3.9.6. In a typical PSM procedure, IRMOF-3 crystals (108 mg, ca. 0.4 mmol eq. of NH_2), paraformaldehyde (24 mg, 0.8 mmol, 2 eq.) and MeOH (32 μL, 0.8 mmol, 2

eq.) were added into a glass vial containing 5 mL toluene. The vial was then sealed, placed in an oven and heated at 50 °C for 1 day. The crystals were then washed with fresh toluene (three times) to remove any residual paraformaldehyde and MeOH in the pores or on the solid surface. The crystals were subsequently treated with pyrazole (54 mg, 0.8 mmol, 2 eq.) in toluene at 80°C for 1 day before quenching the reaction by rinsing the crystals with fresh toluene. The crystals were soaked in toluene for 3 days, replacing the solvent with fresh solvent every 24 hours. The crystals were then isolated *via* filtration. The crystals were stored in an inert atmosphere to avoid crystal degradation.

3.9.8. Synthesis of DMOF-1-NH_2, $[Zn_2(BDC\text{-}NH_2)_2(DABCO)]$

DMOF-1-NH_2 was synthesised using an analogous synthesis to that for DMOF-1, originally reported by Kim and co-workers.[24] In a typical experiment, a mixture of $Zn(NO_3)_2 \cdot 6H_2O$ (500 mg, 1.68 mmol), $H_2BDC\text{-}NH_2$ (304 mg, 1.68 mmol) and DABCO (94 mg, 0.84 mmol) was suspended in DMF (20 mL) and heated in a glass vial at 120°C for 2 days. The resulting brown block crystals were washed and soaked in DMF for 3 days, replacing the solvent with fresh solvent every 24 hours before collecting the crystals by filtration. Prior to PSM reaction, the DMOF-1-NH_2 crystals were washed with toluene over 3 days with the solvent replaced every 24 hours before collecting the crystals by filtration.

3.9.9. Synthesis of $[Zn_3(BDC\text{-}NH_2)_{1.32}(BDC\text{-}NHCH_2N_2C_3H_3)_{1.68}(C_6H_{12}N_2)] \cdot 2C_7H_8$, 2f

The starting material, DMOF-1-NH_2, was synthesised according to the procedure described in Section 3.9.8. In a typical PSM procedure, DMOF-1-NH_2 crystals (120 mg, ca. 0.4 mmol eq. of NH_2), paraformaldehyde (24 mg, 0.8 mmol, 2 eq.) and MeOH (32 μL, 0.8 mmol, 2 eq.) were added into a glass vial containing 5 mL toluene. The vial was then sealed, placed in an oven and heated at 50 °C for 1 day. The crystals were then washed with fresh toluene (three times) to remove any residual paraformaldehyde and MeOH in the pores or on the solid surface. The crystals were subsequently treated with pyrazole (54 mg, 0.8 mmol, 2 eq.) in toluene at 80°C for 1 day before quenching the reaction by rinsing the crystals with fresh toluene. The crystals were soaked in toluene for 3 days, replacing the solvent with fresh solvent every 24 hours. The crystals were then isolated *via* filtration.

3.9.10. Synthesis of DMOF-1-NHCH$_2$C$_3$H$_3$N$_2$ (75%), [Zn$_2$(BDC-NH$_2$)$_{0.7}$(BDC-NHCH$_2$C$_3$H$_3$N$_2$)$_{1.3}$(DABCO)]·2.2C$_7$H$_8$, 2g

The starting material, DMOF-1-NH_2, was synthesised according to the procedure described in Section 3.9.8. In a typical PSM procedure, DMOF-1-NH_2 crystals (120 mg, ca. 0.4 mmol eq. of NH_2), paraformaldehyde (24 mg, 0.8 mmol, 2 eq.) and MeOH (32 µL, 0.8 mmol, 2 eq.) were added into a glass vial containing 5 mL toluene. The vial was then sealed, placed in an oven and heated at 50 °C for 1 day. The crystals were then washed with fresh toluene (three times) to remove any residual paraformaldehyde and MeOH in the pores or on the solid surface. The crystals were subsequently treated with imidazole (54 mg, 0.8 mmol, 2 eq.) in toluene at 80°C for 1 day before quenching the reaction by rinsing the crystals with fresh toluene. The crystals were soaked in toluene for 3 days, replacing the solvent with fresh solvent every 24 hours. The crystals were then isolated *via* filtration.

3.9.11. Synthesis of MIL-68(In)-NH$_2$, [In(OH)(BDC-NH$_2$)]

MIL-68(In)-NH_2 was prepared using an analogous synthesis to that for MIL-68(In), originally reported by Loiseau and co-workers.[29] In a typical procedure, a mixture of $In(NO_3)_3·5H_2O$ (410 mg, 1.05 mmol) and H_2BDC-NH_2 (217 mg,1.2 mmol) was dissolved in DMF (5 mL) in a Teflon-lined autoclave. The autoclave was placed in an oven and heated for 48 h at 100 °C. The resulting yellow crystals were washed and soaked in MeOH for 3 days, replacing the solvent with fresh solvent every 24 hours before collecting the crystals by filtration.

3.9.12. Synthesis of MIL-68(In)-NHCH$_2$OCH$_3$ (59%), [In(OH)(BDC-NH$_2$)$_{0.41}$(BDC-NHCH$_2$OCH$_3$)$_{0.59}$]·0.8C$_4$H$_8$O$_2$, 2i

The starting material, MIL-68(In)-NH_2, was synthesised according to the procedure described in Section 3.9.11. The PSM reaction was performed by adding MIL-68(In)-NH_2 crystals (124 mg, ca. 0.4 mmol eq. of NH_2) and paraformaldehyde (24 mg, 0.8 mmol, 2 eq.) into a glass vial containing 5 mL MeOH. The glass vial was sealed, placed in an oven and heated at 50 °C for 1 day. The crystals were then washed with 1,4-dioxane (three times) *via* filtration to remove any residual paraformaldehyde and MeOH in the pores or on the solid surface. The crystals were subsequently treated with pyrazole (54 mg, 0.8

mmol, 2 eq.) in 1,4-dioxane at 80°C for 1 day before quenching the reaction by rinsing the sample with fresh 1,4-dioxane. The product was soaked in 1,4-dioxane for 3 days, replacing the solvent with fresh solvent every 24 hours, before isolation by filtration.

3.10. References

1. C. Mannich and W. Krösche, *Arch. Pharm.*, 1912, **250**, 647.
2. M. Senkus, *J. Am. Chem. Soc.*, 1946, **68**, 10.
3. J. S. Fowler, *J. Org. Chem.*, 1977, **42**, 2637.
4. W. Herz and J. L. Rogers, *J. Am. Chem. Soc.*, 1951, **73**, 4921.
5. H. Heaney, G. Papageorgiou and R. F. Wilkins, *Tetrahedron Lett.*, 1988, **29**, 2377.
6. H. D. Hartough and S. L. Meisel, *J. Am. Chem. Soc.*, 1948, **70**, 4018.
7. Y. Luan, Y. Qi, Z. Jin, X. Peng, H. Gao and G. Wang, *RSC Adv.*, 2015, **5**, 19273.
8. Z. Miao, C. Qi, L. Wang, A. M. Wensley and Y. Luan, *Appl. Organomet. Chem.*, 2017, **31**, e3569.
9. J. H. Cavka, S. Jakobsen, U. Olsbye, N. Guillou, C. Lamberti, S. Bordiga and K. P. Lillerud, *J. Am. Chem. Soc.*, 2008, **130**, 13850.
10. B. Eftekhari-Sis, A. Abdollahifar, M. M. Hashemi and M. Zirak, *Eur. J. Org. Chem.*, 2006, **2006**, 5152.
11. M. M. Salter, J. Kobayashi, Y. Shimizu and S. Kobayashi, *Org. Lett.*, 2006, **8**, 3533.
12. R. Hüttel and P. Jochum, *Eur. J. Inorg. Chem.*, 1952, **85**, 820.
13. S. J. Garibay and S. M. Cohen, *Chem. Commun.*, 2010, **46**, 7700.
14. T. Eicher, A. Speicher and S. Hauptmann, *The Chemistry of Heterocycles: Structures, Reactions, Synthesis, and Applications*, Wiley-VCH, Weinheim, 2012.
15. R. Ameloot, M. Aubrey, B. M. Wiers, A. P. Gómora-Figueroa, S. N. Patel, N. P. Balsara and J. R. Long, *Chem. Eur. J.*, 2013, **19**, 5533.
16. Y. Huang, W. Qin, Z. Li and Y. Li, *Dalton Trans.*, 2012, **41**, 9283.
17. M. Kim, J. F. Cahill, K. A. Prather and S. M. Cohen, *Chem. Commun.*, 2011, **47**, 7629.
18. M. Eddaoudi, J. Kim, N. Rosi, D. Vodak, J. Wachter, M. O'Keeffe and O. M. Yaghi, *Science*, 2002, **295**, 469.
19. H. Yim, E. Kang and J. Kim, *Bull. Korean Chem. Soc.*, 2010, **31**, 1041.
20. S. J. Garibay, Z. Wang, K. K. Tanabe and S. M. Cohen, *Inorg. Chem.*, 2009, **48**, 7341.
21. J. He, K.-K. Yee, Z. Xu, M. Zeller, A. D. Hunter, S. S.-Y. Chui and C.-M. Che, *Chem. Mater.*, 2011, **23**, 2940.
22. W. J. Gee, L. K. Cadman, H. Amer Hamzah, M. F. Mahon, P. R. Raithby and A. D. Burrows, *Inorg. Chem.*, 2016, **55**, 10839.
23. K. Hirai, S. Furukawa, M. Kondo, M. Meilikhov, Y. Sakata, O. Sakata and S. Kitagawa, *Chem. Commun.*, 2012, **48**, 6472.
24. D. N. Dybtsev, H. Chun and K. Kim, *Angew. Chem. Int. Ed.*, 2004, **43**, 5033.
25. J. Y. Lee, L. Pan, S. P. Kelly, J. Jagiello, T. J. Emge and J. Li, *Adv. Mater.*, 2005, **17**, 2703.
26. S. E. Nefedov, *Russ.Chem.Bull.*, 2004, **53**, 259.
27. W. J. Gee and S. R. Batten, *Eur. J. Inorg. Chem.*, 2013, 3240.
28. S.-G. Kang, J. Song and J. H. Jeong, *Inorg. Chim. Acta*, 2004, **357**, 605.
29. C. Volkringer, M. Meddouri, T. Loiseau, N. Guillou, J. Marrot, G. Ferey, M. Haouas, F. Taulelle, N. Audebrand and M. Latroche, *Inorg. Chem.*, 2008, **47**, 11892.
30. J. Canivet, S. Aguado, G. Bergeret and D. Farrusseng, *Chem. Commun.*, 2011, **47**, 11650.

31. M. Savonnet and D. Farrusseng, *PCT Appl.*, WO2011048284, 2011.
32. M. Savonnet, E. Kockrick, A. Camarata, D. Bazer-Bachi, N. Bats, V. Lecocq, C. Pinel and D. Farrusseng, *New J. Chem.*, 2011, **35**, 1892.
33. J. G. Vitillo, T. Lescouet, M. Savonnet, D. Farrusseng and S. Bordiga, *Dalton Trans.*, 2012, **41**, 14236.
34. M. Savonnet, D. Bazer-Bachi, N. Bats, J. Perez-Pellitero, E. Jeanneau, V. Lecocq, C. Pinel and D. Farrusseng, *J. Am. Chem. Soc.*, 2010, **132**, 4518.
35. D. Jiang, L. L. Keenan, A. D. Burrows and K. J. Edler, *Chem. Commun.*, 2012, **48**, 12053.
36. G. Sheldrick, *Acta Cryst. A*, 2008, **64**, 112.

4. Inclusion of Ant Alarm Pheromones into Metal-Organic Frameworks and Their Release

4.1. Introduction

In recent years, there has been a growing interest in using porous materials such as zeolites and MOFs as drug delivery agents.[1-5] The interest in MOFs has largely arisen due to their potential for permanent porosity, and the ability to tailor their properties by functionalising the pore surfaces for specific applications. The ultimate aim of employing MOFs as hosts for biologically active molecules is for the slow release of the drug molecules, which can result in better control of drug administration.

To date, there are two ways of incorporating drug molecules within MOFs. The first approach relies on the MOF acting as a host for a drug molecule, with the controlled delivery typically related to slow diffusion of the guest drug molecule from the pores, Figure 4.1(a). This method can be beneficial for drug molecules without ligating ability to the MOF framework, and their 'containment' in the MOF pores is typically aided by other forces such as hydrogen bonding and π-π interactions. An alternative method involves the incorporation of a drug molecule as a component of the framework itself, *via* covalent attachment, Figure 4.1(b). In this case, controlled delivery arises from the slow breakdown of the MOF structure.

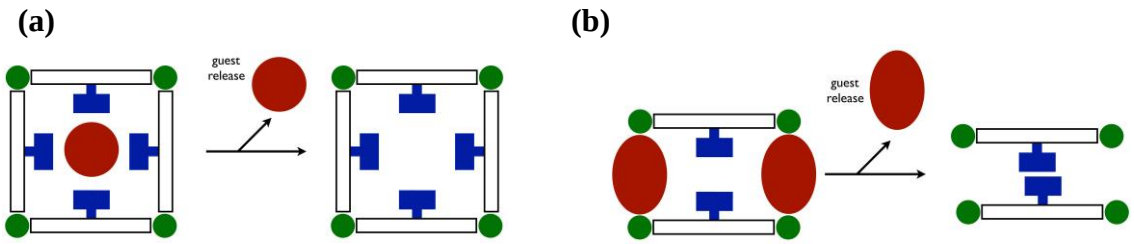

Figure 4.1 Schematic representations of the encapsulation of biologically active molecules within a MOF either **(a)** as a guest or **(b)** as part of the framework, liberated on dissolution. Green circles: metal nodes, white and blue blocks: ligands, dark red circles or ovals: drug molecules.

One of the earliest reports of drug encapsulation in MOFs using the first approach was by Férey *et al.*, in which they described the inclusion and release studies of ibuprofen in $[Cr_3OX(H_2O)_2(BDC)_3]$, MIL-101(Cr) and $[Cr_3OX(H_2O)_2(BTC)_2]$, MIL-100(Cr) (X = OH, F), Figure 4.2 and 4.3.[1] They reported that MIL-101(Cr) and MIL-100(Cr) could host up to 140 wt% and 35 wt% of ibuprofen, respectively. The higher loading in MIL-101(Cr) was attributed to its larger 'cage' size (29 and 34 Å in diameter) compared to

that for MIL-100(Cr) (25 and 29 Å). The kinetics of ibuprofen delivery to simulated body fluid at 37 °C showed that complete release of ibuprofen was achieved after 3 days and 6 days for MIL-100(Cr) and MIL-101(Cr), respectively. The difference in the release kinetics of the drug from each MOF was attributed to the different interactions of each MOF framework with ibuprofen. For example, the release kinetics were slower for MIL-101(Cr) due to the presence of higher proportion of aromatic rings, which increases the number of π-π interactions between the drug molecule and the MOF framework. This method of host-guest interactions to form drug delivery materials has been extended to other MOF systems including MIL-53(Fe) which incorporated 20 wt% of ibuprofen[6] and a chiral zinc MOF based on a triazine-hexacarboxylate ligand which demonstrated encapsulation and release of the anti-cancer drug, 5-fluorouracil.[7]

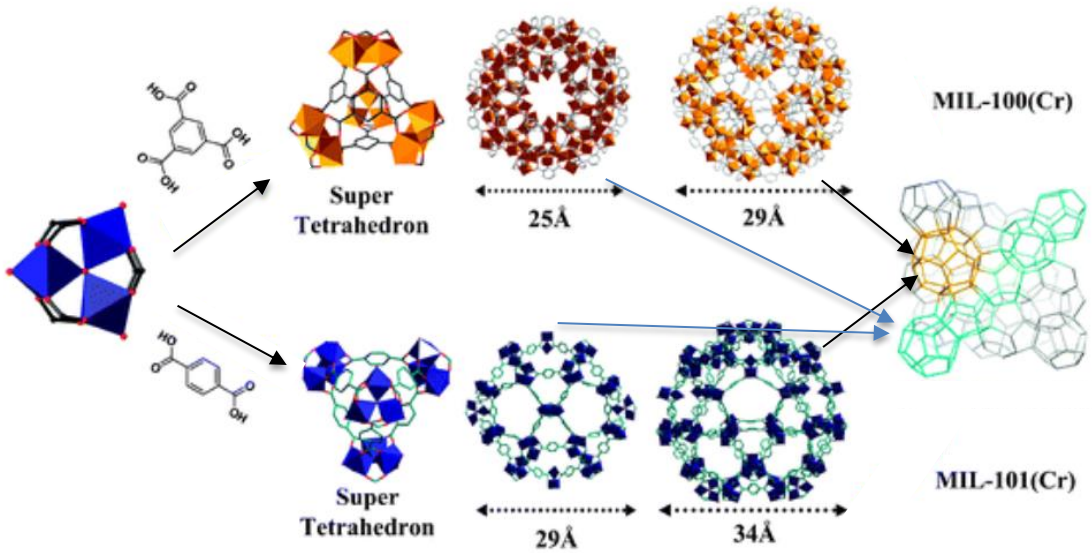

Figure 4.2. Schematic representation of the formation of (top) MIL-100(Cr) and (bottom) MIL-101(Cr) cages.[8]

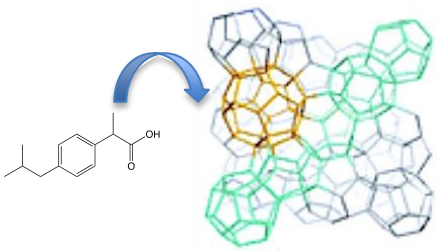

Figure 4.3. Schematic representation of the inclusion of ibuprofen in MIL-100(Cr)/MIL-101(Cr).

In a recent publication, Chowdhuri *et al*. demonstrated the potential of IRMOF-3 as a host for Fe_3O_4 nanoparticles, a MRI contrast agent, and paclitaxel, an anti-cancer drug.[9] The bifunctional MOF was prepared by encapsulating the Fe_3O_4 nanoparticles into the pores of IRMOF-3 followed by paclitaxel *via* diffusion. Rhodamine B isocyanate, a fluorescent tag, was consecutively loaded into the MOF pores for biological imaging applications. The paclitexal molecules were shown to bound to the IRMOF pores due to hydrophobic interactions. A reasonable drug release was observed (65% of the loaded paclitaxel molecules were released in 100 hours) at physiological conditions (pH 7.4). Furthermore, an *in vitro* biological toxicity study revealed that the paclitaxel-loaded MOF targeted and killed cancer cells in a highly effective manner. A magnetic resonance imaging study was also undertaken on the Fe_3O_4 loaded MOF and the results confirmed its effectiveness as an MRI contrast agent.

As described previously, drug molecules can also be incorporated in the MOF frameworks themselves, instead of being hosted in the pores, *via* covalent attachment. Burrows *et al*. reported the synthesis of several zinc-based MOFs with deferiprone being one of the framework constituents.[2] Deferiprone, Figure 4.4, is a drug molecule which can be used to treat β-thalassaemia, an illness which relates to the excess iron in the body, by chelating iron to this drug molecule.

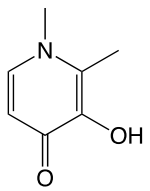

Figure 4.4. Deferiprone.

The use of this drug, in isolation, is not efficient as most of it undergoes biological transformation into a non-chelating compound once introduced into the body. Thus, incorporation of deferiprone as part of the MOF framework, Figure 4.5, is potentially an alternative delivery strategy, as controlled release may assist in preventing the undesirable biotransformations from occurring. It was shown that the release of deferiprone from the MOFs could be achieved by exposing these materials to a phosphate-buffered saline solution or to a dilute acidic (HCl) solution.

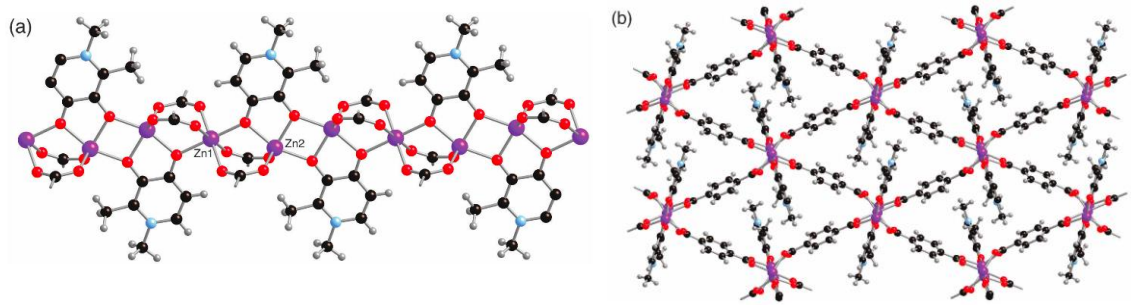

Figure 4.5. The crystal structure of $[Zn_3(BDC)_2(DFP)_2]$ showing **(a)** the infinite SBUs and **(b)** linking of the SBUs into the network. Zn: purple, O: red, N: light blue, C: black, H: silver. DFP: deferiprone.[2]

Drug molecules can also be incorporated on the MOF framework *via* post-synthetic modification (PSM). For example, Lin *et al*. introduced BDC-NH_2 ligands on MIL-101(Fe) framework *via* post-synthetic exchange (PSE) to form a BDC/BDC-NH_2 mixed-ligand system.[10] The amino groups of the BDC-NH_2 linkers were subjected to two different covalent PSM reactions, Figure 4.6. The first reaction was observed with Br-BODIPY (8-bromomethyl-4,4-difluoro- 1,3,5,7-tetramethyl-4-bora-3a,4a-diaza-*s*-indacene), a fluorescent dye used in biosensing, and the second with the anti-cancer drug ESCP (ethoxysuccinato-cisplatin). Covalent grafting of BODIPY and ESCP means that release occurs through decomposition of the framework and therefore is not dependent upon the pore size of the MOF used.

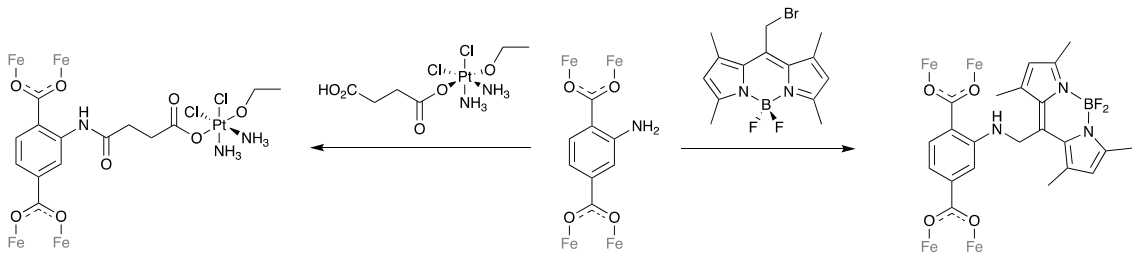

Figure 4.6. Post-synthetic modification of BDC-NH_2 in $[Fe_3OCl(H_2O)_2(BDC)_{3-x}(BDC\text{-}NH_2)_x]$ with the bioactive molecules, ESCP and Br-BIODIPY.[10]

Although there has been considerable effort to incorporate drug molecules in MOFs, other biologically active species have received less attention. These include pesticides and herbicides, which are extensively used in the agricultural industry for crop protection.

With over one billion undernourished people in the world, the need to develop novel crop protection strategies that are easy to implement and transferable to end users is

crucial. Leaf-cutting ants are major pest species of agriculture and forestry in many areas of the Neotropics, where they are considered as a threat to production, with conservative loss estimates in the range of billions of dollars.[11] Attempts to control them are limited by environmental conditions which degrade traditional pesticides, and a lack of target specificity that leads to substantial wastage of pest control products and non-target impacts.

In this context, the use of insect pheromones to attract pest insects to an insecticide bait is an attractive strategy to resolve these problems. Pheromones are chemical substances that insects and other animals release to communicate with other individuals of the same species. In terms of the chemical structure, a large number of insect pheromones are aliphatic carbonyl compounds.[12] Examples of these are shown in Figure 4.7.

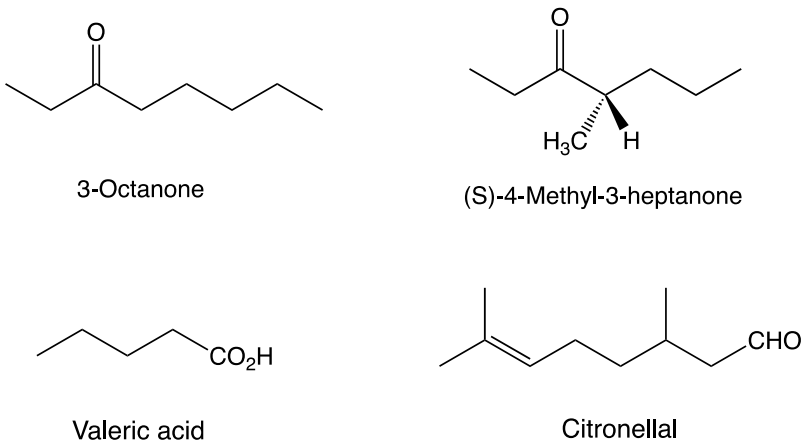

Figure 4.7. Examples of insect pheromones.

In the agricultural industry, the commercial use of pheromones for pest control and detection purposes has progressed rapidly over the last few decades,[13, 14] but it is not as straightforward as it might initially appear. Trail pheromones, used by most ants and termites to organise their foraging, naturally act as short-range signals in a trail, whereas in a control strategy the pheromone is required to act as a long-range attractant to a bait-associated point source. The use of an alarm pheromone as an attractant is counter-intuitive, but leaf-cutting ants (*Atta* and *Acromyrmex* species) typically show an 'aggressive' alarm response, in which workers are attracted by the alarm pheromone to attack the source of the disturbance.[15] Previous work has demonstrated that the most behavioural active components of the alarm pheromones of *Acromyrmex* and *Atta* are 3-octanone and 4-methyl-3-heptanone, respectively,[16, 17] and that these compounds can

attract leaf-cutting ants to an insecticide bait, and then increase bait harvest by the ants as their alarm reaction dissipates to be replaced by foraging behaviour.

However, the high volatility of these compounds makes their use for pest control impractical without a method to bind and then release the compounds in a targeted manner. Thus, controlled-release technology is vital if they are to be used for pest control as this would lead to a more economical and sustainable process. In this context, porous materials such as MOFs offer a novel mechanism of achieving this as these materials allow for slow or environment-specific release of compounds.

A survey of the literature did not reveal any previous studies on the encapsulation of insect pheromones in MOFs. Therefore, the aim of this work was to investigate the possibility of using MOFs as hosts for insect pheromones. The factors which influence the pheromone loading in different MOFs were also investigation targets.

In this study, 3-octanone (OCT), Figure 4.8, was used as a representative insect pheromone as it is relatively cheap and commercially available. As mentioned previously, OCT is an alarm pheromone produced and secreted by ants from a wide variety of species such as *Atta* and *Acromyrmex*.[18] The ants from these species are considered to be a significant agricultural pest as they harvest foliage from live plants. Due to the absence of ligating ability in OCT, the guest-host approach was anticipated for its inclusion in MOFs.

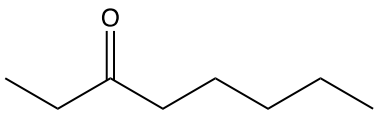

Figure 4.8. 3-Octanone.

4.2. 3-Octanone Loading in Isoreticular Metal-Organic Frameworks, IRMOFs

The IRMOF system was initially selected for the OCT inclusion study due to its ease of functionalisation and high crystallinity. The IRMOFs, Figure 4.9, were chosen based on the postulation that the presence of either a hydrogen bond donor (in IRMOF-3) to interact with the OCT carbonyl group, or an alkyl group (*e.g.* IRMOF-NHPr) to provide

a hydrophobic pore environment, would be beneficial for the OCT uptake. Furthermore, the IRMOF pores (pore aperture 11.0 Å × 11.0 Å in IRMOF-1) were anticipated to be large enough to accommodate OCT which has approximate dimensions of 13.0 Å × 5.5 Å × 4.2 Å.

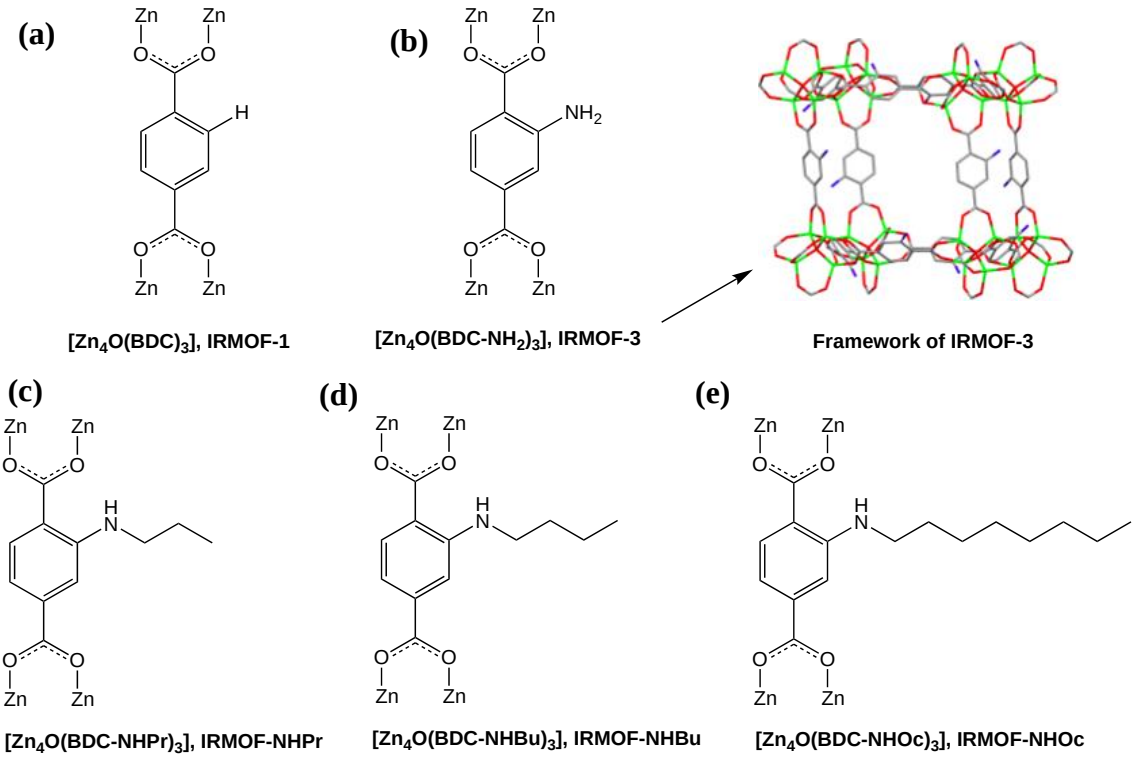

Figure 4.9. The IRMOFs used in the 3-octanone inclusion study. Pr: propyl, Bu: butyl, Oc: octyl. The framework of IRMOF-3 is also shown for reference. Zn: light green, C: grey, N: blue, O: red. Hydrogen atoms omitted for clarity.

4.2.1. 3-Octanone Loading in [$Zn_4O(BDC\text{-}NH_2)_3$], IRMOF-3: An Investigation of Reaction Conditions on the Degree of Inclusion

As a proof of concept, [$Zn_4O(BDC\text{-}NH_2)_3$], IRMOF-3, Figure 4.9(b), was employed as a pilot MOF for the inclusion study. IRMOF-3 was chosen due to the presence of hydrogen atoms from the amino groups as hydrogen bond donor which could interact with the OCT carbonyl group. Furthermore, IRMOF-3 has an aperture size of 9.6 x 9.6 Å, which is large enough for the inclusion of OCT in its pores.

IRMOF-3 was synthesised based on the previously reported procedure by Kim and co-workers.[19] In a typical experiment, $Zn(NO_3)_2 \cdot 6H_2O$ and $H_2BDC\text{-}NH_2$ were dissolved in DMF in a glass vial. The vial was sealed and the reaction mixture was heated at 105 °C

for 48 hours to yield pale brown cubic crystals. The crystals were then washed and soaked in chloroform for 3 days, replacing the solvent with fresh solvent every 24 hours before collecting the crystals by filtration. The crystals were dried under reduced pressure and stored under an inert atmosphere (N_2) to avoid crystal degradation.

In terms of the OCT inclusion procedure, different parameters (reaction temperature, reaction time and amount of OCT) were investigated with the aim of determining the optimum conditions for the highest pheromone inclusion, without adversely affecting the MOF crystallinity. A general procedure for the inclusion experiment is as follows. In a glass vial containing 5 mL DMF, IRMOF-3 crystals were added, followed by OCT. The vial was sealed and the mixture was agitated briskly before leaving it to stand. The crystals were then isolated *via* filtration and rinsed once with fresh DMF (3 mL) to remove any residual OCT on the crystal surfaces. The schematic representation of this general procedure is shown in Scheme 4.1.

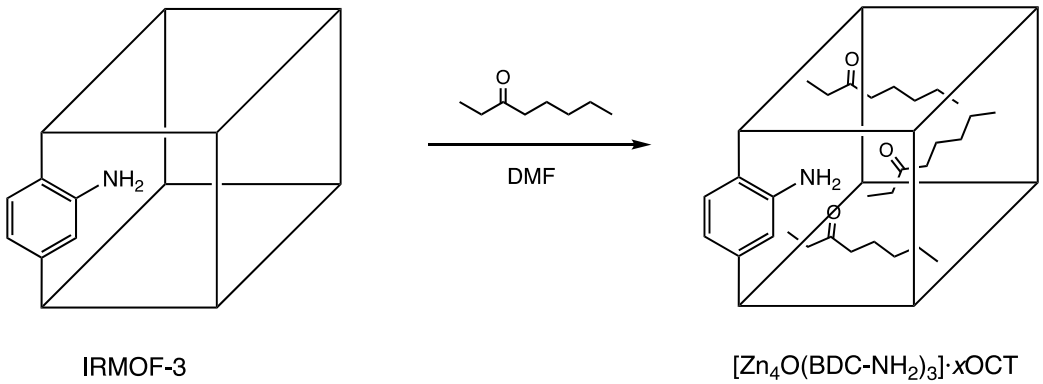

Scheme 4.1. General procedure for the OCT inclusion in IRMOF-3. IRMOF-3 is represented by the cubic polyhedra.

Initially, thermogravimetric analysis (TGA) was employed, in an attempt to determine the amount of OCT in the MOF pores. However, preliminary results highlighted the ambiguity of this method for accessing the OCT loading in MOFs. This is due to the overlapping of mass decrease associated with OCT and the solvent used in this study. Therefore, it was impossible to distinguish the mass loss attributable to OCT alone. Furthermore, the departure of OCT from the pores of MOF could occur over a wide range of temperatures, depending on the strength of interactions between OCT and the MOF framework. Due to these problems, a decision was made to employ ^{1}H NMR spectroscopy to quantify the MOF OCT loadings.

The ^{1}H NMR spectrum of neat OCT, Figure 4.10, shows the presence of peaks in the aliphatic region, which correspond to the alkyl protons of OCT. The presence of these peaks in the ^{1}H NMR spectra of digested OCT treated MOFs would indicate that the inclusion experiment was successful.

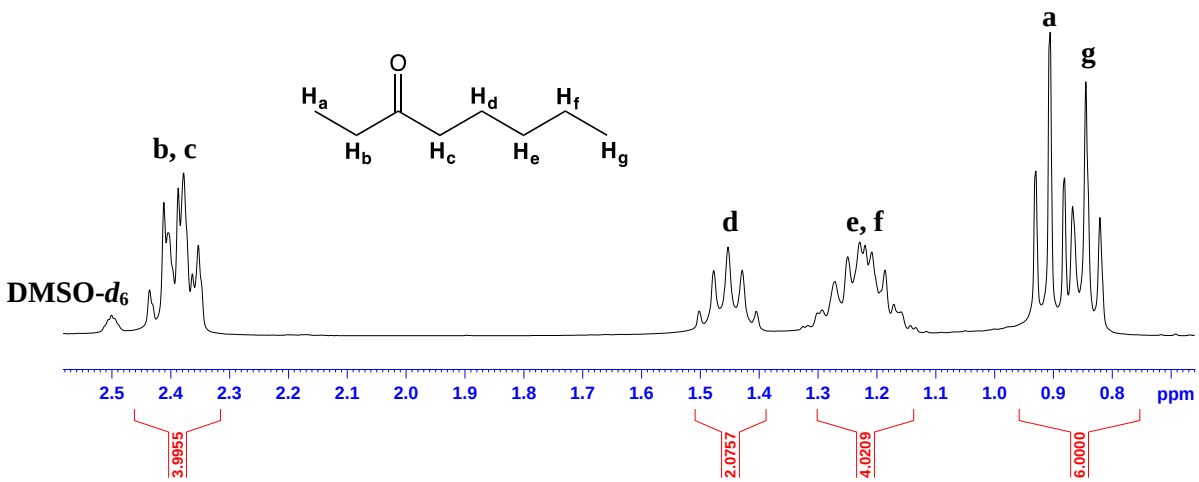

Figure 4.10. ^{1}H NMR spectrum of OCT in DMSO-d_6 and DCl/D_2O.

The degree of OCT inclusion in IRMOF-3 with respect to varying reaction parameters are shown in Table 4.1. The values were obtained based on the ^{1}H NMR analyses of the digested OCT treated MOFs.

Entry	IRMOF-3:OCT (eq.)	Reaction time (days)	Reaction temperature (°C)	$D_2BDC-NH_2$:OCT	Product
1	1:1	1	r.t.	0	$[Zn_4O(BDC-NH_2)_3]$
2	1:2				
3	1:3				
4	1:4				
5	1:1	2			
6	1:2				
7	1:3				
8	1:4				
9	1:1	3			
10	1:2				
11	1:3				
12	1:4			1:0.14	$[Zn_4O(BDC-NH_2)_3]\cdot 0.4OCT$ (6.3 wt%)
13	1:1		50	0	$[Zn_4O(BDC-NH_2)_3]$
14	1:2				
15	1:3				
16	1:4				
17	1:Neat	3	r.t.	1:0.19	$[Zn_4O(BDC-NH_2)_3]\cdot 0.6OCT$ (9.5 wt%)

Table 4.1. The reaction conditions used in the OCT inclusion study in IRMOF-3. Crystals were washed once with DMF upon treatment with OCT. $D_2BDC-NH_2$ represents the deuterated $BDC-NH_2$ ligand in the ^1H NMR digestion solvent.

As shown in Table 4.1, a small quantity of OCT (6.3 wt%) was successfully loaded into the pores of IRMOF-3 using the conditions stated in entry 12 (reaction conditions: 4 eq. of OCT, 3 days, r.t.). Somewhat surprisingly, increasing the reaction temperature did not result in a higher loading. In fact, no OCT was detected when the reaction temperature was increased to 50°C. This is probably due to the high volatility of OCT such that, at 50°C, it may have evaporated from the solution. Performing the reaction in neat OCT (entry 17) also did not lead to a significant increase in OCT uptake (3.2 wt% increase). This shows that performing the inclusion experiment in neat OCT is unlikely to justify the additional expense, especially for inclusion of more expensive pheromones. Thus, the parameters shown in entry 12 were selected as the optimum conditions for the OCT inclusion study, Scheme 4.2.

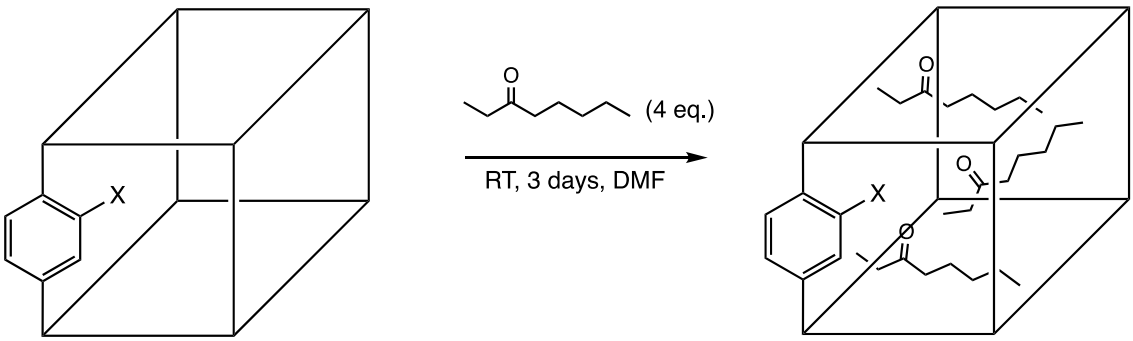

Scheme 4.2. Schematic representation for the OCT inclusion in IRMOFs showing the optimum conditions. The IRMOFs are represented by the cubic polyhedra. X = H, NH_2, NHPr, NHBu, NHOc.

The ^{1}H NMR spectrum of the digested OCT treated MOF (from entry 12), **3a**, is shown in Figure 4.11, and was obtained by digesting the sample in a mixture of DCl/D_2O and DMSO-d_6. Acid digestion had to be used to cleave the Zn-O bonds of the SBUs and to solubilise the MOF. A similar digestion procedure was adopted for all MOFs used in this study.

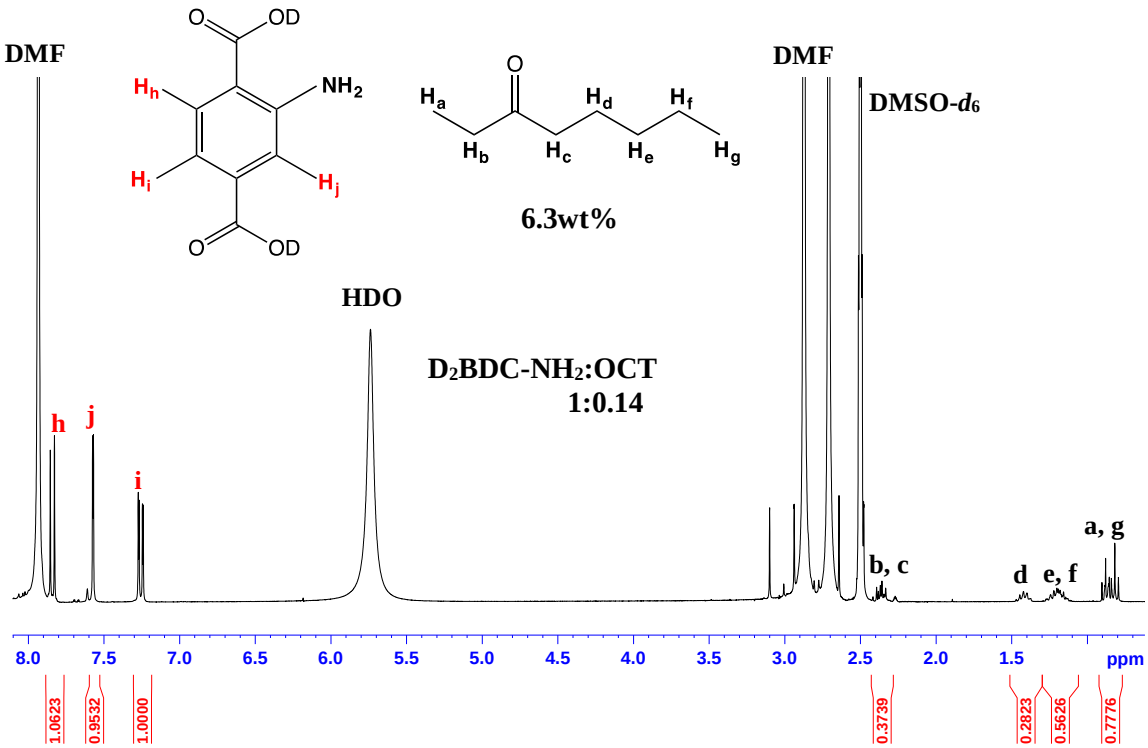

Figure 4.11. The ^{1}H NMR spectrum for **3a** (rinsed once with DMF).

The presence of peaks attributed to the alkyl protons of OCT in the ^{1}H NMR spectrum of digested sample **3a** implies that OCT was successfully loaded in the pores of IRMOF-3. The OCT loading was determined by comparing the integrals at δ 7.26 ppm

and δ 1.45 ppm which correspond to the aryl protons from D_2BDC-NH_2, H_i and alkyl protons, H_d from OCT, respectively. The ratio of D_2BDC-NH_2 to OCT was calculated as being approximately 1:0.14 which gives the formula for **3a** as [Zn_4O(BDC-NH_2)$_3$]·0.4OCT (6.3 wt% OCT loading).

The significant peaks at δ 2.72, 2.88 and 7.93 ppm correspond to the protons from DMF solvent which is in the pores and on the crystal surface. The broad peak at δ 5.78 ppm on the other hand, is attributed to HDO solvent used in the digestion.

To investigate the effect of washing on OCT loading, **3a** was rinsed one further time with DMF (3 mL) and then analysed by ^{1}H NMR spectroscopy following digestion. The ^{1}H NMR spectrum, Figure 4.12, shows the presence of OCT, but in a smaller quantity (D_2BDC-NH_2:OCT = 1:0.06). This gives the formula after a second washing as [Zn_4O(BDC-NH_2)$_3$]·0.2OCT (3.1 wt%).

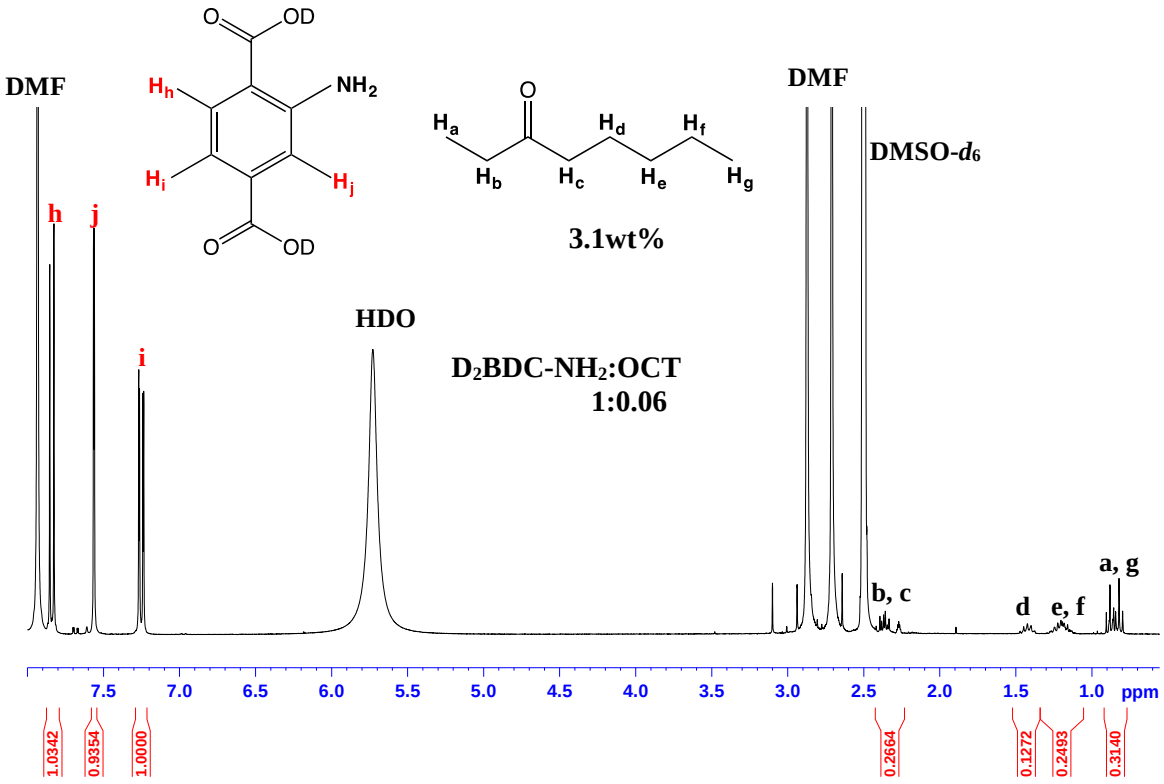

Figure 4.12. The ^{1}H NMR spectrum for **3a** (rinsed one further time with DMF).

This result shows that OCT remained encapsulated in the pores of IRMOF-3 even after washing twice, and this may possibly be attributed to hydrogen bonding interactions.

However, the effect of washing on the OCT loading cannot be neglected, whereby 3.2 wt% (0.2 equivalents) loss was observed on washing twice.

4.2.2. 3-Octanone Loading in $[Zn_4O(BDC)_3]$, IRMOF-1

In order to confirm that hydrogen bond donors contribute to the containment of OCT in IRMOF-3 rather than other factors, a control experiment was performed on $[Zn_4O(BDC)_3]$, IRMOF-1, Figure 4.9(a). This MOF is the simplest in the IRMOF series, bearing no functional groups on the BDC ligand.

IRMOF-1 was synthesised based on the previously reported procedure by Yaghi and co-workers, Scheme 4.3.[20] In a typical procedure, $Zn(NO_3)_2 \cdot 6H_2O$ and H_2BDC were dissolved in DEF in a glass vial. The vial was sealed and the reaction mixture was heated at 105 °C for 48 hours to yield colourless cubic crystals. The crystals were then washed and soaked in chloroform for 3 days, replacing the solvent with fresh solvent every 24 hours before collecting the crystals by filtration. The crystals were dried under reduced pressure and stored under an inert atmosphere (N_2) to avoid crystal degradation.

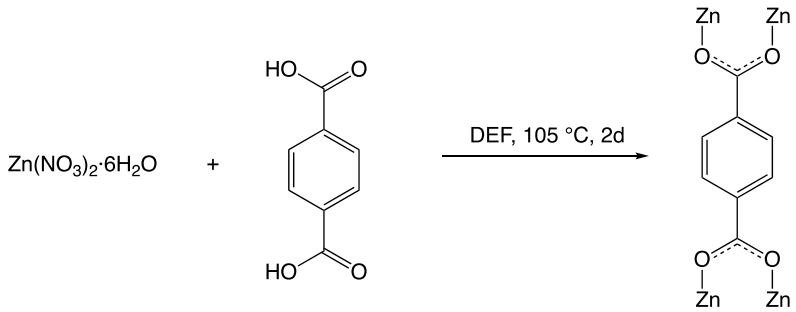

Scheme 4.3. Direct synthesis of $[Zn_4O(BDC)_3]$, IRMOF-1.

The OCT loading in IRMOF-1 was performed using the conditions shown in Scheme 4.4.

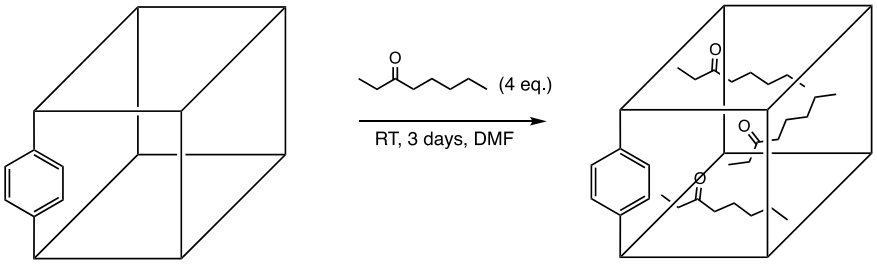

Scheme 4.4. Schematic representation of OCT loading in IRMOF-1.

In a typical procedure, IRMOF-1 crystals were added in a glass vial containing DMF as a solvent. OCT was then added and the vial was sealed. The mixture was agitated briskly before leaving it to stand at room temperature for 3 days. The crystals were then isolated *via* filtration and rinsed once with fresh DMF to remove any residual OCT on the crystal surface.

Analysis of the ^{1}H NMR spectrum of the digested MOF, Figure 4.13, reveals that the ratio of D_2BDC to OCT was calculated as being approximately 1:0.08 which gives the formula for **3b** as $[Zn_4O(BDC)_3]\cdot 0.2OCT$. This corresponds to 3.3 wt% OCT loading.

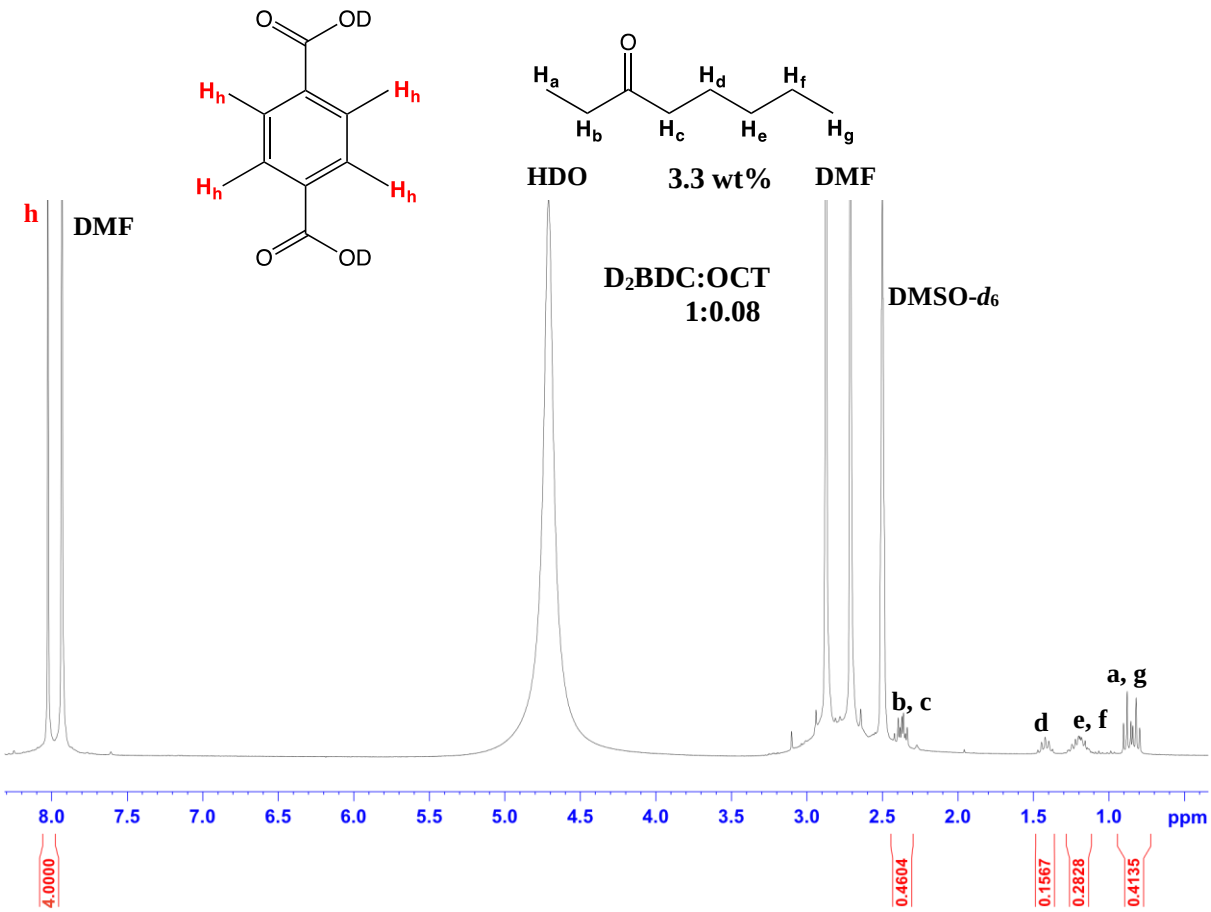

Figure 4.13. The ^{1}H NMR spectrum for **3b** (rinsed once with DMF).

Sample **3b** was rinsed a further time to determine if there was any interaction between OCT and the MOF framework. The ^{1}H NMR spectrum of the digested MOF, Figure 4.14, shows the disappearance of peaks attributed to the protons from OCT. These results suggest that interactions between OCT and the MOF framework are weak, which is evidenced by the very small loading of OCT in IRMOF-1 (3.3 wt% OCT after first wash with DMF) and the ease of removing it by simply washing the sample.

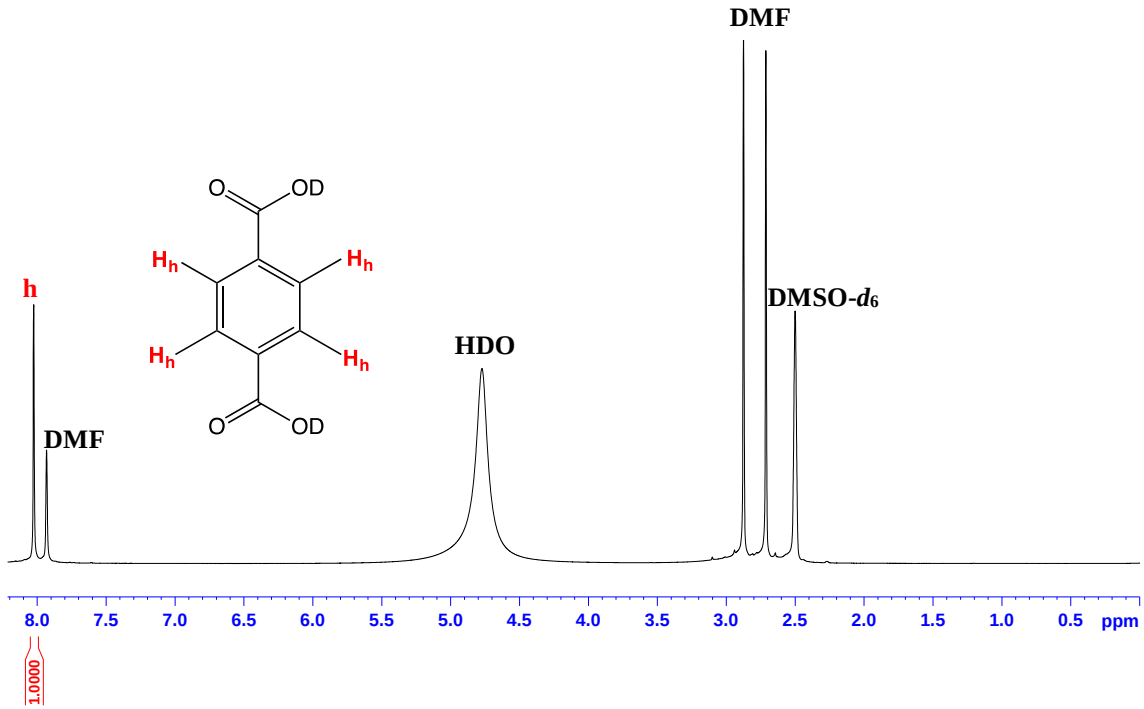

Figure 4.14. The ^{1}H NMR spectrum for **3b** (rinsed twice with DMF).

The ability of IRMOF-3 to host a higher amount of OCT in its pores compared to that in IRMOF-1 validates the hypothesis that the presence of hydrogen atoms from the amino groups is beneficial, as they could form hydrogen bonds with the oxygen atoms in OCT. This means OCT molecules are potentially 'held' in the pores of IRMOF-3 *via* hydrogen bonding.

4.2.3. 3-Octanone Loading in [$Zn_4O(BDC\text{-}NHPr)_3$], IRMOF-NHPr

[$Zn_4O(BDC\text{-}NHPr)_3$], IRMOF-NHPr, Figure 4.9(c), which has propyl groups protruding into its pores, was used in this study to investigate the effect of alkyl groups on OCT uptake.

In terms of the MOF synthesis, the dicarboxylic acid, $H_2BDC\text{-}NHPr$ was first synthesised as it is not available commercially. $H_2BDC\text{-}NHPr$ was prepared using the procedure previously reported by Burrows and co-workers, Scheme 4.5.[21] In a typical procedure, $H_2BDC\text{-}NH_2$ was dissolved in DMF, then propanal was added and the solution was stirred for 1 hour. The solution was cooled in an ice bath and $NaCNBH_3$ was added. The resulting reaction mixture was stirred at room temperature for 1 day,

after which it was acidified with HCl. Water was then added until a yellow solid precipitated. The ^{1}H NMR spectrum of the product confirms the identity of this material (Section 4.11.1.1).

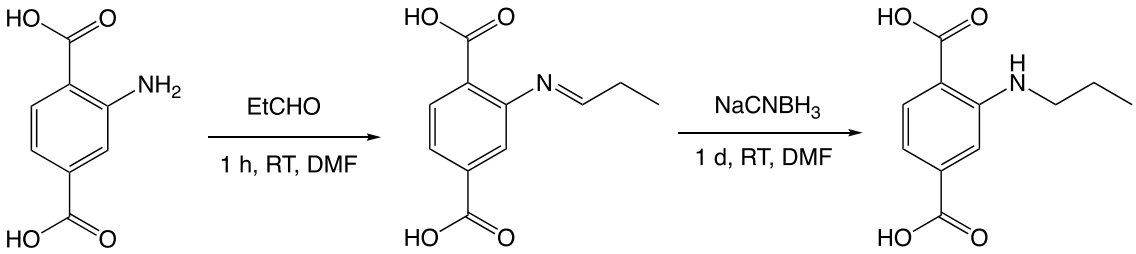

Scheme 4.5. The synthesis of H_2BDC-NHPr.

This dicarboxylic acid was then used to prepare [Zn_4O(BDC-NHPr)$_3$], IRMOF-NHPr, using the procedure previously reported by Burrows and co-workers, Scheme 4.6.[21] Typically, $Zn(NO_3)_2 \cdot 6H_2O$ and H_2BDC-NHPr were dissolved in DMF in a glass vial, which was sealed before heating the reaction mixture at 105 °C for 48 hours, to yield yellow-orange cubic crystals. This product was then washed and soaked in chloroform for 3 days, replacing the solvent with fresh solvent every 24 hours before collecting the crystals by filtration. The crystals were dried under reduced pressure and stored under an inert atmosphere (N_2) to avoid crystal degradation.

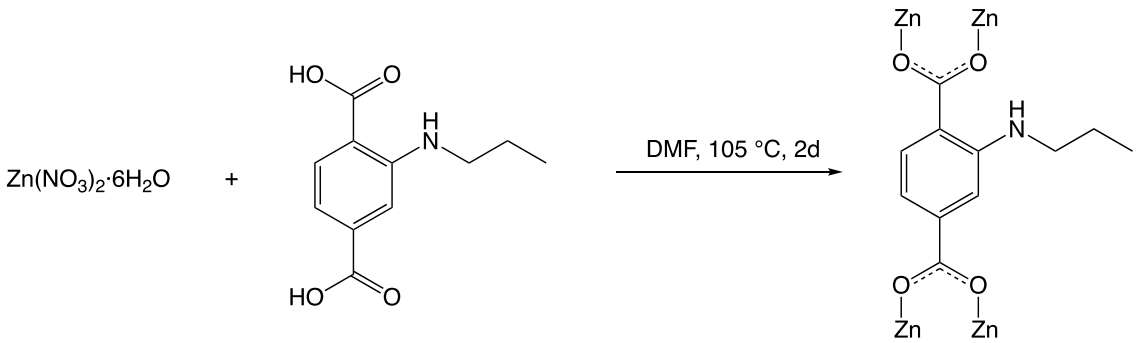

Scheme 4.6. Direct synthesis of [Zn_4O(BDC-NHPr)$_3$], IRMOF-NHPr.

The MOF synthesis was successful, as evidenced by the high similarities of the PXRD patterns of the material and IRMOF-1 (Section 4.11.2.3). This shows that both MOFs are isostructural.

The OCT inclusion in IRMOF-NHPr, Scheme 4.7, was performed using the same procedure as that for IRMOF-3 and IRMOF-1.

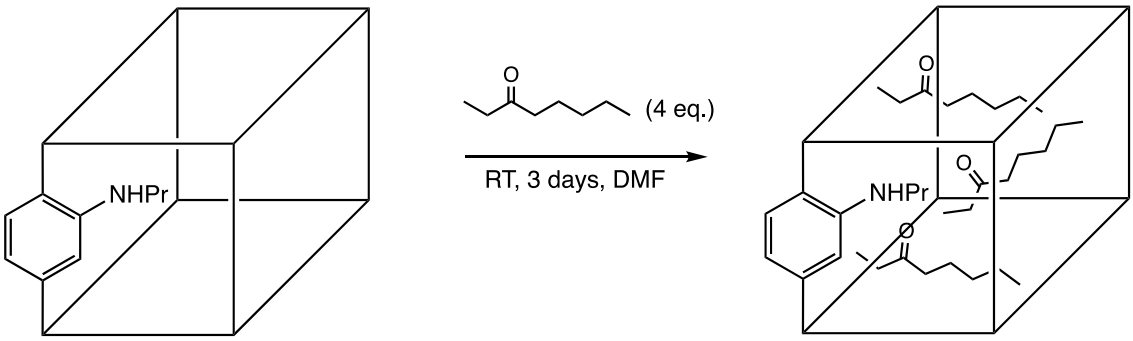

Scheme 4.7. Schematic representation for the OCT inclusion in IRMOF-NHPr. Pr: propyl.

The ^{1}H NMR spectrum of the digested OCT treated MOF, **3c** shows the presence of OCT peaks in addition to the signals which correspond to D_2BDC-NHPr, Figure 4.15.

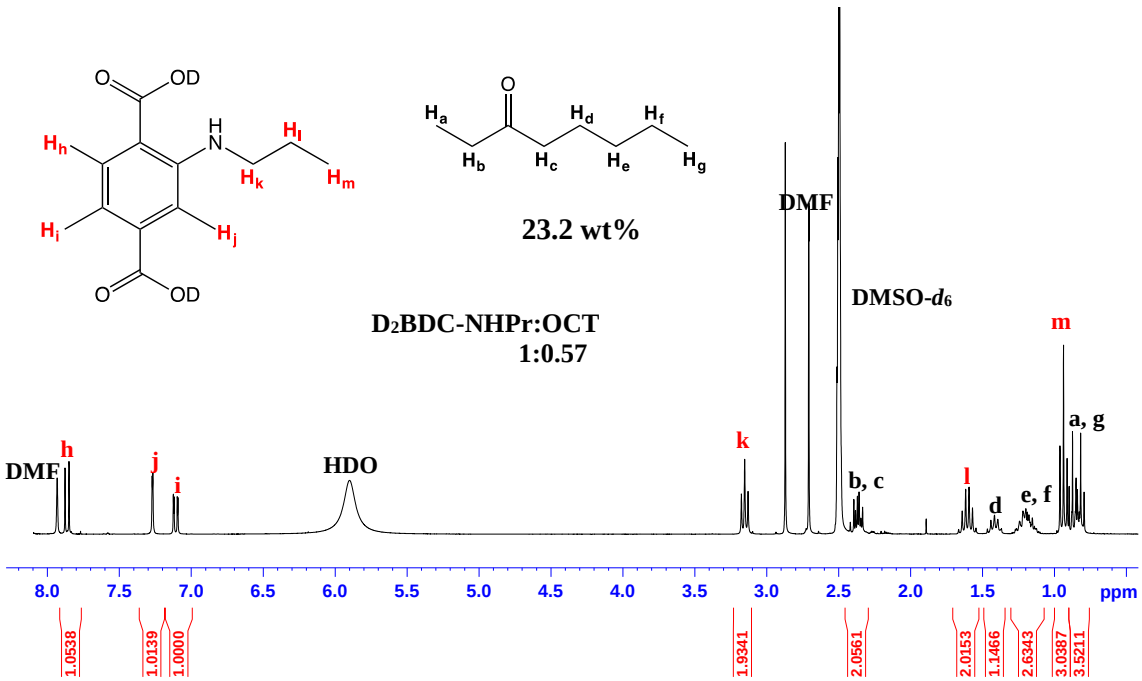

Figure 4.15. The ^{1}H NMR spectrum for **3c** (rinsed once with DMF).

The ratio of D_2BDC-NHPr to OCT was calculated by comparing the integrals at δ 7.14 ppm and δ 1.45 ppm which correspond to the aryl protons from D_2BDC-NH_2, H_i and alkyl protons, H_d from OCT, respectively. This was calculated as being approximately 1:0.57 which gives the formula for **3c** as $[Zn_4O(BDC\text{-}NHPr)_3]\cdot 1.7OCT$ (23.2 wt%).

Sample **3c** was washed a further time with DMF to gauge how easy it was to remove OCT from its pores. The ^{1}H NMR analysis of the sample upon digestion reveals the

chemical composition as $[Zn_4O(BDC\text{-}NHPr)_3]\cdot 1.5OCT$ (20.5 wt%), Figure 4.16. This means that 2.7 wt% OCT loss was observed upon the second wash.

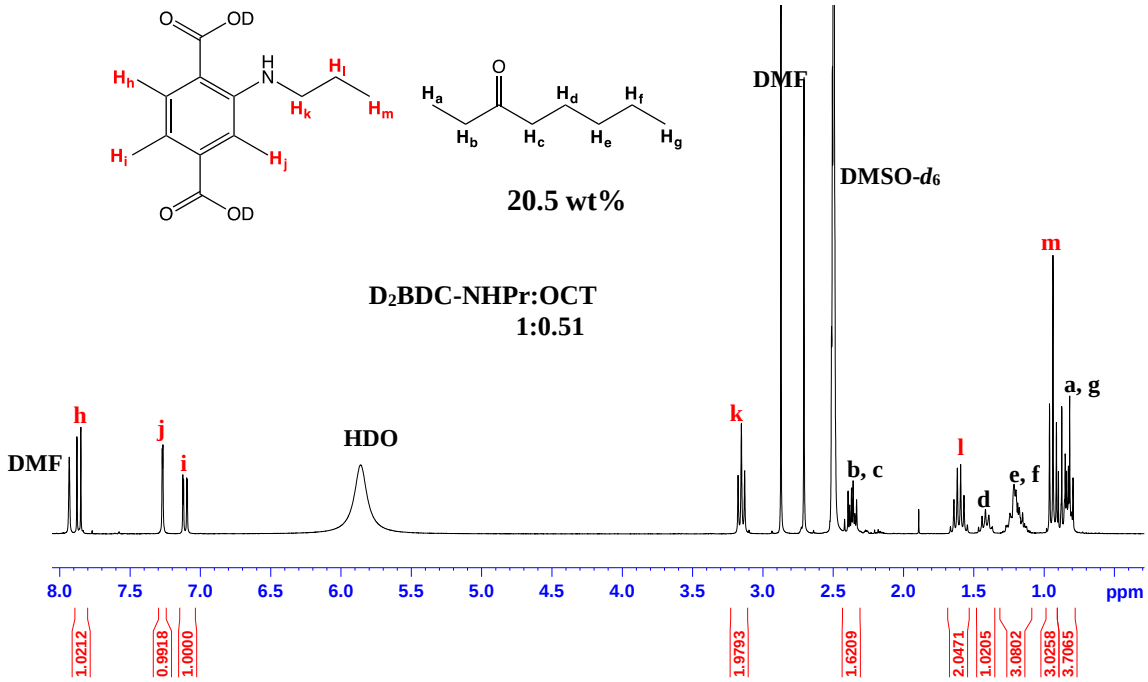

Figure 4.16. The ^{1}H NMR spectrum for **3c** (rinsed twice with DMF).

A third DMF rinse was also performed on **3c** and the ^{1}H NMR spectrum of the digested sample, Figure 4.17, shows a ratio of D_2BDC-NHPr to OCT as 1:0.48 which gives the formula as $[Zn_4O(BDC\text{-}NH_2)_3]\cdot 1.4OCT$ (19.1 wt%). This corresponds to an overall 4.1 wt% loss of OCT upon washing **3c** thrice.

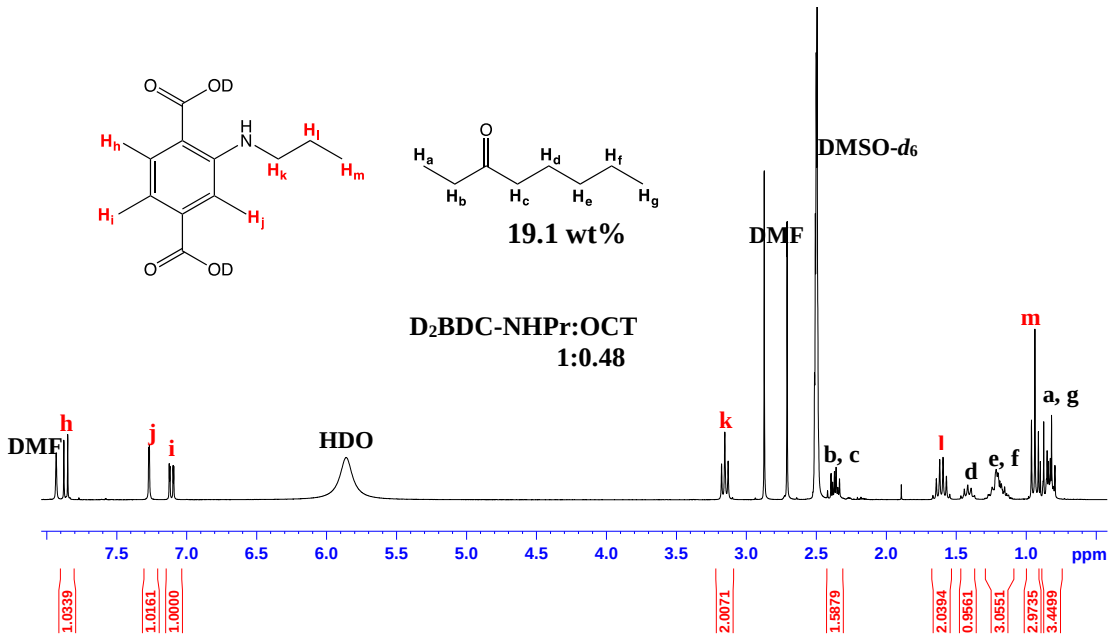

Figure 4.17. The ^{1}H NMR spectrum for **3c** (rinsed three times with DMF).

Based on the results presented thus far, it is clear that IRMOF-NHPr (after first wash = 23.2 wt%, after second wash = 20.5 wt%, after third wash = 19.1 wt%) could accommodate more OCT in its pores than IRMOF-3 (after first wash = 6.3 wt%, after second wash = 3.1 wt%). At first sight, this is surprising since IRMOF-NHPr has a lower surface area (S_{BET} = 1914 m^2/g) than that for IRMOF-3 (S_{BET} = 2613 m^2/g).[2]

However, the higher OCT uptake in IRMOF-NHPr is consistent with the presence of the hydrophobic propyl groups in its pores which have a high affinity towards hydrophobic OCT. Another factor that may contribute to the higher OCT loading in IRMOF-NHPr is the hydrogen bonding between the oxygen of OCT and the hydrogen from the secondary amine group in IRMOF-NHPr.

As stated in Section 4.2.1, in the case of IRMOF-3, performing the inclusion study in neat OCT did not give a significant impact on the OCT uptake. In order to investigate if the same conclusion can be applied to other IRMOFs, a similar experiment was performed on IRMOF-NHPr using the conditions stated in Scheme 4.8.

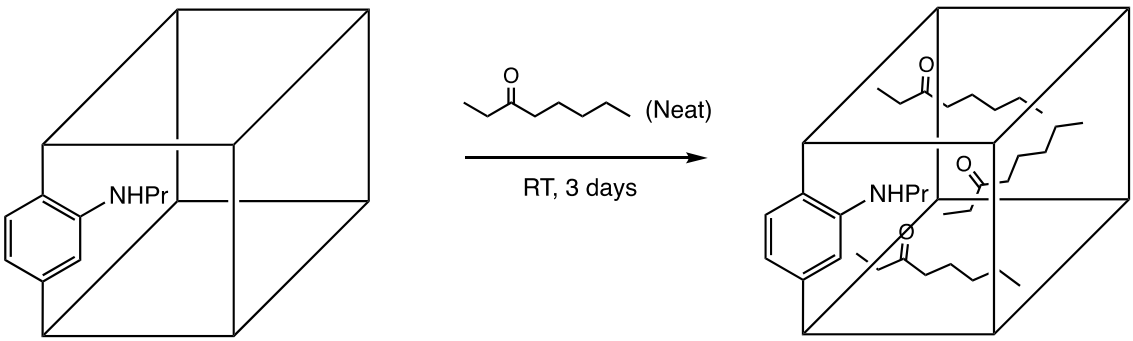

Scheme 4.8. Schematic representation of OCT loading in IRMOF-NHPr in neat OCT. Pr: propyl.

As in the case of IRMOF-3, IRMOF-NHPr crystals were added in a glass vial containing neat OCT. The vial was sealed and the mixture was agitated briskly before leaving it to stand at room temperature for 3 days. The crystals were then isolated *via* filtration.

The crystals were tacky upon isolation from OCT, which suggests that OCT was present on the crystal surfaces, in addition to in the pores. Thus, the crystals were washed once with DMF to remove the residual OCT on the crystal surfaces, after which they became free-flowing which indicates that OCT was no longer present on the external surfaces.

Analysis of the ^{1}H NMR spectrum of the digested MOF, **3d** reveals that the sample contained 36.8 wt% OCT, and could be represented by the formula [$Zn_4O(BDC\text{-}NH_2)_3$]·2.7OCT, Figure 4.18. Further washing with one or two portions of DMF reduced the OCT content to 30.0 wt% (Figure 4.19) and 23.2 wt% (Figure 4.20), respectively.

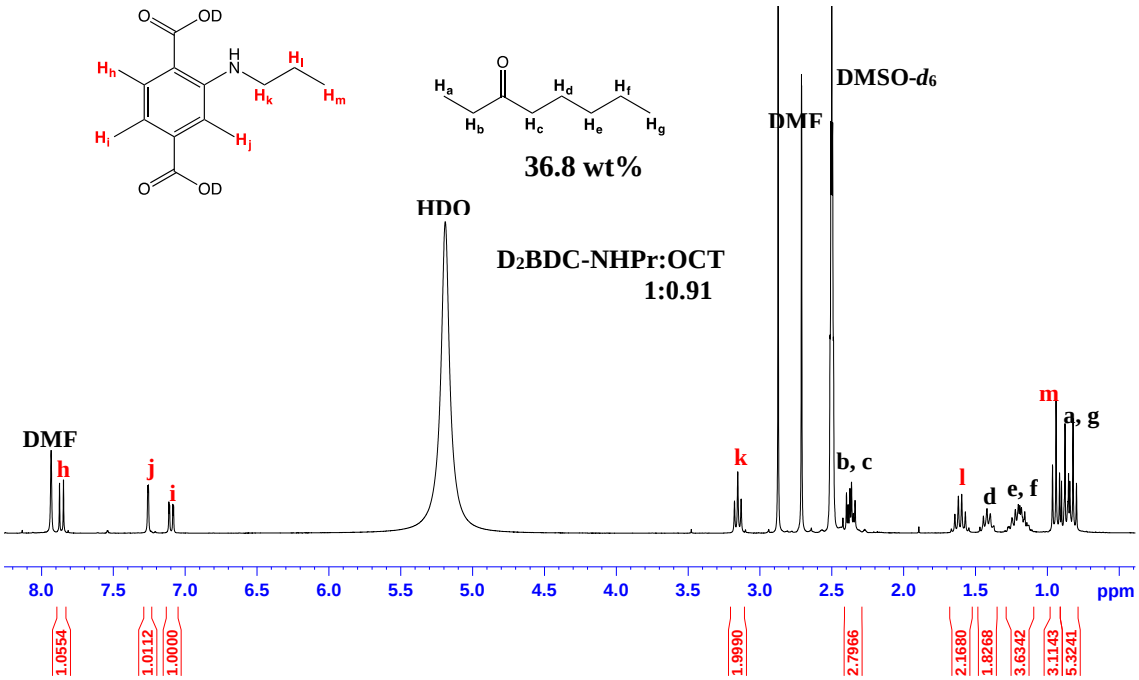

Figure 4.18. The ^{1}H NMR spectrum for **3d** (rinsed once with DMF).

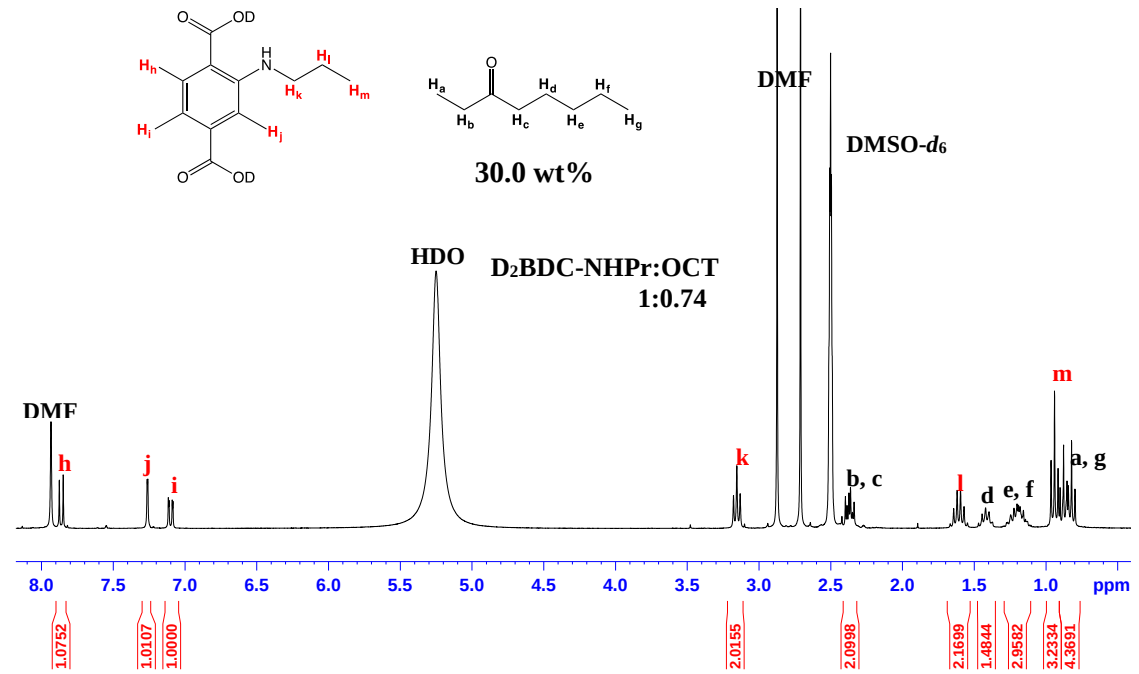

Figure 4.19. The ^{1}H NMR spectrum for **3d** (rinsed twice with DMF).

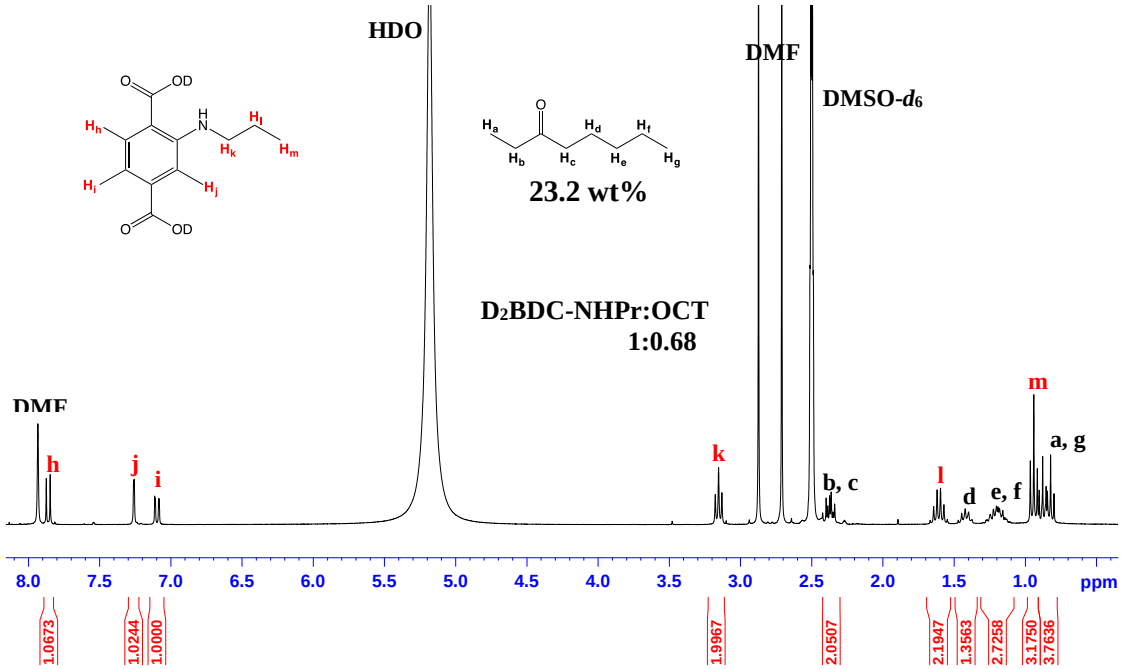

Figure 4.20. The ^{1}H NMR spectrum for **3d** (rinsed three times with DMF).

Similar to the results obtained for IRMOF-3, the OCT loading in IRMOF-NHPr is increased by moving from a solution containing four equivalents of OCT to neat OCT, but this increase in uptake is relatively small (13.6 wt%). Once again, these gains are unlikely to justify the additional expense, especially for inclusion of more expensive pheromones.

4.2.4. 3-Octanone Loading in [$Zn_4O(BDC\text{-}NHBu)_3$], IRMOF-NHBu

The OCT inclusion study on [$Zn_4O(BDC\text{-}NHBu)_3$], IRMOF-NHBu, Figure 4.9(d), was carried out with the aim of investigating the effect of longer alkyl chains on OCT uptake.

In a similar vein to $H_2BDC\text{-}NHPr$ (Section 4.2.3), the dicarboxylic acid, $H_2BDCNHBu$ was first synthesised as it is not available commercially. The synthetic procedure employed was previously reported by Burrows and co-workers, Scheme 4.9.[21] In particular, $H_2BDC\text{-}NH_2$ was dissolved in DMF, then butanal was added and the solution was stirred for 1 hour. The solution was then cooled in an ice bath and $NaCNBH_3$ was added. Stirring at room temperature for 1 day followed, before the mixture was acidified

with HCl. Water was then added until a yellow solid precipitated. The ^{1}H NMR spectrum of the isolated product confirms the identity of the material (Section 4.11.1.2).

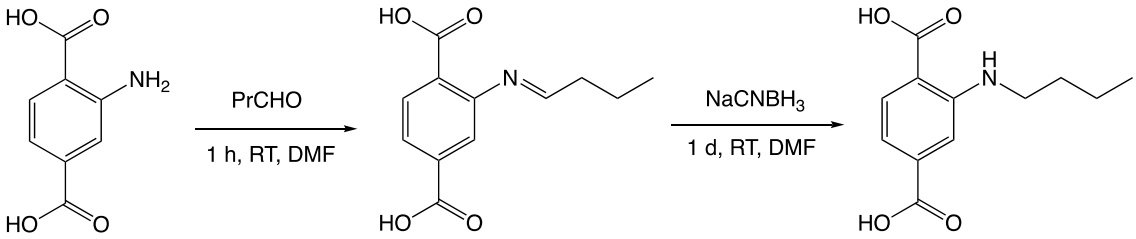

Scheme 4.9. The synthesis of H_2BDC-NHBu.

The MOF [Zn_4O(BDC-NHBu)$_3$], IRMOF-NHBu was synthesised using an analogous synthesis to that of IRMOF-NHPr, Scheme 4.10.[21]

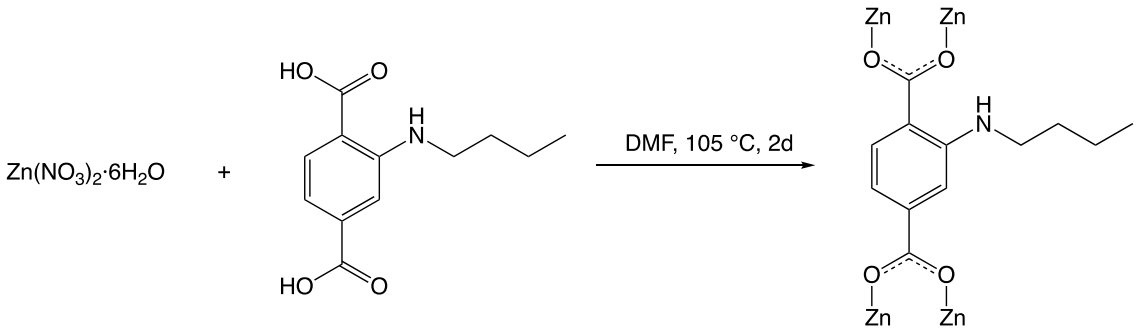

Scheme 4.10. Direct synthesis of [Zn_4O(BDC-NHBu)$_3$], IRMOF-NHBu.

The MOF synthesis was successful, as evidenced by the high similarities of the PXRD patterns between the material and IRMOF-1 (Section 4.11.2.4).

IRMOF-NHBu was then used for the OCT inclusion study, on the basis of the conditions shown in Scheme 4.10.

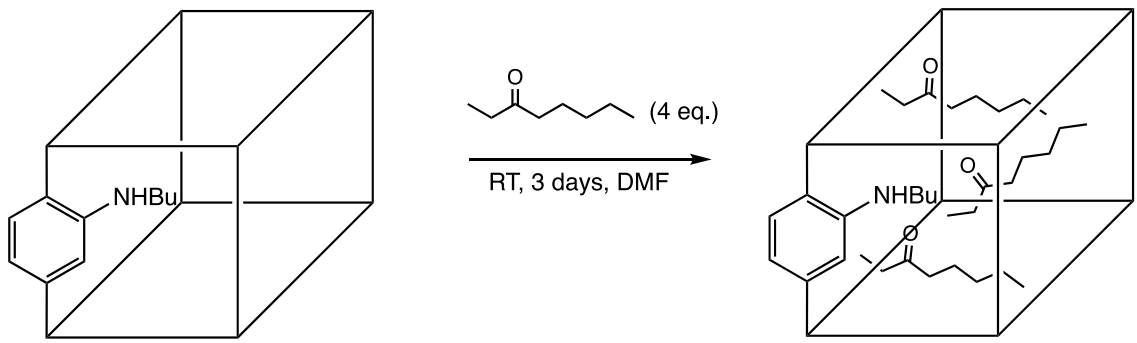

Scheme 4.10. Schematic representation of OCT loading in IRMOF-NHBu. Bu: butyl.

The ^{1}H NMR spectrum of the digested OCT treated MOF, **3e** shows the presence of OCT peaks in addition to the signals which correspond to D_2BDC-NHBu, Figure 4.21.

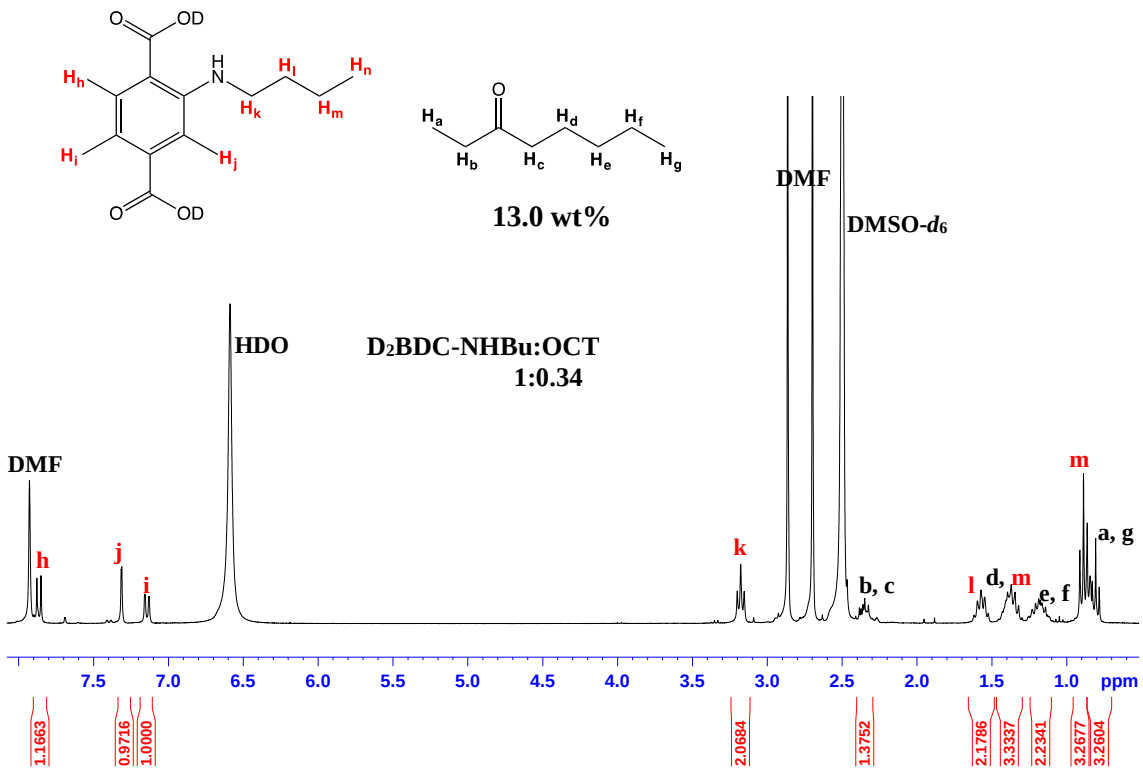

Figure 4.21. The ^{1}H NMR spectrum for **3e** (rinsed once with DMF).

The OCT loading in **3e** was calculated by comparing the integrals at δ 7.13 ppm and δ 2.35 ppm which correspond to an aryl proton of D_2BDC-NHBu, H_i and alkyl protons, $H_{b,c}$ from OCT, respectively. The ratio of D_2BDC-NHBu to OCT was calculated as being approximately 1:0.34 which gives the formula for **3e** as $[Zn_4O(BDC\text{-}NHBu)_3]\cdot 1.0OCT$. This corresponds to 13.0 wt% OCT loading.

The ^{1}H NMR analysis of digested **3e** after rinsing twice with DMF reveals the same quantity of OCT in its pores, Figure 4.22. The formula can be expressed as $[Zn_4O(BDC\text{-}NHBu)_3]\cdot 1.0OCT$. Moreover, further rinsing with DMF also did not reduce the OCT loading (the ^{1}H NMR spectrum can be found in Section 4.11.3.5).

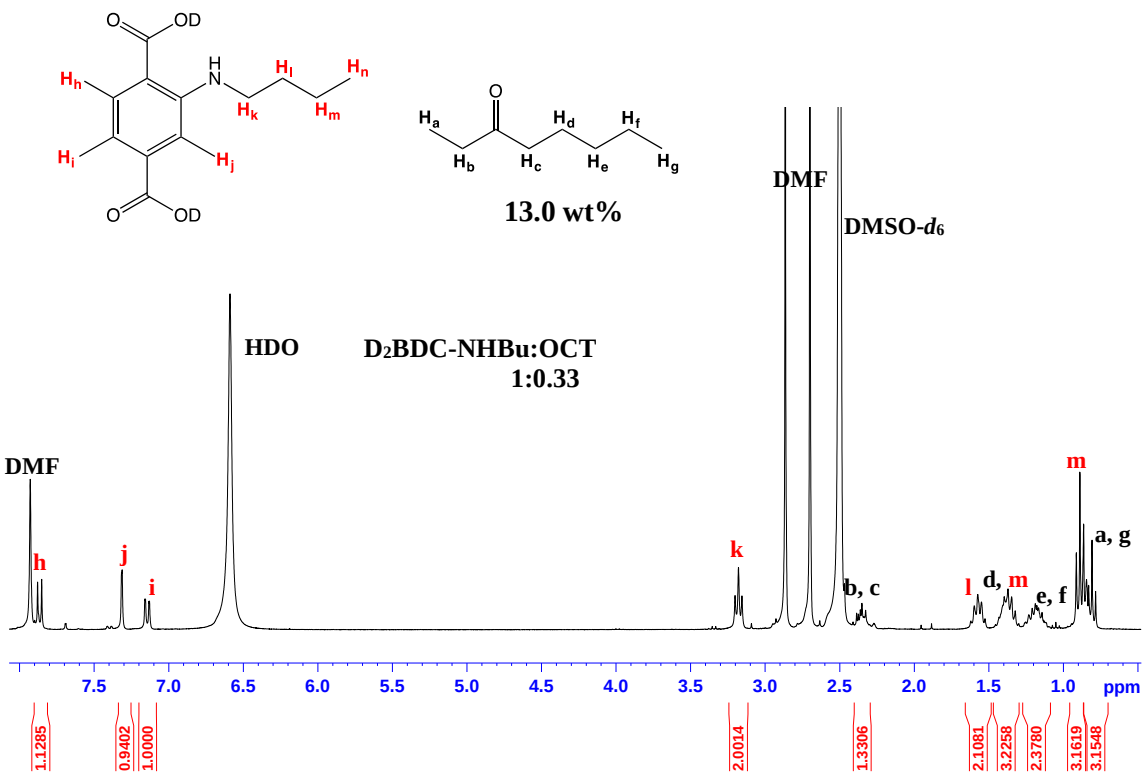

Figure 4.22. The ^{1}H NMR spectrum for **3e** (rinsed twice with DMF).

The compiled findings presented thus far indicate that IRMOF-NHBu has a lower OCT loading (13.0 wt% after first rinse with DMF) than that for IRMOF-NHPr (23.2 wt% after first rinse with DMF), albeit the former possessing longer alkyl chain in its pores. This is probably due to the pore blocking effect caused by the butyl chains in IRMOF-NHBu which may restrict the diffusion of OCT in its pores. In the case of IRMOF-NHBu, the effect of pore blocking outweighs the hydrophobicity effect caused by the butyl chains. Nonetheless, IRMOF-NHBu retains OCT better on washing (no OCT loss was observed upon washing with DMF) compared to IRMOF-NHPr (0.3 equivalents, 4.1 wt% loss on washing thrice).

4.2.5. 3-Octanone Loading in [$Zn_4O(BDC\text{-}NHOc)_3$], IRMOF-NHOc

Another IRMOF that was used in the OCT inclusion study was [$Zn_4O(BDC\text{-}NHOc)_3$], IRMOF-NHOc, Figure 4.9(e). This MOF was selected due to the presence of octyl chains in its pores, which could be beneficial for the OCT uptake.

The dicarboxylic acid, H_2BDCNHOc was synthesised using a similar procedure to the synthesis of H_2BDCNHBu, Scheme 4.23.[21] The ^{1}H NMR spectrum of the isolated product confirms the identity of the material (Section 4.11.1.3).

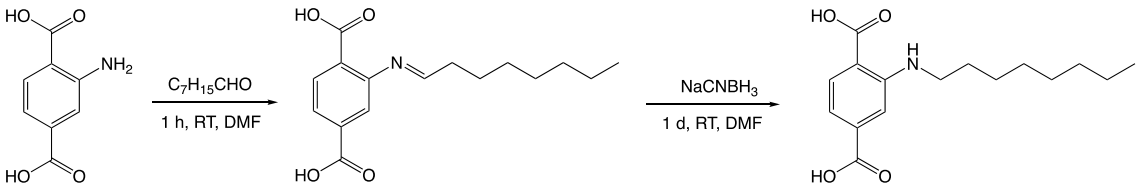

Scheme 4.23. The synthesis of H_2BDC-NHOc.

Once again, the synthesis of IRMOF-NHOc was conducted using the same reaction conditions for the synthesis of IRMOF-NHBu, Scheme 4.24.[21] The PXRD pattern of the synthesised material is similar to that for IRMOF-1, which implies that both MOFs are isostructural (Section 4.11.2.5).

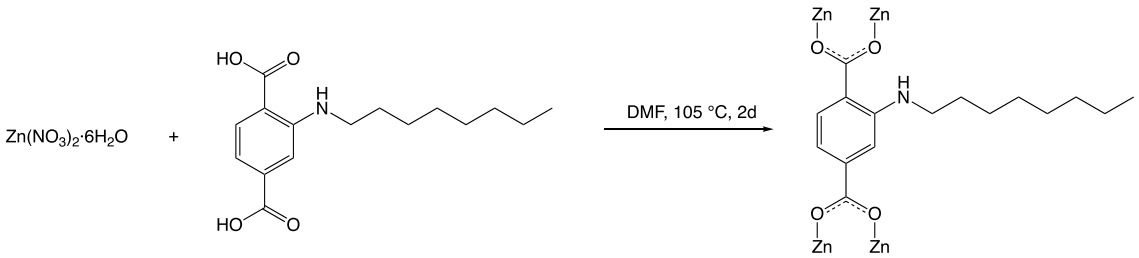

Scheme 4.24. Direct synthesis of [Zn_4O(BDC-NHOc)$_3$], IRMOF-NHOc.

The OCT loading in IRMOF-NHOc was performed using the conditions shown in Scheme 4.25.

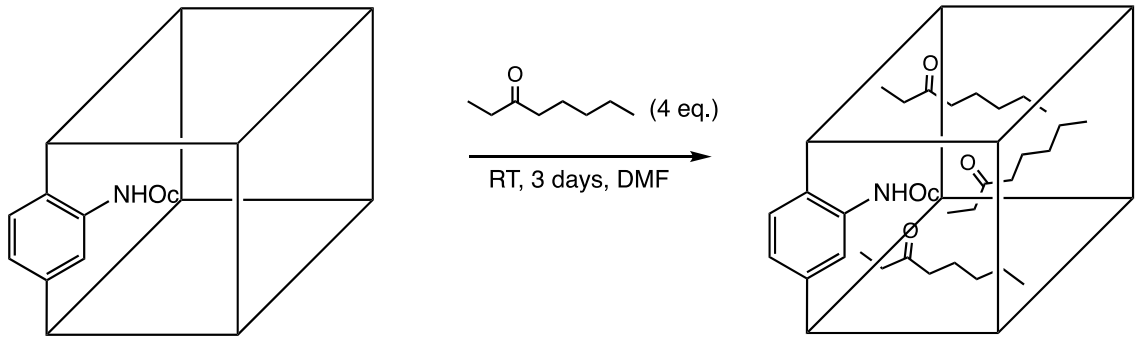

Scheme 4.25. Schematic representation of OCT loading in IRMOF-NHOc.

The ^{1}H NMR spectrum of the digested OCT treated MOF, **3f** shows only traces of OCT, Figure 4.23.

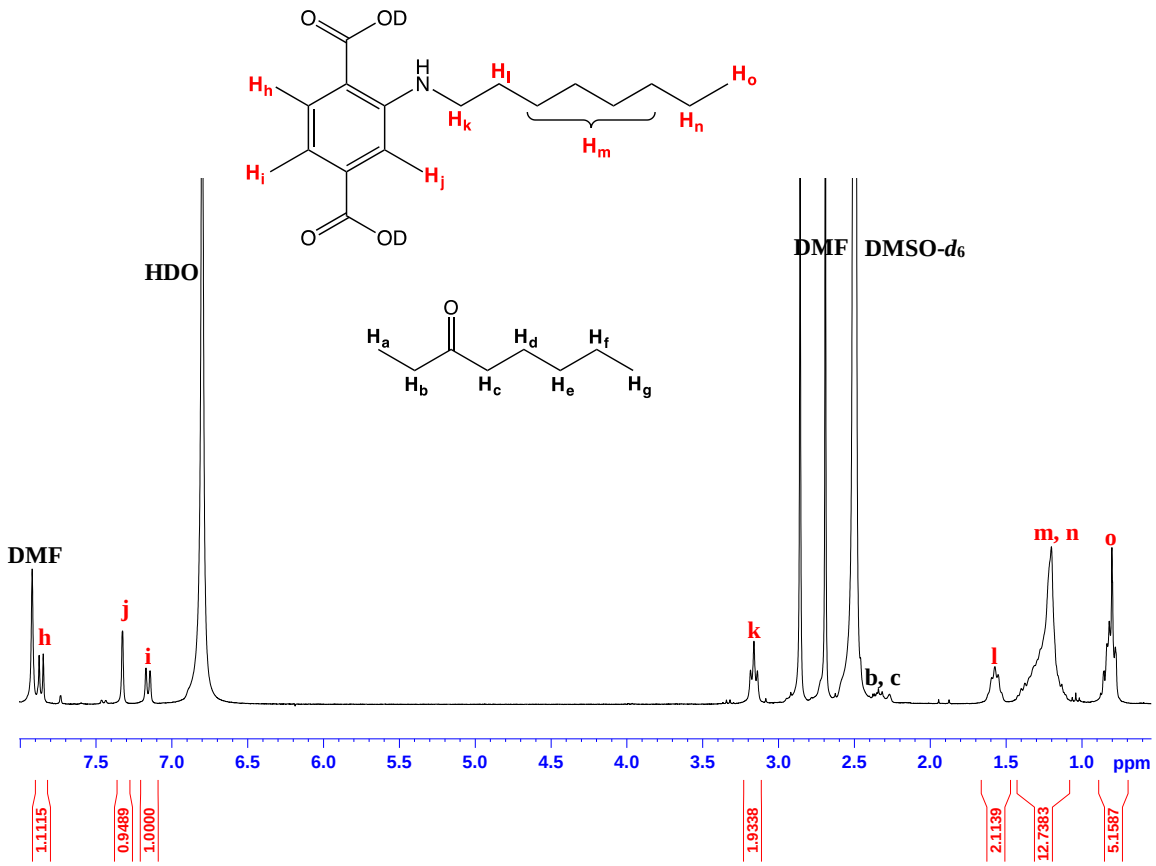

Figure 4.23. The ^{1}H NMR spectrum for **3f** (rinsed once with DMF).

This is probably due to the pore blocking caused by the long octyl chains which restricted the diffusion of OCT into the pores of IRMOF-NHOc. This result shows that although the octyl chains could provide a hydrophobic environment for OCT inclusion/retention, this is overshadowed by the effect of pore blocking, which is greater, in this instance.

4.3. 3-Octanone Loading in $[Zr_6O_4(OH)_4(BDC\text{-}NHPr)_6]$, UiO-66NHPr

While the secondary amine-containing IRMOF-NHR compounds are considerably less moisture sensitive than IRMOF-1 and IRMOF-3, MOFs within the IRMOF series are known to decompose in the presence of water.[22] While this is not necessarily a problem for pheromone delivery, since framework collapse will be accompanied by guest

release, decomposition could make the pheromone release difficult to control. It was therefore decided to also investigate the OCT inclusion into a derivative of UiO-66, a well-known, moisture-stable zirconium(IV) MOF. Given that the study with the IRMOF series had identified BDC-NHPr as the optimum ligand for OCT uptake, the MOF $[Zr_6O_4(OH)_4(BDC\text{-}NHPr)_6]$, UiO-66-NHPr was chosen for the OCT inclusion study.

A survey of the literature did not reveal any reports on the synthesis of UiO-66-NHPr. Therefore, the synthesis of this MOF was attempted by using an analogous procedure to that of UiO-66-NH_2, Scheme 4.26.[23]

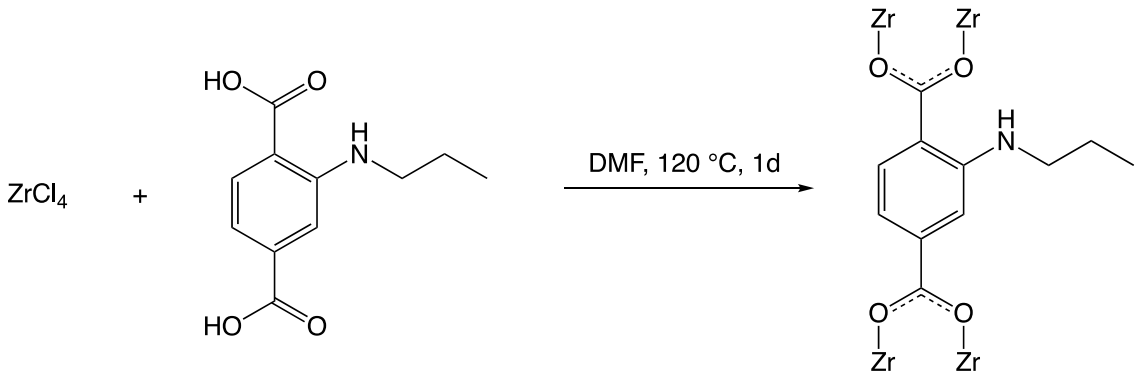

Scheme 4.26. Direct synthesis of $[Zr_6O_4(OH)_4(BDC\text{-}NHPr)_6]$, UiO-66-NHPr.

The dicarboxylic acid, H_2BDC-NHPr was first prepared using the procedure described in Section 4.2.3. The MOF synthesis involves dissolving $ZrCl_4$ and H_2BDC-NHPr in DMF within a Teflon-lined autoclave. The autoclave was then sealed and heated at 120 °C for 24 hours. The resulting yellow powder was then soaked and washed with MeOH for 3 days, replacing the solvent with fresh solvent every 24 hours before isolating the powders by centrifugation. The powder was then dried under reduced pressure.

The MOF synthesis was successful, as evidenced by the high similarities of the PXRD patterns between the material and UiO-66 (Section 4.11.2.6).

The OCT loading in UiO-66-NHPr was performed using the conditions shown in Scheme 4.27, which mirror that used for the formation of **3d** (Section 4.2.3).

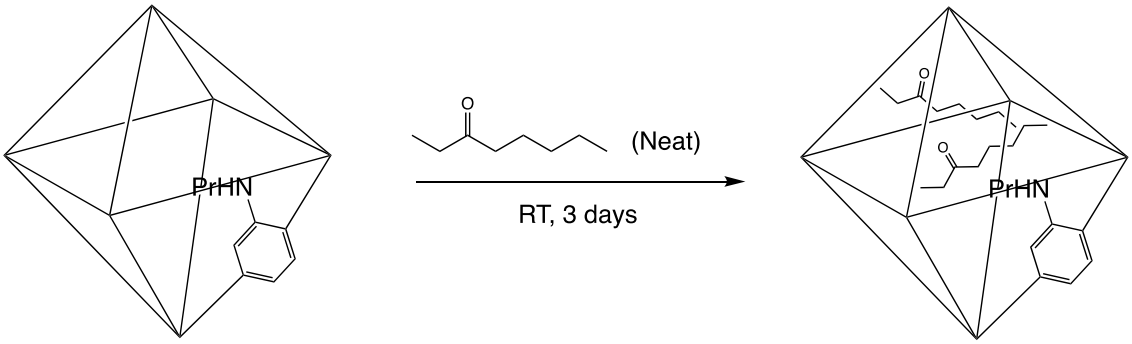

Scheme 4.27. Schematic representation of OCT loading in UiO-66-NHPr.

It is notable that the OCT loading in UiO-66-NHPr was performed in neat OCT instead of a solution containing four equivalents of it. This is due to a request by a collaborator, which was, to prepare UiO-66-NHPr with the highest OCT loading, in order for it to be used for a release study.

This experiment was successful, as evidenced by the presence of OCT peaks in the ^{1}H NMR spectrum of the digested product, **3g**, Figure 4.24.

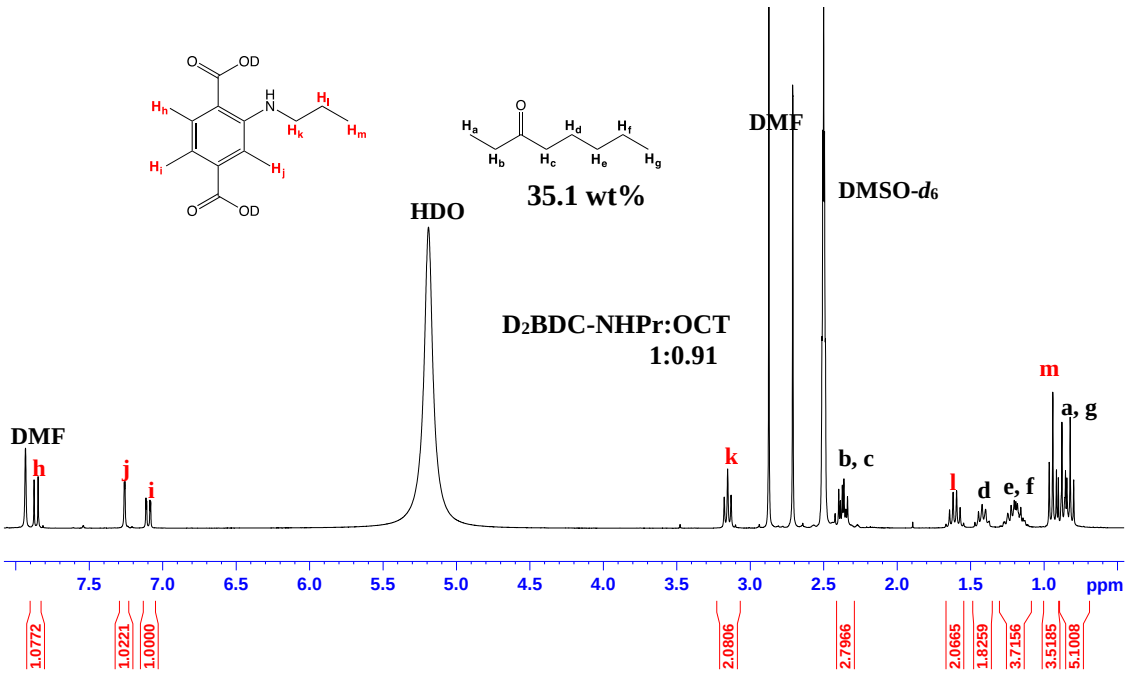

Figure 4.24. The ^{1}H NMR spectrum for **3g** (rinsed once with DMF).

The analysis reveals that the sample contains 35.1 wt% OCT, giving a formula of $[Zr_6O_4(OH)_4(BDC\text{-}NHPr)_6]\cdot 5.5OCT$. UiO-66-NHPr therefore exhibits a broadly similar OCT uptake to that for IRMOF-NHPr (36.8 wt%) in neat OCT. The sample was further

washed once or twice with DMF and also analysed by ^{1}H NMR spectroscopy. The spectra (Figure 4.25 and 4.26) reveal that these further washings reduced the OCT content to 17.9 wt% and 6.4 wt% respectively, demonstrating that OCT is less tightly held in UiO-66-NHPr than in IRMOF-NHPr (30.0 wt% after second wash and 27.3 wt% after third wash).

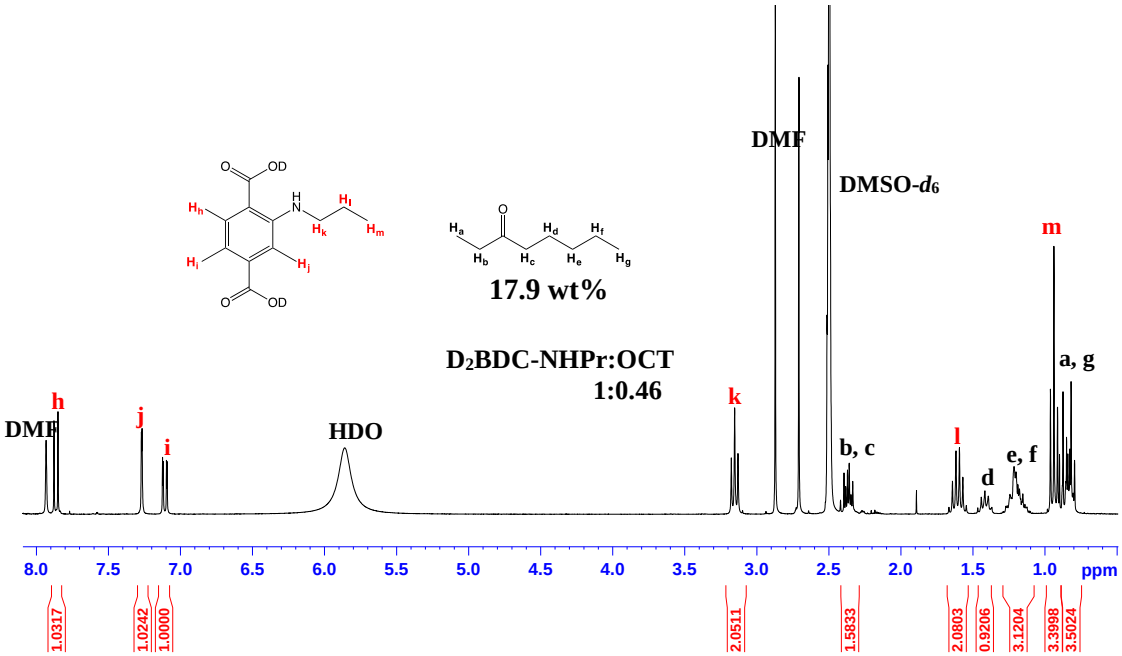

Figure 4.25. The ^{1}H NMR spectrum for **3g** (rinsed twice with DMF).

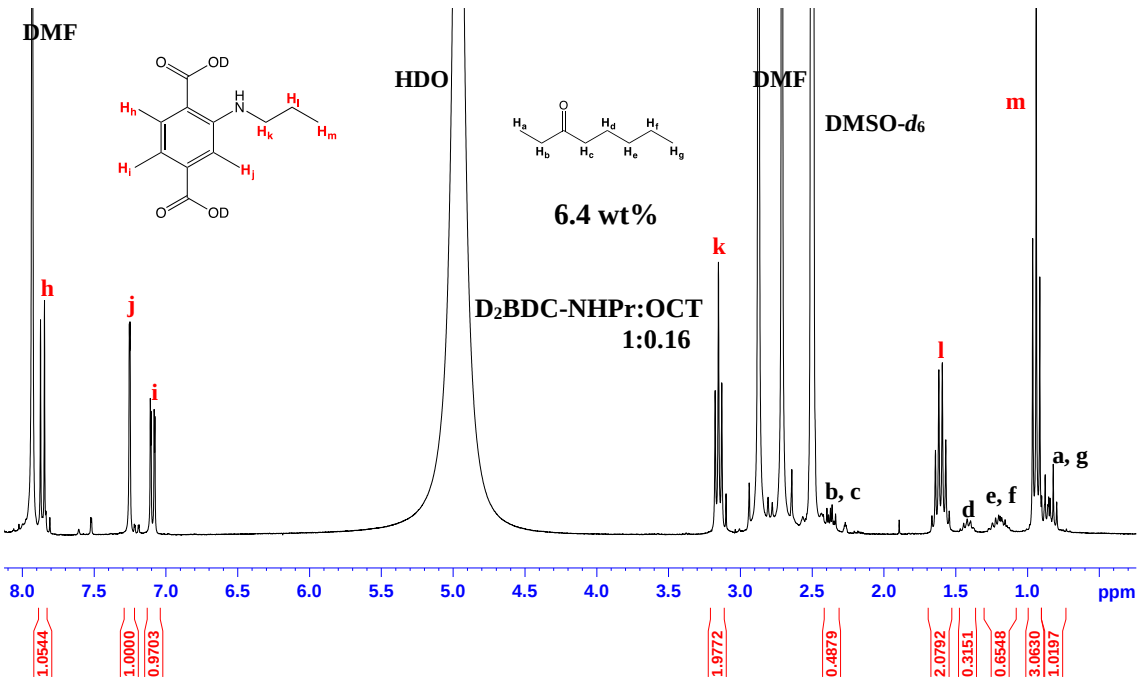

Figure 4.26. The ^{1}H NMR spectrum for **3g** (rinsed three times with DMF).

4.4. (*S*)-4-Methyl-3-Heptanone Loading in $[Zn_4O(BDC\text{-}NHPr)_3]$, IRMOF-NHPr

Following the successful inclusion of OCT in IRMOFs, particularly IRMOF-NHPr, it was decided to investigate if the inclusion study could be expanded to other types of pheromone. For this study, (*S*)-4-methyl-3-heptanone, abbreviated MHP, Figure 4.27, was used as an alternative pheromone. Similar to OCT, MHP also induces an alarm response, and it is secreted by the *Atta sexdens* ant species (Texas leafcutter ants).[24] The *Atta sexdens* species are considered as a major pest of agricultural and ornamental plants. MHP is, in fact, a structural isomer of OCT, but differs in being shorter and wider (approximate dimensions of 11.5 Å × 6.1 Å × 5.5 Å), although still large enough to access IRMOF pore windows.

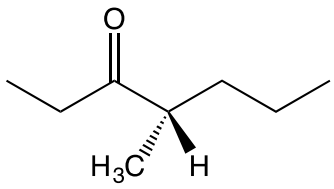

Figure 4.27. (*S*)-4-methyl-3-heptanone (MHP).

The ^{1}H NMR spectrum of MHP, Figure 4.28, shows multiple peaks in the upfield region, which correspond to the alkyl protons of MHP. The presence of these peaks in the ^{1}H NMR spectrum of the digested MHP treated MOFs would indicate that the inclusion experiment was successful.

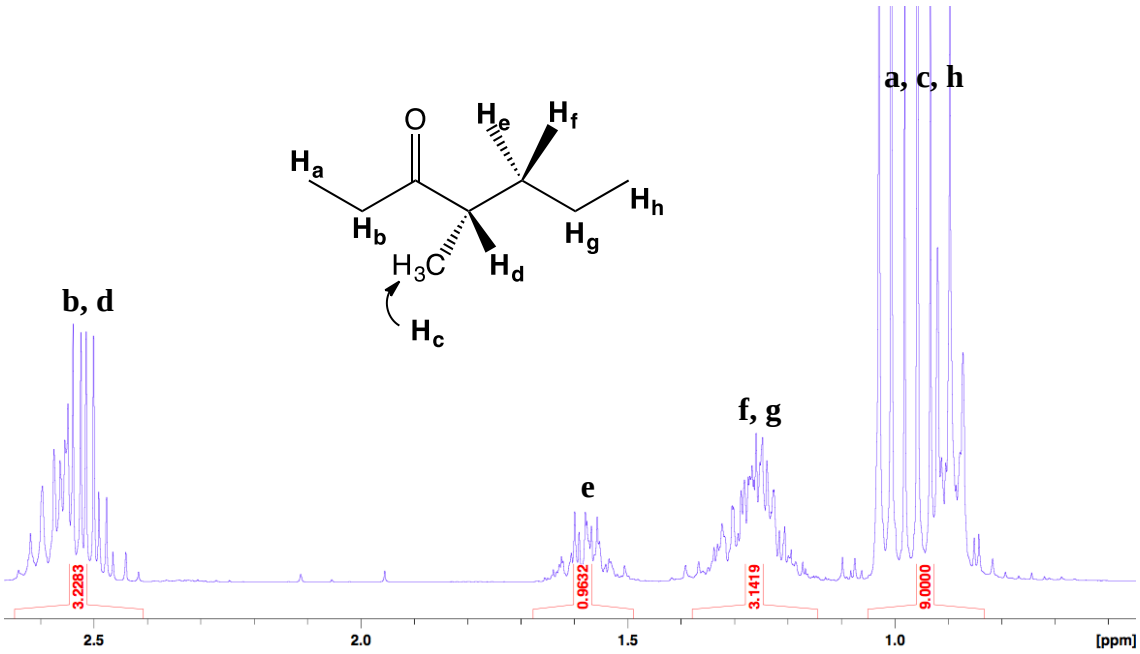

Figure 4.28. ^{1}H NMR spectrum of MHP in DMSO-d_6 and DCl/D_2O.

IRMOF-NHPr was used in this study, as earlier results showed that the highest OCT loading was observed in this MOF. The MHP loading in IRMOF-NHPr was carried out using the conditions shown in Scheme 4.28.

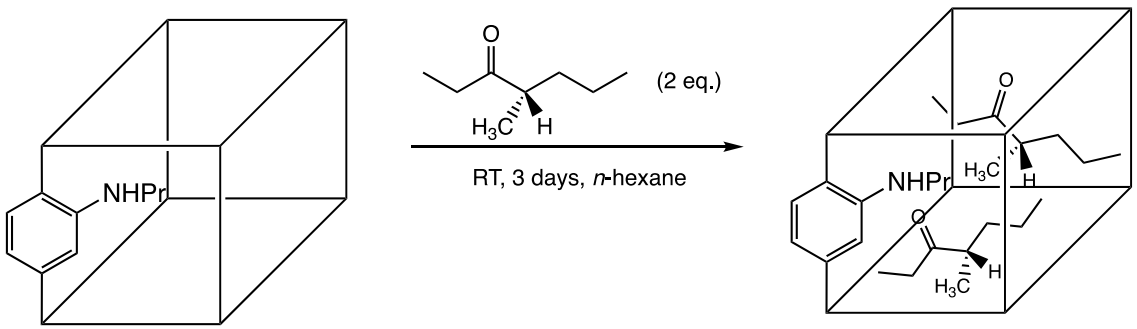

Scheme 4.28. Schematic representation of MHP loading in IRMOF-NHPr in *n*-hexane. IRMOF-NHPr is represented by the cubic polyhedra.

In a typical procedure, IRMOF-NHPr crystals were added in a glass vial containing MHP in *n*-hexane. The vial was sealed and the solution was left to stand for three days at ambient temperature. Upon treatment with MHP, the crystals were isolated *via* filtration and washed once with *n*-hexane to remove any residual MHP on the crystal surface. *n*-Hexane was used as a solvent in preference to DMF, as initial release studies carried out by collaborators on $[Zn_4O(BDC\text{-}NHPr)_3]\cdot 1.7OCT$, **3c** (sample was rinsed

with DMF) indicate that DMF lowered the efficiency of the sample in attracting the insects used in the study.

The ^{1}H NMR spectrum of the digested MHP treated MOF, **3h** shows the presence of peaks attributed to the protons of MHP, Figure 4.29, which indicates that the pheromone loading experiment was successful. The ratio of D_2BDC-NHPr to MHP was calculated by comparing the integrals at δ 7.10 ppm and δ 1.48 ppm which correspond to the aryl protons from D_2BDC-NH_2, H_j and alkyl protons, H_e from MHP, respectively. This was calculated as being approximately 1:0.23 which gives the formula for **3h** as $[Zn_4O(BDC\text{-}NHPr)_3]\cdot 0.7MHP$ (9.5 wt%).

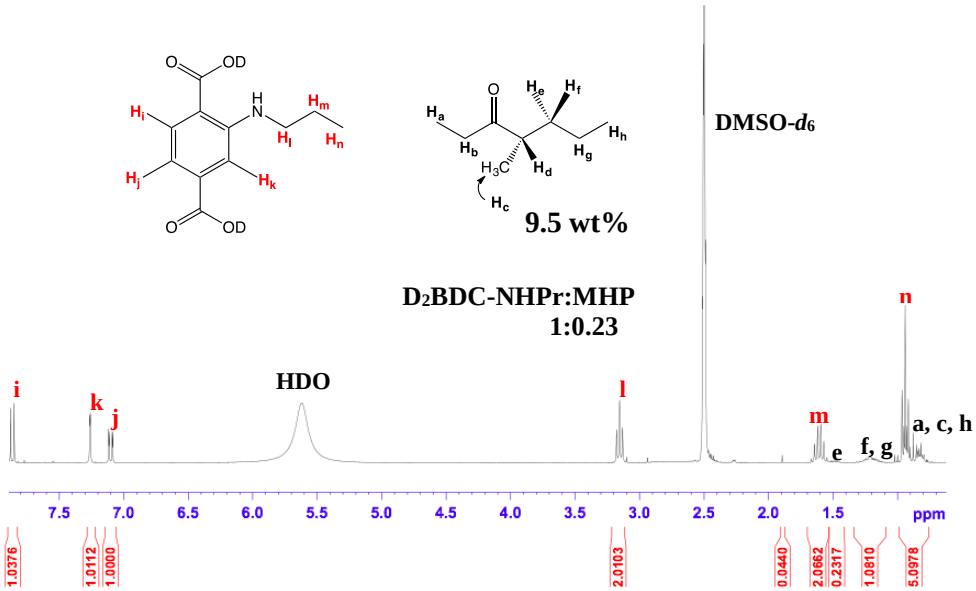

Figure 4.29. The ^{1}H NMR spectrum for **3h**.

Similar to the conclusion made for $[Zn_4O(BDC\text{-}NHPr)_3]\cdot 1.7OCT$, **3c** the successful inclusion of MHP in the pores of IRMOF-NHPr may be attributed to the presence of hydrophobic propyl groups in IRMOF-NHPr which has a high affinity towards MHP. Furthermore, hydrogen bonding involving the –NH groups on the MOF and the carbonyl groups of MHP may also contribute to successful inclusion.

In a separate experiment, IRMOF-NHPr crystals were treated with neat MHP at ambient temperature for three days. This procedure was carried out to investigate if MHP loading in IRMOF-NHPr could be maximised.

The analysis of the ^{1}H NMR spectrum of the digested MHP treated MOF (washed once with *n*-hexane), **3i**, Figure 4.30, reveals a small increase in the quantity of MHP compared to that in sample **3h** (**3h** = $[Zn_4O(BDC\text{-}NHPr)_3]\cdot 0.7MHP$ (9.5 wt%), **3i** = $[Zn_4O(BDC\text{-}NHPr)_3]\cdot MHP$ (13.6 wt%)).

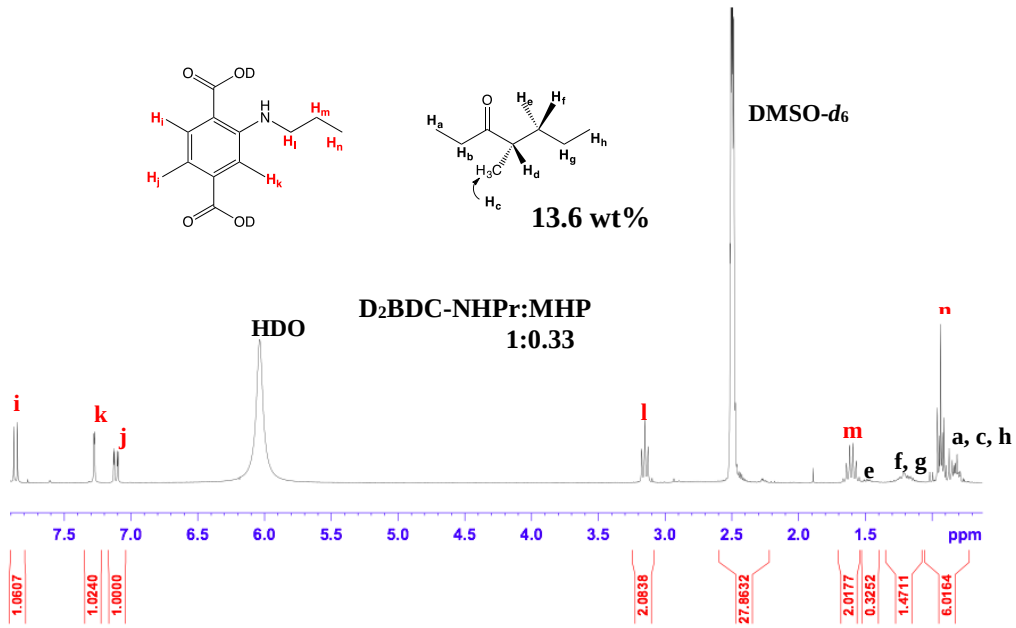

Figure 4.30. The ^{1}H NMR spectrum for **3i**.

In a similar vein to the results obtained for IRMOF-NHPr in neat OCT (Section 4.2.3), MHP loading in IRMOF-NHPr can be increased by performing the inclusion procedure in a neat solution of MHP. However, since the increase is small, it would be unlikely to justify the additional expense (MHP: EUR 1573, 100 mg, Enamine Ltd) if this delivery mode becomes commercially viable.

4.5. Table of Pheromone Loadings in MOFs

The pheromone loadings in the IRMOF and UiO-66-NHPr systems reported in this thesis are summarised in Table 4.2 (OCT) and Table 4.3 (MHP).

MOF	S_{BET} (m^2/g)	Sample	Initial analysis (one DMF wash)		After washing (two DMF washes)		After washing (three DMF washes)	
			wt% uptake	Formula	wt% uptake	Formula	wt% uptake	Formula
IRMOF-1	3800[25]	**3b**	3.3	$[Zn_4O(BDC)_3]\cdot 0.2OCT$	0	–	0	–
IRMOF-3	2613[21]	**3a**	6.3	$[Zn_4O(BDC\text{-}NH_2)_3]\cdot 0.4OCT$	3.1	$[Zn_4O(BDC\text{-}NH_2)_3]\cdot 0.2OCT$	0	–
IRMOF-NHPr	1914[21]	**3c**	23.2	$[Zn_4O(BDC\text{-}NHPr)_3]\cdot 1.7OCT$	20.5	$[Zn_4O(BDC\text{-}NHPr)_3]\cdot 1.5OCT$	19.1	$[Zn_4O(BDC\text{-}NHPr)_3]\cdot 1.4OCT$
IRMOF-NHPr[a]		**3d**	36.8	$[Zn_4O(BDC\text{-}NHPr)_3]\cdot 2.7OCT$	30.0	$[Zn_4O(BDC\text{-}NHPr)_3]\cdot 2.2OCT$	27.3	$[Zn_4O(BDC\text{-}NHPr)_3]\cdot 2.0OCT$
IRMOF-NHBu	1862[21]	**3e**	13.0	$[Zn_4O(BDC\text{-}NHBu)_3]\cdot OCT$	13.0	$[Zn_4O(BDC\text{-}NHBu)_3]\cdot OCT$	13.0	$[Zn_4O(BDC\text{-}NHBu)_3]\cdot OCT$
IRMOF-NHOc	1233[21]	**3f**	Trace	–	0	–	0	–
UiO-66-NHPr[a]	–	**3g**	35.1	$[Zr_6O_4(OH)_4(BDC\text{-}NHPr)_6]\cdot 5.5OCT$	17.9	$[Zr_6O_4(OH)_4(BDC\text{-}NHPr)_6]\cdot 2.8OCT$	6.4	$[Zr_6O_4(OH)_4(BDC\text{-}NHPr)_6]\cdot OCT$

Table 4.2. 3-Octanone (OCT) loading in IRMOFs and UiO-66-NHPr. All experiments were performed at room temperature for three days in a solution containing four equivalents of OCT, with the exception of *a*, which was performed in neat OCT.

MOF	Sample	MOF:MHP	After one *n*-hexane wash	
			wt% uptake	Formula
IRMOF-NHPr	**3h**	1:2	9.5	$[Zn_4O(BDC\text{-}NHPr)_3]\cdot 0.7MHP$
	3i	1:Neat	13.6	$[Zn_4O(BDC\text{-}NHPr)_3]\cdot MHP$

Table 4.3. (*S*)-4-methyl-3-heptanone (MHP) loading in IRMOF-NHPr. Both experiments were performed at room temperature for three days.

4.6. Moisture Stability of [$Zn_4O(BDC\text{-}NHPr)_3$]·1.7OCT, 3b, and $Zn_4O(BDC\text{-}NHPr)_3$]·0.7MHP, 3h

The effect of pheromone loading on the crystal stability of the zinc MOFs towards moisture was investigated using the following representative samples [$Zn_4O(BDC\text{-}NHPr)_3$]·1.7OCT, **3c**, and $Zn_4O(BDC\text{-}NHPr)_3$]·0.7MHP, **3h**. The stability test was performed by exposing the pheromone treated MOFs to atmospheric moisture for a set time period, and measuring the PXRD patterns thereafter. As a control experiment, the moisture stability of IRMOF-NHPr crystals was investigated and the results are shown in Figure 4.31.

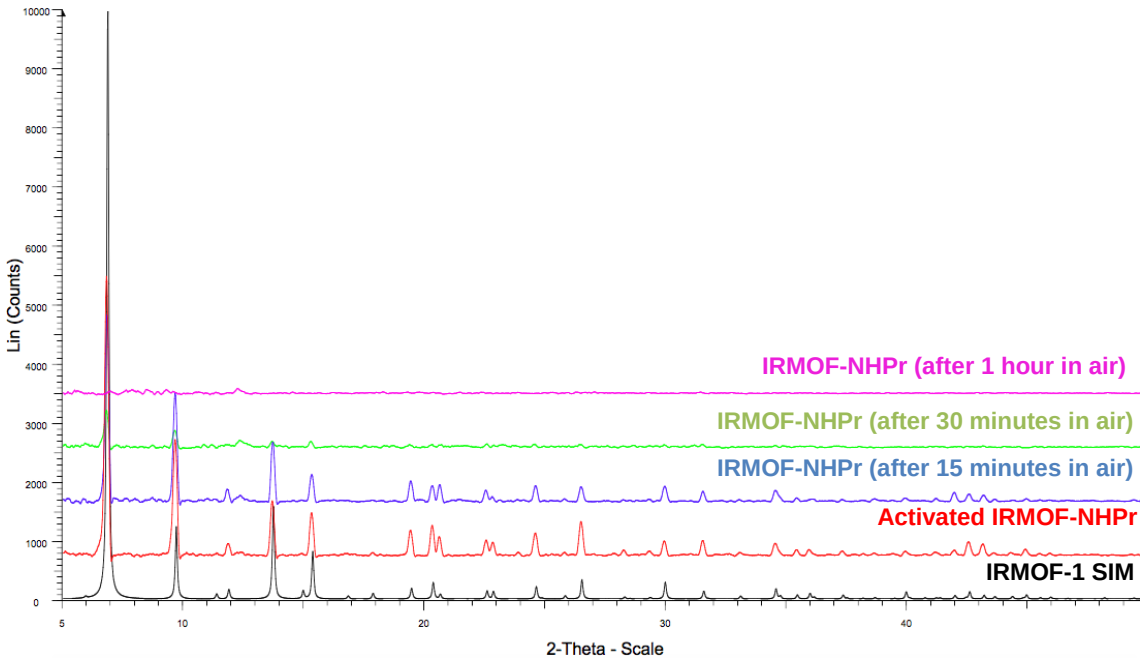

Figure 4.31. Black: Simulated PXRD pattern of IRMOF-1 calculated from the single crystal data.[20] Red: PXRD pattern of activated IRMOF-NHPr. Blue: PXRD pattern of IRMOF-NHPr after 15 minutes in air. Green: PXRD pattern of IRMOF-NHPr after 30 minutes in air. Pink: PXRD pattern of IRMOF-NHPr after an hour in air.

The crystals were shown to retain their crystallinity for up to 30 minutes, after which crystal degradation was observed.

A similar stability test was undertaken with [$Zn_4O(BDC\text{-}NHPr)_3$]·1.7OCT, **3c**, which possesses 23.2 wt% OCT in its pores. The PXRD patterns of the sample, Figure 4.32, reveal that the MOF could retain its crystallinity for longer than when OCT is absent in its pores. In fact, sample **3c** still maintained its crystallinity even after five days in air, which is rarely observed for the IRMOF materials.

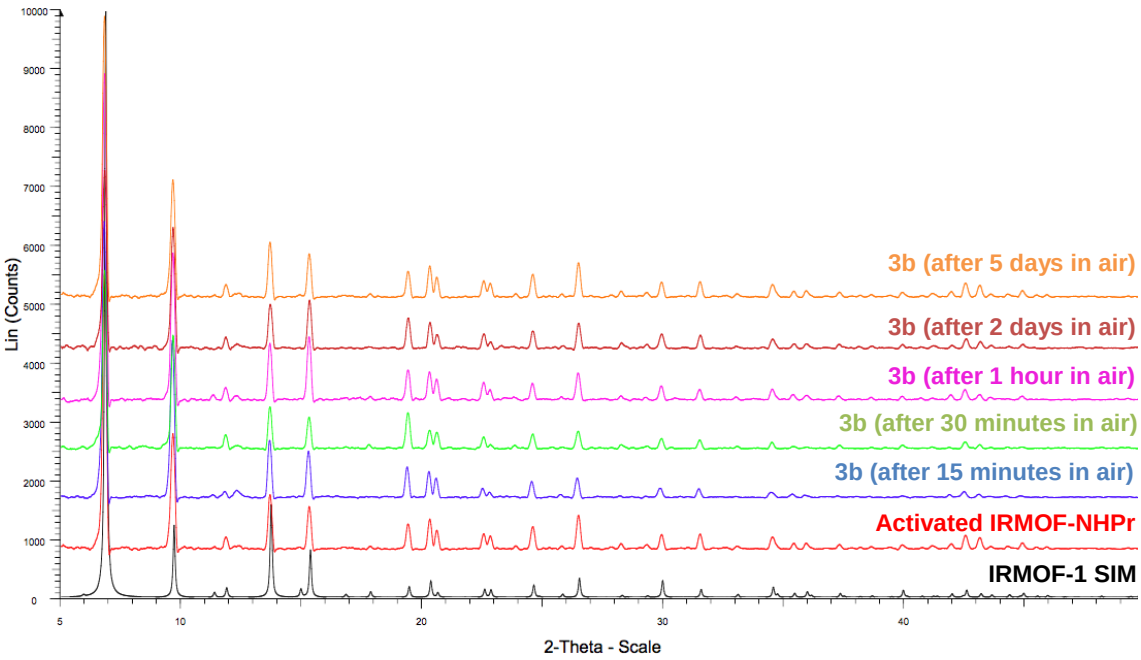

Figure 4.32. Black: Simulated PXRD pattern of IRMOF-1 calculated from the single crystal data.[20] Red: PXRD pattern of activated IRMOF-NHPr. Blue: PXRD pattern of **3b** after 15 minutes in air. Green: PXRD pattern of **3b** after 30 minutes in air. Pink: PXRD pattern of **3b** after an hour in air. Brown: PXRD pattern of **3b** after 2 days in air. Orange: PXRD pattern of **3b** after 5 days in air.

In a similar vein to **3c**, the MHP treated MOF $[Zn_4O(BDC\text{-}NHPr)_3]\cdot 0.7MHP$, **3h** was also subjected to the moisture stability test. This MOF also showed a higher stability to atmospheric moisture compared to when MHP is absent in its pores, Figure 4.33.

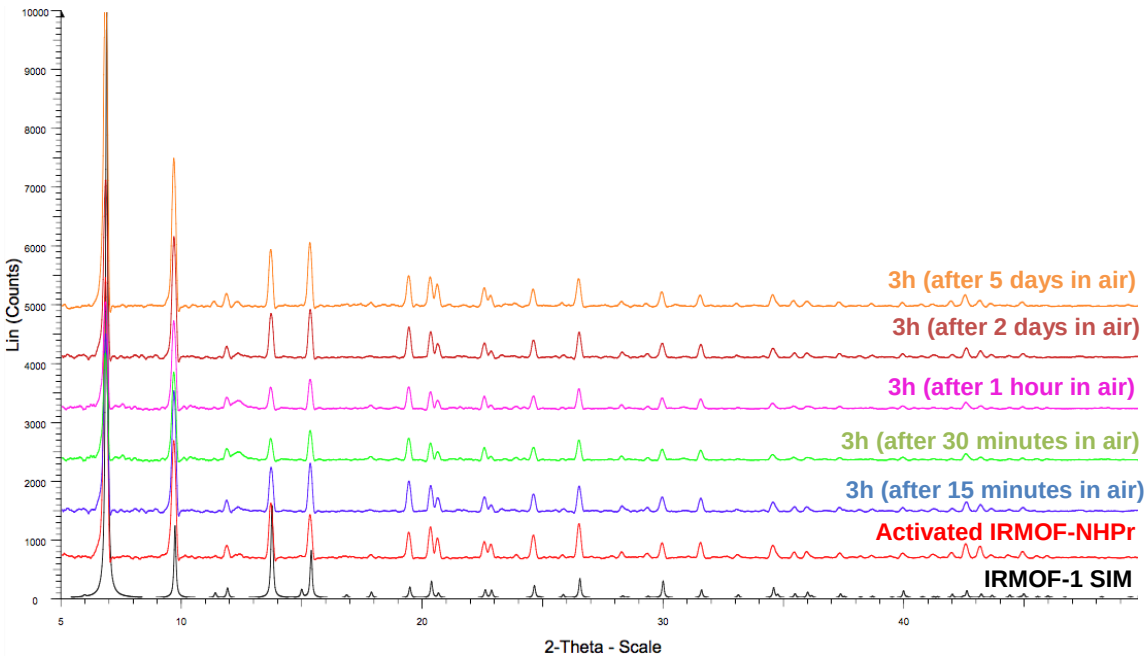

Figure 4.33. Black: Simulated PXRD pattern of IRMOF-1 calculated from the single crystal data.[20] Red: PXRD pattern of activated IRMOF-NHPr. Blue: PXRD pattern of **3h** after 15 minutes in air. Green: PXRD pattern of **3h** after 30 minutes in air. Pink: PXRD pattern of **3h** after an hour in air. Brown: PXRD pattern of **3h** after 2 days in air. Orange: PXRD pattern of **3h** after 5 days in air.

The higher moisture stability of the pheromone loaded MOFs is thought to be attributed to the hydrophobic environment brought by the OCT and MHP molecules in their pores. Based on these findings, it can be concluded that the resistance of IRMOFs towards atmospheric moisture can be increased by introducing hydrophobic guests such as pheromone molecules into their pores.

4.7. Pheromone Release Studies of $[Zn_4O(BDC\text{-}NHPr)_3]\cdot MHP$, 3i

In order to assess if the pheromone-loaded MOFs have a biological impact, the MHP loaded sample $[Zn_4O(BDC\text{-}NHPr)_3]\cdot MHP$, **3i**, was used as a representative MOF for the preliminary biological studies in both laboratory and field settings. These studies were conducted by Prof. William Hughes and co-workers at the University of Sussex. The initial studies were promising, with leaf-cutting ants were shown to respond to the pheromone released from the MOF, Figure 4.34.

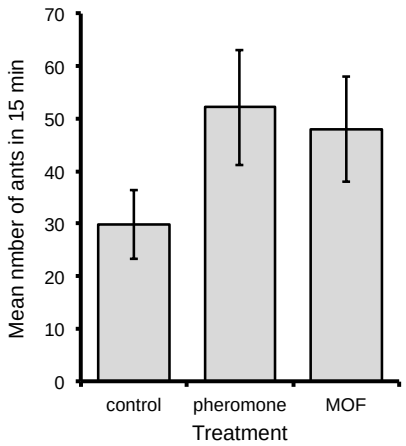

Figure 4.34. Number of leaf-cutting ant workers attracted to control insecticide bait piles, or bait piles enhanced with either MHP or $[Zn_4O(BDC\text{-}NHPr)_3]\cdot MHP$ as an attractant. Data are from field trials with *Atta sexdens* in Brazil.

4.8. Summary

The results presented herein demonstrate the potential of MOFs as hosts for ant alarm pheromones, which has not been reported before. In this work, 3-octanone (OCT) was used in the preliminary inclusion studies as it is relatively cheap and commercially available. The IRMOF system was initially selected for the inclusion study due to its ease of functionalisation and high crystallinity. Four dicarboxylic acids ($H_2BDC\text{-}NHR$, R = Pr, Bu, Oc) were prepared and used for the MOF syntheses. The IRMOFs prepared for this study were IRMOF-1, IRMOF-3, IRMOF-NHPr, IRMOF-NHBu and IRMOF-NHOc.

The OCT loading was assessed by ^{1}H NMR spectroscopy and the results demonstrate a poor inclusion and retention of OCT into IRMOF-1, but higher loadings were observed for IRMOF-3, IRMOF-NHPr and IRMOF-NHBu, despite their lower BET surface areas (Table 4.2). The higher uptake capacities in the amine containing MOFs (IRMOF-3, IRMOF-NHPr and IRMOF-NHBu) are likely to be due to the presence of hydrogen atoms from the -NH groups which have the potential to form hydrogen bonds with the carbonyl oxygen atom in OCT. Furthermore, higher loadings were observed for the alkyl-amino MOFs (IRMOF-NHPr and IRMOF-NHBu) than that for IRMOF-3. On this basis, it is concluded that a hydrophobic pore environment (attributed to the alkyl chains) is also important for OCT inclusion, in addition to the presence of hydrogen bond donors. However, no inclusion was observed under identical conditions using IRMOF-NHOc, presumably due to the pore blocking effect caused by the long octyl chains which could restrict the diffusion of OCT in the MOF pores.

The highest OCT uptake was observed with IRMOF-NHPr (23.2 wt%), although IRMOF-NHBu retained the pheromone guest better on washing (no OCT loss was observed) compared to IRMOF-NHPr (0.3 equivalents, 4.1 wt% lost on washing twice).

The OCT loading can be increased by conducting the inclusion experiment in neat OCT. For example, 13.6 wt% increase was observed when IRMOF-NHPr was treated in neat OCT instead of a DMF solution containing a four equivalent of it.

The concept of OCT loading in MOFs was also extended to a highly robust MOF, UiO-66-NHPr. This MOF was successfully prepared for the first time using an analogous synthesis to that of UiO-66-NH_2. Under identical conditions, the OCT loading in UiO-66-NHPr (35.1 wt%) was shown to be broadly similar to that for IRMOF-NHPr (36.8 wt%).

The versatility of IRMOF-NHPr to host pheromone molecules in its pores was proven by the successful loading of a different alarm pheromone, (*S*)-4-methyl-3-heptanone (MHP) in its pores. An uptake of 9.5 wt% was observed when IRMOF-NHPr was treated in a hexane solution containing two equivalents of MHP, whereas 13.6 wt% uptake was observed in neat MHP.

The stability of the pheromone loaded MOFs $[Zn_4O(BDC\text{-}NHPr)_3]\cdot 1.7OCT$, **3c**, and $Zn_4O(BDC\text{-}NHPr)_3]\cdot 0.7MHP$, **3h** towards atmospheric moisture was assessed *via* PXRD. The MOFs were shown to retain their crystallinity for longer compared to when OCT is absent in its pores. The higher stability of the pheromone loaded MOFs is attributed to the hydrophobic environment brought by the pheromone molecules in their pores.

Preliminary biological studies on $[Zn_4O(BDC\text{-}NHPr)_3]\cdot MHP$, **3i**, have shown that leaf-cutting ants respond to MHP released from the MOF.

In conclusion, taken together, the preliminary synthetic and biological investigations have demonstrated that MOFs can take up alarm pheromones into their pores and release these, leading to responses from the target species. This conclusively shows that the concept underpinning this work is sound and that it is worthy of further study.

4.9. Future Work

As stated in Section 4.8, the presence of hydrogen-bond donors is important to obtain a high pheromone loading in MOFs. In order to verify this, pheromone uptake studies can be performed on MOFs containing linkers that lack hydrogen-bond donors but still contain alkyl chains such as BDC-OPr, Figure 4.35(a), and BDC-Bu, Figure 4.35(b). These linkers have the same chain length as BDC-NHPr but lack the hydrogen bonding group. Comparison of their pheromone uptake capacities will allow one to unambiguously determine the importance of hydrogen bonding in these systems.

(a)

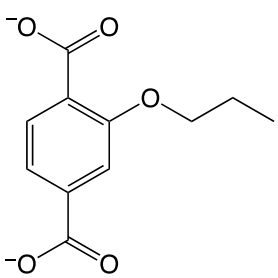

(b)

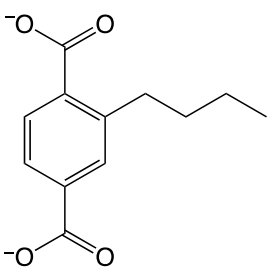

Figure 4.35. (a) 2-propoxy-1,4-benzenedicarboxylate, BDC-OPr **(b)** 2-butyl-1,4-benzenedicarboxylate, BDC-Bu.

There is a perception that MOFs are water-sensitive, and hence unsuitable for many 'real-world' applications. While many MOFs do suffer from this limitation, there are many others that are moisture stable and appropriate for use in moist environments. This include UiO-66-NHPr, which, in this study, was shown to take up OCT in its pores. On the basis of this promising result, the pheromone loading into MOFs can be extended to the other highly stable and robust MOFs such as MIL-101(Al/Fe)-NHPr, CAU-1-NHPr, MIL-53(Al/Fe)-NHPr, MIL-88-NHPr and MIL-68(In)-NHPr, all of which are new MOFs but are expected to have the same framework structures as known -NH_2 functionalised frameworks. However, it is notable that a degree of water sensitivity may be beneficial, so that the MOF does not accumulate in the environment. Investigations on MOFs that degrade slowly in addition to those that are stable to water may also be undertaken to determine the best MOFs for the 'real-world' applications.

In terms of MOF syntheses, MOFs bearing -NH groups and pendant alkyl groups can also be synthesised *via* PSM. This can be achieved by preparing MOFs with open metal sites such as MIL-101(Cr), CPO-27(Mg/Zn) and HKUST-1, and subsequently reacting them with NH_2Pr or $NH_2CH_2CH_2CH_2NH_2$.

MOFs based on cyclodextrins have recently been reported, and were shown to have potential for permanent porosity.[26, 27] These are attractive targets for pheromone inclusion in real world studies as cyclodextrins are produced naturally by the action of bacteria on starch. This means that they are cheap, edible and environmentally friendly, all of which are important for sustainable applications.

The concept of pheromone loading in MOFs can be extended to different type of pheromones such as 2-methyl-2-hepten-6-one and 2-methyl-4-heptanone, Figure 4.36. These alarm pheromones are released by specific type of ant species,[12] and the successful inclusion of these (in addition to other pheromones) in MOFs could lead to a library of pheromone-loaded MOFs that target different ant species.

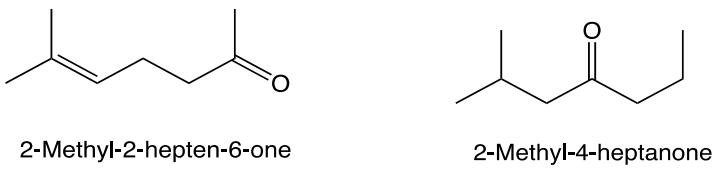

Figure 4.36. Examples of ant pheromones that can be used in the inclusion study.

MOFs can also be used to host insecticides, an application that is in its early stages of investigation.[28] While known MOFs can be readily adapted to facilitate their interactions with pheromones, identifying the best MOFs to host insecticides requires a different approach. Different insecticides have very different structures, meaning that a single MOF is unlikely to be a good host for a broad range of insecticides. In this context, MOF linkers can be tailored to interact with specific functionalities in the insecticides. For example, fluorinated linkers for sulfluramid, hydrogen bonding and/or coordinating groups for imidacloprid or a combination of both approaches for fipronil, Figure 4.37.

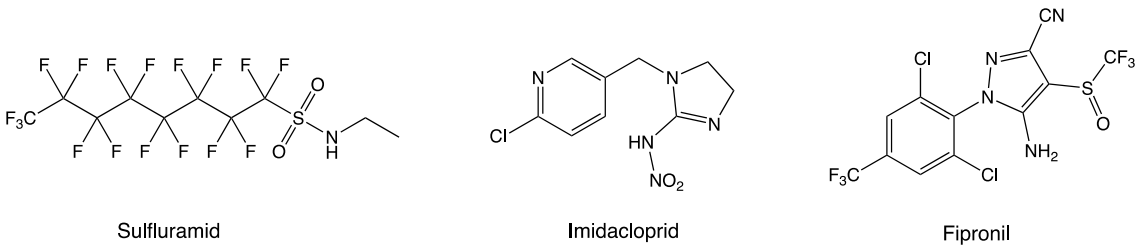

Figure 4.37. Examples of insecticides that may be introduced in MOF pores.

The MOFs can be synthesised *via* direct synthesis or post-synthetic approach. The latter can be achieved by preparing a MOF with a reactive 'tag' group, then introducing the required functionality using PSM. For example, perfluoro chains can be added onto MOFs using the reaction of an amino group with a perfluoro acid anhydride or perfluoro aldehyde followed by reduction of the initial imine, Scheme 4.29.

Scheme 4.29. The syntheses of fluorinated MOFs *via* PSM.

The numerous possibilities for future work detailed in this section demonstrate that the areas of improvement are vast and therefore, the concept of using MOFs as hosts for pheromones/insecticides merits further investigations.

4.10. General Experimental Procedures

4.10.1. Powder X-Ray Diffraction

Powder X-ray diffraction (PXRD) patterns for all samples were recorded on a Bruker AXS D8 Advance diffractometer with copper K_α radiation (wavelength, $\lambda = 1.5406$ Å) at 298 K. The beam slit was set to 1 mm, detector slit set to 0.2 mm and anti-scattering slit set to 1 mm. Samples were ground to a powder using a pestle and mortar. The powders were then packed onto a flat plate and measured over a 2θ range of 5 - 60°. The step size was 0.024° with the scan speed set to 0.3 s per step.

4.10.2. ^{1}H NMR Spectroscopy

^{1}H NMR spectrometry was performed on digested MOF samples at 298 K on a Bruker Avance 300 MHz Ultrashield NMR spectrometer. All ^{1}H NMR spectra were referenced to the residual protio peaks at δ 2.50 ppm for DMSO-d_6.

For the IRMOF materials, the MOF digestions were each carried out using approximately 10 mg of crystalline sample in 0.4 mL of DMSO-d_6 and 0.2 mL of a stock solution of 0.1 mL of 35 wt% DCl/D_2O in 3 mL DMSO. This mixture was sonicated until the solid had completely dissolved.

For the UiO-66 materials, a typical MOF digestion was carried out by adding 10 mg of a crystalline sample into 0.4 mL of DMSO-d_6 and 0.2 mL of a stock solution of NH_4F in D_2O (4.14 M). The mixture was sonicated until the solid had completely dissolved. In some cases, a trace amount of white solid presumably NH_4F salt precipitated out of the solution. The white solid was removed by filtration of the solution prior to recording the ^{1}H NMR spectra.

4.11. Synthetic Procedures

Unless specified, all reagents and solvents used in this work were purchased from Sigma Aldrich and were used without further purification. (*S*)-4-methyl-3-heptanone was obtained from Prof. William Hughes' group at University of Sussex.

4.11.1. Dicarboxylic Acid Syntheses

4.11.1.1. 2-(Propylamino)benzene-1,4-dicarboxylic acid, H_2BDC-NHPr

In a round-bottom flask, H_2BDC-NH_2 (200 mg, 1.104 mmol) was dissolved in DMF (10 mL) with stirring. To this solution, propanal (0.161 mL, 2.208 mmol) was added and

the solution stirred for 1 hour. The solution was then cooled in an ice bath and $NaCNBH_3$ (139 mg, 2.204 mmol) was added. The reaction mixture was stirred at room temperature for 24 h. The mixture was acidified with 1 M HCl, and deionised water was added until a yellow solid precipitated. Yield: 0.201 g (81 %). ^{1}H NMR (300 MHz, DMSO-d_6) δ/ppm: 7.83 (d, 1H, J = 8.0 Hz), 7.20 (d, 1H, J = 1.6 Hz), 7.03 (dd, 1H, J = 8.0 Hz, 1.4 Hz), 3.12 (t, 2H, J = 7.2 Hz), 1.59 (sextet, 2H, J = 7.2 Hz), 0.97 (t, 3H, J = 7.2 Hz).

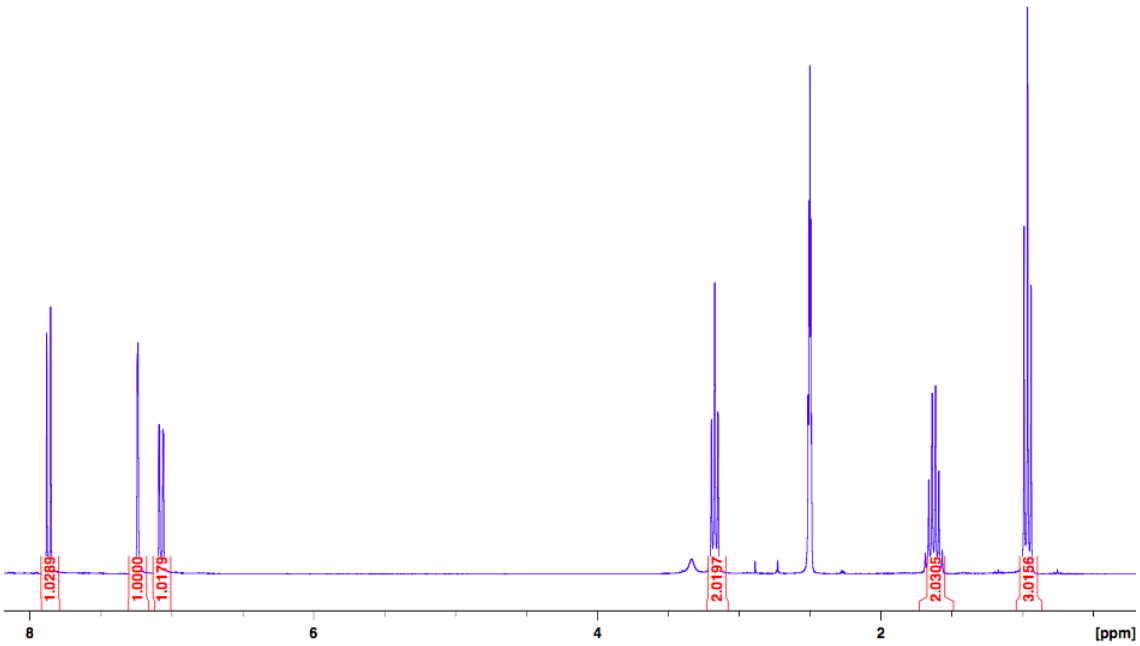

Figure 4.38. ^{1}H NMR spectrum for H_2BDC-NHPr in DMSO-d_6.

4.11.1.2. 2-(Butylamino)benzene-1,4-dicarboxylic acid, H_2BDC-NHBu

In a round-bottom flask, H_2BDC-NH_2 (200 mg, 1.104 mmol) was dissolved in DMF (10 mL) with stirring. To this solution, butanal (0.195 mL, 2.208 mmol) was added and the solution stirred for 1 hour. The solution was then cooled in an ice bath and $NaCNBH_3$ (139 mg, 2.204 mmol) was added. The reaction mixture was stirred at room temperature for 24 h. The mixture was acidified with 1 M HCl, and deionised water was added until a yellow solid precipitated. Yield: 0.232 g (88 %). ^{1}H NMR (300 MHz, DMSO-d_6) δ/ppm: 7.83 (d, 1H, J = 8.2 Hz), 7.22 (d, 1H, J = 1.5 Hz), 7.07 (dd, 1H, J = 7.8 Hz, 1.5 Hz), 3.16 (t, 2H, J = 7.5 Hz), 1.59 (quintet, 2H, J = 6.7 Hz), 1.39 (sextet, 2H, J = 7.5 Hz), 0.90 (t, 3H, J = 6.7 Hz).

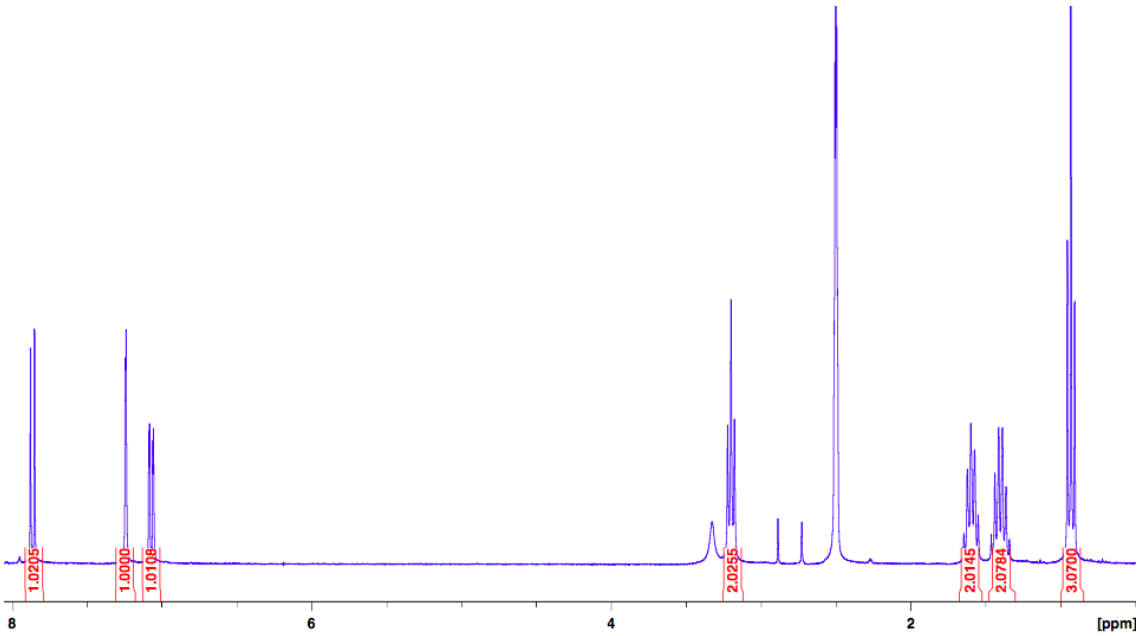

Figure 4.39. ^{1}H NMR spectrum for H_2BDC-NHBu in DMSO-d_6.

4.11.1.3. 2-(Octylamino)benzene-1,4-dicarboxylic acid, H_2BDC-NHC$_8$H$_{17}$

In a round-bottom flask, H_2BDC-NH_2 (200 mg, 1.104 mmol) was dissolved in DMF (10 mL) with stirring. To this solution, octanal (0.345 mL, 2.208 mmol) was added and the solution stirred for 1 hour. The solution was then cooled in an ice bath and $NaCNBH_3$ (139 mg, 2.204 mmol) was added. The reaction mixture was stirred at room temperature for 24 h. The mixture was acidified with 1 M HCl, and deionised water was added until a yellow solid precipitated. Yield: 0.301 g (93 %). ^{1}H NMR (300 MHz, DMSO-d_6) δ/ppm: 7.82 (d, 1H, J = 8.2 Hz), 7.19 (d, 1H, J = 1.4 Hz), 7.08 (dd, 1H, J = 8.2 Hz, 1.4 Hz), 3.17 (t, 2H, J = 7.0 Hz), 1.56 (quintet, 2H, J = 6.3 Hz), 1.39-1.17 (m, 10H), 0.83 (t, 3H, J = 6.9 Hz).

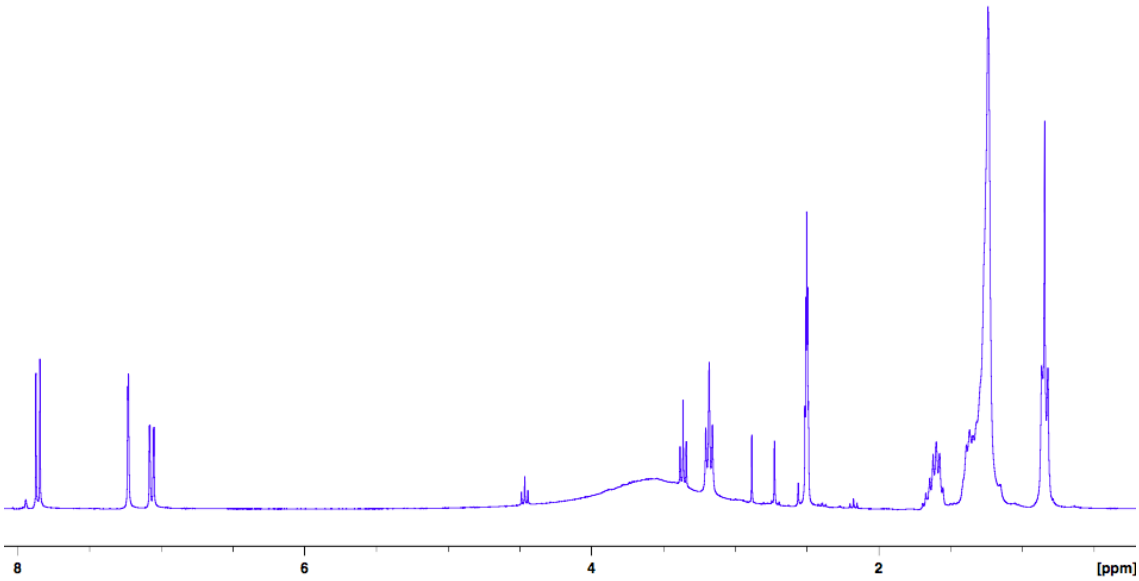

Figure 4.40. ^{1}H NMR spectrum for H_2BDC-NHOc in DMSO-d_6.

4.11.2.MOF Syntheses

4.11.2.1. Synthesis of IRMOF-1, [$Zn_4O(BDC)_3$]

IRMOF-1 was synthesised based on the previously reported procedure by Yaghi and co-workers.[20] In a typical procedure, $Zn(NO_3)_2{\cdot}6H_2O$ (200 mg, 0.672 mmol) and H_2BDC (36.7 mg, 0.221 mmol) were dissolved in DEF (5 mL) in a glass vial. The vial was sealed and the reaction mixture was heated at 105 °C for 48 hours to yield colourless cubic crystals. The crystals were then washed and soaked in chloroform for 3 days, replacing the solvent with fresh solvent every 24 hours before collecting the crystals by filtration. The crystals were dried under reduced pressure and stored under an inert atmosphere (N_2) to avoid crystal degradation.

4.11.2.2. Synthesis of IRMOF-3, [$Zn_4O(BDC\text{-}NH_2)_3$]

IRMOF-3 was synthesised according to a previously reported procedure by Kim and co-workers.[19] In a typical experiment, $Zn(NO_3)_2{\cdot}6H_2O$ (400 mg, 1.34 mmol) and H_2BDC-NH_2 (80 mg, 0.44 mmol) were dissolved in DMF (12 mL) in a glass vial. The vial was sealed and the reaction mixture was heated at 105 °C for 48 hours to yield pale brown cubic crystals. The crystals were then washed and soaked in chloroform for 3 days, replacing the solvent with fresh solvent every 24 hours before collecting the crystals by filtration. The crystals were stored in an inert atmosphere to avoid crystal degradation.

4.11.2.3. Synthesis of IRMOF-NHPr, $[Zn_4O(BDC\text{-}NHC_3H_7)_3]$

IRMOF-NHPr was synthesised according to a previously reported procedure by Burrows and co-workers.[21] In a typical experiment, $Zn(NO_3)_2 \cdot 6H_2O$ (120 mg, 0.402 mmol) and H_2BDC-NHPr (30 mg, 0.134 mmol) were dissolved in DMF (5 mL) in a glass vial. The vial was sealed and the reaction mixture was heated at 105 °C for 48 hours to yellow-orange cubic crystals. The crystals were then washed and soaked in chloroform for 3 days, replacing the solvent with fresh solvent every 24 hours before collecting the crystals by filtration. The crystals were stored in an inert atmosphere to avoid crystal degradation.

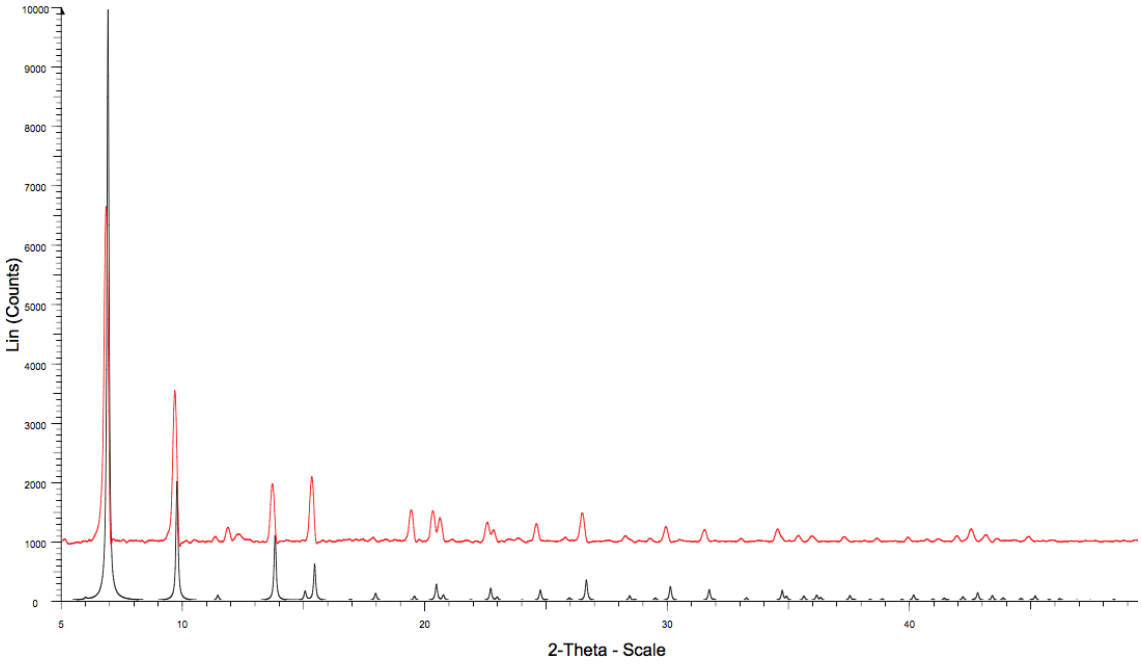

Figure 4.41. Black: Simulated PXRD pattern of IRMOF-1 calculated from the single crystal data.[20] Red: PXRD pattern of IRMOF-NHPr.

4.11.2.4. Synthesis of IRMOF-NHBu, $[Zn_4O(BDC\text{-}NHC_4H_9)_3]$

IRMOF-NHBu was synthesised according to a previously reported procedure by Burrows and co-workers.[21] In a typical experiment, $Zn(NO_3)_2 \cdot 6H_2O$ (112 mg, 0.378 mmol) and H_2BDC-NHBu (30 mg, 0.126 mmol) were dissolved in DMF (5 mL) in a glass vial. The vial was sealed and the reaction mixture was heated at 105 °C for 48 hours to yellow-orange cubic crystals. The crystals were then washed and soaked in chloroform for 3 days, replacing the solvent with fresh solvent every 24 hours before collecting the crystals by filtration. The crystals were stored in an inert atmosphere to avoid crystal degradation.

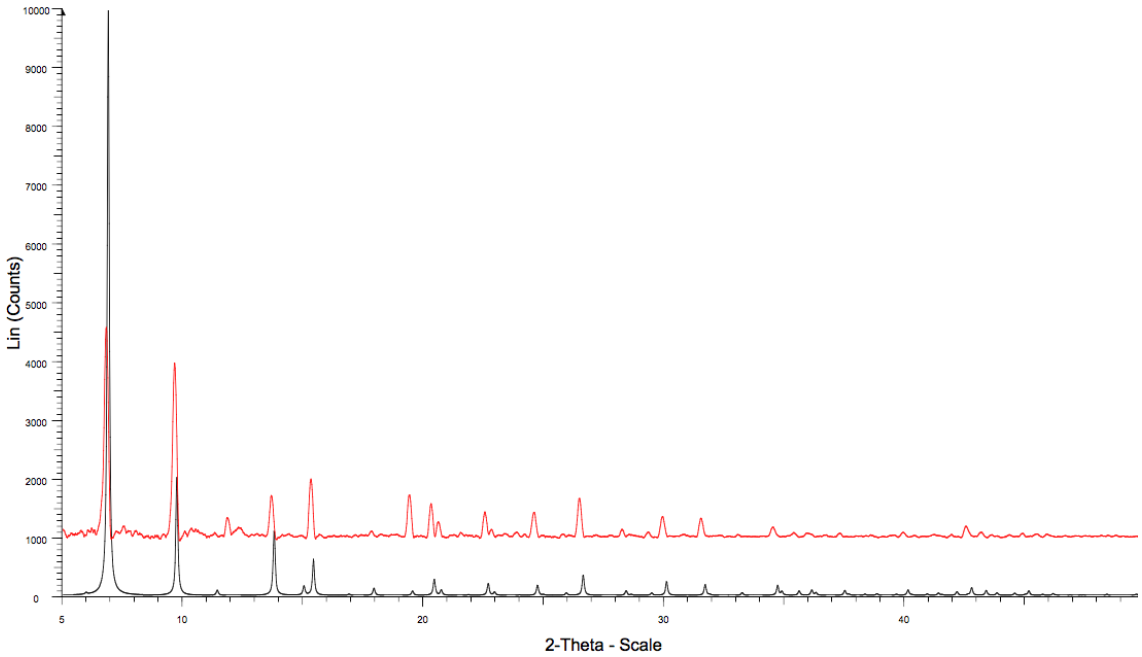

Figure 4.42. Black: Simulated PXRD pattern of IRMOF-1 calculated from the single crystal data.[20] Red: PXRD pattern of IRMOF-NHBu.

4.11.2.5. Synthesis of IRMOF-NHOc, [$Zn_4O(BDC\text{-}NHC_8H_{17})_3$]

IRMOF-NHOc was synthesised according to a previously reported procedure by Burrows and co-workers.[21] In a typical experiment, $Zn(NO_3)_2 \cdot 6H_2O$ (91 mg, 0.306 mmol) and H_2BDC-NHOc (30 mg, 0.102 mmol) were dissolved in DMF (5 mL) in a glass vial. The vial was sealed and the reaction mixture was heated at 105 °C for 48 hours to yellow-orange cubic crystals. The crystals were then washed and soaked in chloroform for 3 days, replacing the solvent with fresh solvent every 24 hours before collecting the crystals by filtration. The crystals were stored in an inert atmosphere to avoid crystal degradation.

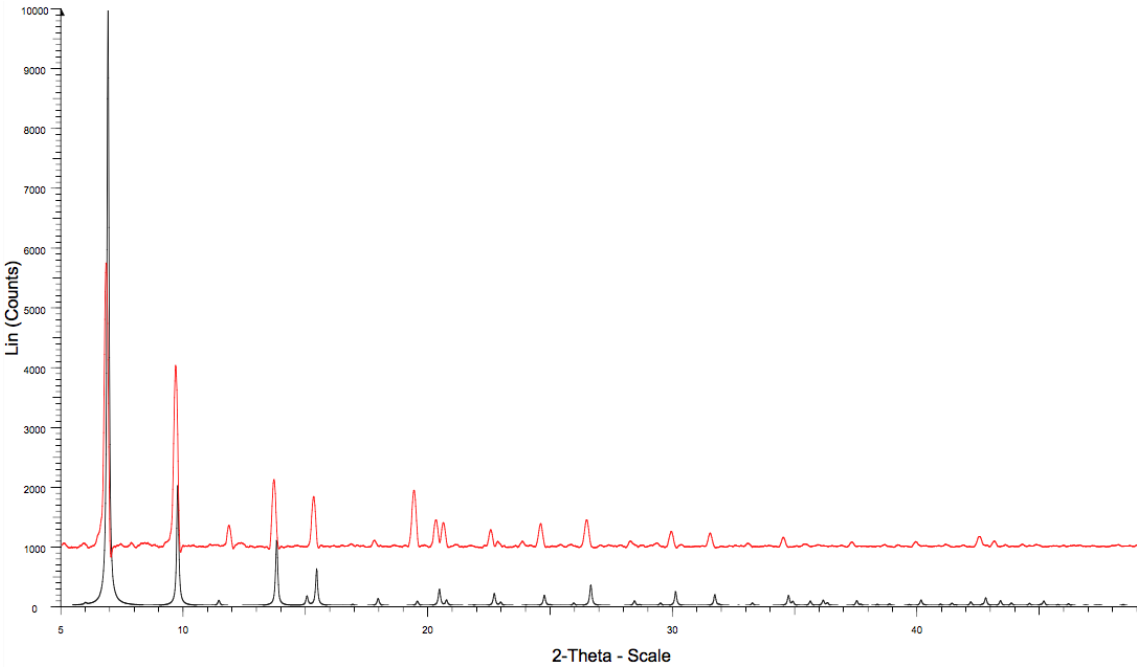

Figure 4.43. Black: Simulated PXRD pattern of IRMOF-1 calculated from the single crystal data.[20] Red: PXRD pattern of IRMOF-NHOc.

4.11.2.6. Synthesis of UiO-66-NHPr, $[Zr_6O_4(OH)_4(BDC\text{-}NHC_3H_7)_6]$

The synthesis UiO-66-NHPr was performed by using an analogous procedure to that of UiO-66-NH_2.[23] In a typical reaction, H_2BDC-NHPr (234 mg, 1.05 mmol) along with $ZrCl_4$ (243 mg, 1.05 mmol) and DMF (12 mL) were loaded into a Teflon lined autoclave. The solution was stirred until the reactants had completely dissolved. The autoclave was placed in an oven and heated at 120 °C for 24 hours. The resulting yellow powder was rinsed and centrifuged with MeOH (6000 rpm for 15 minutes) to remove unreacted H_2BDC-NHPr and residual DMF in the pores. The washing procedure was repeated over 3 days with the solvent replaced every 24 hours. Finally, the UiO-66-NH_2 powder was dried under vacuum at 120 °C for 12 hours.

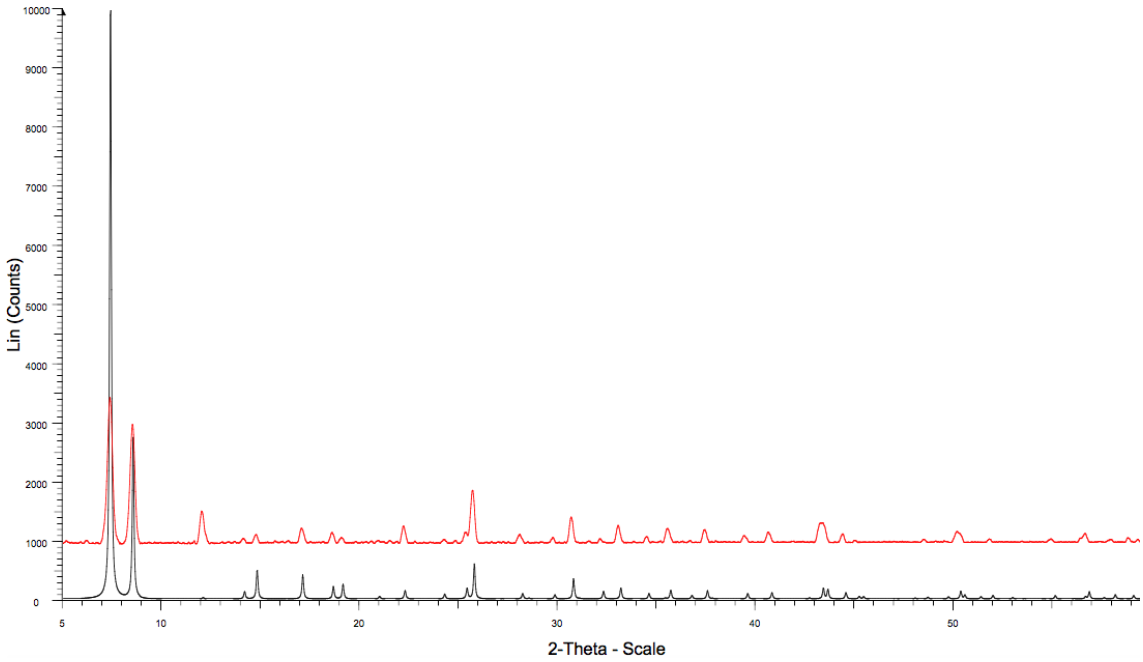

Figure 4.44. Black: Simulated PXRD pattern calculated from the UiO-66 crystal structure.[29] Red: PXRD pattern of UiO-66-NHPr.

4.11.3. Pheromone Loading in MOFs

4.11.3.1. Preparation of $[Zn_4O(BDC\text{-}NH_2)_3]\cdot 0.4OCT$, 3a

IRMOF-3 crystals (100 mg, 0.37 mmol) were added in a glass vial containing 5 mL DMF. OCT (0.23 mL, 1.48 mmol) was then added and the vial was sealed. The mixture was agitated briskly before leaving it to stand at room temperature for 3 days. The crystals were then isolated *via* filtration and rinsed once with fresh DMF (3 mL) to remove any residual OCT on the crystal surface. The crystals were rinsed one further time with fresh DMF (3 mL) to yield $[Zn_4O(BDC\text{-}NH_2)_3]\cdot 0.2OCT$.

4.11.3.2. Preparation of $[Zn_4O(BDC)_3]\cdot 0.2OCT$, 3b

IRMOF-1 crystals (94.7 mg, 0.37 mmol) were added in a glass vial containing 5 mL DMF. OCT (0.23 mL, 1.48 mmol) was then added and the vial was sealed. The mixture was agitated briskly before leaving it to stand at room temperature for 3 days. The crystals were then isolated *via* filtration and rinsed once with fresh DMF (3 mL) to remove any residual OCT on the crystal surface.

4.11.3.3. Preparation of $[Zn_4O(BDC\text{-}NHPr)_3]\cdot 1.7OCT$, 3c

IRMOF-NHPr crystals (116 mg, 0.37 mmol) were added in a glass vial containing 5 mL DMF. OCT (0.23 mL, 1.48 mmol) was then added and the vial was sealed. The mixture was agitated briskly before leaving it to stand at room temperature for 3 days. The crystals were then isolated *via* filtration and rinsed once with fresh DMF (3 mL) to remove any residual OCT on the crystal surface. The crystals were rinsed one further time or twice with fresh DMF (3 mL each wash) to yield $[Zn_4O(BDC\text{-}NHPr)_3]\cdot 1.5OCT$ and $[Zn_4O(BDC\text{-}NHPr)_3]\cdot 1.4OCT$, respectively.

4.11.3.4. Preparation of $[Zn_4O(BDC\text{-}NHPr)_3]\cdot 2.7OCT$, 3d

IRMOF-NHPr crystals (116 mg, 0.37 mmol) were added in a glass vial containing neat OCT. The vial was sealed and the mixture was agitated briskly before leaving it to stand at room temperature for 3 days. The crystals were then isolated *via* filtration and rinsed once with fresh DMF (3 mL) to remove any residual OCT on the crystal surface. The crystals were rinsed one further time or twice with fresh DMF (3 mL each wash) to yield $[Zn_4O(BDC\text{-}NHPr)_3]\cdot 2.2OCT$ and $[Zn_4O(BDC\text{-}NHPr)_3]\cdot 2.0OCT$, respectively.

4.11.3.5. Preparation of $[Zn_4O(BDC\text{-}NHBu)_3]\cdot OCT$, 3e

IRMOF-NHBu crystals (121 mg, 0.37 mmol) were added in a glass vial containing 5 mL DMF. OCT (0.23 mL, 1.48 mmol) was then added and the vial was sealed. The mixture was agitated briskly before leaving it to stand at room temperature for 3 days. The crystals were then isolated *via* filtration and rinsed once with fresh DMF (3 mL) to remove any residual OCT on the crystal surface.

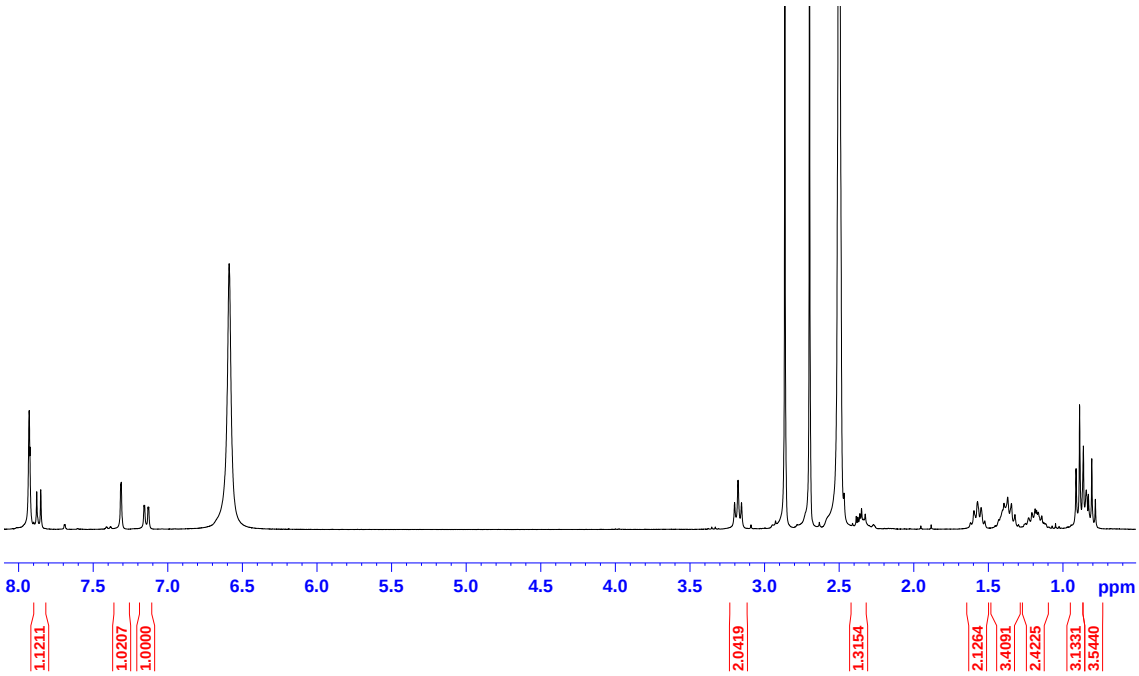

Figure 4.45. The ^{1}H NMR spectrum for **3e** (rinsed three times with DMF).

4.11.3.6. Preparation of $[Zr_6O_4(OH)_4(BDC\text{-}NHPr)_6]\cdot 5.5OCT$, 3g

UiO-66-NHPr powder (124 mg, 0.37 mmol) was added in a glass vial containing neat OCT. The vial was sealed and the mixture was agitated briskly before leaving it to stand at room temperature for 3 days. The powder was then isolated *via* centrifugation and rinsed once with fresh DMF (3 mL) to remove any residual OCT on the MOF surface. The powder was rinsed one further time or twice with fresh DMF (3 mL each wash) to yield $[Zn_4O(BDC\text{-}NHPr)_3]\cdot 2.8OCT$ and $[Zn_4O(BDC\text{-}NHPr)_3]\cdot OCT$, respectively.

4.11.3.7. Preparation of $[Zn_4O(BDC\text{-}NHPr)_3]\cdot 0.7MHP$, 3h

IRMOF-NHPr crystals (116 mg, 0.37 mmol) were added in a glass vial containing 5 mL *n*-hexane. MHP (0.23 mL, 1.48 mmol) was then added and the vial was sealed. The mixture was agitated briskly before leaving it to stand at room temperature for 3 days. The crystals were then isolated *via* filtration and rinsed once with fresh *n*-hexane (3 mL) to remove any residual MHP on the crystal surface.

4.11.3.8. Preparation of $[Zn_4O(BDC\text{-}NHPr)_3]\cdot MHP$, 3i

IRMOF-NHPr crystals (500 mg, 1.60 mmol) were added in a glass vial containing neat MHP. The vial was sealed and the mixture was agitated briskly before leaving it to stand at room temperature for 3 days. The crystals were then isolated *via* filtration and

rinsed once with fresh *n*-hexane (3 mL) to remove any residual MHP on the crystal surface.

4.12. References

1. P. Horcajada, C. Serre, M. Vallet-Regi, M. Sebban, F. Taulelle and G. Ferey, *Angew. Chem. Int. Ed.*, 2006, **45**, 5974.
2. A. D. Burrows, M. Jurcic, L. L. Keenan, R. A. Lane, M. F. Mahon, M. R. Warren, H. Nowell, M. Paradowski and J. Spencer, *Chem. Commun.*, 2013, **49**, 11260.
3. S. Rojas, F. J. Carmona, C. R. Maldonado, P. Horcajada, T. Hidalgo, C. Serre, J. A. R. Navarro and E. Barea, *Inorg. Chem.*, 2016, **55**, 2650.
4. E. Khodaverdi, H. A. Soleimani, F. Mohammadpour and F. Hadizadeh, *Chem. Biol. Drug Des.*, 2016, **87**, 849.
5. R. Amorim, N. Vilaca, O. Martinho, R. M. Reis, M. Sardo, J. Rocha, A. M. Fonseca, F. Baltazar and I. C. Neves, *J. Phys. Chem. C*, 2012, **116**, 25642.
6. P. Horcajada, C. Serre, G. Maurin, N. A. Ramsahye, F. Balas, M. Vallet-Regí, M. Sebban, F. Taulelle and G. Férey, *J. Am. Chem. Soc.*, 2008, **130**, 6774.
7. C.-Y. Sun, C. Qin, C.-G. Wang, Z.-M. Su, S. Wang, X.-L. Wang, G.-S. Yang, K.-Z. Shao, Y.-Q. Lan and E.-B. Wang, *Adv. Mater.*, 2011, **23**, 5629.
8. W. Xuan, C. Zhu, Y. Liu and Y. Cui, *Chem. Soc. Rev.*, 2011, **41**, 1677.
9. A. R. Chowdhuri, D. Bhattacharya and S. K. Sahu, *Dalton Trans.*, 2016, **45**, 2963.
10. K. M. Taylor-Pashow, J. Della Rocca, Z. Xie, S. Tran and W. Lin, *J. Am. Chem. Soc.*, 2009, **131**, 14261.
11. J. Montoya-Lerma, C. Giraldo-Echeverri, I. Armbrecht, A. Farji-Brener and Z. Calle, *Int. J. Pest Manage.*, 2012, **58**, 225.
12. F. E. Regnier and J. H. Law, *J. Lipid Res.*, 1968, **9**, 541.
13. D. Bhagat, S. K. Samanta and S. Bhattacharya, *Sci. Rep.*, 2013, **3**.
14. S. W. Robinson and J. M. Cherrett, *Bull. Entomol. Res.*, 1978, **68**, 159.
15. W. O. H. Hughes and D. Goulson, *Bull. Entomol. Res.*, 2002, **92**, 213.
16. R. G. Riley, R. M. Silverstein and J. C. Moser, *J. Insect Physiol.*, 1974, **20**, 1629.
17. V. C. Norman, T. Butterfield, F. Drijfhout, K. Tasman and W. O. H. Hughes, *J. Chem. Ecol.*, 2017, **43**, 225.
18. R. M. Crewe, M. S. Blum and C. A. Collingwood, *Comp. Biochem. Physiol. B: Comp. Biochem.*, 1972, **43**, 703.
19. H. Yim, E. Kang and J. Kim, *Bull. Korean Chem. Soc.*, 2010, **31**, 1041.
20. M. Eddaoudi, J. Kim, N. Rosi, D. Vodak, J. Wachter, M. O'Keeffe and O. M. Yaghi, *Science*, 2002, **295**, 469.
21. L. L. Keenan, H. Amer Hamzah, M. F. Mahon, M. R. Warren and A. D. Burrows, *CrystEngComm*, 2016, **18**, 5710.
22. S. J. Yang and C. R. Park, *Adv. Mater.*, 2012, **24**, 4010.
23. S. J. Garibay and S. M. Cohen, *Chem. Commun.*, 2010, **46**, 7700.
24. J. C. Moser, R. C. Brownlee and R. Silverstein, *J. Insect Physiol.*, 1968, **14**, 529.
25. O. K. Farha, A. Özgür Yazaydın, I. Eryazici, C. D. Malliakas, B. G. Hauser, M. G. Kanatzidis, S. T. Nguyen, R. Q. Snurr and J. T. Hupp, *Nat. Chem.*, 2010, **2**, 944.
26. R. A. Smaldone, R. S. Forgan, H. Furukawa, J. J. Gassensmith, A. M. Z. Slawin, O. M. Yaghi and J. F. Stoddart, *Angew. Chem. Int. Ed.*, 2010, **49**, 8630.
27. M. K. Smith, S. R. Angle and B. H. Northrop, *J. Chem. Educ.*, 2015, **92**, 368.
28. R. M. Abdelhameed, H. Abdel-Gawad, M. Elshahat and H. E. Emam, *RSC Adv.*, 2016, **6**, 42324.

29. J. H. Cavka, S. Jakobsen, U. Olsbye, N. Guillou, C. Lamberti, S. Bordiga and K. P. Lillerud, *J. Am. Chem. Soc.*, 2008, **130**, 13850.